

Electro-Optically Induced Responses and Diffractive Effects in Liquid Crystal Cells; Investigating Experiments & Simulations

Thesis

for the degree of

doctor rerum naturalium (Dr. rer. nat.)

approved by the Faculty of Natural Sciences of Otto von Guericke
University Magdeburg

by **Atefeh Habibpournoghadam, M.Sc.**

born on 25.04.1986 in Shiraz, Iran

Examiners: Prof. Dr. rer. nat. habil. Ralf Stannarius
Prof. Dr. rer. nat. Uwe Thiele

submitted on: 13.10.2020

defended on: 11.05.2021

Table of Contents

Table of Contents	i
List of Figures	v
Abstract	ix
Abstrakt	xi
Introduction & Motivation	xiii
References	xvii

Chapter 1: Introduction of Director Field, Q -Tensor & Free Energies of an LC System

1.1. Introduction to nematics	1
1.2. Introduction to nematic cholesterics	2
1.3. Order parameter	4
1.4. Q -tensor definition	7
1.5. Landau-de Gennes theory	10
1.6. Frank-Oseen elastic free energy and elastic constants	11
1.7. LC response to an electric field	12
References	15

Chapter 2: Optical Properties of Uniaxial LCs

2.1. Introduction	19
2.2. Light propagation in the LC	19
2.3. Transmitted light wave between crossed linear polarizers	22
References	25

Chapter 3: Discussion on the Photovoltaic Effects

3.1. Introduction	27
3.2. Photovoltaic (PV) effect	27
3.3. Photovoltaic effect in p-n junction semiconductors	30
3.4. Photovoltaic effect in ferroelectric materials, so-called bulk photovoltaic (BPV) effect	33
3.5. Microscopic investigation of the BPV effect	34
3.6. Scalar formulation of the BPV current	35
3.7. Phenomenological formulation of the BPV current	37
3.8. One-center charge transport scheme and rate equations	38
3.9. Light spectrum and optical response of the LiNbO ₃ and Fe:LiNbO ₃ (Fe:LN)	40
3.10. Permittivity and refractive indices	41
References	42

Chapter 4: Photorefractive Effect in NLC Cells Caused by Anomalous Electrical Properties of ITO Electrodes

4.1. Abstract	47
4.2. Introduction	48
4.3. ITO electrode as the SPR effect source in the neat NLC cells	50
4.3.1. Opto-electronic behavior of ITO thin films	51
4.3.2. Frequency dependent-conductivity of ITO thin films	54
4.3.3. ITO conductivity in very low DC operating regime	57
4.4. A brief review of the self-action of a visible light beam in the NLC cells biased with a DC electric field	58
4.4.1. The SPR effect manifested in the formation of the aberration patterns	59
4.4.2. Generation of optical vortices in the NLC context due to the SPR effect	61
4.4.3. SPR effect-assisted formation of umbilical defects in a NLC cell made from a photo-responsive substrate	64
4.5. Conclusions	66
References	67

Chapter 5: Theoretical Prediction of Umbilics Creation in NLCs with Positive Dielectric Anisotropy

5.1. Abstract	75
5.2. Introduction	76
5.3. Simulation of the photo-generated electric field in the hybridized LC cells equipped with an ITO layer	78
5.4. Discussion on the charge carrier accumulation in the ITO thin film	81
5.5. Modeling of the director field in a splay umbilic observed in NLC with negative anisotropy (model umbilic)	83
5.6. Formation of a splay umbilic in NLC with positive dielectric anisotropy	87
5.7. Simulation of the output intensity patterns	91
5.8. Conclusions	97
References	98

Chapter 6: Topological Defect Creation in NLC Cells with Photoresponsive Substrates

6.1. Introduction	103
6.2. Nematic disclinations in two-dimensions (2D)	105
6.3. Experimental procedures	108
6.4. Electric fields in the studied LC cells	110
6.5. Defect formation in LC samples without ITO application	112
6.5.1. Defects formation in open LC samples	112
6.5.2. Theoretical investigations and simulation of an induced topological defect localized at the laser beam spot	115
6.5.3. Defects formation in confined LC samples	119
6.6. Defects formation in LC cells covered with glass plates and equipped with ITO layers (without coating)	122
6.7. Defects formation in LC test cells covered with uniaxially rubbed polyimide coated, ITO-equipped glasses	127
6.8. Conclusions	129
References	132

Chapter 7: Tunable Diffraction Gratings Driven in In-Plane Switching (IPS) LC Cells

7.1. Abstract	135
7.2. Discussion on the diffraction properties of the model grating	136
7.3. Conclusions	139
7.4. Tunable diffraction gratings in copolymer network liquid crystals driven with interdigitated electrodes	141
7.4.1. Introduction to the application of PNLCs in diffraction gratings	141
7.4.2. Materials and experimental methods	143
7.4.3. Domain sizes and electro-optic responses	145
7.4.4. Experimental diffraction behavior	148
7.4.5. Theoretical investigations and simulations	152
7.4.6. Director field simulation and observation of disclination walls	158
7.4.7. Simulated optical phase delays	164
7.4.8. Simulated diffraction patterns	166
7.4.9. Conclusions	169
References	171

Appendix

Appendix A	175
Appendix B	177
Appendix C	179

List of Figures

1.1. Formation of the cholesteric LC	2
1.2. Schematic representation of the cholesteric	3
1.3. Orientational probability functions for the nematic (generic form) and the isotropic phases	5
1.4. a) and b) Representation of director fields in uniaxial and biaxial LC phases	8
1.5. Deformations in biaxial NLCs	12
2.1. Effective refractive index	21
2.2. The situation of the director field relative to the polarization direction	23
3.1. Diagram of the photovoltaic apparatus	28
3.2. Thin film Se photovoltaic device	29
3.3. a) forward biased p-n junction	30
3.4. Current-voltage characteristics of a p-n junction diode	32
3.5. a) Equivalent circuit of a forward biased p-n junction	32
3.6. Photographs of a) and b) congruent pure LiNbO ₃ and Fe:LN crystals	35
3.7. Formation of the PV electric field	36
3.8. Schematic presentation of charge transition in a one-center model	39
3.9. a) The absorption spectra of LiNbO ₃	40
4.1. Graph of the particular ITO transmission T , reflectance R , and absorption A spectrum	54
4.2. Simulated ITO conductivity	56
4.3. Removal of the DC electric field-screening by the light beam	60
4.4. Director field reorientation in NLCs	62

4.5. Schematic of a hybridized LC test cell	64
4.6. Electric field distribution in the hybridized LC test cell	65
5.1. Schematic of a hybridized LC test cell	77
5.2. Schematic of photogenerated electric field	79
5.3. The photovoltaic electric field (E_{PV})	81
5.4. Numerically obtained electric potential (in volts) distribution	82
5.5. Charge carrier density accumulated at the boundary of ITO	83
5.6. a) Demonstration of the coordinate system elements	85
5.7. Simulated director field of the model umbilic defect	86
5.8. Optically-assisted electric field distribution	89
5.9. Simulated splay umbilic director field	91
5.10. Simulated phase change profiles	92
5.11. Simulated output intensities	95
5.12. Transmitted intensity profiles	96
6.1. Schematic of LC cells	104
6.2. (a) Schlieren texture of a thin nematic LC film	106
6.3. Director profiles of different disclinations	107
6.4. Photograph of a covered film sample	108
6.5. Schematic of the experimental setup	109
6.6. Simulated electric-field distributions	111
6.7. Photographs of the open film samples	113
6.8. Images of the defects created in the open film samples	114
6.9. a) The electric field distribution	116
6.10. Demonstration of the hyperbolic defect induced	118
6.11. Formation of defects in a confined LC cell	119
6.12. Studying defect formation in a confined film sample	121
6.13. Images recorded in the ITO-equipped nematic	122
6.14. Simulated electric field distribution	122
6.15. The director field n distribution in the LC cell	123
6.16. Photo-induced non-singular radial defects created	124
6.17. Modelling results of the transmitted intensity	125
6.18. Radius of the electrically induced non-singular optical patterns	126
6.19. The response times of the ITO-equipped LC cells	126
6.20. Micrographs of the photo-induced optical ring patterns	127
6.21. Variation of the maximum radius associated to the optical ring patterns	128

6.22. The response times of the LC cells	128
7.1. Structures of two different phase gratings	136
7.2. a) and b) Normalized diffraction intensity distributions	139
7.3. Normalized diffraction patterns of the overall grating	139
7.4. Schematic of an IPS test cell investigated	143
7.5. (a) POM image recorded in a PNLC	146
7.6. Dark field microscopy images	147
7.7. SEM image recorded in a PNLC sample	147
7.8. Experimental diffraction patterns in the neat NLC	148
7.9. Experimental diffraction patterns in PNLC (with 6% OPC)	149
7.10. Experimental results of diffraction patterns in PNLC (with 8% OPC)	150
7.11. Experimental diffraction efficiencies	150
7.12. The impact of the analyzer on the intensity modulations	151
7.13. (a) and (b) Cross-sectional view of the geometry	153
7.14. (a) The electric field distribution in one period	154
7.15. Simulated director field in a sample filled with undoped E7	159
7.16. Director field distribution in the PNLC	161
7.17. Voltage induced evolution of the azimuthal and polar angles	162
7.18. Simulated transmittance of an IPS cell filled with neat E7 LC	163
7.19. Numerically calculated phase change profiles	165
7.20. Simulated normalized diffraction intensities for the neat NLC	167
7.21. Simulated normalized diffraction intensities in the PNLC	167
7.22. Numerically calculated the 0th and 1st diffraction orders efficiencies	168

Abstract

This thesis aims at developing theories and numerical modeling of electro-optical responses induced in nematic liquid crystal (NLC) cells. Studies were done in couple of test cells with different configurations and designs. Simulations were performed by means of Q -tensor approach.

In planar test cells with specific application of a ferroelectric substrate, i.e., iron doped lithium niobate (Fe:LiNbO₃), director field realignment and defect generations were investigated. In such test cells, a photovoltaic (PV) electric field was induced in the ferroelectric substrate due to the charge carrier separation, which had a bell shape distribution in the LC film near to the interface of LC with substrate. The photovoltaic (PV) electric field can exceed the Fréedericksz threshold inducing director field realignment.

Equipping test cells with indium tin oxide (ITO) as thin electrode enhanced the LC responses due to the surface photorefractive effect. Impact of the electric behavior of the ITO and its semiconducting mode of operation on the undoped NLC realignment was mysterious and unclear to some extents. There were some complexities remaining to be solved and explained. In this thesis, the key role of ITO in the surface photorefractive effect, hence LC director reconfiguration, was explained and clarified.

Studying the impact of ITO on the director field realignment in hybrid test cells with the ferroelectric substrate led to a new finding regarding generation of optical vortices (OVs) as a result of umbilical defect creation in the nematic liquid crystals with positive dielectric anisotropy. For comparison, umbilical defect formation in LC slab filled with nematic LC with negative dielectric anisotropy was studied. Slab was lit by a plane light beam being incident normally on the surface. LC was initially in homeotropic alignment provided by a suitable anchoring agent on the surfaces. Director field realignment was induced by a static electric field with a uniform distribution in the slab and being initially aligned with the LC optical axis.

Phase grating in neat LC cell and in cells incorporated with polymer in an in-plane switching (IPS) geometry (striped electrodes) were investigated. As the first step, diffraction properties of ideal rectangular gratings attributed to the IPS cells were studied. The model was further developed by modeling director field realignments as a function of applied voltage. Director field reorientation from initial planar alignment induces phase delay between the extraordinary and ordinary waves of the incoming electromagnetic light beam, hence creating phase grating due to the fringe electric field distribution in the IPS cells.

The phase gratings in the neat NLC cell and in polymer network NLC cells were simulated. By means of fast Fourier transform method, diffraction patterns were modeled and compared with the experimental results. Disclination walls located on top of the electrodes were obtained in IPS test cells filled with neat NLC, where the rubbing angle was supposed equal to zero.

Abstrakt

Diese Arbeit zielt darauf ab, Theorien und numerische Modelle elektro-optischer Reaktionen zu entwickeln, die in nematischen Flüssigkristallzellen (NLC-Zellen) induziert werden. Untersuchungen wurden in Testzellen mit unterschiedlichen Konfigurationen und Ausführungen durchgeführt. Die Simulationen erfolgten mittels eines Q-Tensor-Ansatzes. In planaren Testzellen mit spezifischer Beschichtung mit einem ferroelektrischen Substrat, d. H. eisendotiertem Lithiumniobat (Fe: LiNbO₃), wurden die Umorientierung des Direktorfeldes und die Entstehung von Defekten untersucht. In solchen Testzellen wird im ferroelektrischen Substrat ein elektrisches Photovoltaik-Feld induziert. Das geschieht aufgrund der Ladungsträgertrennung, im LC-Film nahe der Grenzfläche von LC und Substrat, die eine Glockenformverteilung aufweist. Das elektrische Feld der Photovoltaik (PV) kann die Fréedericksz-Schwelle überschreiten, was zu einer Neuausrichtung des Direktorfeldes führt.

Die Ausrüstung von Testzellen mit Indiumzinnoxid (ITO) als dünner Elektrode verbesserte die LC-Reaktionen aufgrund des photorefraktiven Oberflächeneffekts. Der Einfluss des elektrischen Verhaltens des ITO und seiner halbleitenden Eigenschaften auf die Umorientierung des undotierten NLC war rätselhaft und teilweise unklar. Es blieben dabei noch einige komplexe Fragen zu lösen und zu klären. In der vorliegenden Arbeit wird die Schlüsselrolle des ITO für den photorefraktiven Oberflächeneffekt und damit für die Umorientierung des LC-Direktors beschrieben und geklärt.

Die Untersuchung des Einflusses von ITO auf die Neuausrichtung des Direktorfeldes in Hybrid-Testzellen mit dem ferroelektrischen Substrat führte zu einem neuen Ergebnis hinsichtlich der Erzeugung optischer Wirbel (OVs) als Ergebnis der Entstehung von Nabeldefekten (Umbiliken) in nematischen Flüssigkristallen mit positiver dielektrischer Anisotropie. Zum Vergleich wurde die Bildung solcher Nabeldefekte in einer mit nematischem LC gefüllten LC-Platte mit negativer

dielektrischer Anisotropie untersucht. Die Platte wurde von einem ebenen Lichtstrahl beleuchtet, der normal auf die Oberfläche fiel. Der LC befand sich anfänglich in homöotroper Ausrichtung, die durch geeignete Verankerung an den Oberflächen realisiert wurde. Die Reorientierung des Direktorfeldes wurde durch ein statisches elektrisches Feld mit einer gleichmäßigen Verteilung in der Platte induziert, das anfänglich mit der optischen Achse des LC ausgerichtet war.

Phasengitter wurden in reinen LC-Zellen untersucht und in Zellen mit In-Plane-Switching-Geometrie (IPS, Streifenelektroden), die ein inneres Polymergerüst enthielten. Im ersten Schritt wurden die Beugungseigenschaften idealer rechteckiger Gitter untersucht, die den IPS-Zellen vergleichbar sind. Das Modell wurde weiterentwickelt, indem Feldausrichtungen des Direktors als Funktion der angelegten Spannung modelliert wurden. Die Umlagerung des Direktorfeldes von der anfänglichen planaren Ausrichtung induziert eine Phasenverzögerung zwischen den außerordentlichen und ordentlichen Wellen des einfallenden elektromagnetischen Lichtstrahls, wodurch aufgrund der Verteilung des elektrischen Randfeldes in den IPS-Zellen ein Phasengitter erzeugt wird.

Die Phasengitter in der reinen NLC-Zelle und in Polymernetzwerk-NLC-Zellen wurden simuliert. Mittels der schnellen Fourier-Transformation wurden Beugungsmuster modelliert und mit den experimentellen Ergebnissen verglichen. Über den Elektroden befindliche Splay-Wände des Direktors wurden in IPS-Testzellen gefunden, die mit reinem NLC gefüllt waren, wobei ein Reibwinkel (Vorzugsorientierung) von Null angenommen wurde.

Introduction & Motivation

“LCs are beautiful and mysterious.”

P. G. de Gennes

Matter is commonly categorized as solid, liquid or gas based on the type and degree of ordering of constituent molecules with respect to their neighbors. Perfect long-range positional and orientational ordering are observed in crystalline solid structures, while commonly only short-range orientational ordering exists in the liquid states. On the other hand, gases, isotropic liquids and amorphous solids are statistically characterized by long-range disorders¹. Liquid crystal (LC) as a mesophase state (: an intermediate state between solid and liquid) exhibits long-range orientational ordering and in some cases positional ordering as well².

The main focus of this thesis is calamitic nematic LCs, briefly called nematics and noted as NLC. The molecular arrangement in a NLC is schematically shown in Figure 1a. Anisotropy in the structure of the NLC leads to temperature dependent electrical and optical anisotropies, which open new avenue for designing opto-electronic devices based on LC applications.

Complexity in the electro-optical behavior has made numerical modeling an essential tool for studying LC cells. Simulations can provide expert insight into the LC systems as shown in this thesis. When it comes to providing materials and making test cells, chemistry is very helpful. However, physics comes from the necessity to understand electro-optic mechanisms and responses in the LC systems. Theories were developed by taking into account the real aspects of each system, while considering and comparing the numerical results with the ones obtained for the corresponding ideal cases were useful and instructive. The theoretical results were

obtained by means of numerical modeling with Comsol and Matlab softwares. As it will be seen, the simulations were able to describe and predict the responses seen in the LC cells and verified in the experiments.

In the studied LC cells, the director field \mathbf{n} (: representing the average alignment of the LC molecules) was simulated by means of a \mathbf{Q} -tensor approach (discussed in Chapters 1 and applied in Chapters 5, 6 and 7). By numerically solving the **Euler-Lagrange** equation coupling the director field with present electric fields, the evolution of the \mathbf{Q} -tensor elements induced by the electric field was obtained. Director field realignments relative to the light beam propagation direction (shown in Figure 1.b, c, as examples) can cause a locally modulation of the effective refractive index, which induces optical phase delay in the transmitted light beam, as discussed theoretically in Chapter 2. Projection of the realigned director field in the transverse plane (normal to the propagation direction) together with the optical phase delay determine characteristics of output optical patterns associated with the transmitted beam between polarizers.

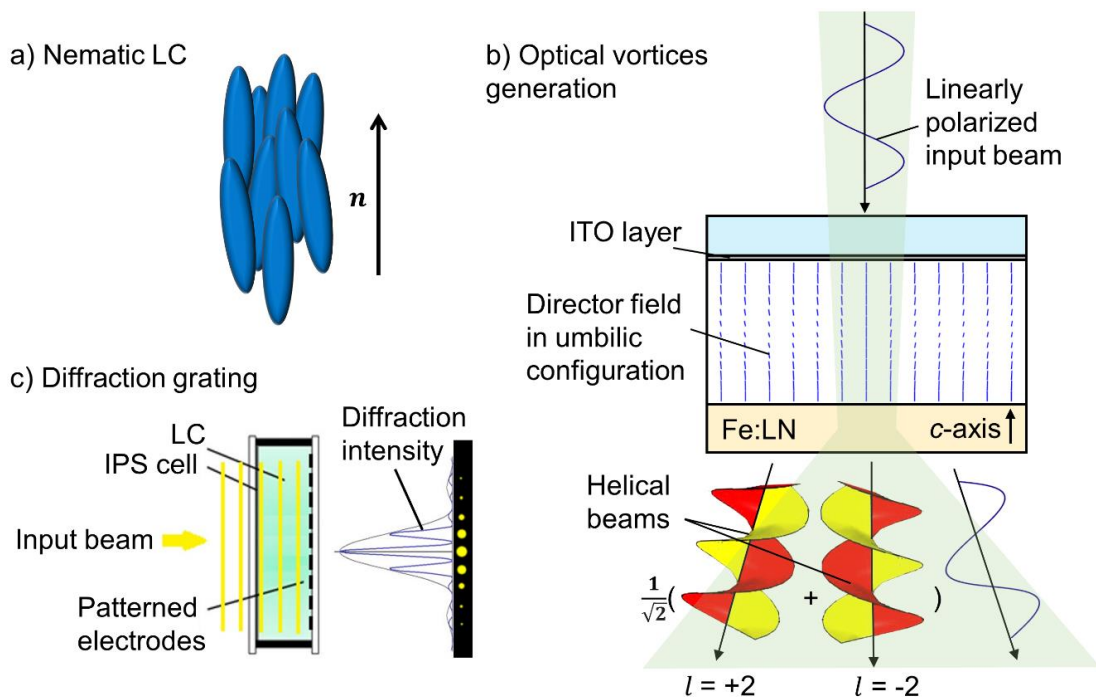


Figure 1. Schematic diagram of a) the molecular arrangement in a NLC, b) generation of entangled optical vortices by means of umbilic formation in the NLC, and c) application of a LC film in diffraction grating.

Photosensitive ferroelectric substrates of iron-doped lithium niobate (LiNbO₃:Fe, Fe:LN) were employed in the LC cells in order to optically drive a photovoltaic (PV) electric field as a result of charge carriers separation in the bulk

Fe:LN. It was found that the optically-induced electric fields can efficiently reorient the LC director field, giving rise to umbilical configurations and topological defects. Different approaches of generating the PV electric field, as well as their widespread applications are discussed in detail in Chapter 3.

An important aspect of NLCs are topological defects emerging from breaking the orientational order. Because of similarities with dislocations in the positional order of solid crystals, they are called disclinations³. Frank point defects appear as singular defects, whereas, umbilical defects (with non-singular director configurations and commonly seen as vortices in the director orientations) possess a continuous core⁴.

NLCs with negative dielectric anisotropy and homeotropic anchoring have been extensively employed as effective templates for a creation of helical waves, known as optical vortices (OVs)^{5,6}, through umbilical defects (in short 'umbilics'). An example is shown in Figure 1b. OVs with screw phase dislocations in their wave front carry orbital angular momentum where the light intensity goes to zero at centers in the place of phase singularities⁷. OVs are commonly formed from N spiral arms, where N is equal to the optical topological charge l giving the amount of orbital angular momentum per photon as $l\hbar$, and the sign of l determines the wave helicity⁵.

Recently it is shown that the NLCs with positive dielectric anisotropy and homeotropic anchoring can also serve as efficient umbilical contexts for the creation of optical vortices, as discussed in Chapters 4 and 5, by means of an optically assisted photovoltaic field⁸ due to the surface photorefractive (SPR) effect (introduced in Chapter 5).

In Chapter 6, topological defects generated in the LC cells assembled with photosensitive ferroelectric substrates of Fe:LiNbO₃ and covered with plain glass covers were studied. The photovoltaic electric field with a bell shape distribution on top of the LC/Fe:LN interface induces the formation of topological defects with strength -1 associated with hyperbolic configurations. Simulated transmitted intensities are seen as Maltese cross patterns between cross linear polarizers in good agreement with experiments⁹.

My background in studying Fourier transforms and publishing the book of "*Fourier transforms, Concepts and its Applications Using Matlab*" in Persian, and bringing them into applications as my interests, motivated me to develop a theory regarding LCs diffraction gratings, as well as diffraction grating tuning by means of introducing polymer network into the NLC cells.

Diffraction gratings are extensively exploited in modern optoelectronic technologies. LCs as birefringent media can create diffraction gratings by means of inducing phase retardation (change) on the incoming electromagnetic waves,

emerging from the reorientation of the LC director field in response to a biased electric field^{10,11,12,13,14}. High responsivity to an applied electric or magnetic field makes the NLCs promising candidates for diffraction gratings applications. In-plane switching (IPS) cells filled in with neat LCs were utilized as diffraction phase grating (schematically shown in Figure 1c), which is discussed thoroughly in Chapter 7.

Introducing polymer into the NLCs via a polymerization process of monomers generates polymer network (stabilized) LCs, composed of a continuous matrix of the LC while containing a small amount ($\approx 5\text{wt } \%$) of dispersed cross-linked polymers^{3,15}. The structure and distribution of the polymer network is affected by the initial alignment of the LC, and, in turn, it controls the alignment of the LC after its formation^{3,16} through elastic interactions and anchoring energy. As a result, the stabilization of the LCs by means of the polymer network is achievable. Polymer network liquid crystals (PNLCs) have potential application in direct view reflective displays¹⁷ and tunable diffraction gratings³, later discussed in Chapter 7.

References

- ¹ Hansen, J. P., & McDonald, I. R. *Theory of simple liquids: with applications to soft matter*. Academic Press, 2013.
- ² Andrienko, D. Introduction to liquid crystals. *Journal of Molecular Liquids*. 2018, 267, 520-541.
- ³ Frank, F. C. (1958). I. Liquid crystals. On the theory of liquid crystals. *Discussions of the Faraday Society*, 25, 19-28.
- ⁴ Rapini, A. *Statistic properties and shear-induced displacements*. *J. Math. Phys.* 1973, 34, 629-633.
- ⁵ Marrucci, L. (2008). Generation of helical modes of light by spin-to-orbital angular momentum conversion in inhomogeneous liquid crystals. *Molecular Crystals and Liquid Crystals*, 488(1), 148-162.
- ⁶ Barboza, R.; Bortolozzo, U.; Clerc, M. G.; Residori, S.; Vidal-Henriquez, E. Optical vortex induction via light-matter interaction in liquid-crystal media. *Adv. Opt. Photonics* 2015, 7, 635-683.
- ⁷ Desyatnikov, A. S., Torner, L., & Kivshar, Y. S. (2005). Optical vortices and vortex solitons. *arXiv preprint nlin/0501026*. *Progress in Optics* 47, 291-391 (2005).
- ⁸ Habibpournmoghadam, A. (2019). Theoretical Prediction of Umbilics Creation in Nematic Liquid Crystals with Positive Dielectric Anisotropy. *ACS omega*, 4(25), 21459-21468. (<https://doi.org/10.1021/acsomega.9b03158>, Copyright © 2019 American Chemical Society)
- ⁹ Habibpournmoghadam, A., Jiao, L., Reshetnyak, V., Evans, D. R., & Lorenz, A. (2017). Optical manipulation and defect creation in a liquid crystal on a photoresponsive surface. *Physical Review E*, 96(2), 022701. (<https://doi.org/10.1103/PhysRevE.96.022701>, Copyright ©2017 American Physical Society)
- ¹⁰ Habibpournmoghadam, A., Wolfram, L., Jahanbakhsh, F., Mohr, B., Reshetnyak, V., & Lorenz, A. (2019). Tuneable Diffraction Gratings in Copolymer Network Liquid Crystals Driven with Interdigitated Electrodes. *ACS Applied Electronic Materials*, 1(12), 2574-2584. (<https://doi.org/10.1021/acsaelm.9b00579>, Copyright © 2019 American Chemical Society)
- ¹¹ Xu, D., Tan, G., & Wu, S. T. (2015). Large-angle and high-efficiency tunable phase grating using fringe field switching liquid crystal. *Optics Express*, 23(9), 12274-12285.
- ¹² Kim, J., Na, J. H., & Lee, S. D. (2012). Fully continuous liquid crystal diffraction grating with alternating semi-circular alignment by imprinting. *Optics express*, 20(3), 3034-3042.
- ¹³ Bellini, B., Geday, M., Bennis, N., Spadło, A., Quintana, X., Otón, J., & Dąbrowski, R. (2006). Design and simulation of single-electrode liquid crystal phased arrays. *Opto-Electronics Review*, 14(4), 269-273.
- ¹⁴ Lindquist, R. G., Kulick, J. H., Nordin, G. P., Jarem, J. M., Kowel, S. T., Friends, M., & Leslie, T. M. (1994). High-resolution liquid-crystal phase grating formed by fringing fields from interdigitated electrodes. *Optics letters*, 19(9), 670-672.

¹⁵ Dierking, I. (2000). Polymer network–stabilized liquid crystals. *Advanced Materials*, 12(3), 167-181.

¹⁶ Ma, R. Q., & Yang, D. K. (2000). Freedericksz transition in polymer-stabilized nematic liquid crystals. *Physical Review E*, 61(2), 1567.

¹⁷ Wu, S. T., & Yang, D. K. (2001). *Reflective liquid crystal displays*. John Wiley & Sons Inc.

Chapter 1: Introduction of Director Field, Q -Tensor & Free Energies of an LC System

1.1. Introduction to nematics

In general, liquid crystalline materials can be divided into three classes: Thermotropic, lyotropic and metallotropic¹. While in thermotropic LCs the structural ordering depends only on temperature, the ordering in lyotropic LCs (: typically formed by aqueous solution of amphiphilic molecules (surfactants)) additionally depends on the surfactant concentration². In metallotropic LCs, the behavioral phase depends not only on temperature and concentration but also on the inorganic-organic composition ratio³.

In thermotropic LCs, the first phase transition from isotropic during cooling process is usually nematic⁴, which is one of the most common liquid crystalline phase. If either the constituting molecules are chiral or if chiral dopant molecules are dissolved in a nematic phase (: an achiral host phase), as schematically shown in Figure 1.1, the director becomes spatially twisted giving rise to a helical structure called cholesteric or chiral (*) nematic shown as $N^{*4,5,6}$. In the next section, nematic cholesterics will be discussed briefly.

Isotropic liquids composed from spherically symmetric molecules show both rotational, $O(3)$, and translational, $T(3)$, symmetries⁷. Nematic phases show only translational symmetry $T(3)$ through a uniaxial or a biaxial symmetry group, i.e, $D_{\infty h}$ or D_{2h} , because of the anisotropy in the structure of molecules⁷, as rod-like or disc-

shaped, called calamitic nematic or discotic nematic⁸, respectively. Because of the translational symmetry $T(3)$, there is long-range orientational ordering in the nematic phase: On average, molecules take alignment along a preferential direction, so called director \mathbf{n} , where \mathbf{n} and $-\mathbf{n}$ are principally equivalent^{4,8,9} (as can be seen from Figure 1.1a).

1.2. Introduction to nematic cholesterics

Chiral nematic N^* ^{4,5,6} exhibits long range order in the orientation of molecules, and it can be described by the director field \mathbf{n} , both in common with the nematic phase. In the cholesteric, the director twists in a regular way around an axis perpendicular to the director \mathbf{n} , i.e., the twist axis, as exhibiting a right- or left-handed helical modulation (Figure 1.2) even in an unstrained state. The pitch of the cholesteric p is defined as the length at which the director turns for 2π , **where the periodicity length can be defined as $p/2$, because of indistinguishability of \mathbf{n} and $-\mathbf{n}$** . The pitch p measures the strength of the chirality and commonly is in the range of $0.1 \mu\text{m}$ to several hundred μm . If the pitch p goes to infinity, a cholesteric becomes nematic, as a result, there is no phase transition between nematic and cholesteric mesophases. The pitch p can be changed as a function of temperature, applied magnetic or electric fields, chemical composition, and flow¹⁰.

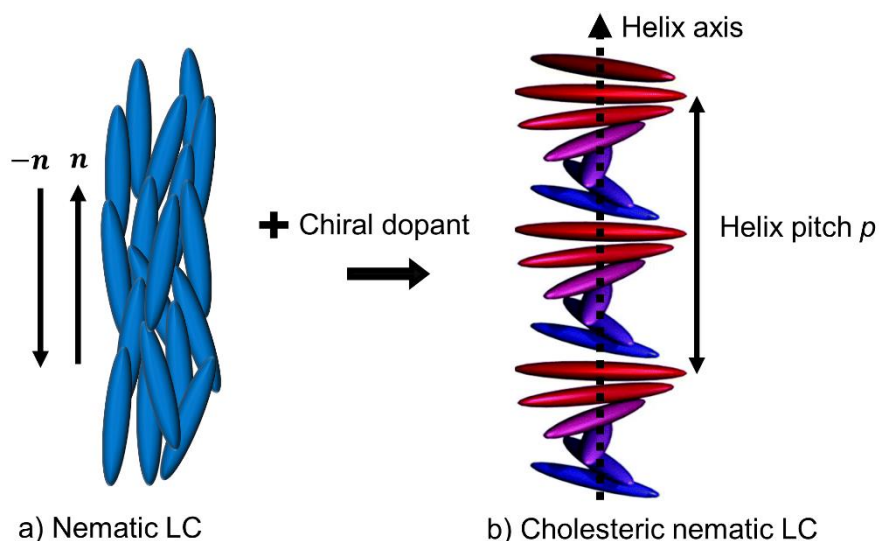


Figure 1.1. Formation of the cholesteric LC as a result of doping the nematic LC with chiral molecules. Here, \mathbf{n} and p represent the nematic director and the cholesteric pitch, respectively.

The size of the pitch p determines the optical behavior of N^* ; if p is much larger than the wavelength of the transmitted light, i.e., $\lambda = \lambda_0/\bar{n}$ (where \bar{n} being the mean refractive index of the chiral nematic phase), in other word $p \gg \lambda$. Then, the LC medium acts as a waveguide in the **Mauguin regime**; when the plane of polarization is strongly rotated⁸ as a function of incident light wavelength¹¹.

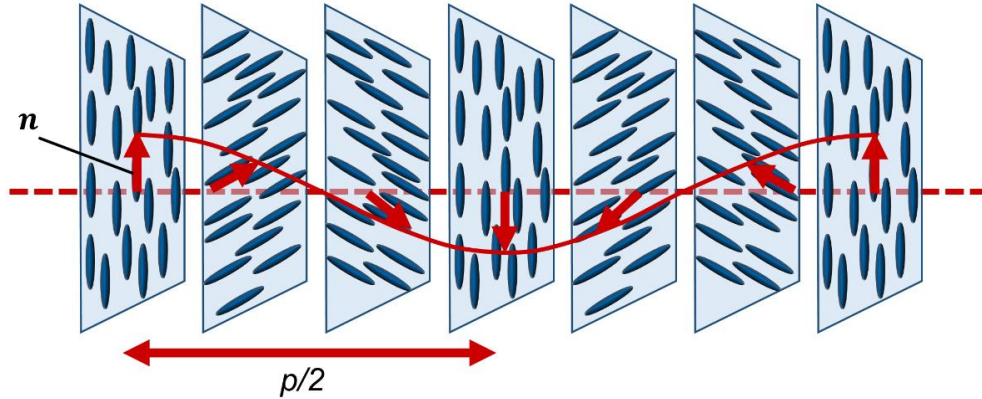


Figure 1.2. Schematic representation of the cholesteric (: a twisted nematic) arrangement on the imaginary planes in one pitch p . The director n is selectively shown. As seen, the director makes a full rotation of 2π in one pitch p .

Figure was inspired from Figure 2.5 in Ref: Enz, E. (2013). *Electrospun polymer-liquid crystal composite fibers* (Doctoral thesis, Martin-Luther-University, Halle-Wittenberg, Germany).

The N^* phase can show selective reflection^{11,12} known as the **Bragg reflection**, if the pitch p is of the order of the incident wavelength λ_0 . Then, the diffraction pattern at a wavelength λ , corresponding to a spectral band width of $\Delta\lambda = \lambda_0/\Delta n$ ($\Delta n = n_e - n_o$ is the birefringence of the nematic layer perpendicular to the helix axis measured as the difference of extraordinary and ordinary refractive indices, n_e and n_o , respectively), can be described by the relation¹¹,

$$m\lambda = p\sin\theta \quad (1.1)$$

where m and θ are the diffraction order and the angle between the incoming light beam and the surface of the cholesteric material, respectively, and as introduced, p is the cholesteric pitch. From relation (1.1), it can be expected that the reflected wavelength decreases at oblique angles¹³. The maximum reflected wavelength is equal to the **Bragg wavelength** $\lambda_B = \lambda_0/\bar{n}$. The selective reflection seen in the N^* is elliptically polarization-based^{14,15,16}; N^* acts as a guide for elliptically polarized light depending on the polarization handedness with respect to the helix handedness; the beam with

opposite handedness will be transmitted, while the light beam with the same handedness is strongly reflected giving rise to Bragg reflection. An unpolarized light incident on N^* sample is divided into two circular beams with 50:50 ratio; the beam matching the helix circular handedness is strongly reflected while the one with opposite handedness transmitted¹⁷. Additionally, N^* can be employed for tuning the polarization direction of linearly polarized light⁸. In case of short-pitch N^* (p on the order of 300-500 nm), N^* exhibits a huge optical rotatory power for light in the visible range, as well as a sign change in the optical anisotropy (birefringence $\Delta n = n_e - n_o$) compared to the non-chiral counterpart¹⁸ because of the rotation of the optic axis from alignment along the director \mathbf{n} to placing along the helix axis.

The discussed effects have found tremendous applications such as the electrically controlled *Mauguin regime* in twisted nematic displays.

1.3. Order parameter

Orientalional ordering of the constituent molecules of the LCs can be described by an order parameter S , which can be quantitatively determined. If every individual molecule is represented by a unit vector \mathbf{u} oriented along its time-averaged long axis, then averaging over all the vectors \mathbf{u} gives the director \mathbf{n} . The director \mathbf{n} can be supposed as a continuous field if the volume of averaging, V , has dimensions much larger than the average sizes of the LC molecules and smaller than the LCs' deformation lengths⁸.

By choosing an arbitrary reference frame $x'y'z'$ where the director \mathbf{n} aligns along the z' -axis, the orientation vector \mathbf{u} attributed to each molecule located around the director \mathbf{n} can be described based on the polar and azimuth coordinates, θ' and ϕ' , respectively, as¹⁹,

$$\mathbf{u} = (u_x, u_y, u_z) = (\cos\theta' \cos\phi', \cos\theta' \sin\phi', \sin\theta'). \quad (1.2)$$

In the supposed volume V , the probability density of finding a molecule oriented between \mathbf{u} and $\mathbf{u} + d\mathbf{u}$ within a solid angle $d\Omega' = \sin\theta' d\theta' d\phi'$ can be defined as¹⁹,

$$d\Psi = \frac{1}{4\pi} f(\theta', \phi') d\Omega' \quad (1.3)$$

where $f(\theta', \phi')$ is the orientational probability describing orientational state of individual molecules. Equivalence of the directions \mathbf{u} and $-\mathbf{u}$ in the uniaxial nematic bulk under the transformation of $\theta' \rightarrow \pi - \theta'$ ¹⁹ implies that $f(\theta', \phi') \equiv f(\pi - \theta', \phi')$, which means the probabilities of finding molecules in any direction or its opposite are equal¹⁰. The orientational probability $f(\theta', \phi')$ is also independent of the azimuth angle ϕ' because of the axisymmetry around \mathbf{n} ¹⁰; thus, $\partial f(\theta', \phi')/\partial \phi' = 0$ ⁸. As a result, the orientational probability function can be simplified as $f(\theta')$. Since the LC orientation can be found only in the interval $0 \leq \theta' < \pi$, the orientational probability would have a distribution between 0 to 1. So, $f(\theta')$ can be considered as a normalized function⁸ as,

$$\iint f(\theta', \phi') d\Omega' = 2\pi \int_0^\pi f(\theta') \sin\theta' d\theta' = 1. \quad (1.4)$$

In the isotropic phase (with no order), the orientational probability for all possible values of θ is the same, as a result it can be shown from above equation that the $f(\theta')$ is constant over the interval $0 \leq \theta' < \pi$ equal to $1/4\pi$. In the crystalline phase (most ordered state), where all the molecules are aligned along the director field in the z-direction, as $\theta' = 0$ everywhere, the orientational probability is $f(\theta') = \delta(\theta')/4\pi$ (δ is Dirac function). The general form of the orientational probability $f(\theta')$ for the nematic phase is shown schematically in Figure 1.3, and compared with the isotropic one, where the distribution function is constant equal to $1/4\pi$ over the θ' domain⁸.

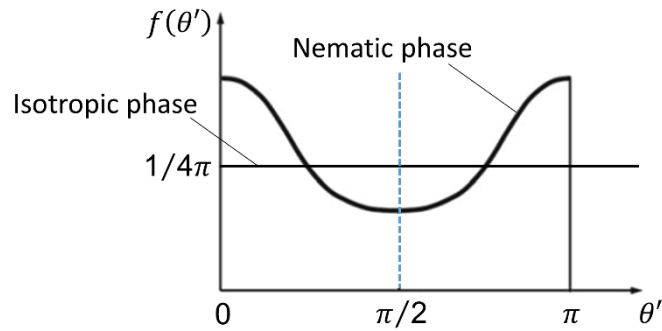


Figure 1.3. Orientational probability functions $f(\theta')$ for the nematic (generic form) and the isotropic phases are schematically shown. Figure was taken from Ref. 19.

Based on the spectral decomposition theorem, the orientational probability $f(\theta')$ can be expanded in terms of Legendre polynomials $P_n(\cos \theta')$ (which form a complete set of orthonormal functions), as^{19,20},

$$f(\theta') = \sum_{n=0}^{\infty} f_n P_n(\cos \theta') \quad (1.5)$$

where the coefficients f_n can be obtained from the orthogonality relations, as^{19,20},

$$f_n = \frac{(2n+1)}{2} \int_{-1}^1 f(\theta') P_n(\cos \theta') d(\cos \theta'). \quad (1.6)$$

The coefficients f_n can be interpreted as the ensemble average denoted as $f_n \propto \langle P_n(\cos \theta') \rangle$, where $\langle P_n(\cos \theta') \rangle = 2\pi \int_{-1}^1 f(\theta') P_n(\cos \theta') d(\cos \theta')$. The first terms of the Legendre polynomials $P_n(\cos \theta')$ are as follows:

$$P_0 = 1 \quad (1.7)$$

$$P_1(\cos \theta') = \cos \theta' \quad (1.8)$$

$$P_2(\cos \theta') = \frac{1}{2}(3\cos^2 \theta' - 1) \quad (1.9)$$

$$P_3(\cos \theta') = \frac{1}{2}(5\cos^3 \theta' - 3\cos \theta') \quad (1.10)$$

$$P_4(\cos \theta') = \frac{1}{8}(35\cos^4 \theta' - 30\cos^2 \theta' + 3), \dots \quad (1.11)$$

Legendre polynomials P_n can be formulated as $P_n(-\theta') = (-1)^n P_n(\theta')$. From this relation, it is easy to see that only even number terms stay invariant under the transformation of $\theta' \rightarrow \pi - \theta'$. Since the orientational probability $f(\theta')$ is symmetric, the coefficients f_n (obtained from relation (1.6)) are non-zero only for zero and even numbered terms of the P_n . In general, the order parameter (the degree of order) $S(T)$ is defined as⁸,

$$S(T) = \frac{4\pi}{5} f_2 = \langle P_2(\cos \theta') \rangle \quad (1.12)$$

which is commonly referred to as the **scalar order parameter**, first introduced by Tsvetkov²¹. The order parameter can be determined experimentally via different techniques such as optical birefringence, nuclear magnetic resonance, diamagnetic anisotropy, or dichroism²². Since ordering is temperature dependent, S is also a function of temperature $S(T)$. From the orientational probability $f(\theta')$ for the isotropic and crystalline phases, S equals to 0 and 1, respectively. The scalar order S can lie in the range $-1/2 \leq S \leq 1$, where the rare case of $S = -1/2$ corresponds to the state of randomly distribution of the molecules on a plane perpendicular to the director \mathbf{n} . S has

a value between 0 and 1 for the nematic phase with elongated molecules¹⁰. In practice, it usually ranges between 0.3 and 0.7.

By means of equation (1.5), the orientational probability function may be extended up to the second order¹⁹, as,

$$f(\theta) = f_0 P_0 + f_2 P_2 \quad (1.13)$$

where $f_0 = \frac{1}{2} \int_{-1}^1 f(\theta') d(\cos \theta') = \frac{1}{4\pi}$, then:

$$\begin{aligned} f(\theta) &= \frac{1}{4\pi} + \left(\frac{5}{4\pi}\right) \left(\frac{S}{2} (3\cos^2\theta' - 1)\right) \\ &= \frac{1}{4\pi} + \left(\frac{5}{4\pi}\right) \left(\frac{S}{2} (3(\mathbf{n} \cdot \mathbf{u})^2 - 1)\right). \end{aligned} \quad (1.14)$$

In the Cartesian reference frame xyz , the scalar product of the director \mathbf{n} with the unit vector \mathbf{u} can be obtained as $\mathbf{n} \cdot \mathbf{u} = n_i u_i$ which gives $(\mathbf{n} \cdot \mathbf{u})^2 = n_i n_j u_i u_j$. Consequently, the above relation can be re-casted in tensorial form by considering unitary property of the molecule's vector which implies that $u_i u_j \delta_{ij} = 1$,

$$\begin{aligned} f(\theta) &= \frac{1}{4\pi} + \left(\frac{5}{4\pi}\right) \left(\frac{S}{2} (3n_i n_j u_i u_j - u_i u_j \delta_{ij})\right) \\ &= \frac{1}{4\pi} + \left(\frac{5}{4\pi}\right) \left(\frac{S}{2} (3(\mathbf{n} \otimes \mathbf{n})_{ij} - \delta_{ij})\right) u_i u_j \end{aligned} \quad (1.15)$$

where δ_{ij} is Kronecker delta function, and it can be considered as the identity tensor. This relation can be used in defining the \mathbf{Q} -tensor formalism.

1.4. \mathbf{Q} -tensor definition

From the relation (1.15), the \mathbf{Q} -tensor (a second rank tensor) can be defined as¹⁹,

$$\mathbf{Q}_{ij} = \frac{3}{2} S \left((\mathbf{n} \otimes \mathbf{n})_{ij} - \frac{\delta_{ij}}{3} \right) \quad (1.16)$$

where the director \mathbf{n} can be interpreted as an eigenvector of Q independent of the coordinate system with a corresponding eigenvalue. The Q -tensor is always diagonalized where \mathbf{n} is along one of the coordinate axes.

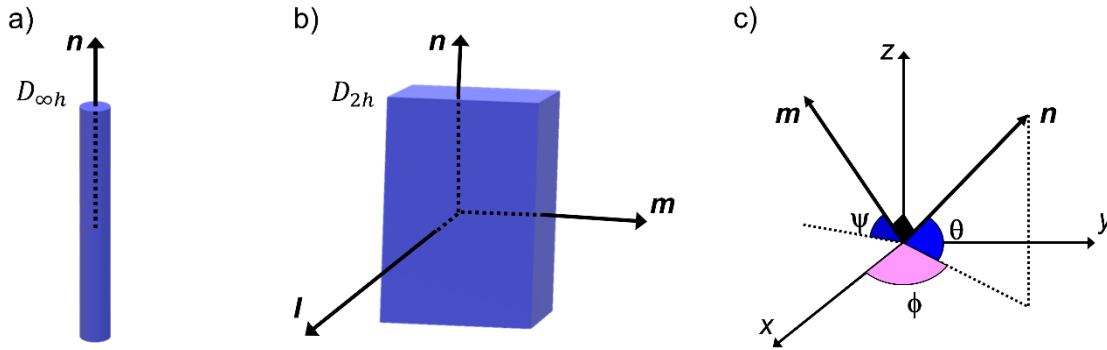


Figure 1.4. a) and b) Representation of director fields in uniaxial and biaxial LC phases, respectively. c) The directors \mathbf{n} and \mathbf{m} are shown in the laboratory frame of reference. Figure was inspired from Figure 1.1 in Ref: Senyuk, B. (2010). *Dielectric response of liquid crystals formed by bent-core and chiral molecules* (Doctoral dissertation, Kent State University).

A nematic LC in a biaxial state is described by two directors \mathbf{n} and \mathbf{m} with unit lengths ($|\mathbf{n}| = 1$ and $|\mathbf{m}| = 1$), as well as two scalar order parameters S_1 and S_2 . The scalar order parameters S_1 and S_2 measure the degree of orientational order around the directors \mathbf{n} and \mathbf{m} , correspondingly. The director \mathbf{n} is usually associated with the time-average long axis of molecules in the uniaxial nematics (this is the only conventional symmetry axis in the most common uniaxial nematics seen as an averaged property over time), where in the biaxial phase with conventional rectangular parallelepiped-shaped molecules, the director \mathbf{m} is perpendicular to \mathbf{n} , as $\mathbf{n} \times \mathbf{m} = \mathbf{I}$ (\mathbf{I} : unit vector) (Figure 1.4a, b); the unit vectors \mathbf{n} , \mathbf{m} , and \mathbf{I} form a local orthonormal triad²³. In the uniaxial nematic phase, cylindrical-shaped molecules are usually described by a symmetry axis $D_{\infty h}$ or D_{∞} . In the biaxial phase, nematic molecules possess D_{2h} symmetry as the order parameters stay unchanged by any mirror reflection of $\mathbf{n} \rightarrow -\mathbf{n}$, $\mathbf{m} \rightarrow -\mathbf{m}$ and $\mathbf{I} \rightarrow -\mathbf{I}$ ²³. The directors \mathbf{n} and \mathbf{m} can be represented in terms of the standard **Euler angles** (illustrated in Figure 1.4c), as²⁴,

$$\mathbf{m} = (\sin\phi\cos\psi - \cos\phi\sin\psi\sin\theta, -\sin\phi\sin\psi\sin\theta - \cos\phi\cos\psi, \sin\psi\cos\theta) \quad (1.17)$$

while,

$$\mathbf{n} = (\cos\theta\cos\phi, \cos\theta\sin\phi, \sin\theta). \quad (1.18)$$

As a result, the system can be described based on five independent variables θ , ϕ , ψ , S_1 and S_2 ²⁴. In biaxial nematic LC, the long-range orientational order can be described by a \mathbf{Q} -tensor based on the orthogonal unit directors \mathbf{n} and \mathbf{m} (or \mathbf{n} , \mathbf{m} and \mathbf{l}), as²⁴,

$$\mathbf{Q} = \frac{3}{2}S_1 \left((\mathbf{n} \otimes \mathbf{n})_{ij} - \frac{\delta_{ij}}{3} \right) + \frac{3}{2}S_2 \left((\mathbf{m} \otimes \mathbf{m})_{ij} - \frac{\delta_{ij}}{3} \right). \quad (1.19)$$

The above relation can be recast based on the unit directors \mathbf{m} and \mathbf{l} ²⁵. The scalar order parameter S_2 is introduced as the *biaxiality parameter*¹⁹, where $S_2 = 0$ in above relation gives \mathbf{Q} -tensor for the nematic phase.

The tensor order parameter \mathbf{Q} is a symmetric traceless tensor, as the \mathbf{Q} elements, i.e Q_{ij} , fulfil the conditions $Q_{ij} = Q_{ji}$ and $Q_{11} + Q_{22} + Q_{33} - 1 = 0$. The \mathbf{Q} -tensor can be simplified as²⁴,

$$\mathbf{Q} = \begin{pmatrix} q_1 & q_2 & q_3 \\ q_2 & q_4 & q_5 \\ q_3 & q_5 & -q_1 - q_4 \end{pmatrix} \quad (1.20)$$

where the elements q_i can be obtained from relations (1. 17) to (1. 19) based on the three independent parameters in the uniaxial phase including scalar order parameter S , polar and azimuth angles, θ and ϕ , respectively, and five independent parameters in biaxial nematic LC, i.e., S_1 , S_2 and θ , ϕ , ψ introduced earlier. Unlike the biaxial system which exhibits no axis of complete rotational symmetry, the uniaxial state can be characterized with a cylindrical symmetry²⁴ (Figure 1.4a). In the uniaxial state, the director field \mathbf{n} can be determined experimentally²⁶, that is **the optical axis of the NLC oriented along the largest principal axis of \mathbf{Q}** ²⁷. For the uniaxial nematic, the elements q_i can be simplified as,

$$q_1 = \frac{3S}{2} \left(\cos^2\theta \cos^2\phi - \frac{1}{3} \right) \quad (1.21)$$

$$q_2 = \frac{3S}{2} \cos^2\theta \cos\phi \sin\phi \quad (1.22)$$

$$q_3 = \frac{3S}{2} \cos\theta \cos\phi \sin\theta \quad (1.23)$$

$$q_4 = \frac{3S}{2} \left(\cos^2\theta \sin^2\phi - \frac{1}{3} \right) \quad (1.24)$$

$$q_5 = \frac{3S}{2} \cos\theta \sin\phi \sin\theta, \quad (1.25)$$

which are the fundamental elements of the theoretical discussions in this thesis.

1.5. Landau-de Gennes theory

The free energy per unit volume of the LC can be described as a function of temperature T and \mathbf{Q} -tensor elements Q_{ij} as $E_f(T, \mathbf{Q}_{ij})$, if the dependence on the density can be discarded. The free energy density $E_f(T, \mathbf{Q}_{ij})$ can be expanded as a power series based on the tensor order parameter, as²⁸,

$$E_f(T, \mathbf{Q}_{ij}) = f_0 + \alpha Q_{ii} + \frac{1}{2} a Q_{ij} Q_{ji} - \frac{1}{3} b Q_{ij} Q_{jk} Q_{ki} + \frac{1}{4} c (Q_{ij} Q_{ji})^2 + \dots \quad (1.26)$$

where these can be assumed that f_0 and $\alpha(T)$ are equal to zero, $a(T) = a_0(T - T^*)$ where a_0 is a positive constant and T^* is the pseudocritical temperature (also called spinodal temperature) where below that the isotropic phase becomes unstable, and parameters b and c can be considered as positive constants. Relation (1.26) is usually referred as **Landau-de Gennes potential energy density**, denoted as E_{LDG}^P . With the assumption of a reference frame with $z \parallel n$ and considering the relation of $Q_{ij} = \frac{3}{2} S \left((n \otimes n)_{ij} - \frac{\delta_{ij}}{3} \right)$ for the uniaxial nematic, the free energy density can be simplified as¹⁰,

$$E_{LDG}^P(T, \mathbf{Q}) = \frac{1}{2} A(T) \text{tr}(\mathbf{Q}^2) - \frac{1}{3} B \text{tr}(\mathbf{Q}^3) + \frac{1}{4} C (\text{tr}(\mathbf{Q}^2))^2 + \dots \quad (1.27)$$

where $A(T) = A_0(T - T^*)$ as $A_0 = \frac{2}{3} a_0$, $B = \frac{2}{9} b$ and $C = \frac{4}{9} c$, respectively. By substituting $\text{tr}(\mathbf{Q}^2) = \frac{3}{2} S^2$ and $\text{tr}(\mathbf{Q}^3) = \frac{3}{4} S^3$ in the relation (1.27), the **Landau-de Gennes** potential energy density can be obtained as a function of the scalar order parameter S ¹⁹.

In a uniaxial LC with a constant degree of orientation $S = S_0$ everywhere of the volume, the Landau-de Gennes potential gives a constant value additive to the total energy density of the system²⁷.

1.6. Frank-Oseen elastic free energy and elastic constants

When the director field \mathbf{n} has a uniform orientation in absence of any external constraints, the free energy density of the system is equal to zero $E_f = 0^{10}$. If the system is slightly distorted from its ground state, as $a|\nabla\mathbf{n}| \ll 1$ (: where a stands for mean inter-molecule distance), and with the assumption that the local order parameter S stays constant at a fixed temperature, the free energy density stemming from the elastic distortion E_f^e can be expanded in a power series based on the spatial derivatives of \mathbf{n} , formulated as²⁹,

$$E_f^e = \frac{1}{2}K_1(\nabla \cdot \mathbf{n})^2 + \frac{1}{2}K_2(\mathbf{n} \cdot \nabla \times \mathbf{n})^2 + \frac{1}{2}K_3(\mathbf{n} \times \nabla \times \mathbf{n})^2 + \frac{1}{2}K_{24}\nabla \cdot (\mathbf{n}\nabla \cdot \mathbf{n} + \mathbf{n} \times \nabla \times \mathbf{n}) + K_{13}\nabla \cdot (\mathbf{n}\nabla \cdot \mathbf{n}) \quad (1.28)$$

where the first, second and the third terms correspond to a splay, twist and bend deformation, respectively. The terms K_{24} and K_{13} are generally considered of less importance. Physically speaking, the integral of these terms over the nematic volume V can be written as a surface integral over the entire boundary s , which mostly can be neglected as a consequence of geometric surface anchoring conditions considerations¹⁰. As a result, the free energy density of the uniaxial nematics associated with the elastic distortion can be re-casted in the simplified **Frank-Oseen** formalism, as,

$$E_f^e = \frac{1}{2}K_1(\nabla \cdot \mathbf{n})^2 + \frac{1}{2}K_2(\mathbf{n} \cdot \nabla \times \mathbf{n})^2 + \frac{1}{2}K_3(\mathbf{n} \times \nabla \times \mathbf{n})^2 \quad (1.29)$$

where K_1 , K_2 and K_3 are called Frank elastic constants attributed to the splay, twist and bend deformations, orderly (shown in Figure 1.5). This energy density is also called **Landau-de Gennes elastic energy density**, denoted as E_{LdG}^e . For the cholesteric case, the chirality $q_0 = 2\pi/p$ (p : the chiral pitch) is considered as an additive to the term in the second parentheses, as,

$$E_{LdG}^e = \frac{1}{2}K_1(\nabla \cdot \mathbf{n})^2 + \frac{1}{2}K_2(\mathbf{n} \cdot \nabla \times \mathbf{n} + q_0)^2 + \frac{1}{2}K_3(\mathbf{n} \times \nabla \times \mathbf{n})^2 \quad (1.30)$$

as a result, an additional term $E^{ch} = k_2(\mathbf{n} \cdot \nabla \times \mathbf{n})$ appears, which represents the free energy density associated with the chirality, and is not invariant under inversion as it changes the sign³⁰.

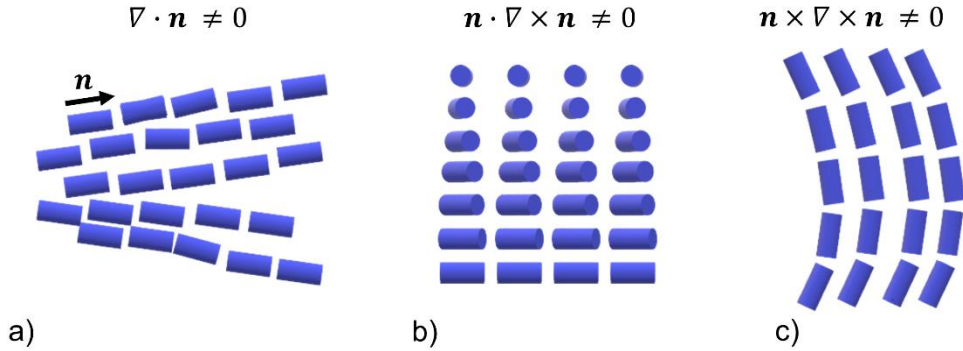


Figure 1.5. Deformations in biaxial NLCs corresponding to a) splay; b) twist; c) bend distortions. The director \mathbf{n} is along the time-averaged long axis of molecule.

Figure was inspired from Figure 1.2 in Ref: Senyuk, B. (2010). *Dielectric response of liquid crystals formed by bent-core and chiral molecules* (Doctoral dissertation, Kent State University).

Based on the \mathbf{Q} -tensor formalism, the elastic energy density up to second order can be obtained, as³¹,

$$E_{LdG}^e(\mathbf{Q}, \nabla \mathbf{Q}) = \frac{1}{2} L_1 (\nabla \cdot \mathbf{Q})^2 + \frac{1}{2} L_2 |\nabla \mathbf{Q}|^2, \quad (1.31)$$

where $L_1 = \frac{1}{3S^2}(K_1 + K_3 - K_2)$ and $L_2 = \frac{1}{3S^2}K_2$ (K_1 , K_2 and K_3 defined as the splay, twist and bend constants, orderly). From the definition of the elastic constant L_1 , it can be deduced that in this presentation, the splay and bend deformations are not distinguishable³¹. Assumption of one-elastic constant (L) approximation can further simplify the elastic energy density relation (1.31) as³²,

$$E_{LdG}^e(\mathbf{Q}, \nabla \mathbf{Q}) = L |\nabla \mathbf{Q}|^2. \quad (1.32)$$

1.7. LC response to an electric field

Unlike the isotropic phase, the electric field \mathbf{E} in the LC medium is not in the same direction as the electric displacement field \mathbf{D} with elements defined as $D_i = \varepsilon_{ij} E_j$ ⁸, where ε_{ij} is the dielectric permittivity tensor. The relative permittivity, also known

as dielectric constant, with the notation of ϵ_{ij} , can be obtained from the permittivity via the relation of $\epsilon_{ij} = \epsilon_{ij}/\epsilon_0$. So, the dielectric permittivity tensor ϵ_{ij} can be obtained from the \mathbf{Q}_{ij} elements as^{10,33},

$$\epsilon_{ij} = \bar{\epsilon}\delta_{ij} + \Delta\epsilon\mathbf{Q}_{ij} \quad (1.33)$$

where $\bar{\epsilon} = \frac{1}{3}(\epsilon_{\parallel} + 2\epsilon_{\perp})$ represents the isotropic part (also introduced as ϵ^{iso} and being the average relative permittivity obtained from the ϵ tensor eigenvalues) and $\Delta\epsilon = \epsilon_{\parallel} - \epsilon_{\perp}$ represents the anisotropy of the relative permittivity¹⁰. Relation (1.33) can be expanded as,

$$\epsilon \equiv \begin{pmatrix} \epsilon_{xx} & \epsilon_{xy} & \epsilon_{xz} \\ \epsilon_{yx} & \epsilon_{yy} & \epsilon_{yz} \\ \epsilon_{zx} & \epsilon_{zy} & \epsilon_{zz} \end{pmatrix} = \begin{pmatrix} \bar{\epsilon} + \Delta\epsilon\mathbf{Q}_{11} & \Delta\epsilon\mathbf{Q}_{12} & \Delta\epsilon\mathbf{Q}_{13} \\ \Delta\epsilon\mathbf{Q}_{21} & \bar{\epsilon} + \Delta\epsilon\mathbf{Q}_{22} & \Delta\epsilon\mathbf{Q}_{23} \\ \Delta\epsilon\mathbf{Q}_{31} & \Delta\epsilon\mathbf{Q}_{32} & \bar{\epsilon} + \Delta\epsilon\mathbf{Q}_{33} \end{pmatrix}. \quad (1.34)$$

As expected, the relative permittivity tensor ϵ has the same tensorial properties as the \mathbf{Q} -tensor of being second rank and symmetric for an uniaxial LC such as nematics. Elements of the relative permittivity tensor ϵ can be obtained from the introduced five independent elements q_i (relations 1. 21-25). Additionally, the dielectric tensor (relation 1. 34) can be diagonalized along the principal axes of the LC; for the uniaxial LCs such as nematics, when the director \mathbf{n} aligns along the z-direction, the relative permittivity tensor ϵ can be simplified as diagonal in the Cartesian coordinate, as¹⁰,

$$\epsilon \equiv \begin{pmatrix} \epsilon_x & 0 & 0 \\ 0 & \epsilon_y & 0 \\ 0 & 0 & \epsilon_z \end{pmatrix} = \begin{pmatrix} \bar{\epsilon} + \mathbf{Q}_{11}\Delta\epsilon & 0 & 0 \\ 0 & \bar{\epsilon} + \mathbf{Q}_{22}\Delta\epsilon & 0 \\ 0 & 0 & \bar{\epsilon} + \mathbf{Q}_{33}\Delta\epsilon \end{pmatrix}, \quad (1.35)$$

where ϵ_x , ϵ_y , and ϵ_z are called the principal relative permittivities or dielectric constants³⁴. ϵ_x and ϵ_y have the same values relative to the directions perpendicular to the z-direction because of the cylindrical symmetry of the uniaxial nematic, as both can be introduced as the relative permittivity perpendicular to the nematic director, i.e., ϵ_{\perp} , while the relative permittivity along the nematic director ϵ_z can be introduced as ϵ_{\parallel} .

Because of the interaction of the LC with the electric field \mathbf{E} ($E_j = \partial_j U$, where U is the electric potential), electric potential energy can be stored in the LC volume, which can be calculated from $E_E = -\mathbf{D} \cdot \mathbf{E}/2$ per unit volume of the LC. The electric

energy density E_E can be expanded based on the dielectric anisotropy $\Delta\epsilon$, the average dielectric constant $\bar{\epsilon}$, and \mathbf{Q} elements^{35,36} as,

$$E_E(\mathbf{Q}_{ij}) = -\frac{1}{2}\epsilon_0 (\bar{\epsilon} \delta_{ij}(\partial_i U)(\partial_j U) + \Delta\epsilon(\partial_j U)(\partial_k U)\mathbf{Q}_{jk}). \quad (1.36)$$

The above relation was utilized to obtain the **Euler-Lagrange** equation³⁷ describing the director field realignment in a static electric field, discussed in Chapters 5, 6 and 7.

References

- ¹ Vertogen, G., & De Jeu, W. H. (2012). *Thermotropic liquid crystals, fundamentals* (Vol. 45). Springer Science & Business Media.
- ² Hansen, J. P., & McDonald, I. R. (2013). *Theory of simple liquids: with applications to soft matter*. Academic Press.
- ³ Martin, J. D., Keary, C. L., Thornton, T. A., Novotnak, M. P., Knutson, J. W., & Folmer, J. C. (2006). Metallotropic liquid crystals formed by surfactant templating of molten metal halides. *Nature materials*, 5(4), 271-275.
- ⁴ Andrienko, D. (2018). Introduction to liquid crystals. *Journal of Molecular Liquids*, 267, 520-541.
- ⁵ Dierking, I. (2003). *Textures of liquid crystals*. John Wiley & Sons.
- ⁶ Chilaya, G. (2001). Cholesteric liquid crystals: Optics, electro-optics, and photo-optics. In *Chirality in liquid crystals* (pp. 159-185). Springer, New York, NY.
- ⁷ De Vicente, J. (Ed.). (2012). *Rheology*. BoD—Books on Demand.
- ⁸ Kleman, M., & Laverntovich, O. D. (2007). *Soft matter physics: an introduction*. Springer Science & Business Media.
- ⁹ Turzi, S. S. (2011). On the Cartesian definition of orientational order parameters. *Journal of mathematical physics*, 52(5), 053517.
- ¹⁰ Oswald, P., & Pieranski, P. (2005). *Nematic and cholesteric liquid crystals: concepts and physical properties illustrated by experiments*. CRC press.
- ¹¹ Bahr, C., & Kitzerow, H. S. (2001). *Chirality in liquid crystals*. Heidelberg: Springer.
- ¹² De Vries, H. (1951). Rotatory power and other optical properties of certain liquid crystals. *Acta Crystallographica*, 4(3), 219-226.
- ¹³ Gray, D. G. (2016). Recent advances in chiral nematic structure and iridescent color of cellulose nanocrystal films. *Nanomaterials*, 6(11), 213.
- ¹⁴ De Gennes, P. G., & Prost, J. (1993). *The physics of liquid crystals* (Vol. 83). Oxford university press.
- ¹⁵ Sanchez-Castillo, A., Eslami, S., Giesselmann, F., & Fischer, P. (2014). Circular polarization interferometry: circularly polarized modes of cholesteric liquid crystals. *Optics express*, 22(25), 31227-31236.
- ¹⁶ Bitri, N., Gharbi, A., & Marcerou, J. P. (2008). Scanning conoscopy measurement of the optical properties of chiral smectic liquid crystals. *Physica B: Condensed Matter*, 403(21-22), 3921-3927.
- ¹⁷ Kim, D. Y., Lee, K. M., White, T. J., & Jeong, K. U. (2018). Cholesteric liquid crystal paints: in situ photopolymerization of helicoidally stacked multilayer nanostructures for flexible broadband mirrors. *NPG Asia Materials*, 10(11), 1061.

-
- ¹⁸ Geng, Y., Noh, J., & Lagerwall, J. P. (2016, March). Transmission polarized optical microscopy of short-pitch cholesteric liquid crystal shells. In *Emerging Liquid Crystal Technologies XI* (Vol. 9769, p. 97690U). International Society for Optics and Photonics.
- ¹⁹ Sengupta, A. (2013). *Topological microfluidics: nematic liquid crystals and nematic colloids in microfluidic environment*. Springer Science & Business Media.
- ²⁰ Bauman, D., & Wolarz, E. (1996). Study of Orientational Order of Liquid Crystal 8 OCB Doped with Perylene-like Dyes by Means of Polarized Optical Spectroscopy. *Zeitschrift für Naturforschung A*, 51(12), 1192-1196.
- ²¹ Tsvetkov, V. (1942). On molecular order in the anisotropic liquid phase. *Acta Physicochim. URSS*, 16, 132-147.
- ²² Singh, S., & Dunmur, D. A. (2002). *Liquid crystals: fundamentals*. World Scientific.
- ²³ Turzi, S. S. (2011). On the Cartesian definition of orientational order parameters. *Journal of Mathematical Physics*, 52(5), 053517.
- ²⁴ Mottram, N. J., & Newton, C. J. (2014). Introduction to \mathbf{Q} -tensor theory. *arXiv preprint arXiv:1409.3542*.
- ²⁵ Zheng, X., & Palffy-Muhoray, P. (2011). One order parameter tensor mean field theory for biaxial liquid crystals. *Discrete and Continuous Dynamical Systems, Series B*, 15(2), 475.
- ²⁶ De Gennes, P. G., & Prost, J. (1993). *The physics of liquid crystals* (Vol. 83). Oxford university press.
- ²⁷ Biscari, P., & Sluckin, T. J. (2003). Expulsion of disclinations in nematic liquid crystals. *European Journal of Applied Mathematics*, 14(1), 39-59.
- ²⁸ De Gennes, P. G. (1971). Short range order effects in the isotropic phase of nematics and cholesterics. *Molecular Crystals and Liquid Crystals*, 12(3), 193-214.
- ²⁹ Nehring, J., & Saupe, A. (1972). Calculation of the elastic constants of nematic liquid crystals. *The Journal of Chemical Physics*, 56(11), 5527-5528.
- ³⁰ Crawford, G. P., Svenšek, D., & Žumer, S. (2001). Some aspects of polymer dispersed and polymer stabilized chiral liquid crystals. In *Chirality in Liquid Crystals* (pp. 375-432). Springer, New York, NY.
- ³¹ Barberi, R., Ciuchi, F., Durand, G. E., Iovane, M., Sikharulidze, D., Sonnet, A. M., & Virga, E. G. (2004). Electric field induced order reconstruction in a nematic cell. *The European Physical Journal E*, 13(1), 61-71.
- ³² Kralj, S., Virga, E. G., & Žumer, S. (1999). Biaxial torus around nematic point defects. *Physical Review E*, 60(2), 1858.
- ³³ James, R., Willman, E., Fernandez-Fernandez, F. A., & Day, S. E. (2006). Finite-element modeling of liquid-crystal hydrodynamics with a variable degree of order. *IEEE Transactions on Electron Devices*, 53(7), 1575-1582.

-
- ³⁴ Davis, C. C. (1996). *Lasers and electro-optics: fundamentals and engineering*. Cambridge university press.
- ³⁵ Mori, H., Gartland Jr, E. C., Kelly, J. R., & Bos, P. J. (1999). Multidimensional director modeling using the \mathbf{Q} tensor representation in a liquid crystal cell and its application to the π cell with patterned electrodes. *Japanese journal of applied physics*, 38(1R), 135.
- ³⁶ Lee, G. D., Bos, P. J., Ahn, S. H., & Kim, K. H. (2003). Fast \mathbf{Q} -tensor method for modeling the dynamics of defects in a liquid crystal director field. *Physical Review E*, 67(4), 041715.
- ³⁷ Habibpournoghdam, A., Jiao, L., Reshetnyak, V., Evans, D. R., & Lorenz, A. (2017). Optical manipulation and defect creation in a liquid crystal on a photoresponsive surface. *Physical Review E*, 96(2), 022701.

Chapter 2: Optical Properties of Uniaxial LCs

2.1. Introduction

LC cells are made from a thin LC film (of the order of microns) confined between treated or non-treated glass slabs. Utilizing a LC with large birefringence can result in good contrast between regions with different orientations of the optical axis (which coincides with the director in uniaxial nematic as mentioned before, as well as in the smectic A phase).

Mostly, liquid crystal structures can be readily studied between crossed polarizers by investigating the LC unperturbed texture and comparing it with the altered structure after a director field reorientation happened from its initial alignment. Applying external stimuli, such as electric or magnetic fields to the LC can change the optical properties of the medium. Therefore, it is of great importance to gain some background on the basic principles of light propagation in the LCs media under study.

2.2. Light propagation in the LC

If the LC medium is assumed non-absorbing, then the relative permittivity tensor ϵ is real. For a plane monochromatic wave with electric field $\mathbf{E}(\mathbf{r}, t) = \mathbf{E}_0 e^{i(\mathbf{k}\cdot\mathbf{r} - \omega t)}$ (where \mathbf{E}_0 and \mathbf{k} are the electric field amplitude and the wave vector, respectively, ω is the frequency, and \mathbf{r} is the radius vector directed from the light source to the point of observation), it can be shown from the Maxwell equations^{1,2} that the

electric and magnetic fields are perpendicular, and in addition the set of \mathbf{k} , \mathbf{H} , and \mathbf{D} (however not generally true for \mathbf{E}) vectors are mutually perpendicular, as well.

In the case of negligible magnetization when $|\mathbf{M}| \ll |\mathbf{B}|$, the magnetic field can be obtained from $\mathbf{B} = \mu_0 \mathbf{H}$ (where in general, $\mathbf{B} = \mu_0 \mathbf{H} + \mathbf{M}$). Thus, the generalized form of Maxwell's equation can be obtained as,

$$\mathbf{k} \times \mathbf{k} \times \mathbf{E} = -\mu_0 \omega^2 \mathbf{D} \quad (2.1)$$

simplifying the above relation using "BAC-CAB" rule, $\mathbf{A} \times (\mathbf{B} \times \mathbf{C}) = \mathbf{B}(\mathbf{A} \cdot \mathbf{C}) - \mathbf{C}(\mathbf{A} \cdot \mathbf{B})$, gives,

$$\mathbf{k}(\mathbf{k} \cdot \mathbf{E}) - \mathbf{E}(\mathbf{k} \cdot \mathbf{k}) = -\mu_0 \omega^2 \mathbf{D}. \quad (2.2)$$

The wave vector \mathbf{k} is defined as $\mathbf{k} = \frac{\omega}{c} \mathbf{N}$, where $c = \frac{1}{\sqrt{\epsilon_0 \mu_0}}$ is the speed of light in vacuum, and \mathbf{N} is the refractive index vector in the same direction as \mathbf{k} . In general, the refractive index vector \mathbf{N} is complex valued as $N = n + i\kappa$, where the real and imaginary parts of n and κ are the refractive index and the extinction coefficient, respectively³. The relation (2.2) can be re-casted based on the \mathbf{N} and \mathbf{D} constituent elements, where, as introduced in Chapter 1, $D_i = \epsilon_0 \epsilon_{ij} E_j$. Hence¹,

$$(N^2 \delta_{ij} - N_i N_j - \epsilon_{ij}) E_j = 0. \quad (2.3)$$

In a uniaxial medium with diagonalized dielectric tensor in an arbitrary reference frame $x'y'z'$ where director field is supposed along the z' -direction, there are $\epsilon_{x'} = \epsilon_{y'} = \epsilon_{\perp}$ and $\epsilon_{z'} = \epsilon_{\parallel}$, the homogeneous system of linear equations based on $E_{x'}$, $E_{y'}$, and $E_{z'}$ can be obtained in the matrix form as,

$$\begin{pmatrix} (-N_{y'}^2 - N_{z'}^2 + \epsilon_{\perp}) & N_{x'} N_{y'} & N_{x'} N_{z'} \\ N_{x'} N_{y'} & (-N_{x'}^2 - N_{z'}^2 + \epsilon_{\perp}) & N_{y'} N_{z'} \\ N_{x'} N_{z'} & N_{y'} N_{z'} & (-N_{x'}^2 - N_{y'}^2 + \epsilon_{\parallel}) \end{pmatrix} \begin{pmatrix} E_{x'} \\ E_{y'} \\ E_{z'} \end{pmatrix} = \begin{pmatrix} 0 \\ 0 \\ 0 \end{pmatrix} \quad (2.4)$$

The system has a nontrivial (nonzero) solution in N , if the determinant of coefficients is zero, thus it can be shown¹,

$$(N^2 - \epsilon_{\perp})(\epsilon_{\parallel}N_z^2 + \epsilon_{\perp}(N_x^2 + N_y^2) - \epsilon_{\parallel}\epsilon_{\perp}) = 0 \quad (2.5)$$

Equation (2.5) indicates that the surface of refractive indices (of degree four) splits into a sphere with radius $N^2 = \epsilon_{\perp}$ and an spheroid with the relation $(N_z^2/\epsilon_{\perp}) + ((N_x^2 + N_y^2)/\epsilon_{\parallel}) = 1$. The LC medium supports the propagation of ordinary and extraordinary waves¹ as isotropically for the ordinary wave and anisotropically for the extraordinary wave, with ordinary and extraordinary refractive indices of $n_o = \sqrt{\epsilon_{\perp}}$ and $n_e = \sqrt{\epsilon_{\parallel}}$ — perpendicular and along the optic axis — respectively. If the optic axis (director field) is oriented in an oblique angle ϑ with respect to the propagation direction (Figure 2.1), the effective refractive index $N(\vartheta)$ can be obtained from the relation $(N_z^2/\epsilon_{\perp}) + ((N_x^2 + N_y^2)/\epsilon_{\parallel}) = 1$ by considering the relations $N_z^2 = N^2 \cos^2 \vartheta$ and $(N_x^2 + N_y^2) = N^2 \sin^2 \vartheta$, and substituting the dielectric anisotropies as $\epsilon_{\perp} = n_o^2$ and $\epsilon_{\parallel} = n_e^2$, as¹,

$$N(\vartheta) = \frac{n_o n_e}{\sqrt{n_e^2 \cos^2 \vartheta + n_o^2 \sin^2 \vartheta}} \quad (2.6)$$

where the effective refractive index $N(\vartheta)$ is commonly denoted as $n_{\text{eff}}(\vartheta)$ employed from now on.

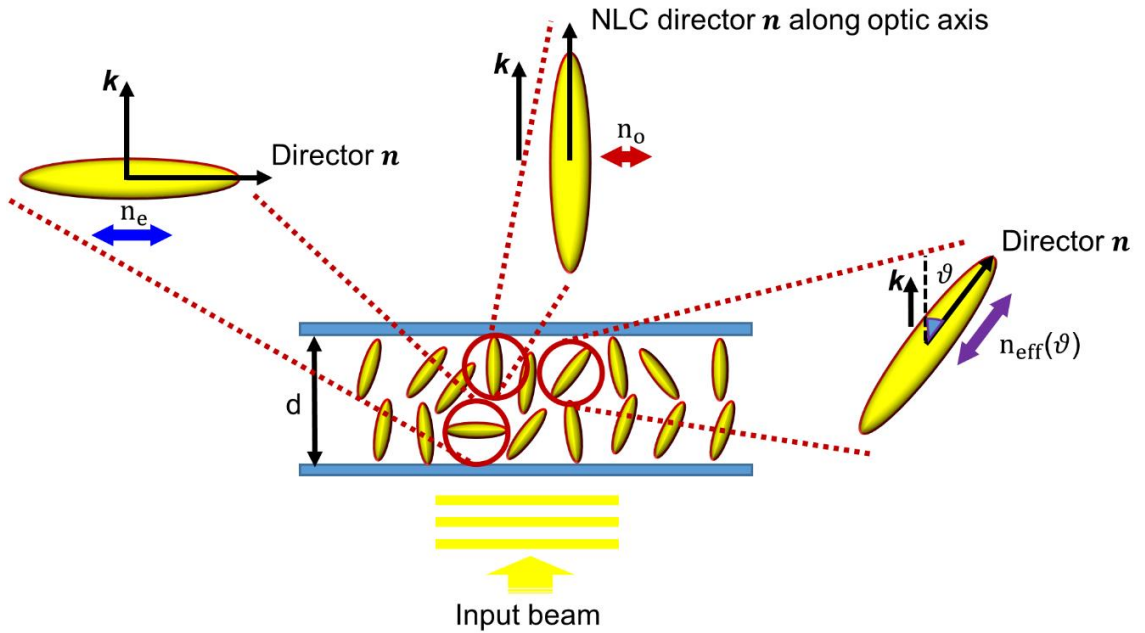


Figure 2.1. Effective refractive index seen by the light beam passing through the nematic LC cell as a function of the optic axis (director) alignment with respect to the light propagation direction along \mathbf{k} .

When light enters a *homogenously* aligned LC film, the ordinary and extraordinary waves are in phase before interaction with the medium. Since they travel in the medium in different time intervals described as $n_o d / C$ and $n_e d / C$ (: where d is the film thickness and C is the speed of light in vacuum) they acquire an accumulated phase difference (: $\Delta\phi = \omega_0 \Delta t = (2\pi C / \lambda_0) \Delta t$) of $2\pi n_o d / \lambda_0$ and $2\pi n_e d / \lambda_0$, respectively. As a result, the phase shift between ordinary and extraordinary waves at the exit point can be described as $\Delta\phi = 2\pi d(n_e - n_o) / \lambda_0$. If the director field is distributed *non-uniformly*, then the phase shift can be calculated from the definition of the effective refractive index $n_{\text{eff}}(\vartheta)$, as⁴,

$$\Gamma = \left(\frac{2\pi}{\lambda_0}\right) \int_0^d (n_{\text{eff}}(\vartheta) - n_o) dz. \quad (2.7)$$

2.3. Transmitted light wave between crossed linear polarizers

A simple test cell made of an LC film sandwiched between two glass slabs is assumed between crossed linear polarizers. If the director field is in the xy -plane, the incoming linearly polarized light from the polarizer into the LC media, with amplitude of A splits into the ordinary and extraordinary waves with corresponding amplitudes of $A \sin\beta$ and $A \cos\beta$ in the y - and x -directions, respectively. The ordinary wave is always linearly polarized in the direction perpendicular to the director field, while the polarization plane of the extraordinary wave always involves the director. The projections of these two elements along the polarization direction of the analyzer give $A \sin\beta \cos\beta$ and $A \cos\beta \cos\left(\frac{\pi}{2} + \beta\right) = -A \cos\beta \sin\beta$ in the y and x directions, respectively. When two waves meet at the analyzer, the superposition of corresponding electric fields along the analyzer direction, by considering the phase changes, can be described as,

$$E = E_o + E_e = A \sin\beta \cos\beta e^{-i(\omega t - 2\pi n_o d / \lambda_0)} - A \cos\beta \sin\beta e^{-i(\omega t - 2\pi n_e d / \lambda_0)} \quad (2.8)$$

Consequently, the transmitted light intensity at the analyzer can be obtained from $I = |E||E^*| = |E_o + E_e||E_o + E_e|^*$ as,

$$I = I_0 \sin^2(2\beta) \sin^2(\pi d \Delta n / \lambda_0) \quad (2.9)$$

where $I_0 = A^2$ is the input intensity, and Δn is the birefringence; $\Delta n = n_e - n_o$. Depending on the value of β , different light modes can pass through the LC media as pure ordinary, pure extraordinary mode, or a linear combination of ordinary and extraordinary modes.

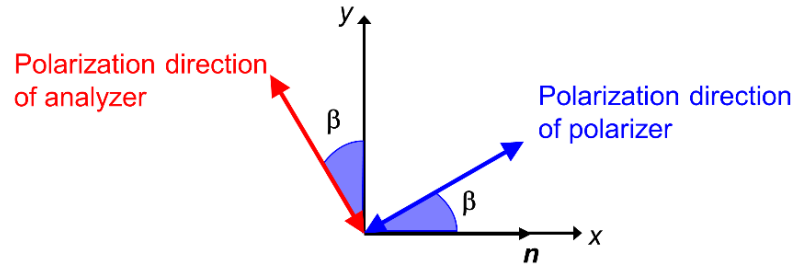


Figure 2.2. The situation of the director field relative to the polarization direction of both polarizer and analyzer.

For example, the condition of $\beta = 0$ (\mathbf{n} parallel to the polarizer) corresponds to the propagation of the pure extraordinary wave and this wave gets blocked in the analyzer, associated with $I = 0$. On the other hand, in the condition of $\beta = \pi/2$ (\mathbf{n} perpendicular to the polarizer), only the ordinary mode transmits through the LC film (as can be deduced from Figure 2.2), and it corresponds to the condition $I = 0$. In both cases, the transmitted intensity in between crossed polarizers is equal to zero.

In general, when the director field has an arbitrary distribution in three dimensions (3D) with the local tilt angle ϑ with respect to the propagation direction (supposed in the z-direction), the output intensity holds the following relation^{1,4},

$$I = I_0 \sin^2 2\beta \sin^2 \frac{\Gamma}{2} \quad (2.10)$$

where Γ is the phase shift. Under homeotropic anchoring conditions, where the director field \mathbf{n} is parallel to the propagation direction \mathbf{k} , only the ordinary wave propagates into the LC medium, and then it is absorbed in the analyzer. Since the tilt angle ϑ is equal to zero everywhere, the effective refractive index $n_{\text{eff}}(\vartheta)$ is equal to the ordinary refractive index n_o which gives $\Gamma = 0$. As a result, under the homeotropic condition, the LC test cell is dark ($I = 0$) in between crossed linear polarizers, which will be seen in Chapter 5 in studied cases.

It can be shown that if in general $\vartheta \neq 0$, and the projection of the director field in the xy -plane is parallel or perpendicular to the polarizer with one of the possible values of $\beta = 0, \pm \frac{\pi}{2}, \dots$, then only the ordinary wave passes through the LC, and it gets

blocked in the analyzer. It can be verified in the observation of disclination walls (seen in dark) in IPS cells filled with neat NLC between crossed polarizers in Chapter 7, where the director field keeps its initial alignment along the electrodes (being parallel to the polarizer) at the electrode centers. The disclination walls are extended in regions around the electrode centers where the director field is gradually tilted from its initial alignment by the electric field element E_y in a plane involving the polarizer.

References

- ¹ Kleman, M., & Laverntovich, O. D. (2007). *Soft matter physics: an introduction*. Springer Science & Business Media.
- ² Purcell, E. M., & Morin, D. J. (2013). *Electricity and magnetism*. Cambridge University Press.
- ³ Peatross, J., & Ware, M. (2011). *Physics of light and optics*. in *Frontiers in Optics 2010/Laser Science XXVI, OSA Technical Digest (CD)* (Optical Society of America, 2010), paper JWA64.
- ⁴ Pereira, A. C., & Rosato, A. (1975). Transmission of nematic liquid crystals in electric fields. *Revista Brasileira de Fisica*, 5(2), 237-241.

Chapter 3: Discussion on the Photovoltaic Effects

3.1. Introduction

Hybridized LC cells were made from a LC thin film confined between a cover slab engineered with specific properties and a ferroelectric substrate of LiNbO₃:Fe (Fe:LN). The induced photovoltaic (PV) field in the substrate desirably has a distribution in the LC thin film being capable to reorient the LC director field from its initial alignment, generating topological defects.

Because of the importance of knowing the photovoltaic (PV) effect, this topic is discussed thoroughly in the current chapter.

3.2. Photovoltaic (PV) effect

The process of generating photo-current from light absorption in a semiconductor is called **photovoltaic (PV) effect**. The PV effect can occur in any inhomogeneous semiconductor (although the magnitude depends on the material properties and device structure) by means of an induced internal electromotive force (emf) created by the inhomogeneity of the device¹. Absorption of the impinging light on the semiconductor can cause electron-hole pair generation in the semiconductor, which can be separated by the internal electric field. The separated pairs can contribute to an external electric current, referred to as PV current. Photo-induced emf in the PV effect must be distinguished from the **Dember effect**^{2,3}.

The Dember effect^{2,3} is seen when an inhomogeneous, strong excitation is applied in a highly absorbing homogeneous semiconductor: enormous amounts of photo-carriers (: electron-hole pairs), compared with the majority carrier concentration in the dark, are generated near the surface with a strong spatial gradient perpendicular to the surface. As a result, the photo-carriers diffuse into the interior, since electrons are more mobile than holes, they diffuse faster (from Einstein's diffusion relation $D = \mu K_B T / q$, where D is the diffusion constant, μ is the charge mobility, K_B is the Boltzmann's constant, T is the temperature, and q is the electrical charge). The separation of electron and hole densities builds up an electric potential between the surface ($x = 0$) and interior ($x = \infty$) of the semiconductor.

Historically, the photovoltaic effect was first reported by Edmond Becquerel in 1839. He generated electricity by illuminating an electrode inserted into acidic solution with light, schematically shown in Figure 3.1a. He observed the best results with application of platinum (Pt) electrodes coated with light sensitive material such as silver chloride (AgCl) or silver bromide (AgBr), and shone blue or ultraviolet light^{4,5}.

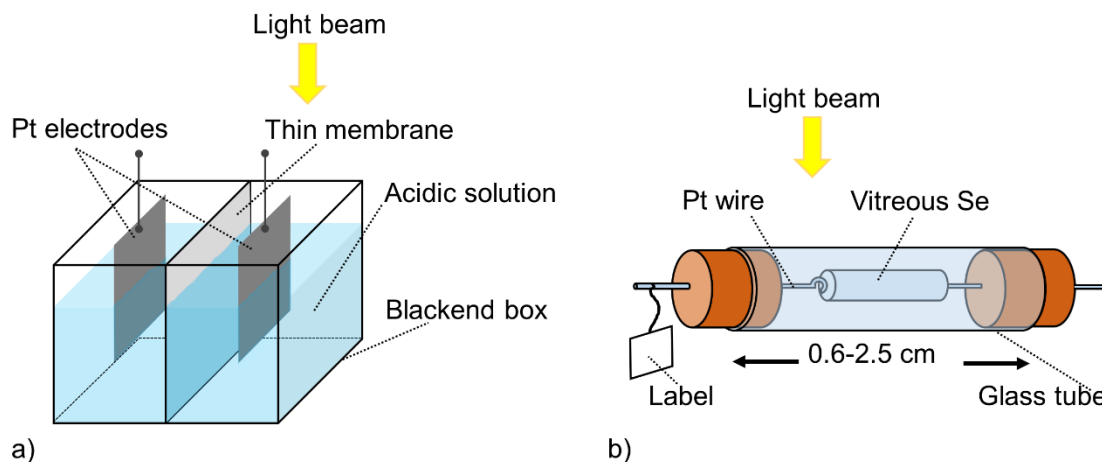


Figure 3.1. Diagram of the photovoltaic apparatus proposed by a) Edmond Becquerel in 1839 in aqua, b) Adams and Day in 1876 in solid state, respectively.

{Figure was inspired from Figure 2 in Ref: Green, M. A. (2002). Photovoltaic principles. *Physica E: Low-dimensional Systems and Nanostructures*, 14(1-2), 11-17}.

The photovoltaic effect in solid state was first observed by Adams and Day in 1876⁶, when they were investigating the photoconductive behavior of selenium (Se) (their photovoltaic apparatus is schematically shown in Figure 3.1b). They discovered that in the light off-state, the resistance of Se is directly proportional to the battery-power. In addition, the resistance can be changed by reversing the current direction; Flow of current through the Se bar can result in permanent polarization along the

current path as it can cause the increase of electrical resistance for this current, but it diminishes resistance if a subsequent current is applied in the opposite direction^{6,7}. When the passage of current is exposed to light, an electromotive force is induced within the selenium as opposed to the electromotive force due to the polarization and hence can facilitate the current flow. On the other hand, it was found that in a virgin Se piece (which never conducted an electrical current), identified by a label as shown in the picture, because of the inhomogeneity of the crystal structure, an electric potential difference can be induced only by means of light, which then induces an electric current through the medium⁶. This discovery opened the path towards the construction of the first "thin-film" photovoltaic device (: solar cell) operating based on the metal-semiconductor heterojunction of Se with an ultrathin layer of gold, by Charles Fritts in 1883⁸ (the designed device is demonstrated in Figure 3.2). By 1930, both the Se cell and copper oxide cell were being employed in light sensitive devices. The early photovoltaic devices were inefficient with light-electricity conversion efficiencies of less than 1%⁷. In 1939, the first p-n junction (made from slowly crystallized Se) was discovered by R. S. Ohl of Bell Laboratories⁹. Studying the behavior of p-n junctions revealed the role of donor and acceptor impurities in electrical properties of semiconductors¹⁰.

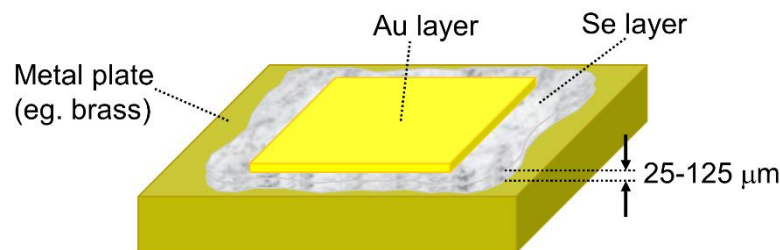


Figure 3.2. Thin film Se photovoltaic device suggested by Charles Fritts in 1883.

Later in 1950s, different semiconductor materials were explored in PV devices such as Si¹¹ as the monocrystalline, Cu_xS/CdS heterojunction¹² and GaAs¹³ fabricated by developing physical growth techniques. They exhibited considerable conversion efficiency of about 6% and, interestingly, long lifetime. The conversion efficiency of Si solar cells has reached the promising maximum value of 26.7 %, now¹⁴.

The PV as a source of direct energy conversion was employed as power supply early in the radio transmitter and space applications⁷, and then as a replacement for fossil energy sources in terrestrial applications.

Most of the photovoltaic systems up to date are based on inorganic semiconductor p-n junctions, specifically made from silicon (Si). Binary (belonged to

the groups of II-VI (Eg, CdTe) and III-V (Eg, GaAs)), ternary (from the group of I-III-VI₂ (CuInSe₂ and Cu(In,Ga)Se₂/CIGS)), and quaternary (from the group of I₂-II-IV-VI₄) compound semiconductors were found highly desirable for PV applications^{15,16}.

In the next section, the basic mechanism of photovoltaic effect is discussed in homogeneous semiconductor p-n junction, in detail.

3.3. Photovoltaic effect in p-n junction semiconductors

A p-n junction diode can be formed at interface of uniformly doped n-type (donor doped) and p-type (acceptor doped) layers of a homogeneous semiconductor, called homojunction, or of two different semiconductors (with different band gap energies) classified as heterojunction¹⁷.

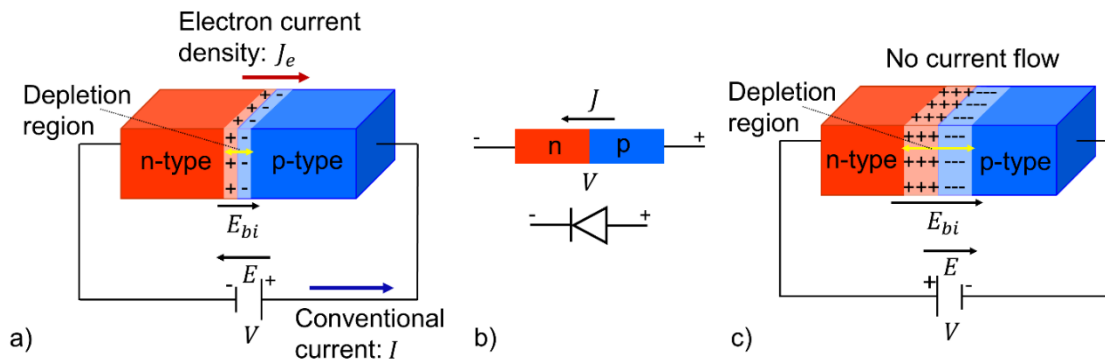


Figure 3.3. a) forward biased p-n junction, b) corresponding circuit symbol of the diode, and c) reverse biased p-n junction, respectively.

The p-n junction is typically specified for its conduction characteristics as they operate as a single-side conductor. Once the p-n junction is made, near the interface, electron charge carriers from the n-type side diffuse into the p-type region because of the charge density gradient, and they leave behind positively charged ions. The same mechanism happens for the hole charge carriers in the p-type region as they diffuse towards the n-type region, and they leave behind negatively charged ions near the p-n junction. Presence of fixed ions with opposite charges induces an electric field at the junction called 'built-in', E_{bi} . The voltage (V_{bi}) associated to the built-in electric field can be obtained from¹⁷,

$$V_{bi} = V_T \ln \left(\frac{N_d N_a}{n_i^2} \right) \quad (3.1)$$

here $V_T = (K_B T / e)$ is the thermal voltage¹⁸, N_d and N_a are thermal equilibrium majority charge carrier (donor and acceptor, orderly) concentrations in the n- and p-type regions, respectively, and n_i is the intrinsic concentration of the depletion region. When the charge carriers diffuse from one region into the adjacent, the built-in electric field (E_{bi}) pushes them back into the original region. Eventually, the net charge flow across the junction goes to zero (when the equilibrium condition is established), and a region depleted from mobile charges is formed at the p-n junction, called '*depletion region*'. The depletion region acts as a voltage-controlled resistor: If the biased electric field is in the opposite direction of the built-in electric field corresponding to the '*forward bias condition*', the net electric field in the depletion region is reduced below the equilibrium value (equal to the built-in electric field). This leads to shrinkage of the depletion region and decrease of the resistance. On the other hand, inversely, when the external electric field is in the same direction as the built-in electric field associated as '*reverse bias condition*', the width of the depletion region (shown in Figure 3.3), as well as, the resistance increase.

In the dark state, when a voltage is applied to the p-n junction, the total current density in an ideal p-n junction (along the junction) can be obtained from¹⁷,

$$J = J_s \left(e^{\left(\frac{V}{V_T}\right)} - 1 \right) \quad (3.2)$$

reverse saturation current density measured at the reverse bias condition. In forward bias condition ($V > 0$), the majority charge carriers from each region are able to cross the depletion region and reach the opposite region with different doping condition (as a consequence of both the E_{bi} strength and the depletion width reduction), thereby increasing the minority carrier density in the opposite region (counted as the excess minority carriers). As long as the p-n junction is biased, the injection of charge carriers across the depletion region continuously happen, and the current density J (as summation of hole current density J_p (from p-side to n-side) and electron current density J_e (in opposite direction)) is created in the junction (although, only a fraction of this current can reach the external circuit before the recombination process happened to the mobile charge carriers). The total current density is from the p-type side to the n-type side in the same direction as the conventional current I (: hole current from positive to negative polarity of the battery) defined in the electrical circuits, governed by the diffusion mechanism. In the reverse bias condition ($V < 0$), there is a small current in the junction despite the induced high resistance. By increasing V by only a

few V_T , the current flow saturates at a very small amount. However, breakdown can happen if the reverse bias voltage increases beyond a critical value called *breakdown voltage*, which results to a rapid huge current flow in the p-n junction. Breakdown can happen due to two different mechanisms: **Zener** and **avalanche**¹⁷. The former (known as tunneling mechanism) can happen in highly doped p-n junctions, where the electrons are able to tunnel from the valence band on the p side into the sufficiently close conduction band on the n side of the junction¹⁷. In the latter, free electrons are rapidly generated from the collision of the accelerated high energetic electrons with the atoms in the depletion region¹⁷. The current-voltage characteristics of a p-n junction diode is shown in Figure 3.4.

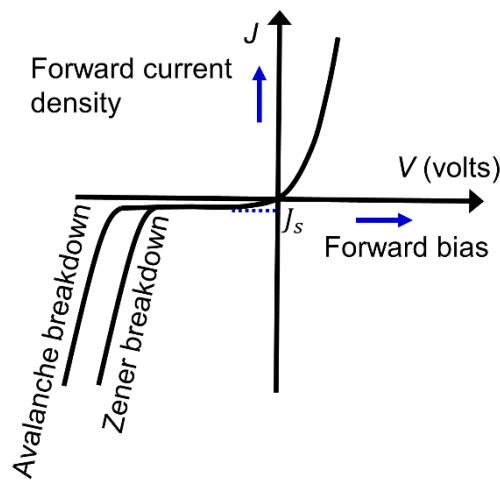


Figure 3.4. Current-voltage characteristics of a p-n junction diode.

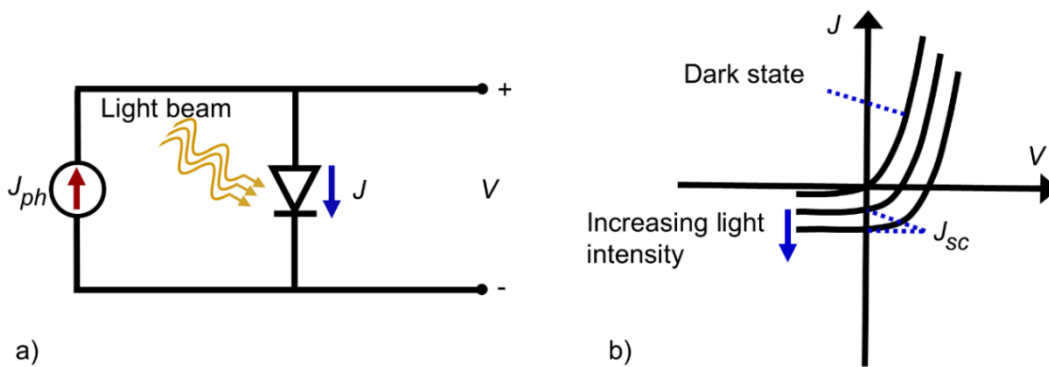


Figure 3.5. a) Equivalent circuit of a forward biased p-n junction under light illumination. b) Schematically representation of the photocurrent characteristics of a p-n junction with illumination compared with dark state.

Under light illumination, pairs of electron-hole can be generated throughout the whole device, and then they diffuse through the material. If photo electron-hole pairs

can be affected by the built-in electric field before they recombine, they can get separated, and contribute to the current flow across the junction: A photo-current density can be formed from the electron flow toward the n-type side and the hole flow toward the p-type side under the action of the built-in electric field, at the same time (: the generated photo-current density is always in opposite direction of the conventional current density in the forward bias condition in the dark state, considered as reverse current, Figure 3.5a). The photo-current density is usually independent of the biased voltage V , and it is measured at 'short-circuit' condition (: where the sides of the p-n junction are simply connected with a low-resistance wire), for this specific reason shown as J_{SC} . In the light-on state, the net current density has the same characteristics as the dark photo-current density (described by Equation (3.2)), but shifted in negative current direction because of superposition with the photo-current density J_{SC} ¹⁸ (Figure 3.5b).

3.4. Photovoltaic effect in ferroelectric materials, so-called bulk photovoltaic (BPV) effect

Lithium niobate (LiNbO₃, LN) is a synthetic dielectric material¹⁹, which belongs to the ferroelectrics (: AB₃O₃-type)²⁰, a congruent pure LiNbO₃ crystal is demonstrated in Figure 3.6a. It was first introduced by Zachariassen in 1928¹⁹, and reported as ferroelectric by Matthias and Remeika in 1949²¹. Since 1965, when a large homogeneous single LiNbO₃ crystal was grown by Ballman²² and Fedulov et. al²³ for the first time, tremendous attention was drawn to LiNbO₃ applications in different fields of optics, acoustics and technology over decades¹⁹.

Historically, Fridkin discovered the **bulk photovoltaic (BPV) effect** in an experimental investigation of a ferroelectric SbS(l, Br) crystal in 1970²⁴, which was later explained by Glass et al. in 1974, through photocurrent investigations of iron- and copper-doped crystals of LiNbO₃^{25,26}.

The BPV effect can happen in non-centrosymmetric (: without a center of symmetry) crystals²⁰, including pyroelectrics, piezoelectrics and gyrotropic materials, when suitably doped, such as LiNbO₃, KNbO₃, BaTiO₃ and LiTaO₃^{20,27}. The light-induced photovoltage in BPV effect depends on the polarization state of the incident light, and the attributed energy can exceed the crystal band gap energy by several orders of magnitude under a moderate level of light intensity (the response wavelength depends on type and doping of the crystal). A LiNbO₃ crystal properly doped with iron exhibits a strong photovoltaic effect^{27,28}, as it can give rise to a bulk electric field on the

order of 140 kV/cm²⁸. The induced electric field in the BPV effect can modulate the refractive index of the crystal via a linear electro-optic effect^{20,29,30}. The BPV effect differs from the PV effect seen in semiconductor junctions: unlike the PV effect, it does not require an inhomogeneity of the optical field or of the medium as a precondition. The BPV effect is discussed in detail in the following sections.

3.5. Microscopic investigation of the BPV effect

The BPV effect can be explained based on the small strong-coupling polaron model³¹ where the polaron radius is less than a single lattice site²⁰, which indicates that the neighboring sites are kept almost intact³². In this case, a small bound polaron (: a photoexcited charge carrier coupled with phonons³³) state is created due to the Coulomb interaction with the distorted host ions²⁰. The transport of the small polarons is described as thermally activated hopping between different sites²⁰, and finally being trapped by crystal defects and impurities.

In the congruent LiNbO₃ crystal, point defects with inevitable high densities (such as extrinsic substitutional antisite defects Nb_{Li}^{5+} or Li vacancy V_{Li}^-) basically contribute to the polaron formation. In general, there are four different types of small polarons in LiNbO₃³⁴: free electron polarons (FPs)^{34,35} which form at regular Nb_{Nb}^{5+} sites; bound electron polarons (GPs)^{34,35} attributed to the defective site Nb_{Li}^{4+} (: emerged from an electron self-trapped by Nb_{Li}^{5+}); and bipolarons (BPs)^{34,35} as a linear combination of the free and the bound polaron associated with neighboring sites Nb_{Nb}^{4+} and Nb_{Li}^{4+} , respectively; and bound hole polarons (HP)³⁴ localizing at O^- ions as a result of band-to-band excitation under high energy irradiation condition. In LiNbO₃: Fe (crystal and crystallographic structures shown in Figure 3.6b and c, respectively), the impurity centers of Fe^{2+} and Fe^{3+} incorporated at the Li site generate donor/acceptor $Fe_{Li}^{2+/3+}$ defects, which additionally introduce another bound electron polaron^{20,34,36}, localized at the Fe impurities. Depending on the type of polaron, the activation energy is different.

The BPV effect in LiNbO₃ stems from the non-centrosymmetric structure of the crystal^{31,37}. On the atomic basis, the probability of the electron coherent transition from Fe_{Li}^{2+} to one of the eight unequally located surrounding neighbor Nb_{Nb}^{5+} conduction band states depends strongly on the $Fe_{Li}^{2+} - Nb_{Nb}^{5+}$ distances. Each transfer is associated with a time-dependent dipole moment, which locally triggers coherent photo-current densities in the crystal³⁷. Because of the polar structure of Fe:LN, all induced photo-

current densities add up to a non-zero net flow J_{coh} along the polar crystallographic c -axis^{31,37} of the crystal.

Principally, the small bound electron polaron transition from Fe_{Li}^{2+} to Nb_{Nb}^{5+} is followed by the creation of free small polarons Nb_{Nb}^{4+} (within $\sim 10^{-13}$ s at room temperature), which incoherently hop in the crystal and participate in a thermally activated incoherent current density J_{incoh} (eventually measured as the BPV current) during their lifetime τ , before being trapped by deep defect sites^{31,37} such as Nb_{Li}^{5+} and Fe_{Li}^{3+} . The incoherent current density J_{incoh} flows in the same direction as the coherent current density J_{coh} i.e., along the c -direction, in order to fulfill the continuity condition³⁷.

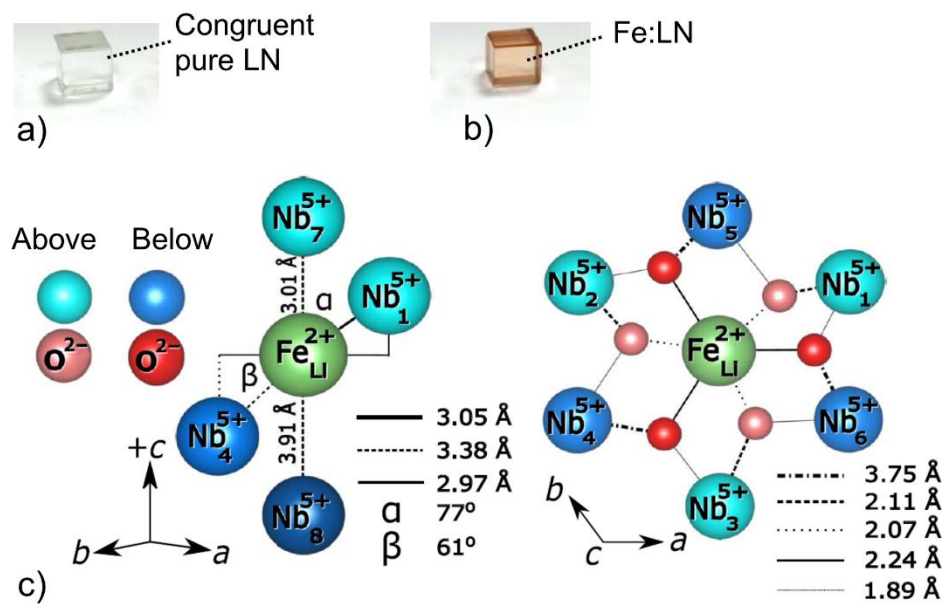


Figure 3.6. Photographs of a) and b) congruent pure LiNbO₃ and Fe:LN crystals, respectively. c) Schematical depiction of the crystallographic structure of Fe:LN based on interatomic distances in two different views of the crystallographic c -axis as seen in left (with all O^{2-} omitted), and normal to the surface (right, with some O^{2-} omitted)³¹. {The figure was taken from Ref. 31}.

3.6. Scalar formulation of the BPV current

Based on the scalar formalism, the BPV current density along the crystal can be introduced as³⁸,

$$J_{PV} = q\alpha(\lambda)l_{PV}(I/h\nu) \quad (3.3)$$

where q is the elementary (electron) charge, $\alpha(\lambda)$ is the absorption coefficient as a function of the wavelength λ , l_{PV} is the photovoltaic drift length (on the order of 1-5 Å), I is the light intensity, h is the Plank constant and ν is the light frequency. By substituting the absorption coefficient relation as, $\alpha = sN_D$ (: where s and N_D are the photoinization cross section and the concentration of donors (Fe^{2+}), respectively), the above mentioned relation can be rewritten as^{27,38},

$$J_{PV} = qsN_D l_{PV}(I/h\nu), \quad (3.4)$$

which is known as the short-circuit current. An equivalent circuit of photovoltaic current J_{PV} and induced photovoltage V_{ph} is depicted in Figure 3.7.

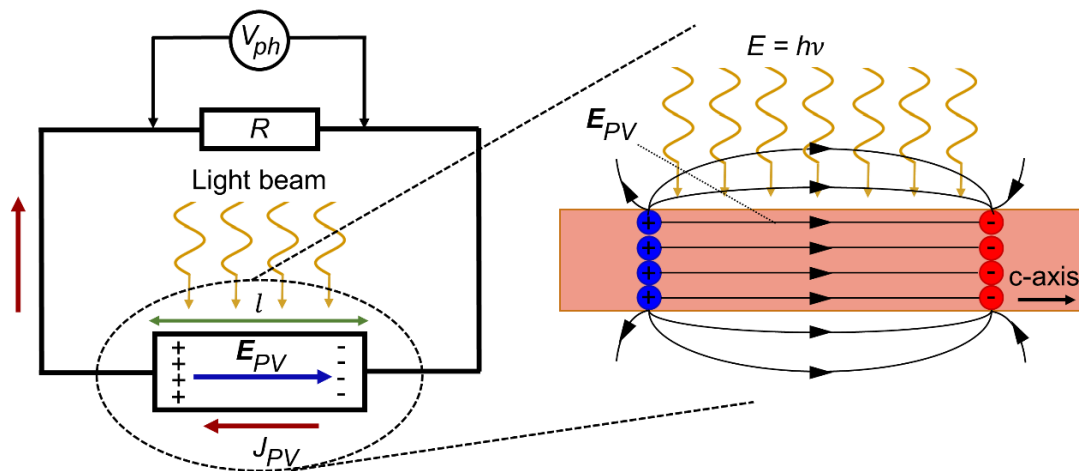


Figure 3.7. Formation of the PV electric field as a consequence of the BPV effect shown in an equivalent circuit of photovoltaic current J_{PV} and photovoltage V_{ph} .

If the sample is uniformly illuminated and the electrodes are disconnected (: open circuit condition), the induced photocurrent J_i creates a photovoltage across the sample corresponding to the correlated space-charge field (which distributes both inside, in opposite direction of the current density, and outside of the crystal), called photovoltaic field E_{PV} shown in Figure 3.7. The current density in the open circuit condition goes to zero when the induced photovoltaic field fully suppresses the charge carriers transport in the crystal. The photovoltage V_{ph} can be calculated from Ohm's law, as^{39,41},

$$V_{ph} = \frac{J_{PV}}{\sigma_d + \sigma_{ph}} l \quad (3.5)$$

where l is the width of the crystal (: the distance between electrodes), σ_d is the dark conductivity, which is commonly negligible (order of about $10^{-15}/\Omega\text{cm}$), and σ_{ph} is the crystal photoconductivity, respectively. The induced photovoltage is usually high and it is not limited by the band gap energy. The photoconductivity is proportional to the photoexcited electron density n , via the relation²⁰,

$$\sigma_{ph} = q\mu n \quad (3.6)$$

where μ is the electron mobility. The photoexcited free electron density n is defined as^{20,27},

$$n = \frac{sN_D}{\gamma N_A} (I/h\nu) \quad (3.7)$$

where N_A and γ are the acceptor concentration ($[Fe^{3+}]$) and the associated trapping coefficient, respectively. As a result, the value of the photovoltaic field can be calculated from²⁷,

$$E_{PV} = \frac{l_{PV}\gamma N_A}{\mu}. \quad (3.8)$$

In the highly doped LiNbO₃ crystal with iron (0.1% wt) shone by a light intensity of 10 W/cm² with wavelength $\lambda = 532$ nm, the parameters²⁷ $s = 2 \times 10^{-18}$ cm², $N_D = 10^{18}$ cm³, $N_A = 10^{19}$ cm⁻³, $\gamma = 10^{-9}$ cm³/s, $\mu = 5 \times 10^{-3}$ cm²/V.s, $l_{PV} = 5$ Å can be used in the calculation of the photovoltaic current J_{PV} , the anomalously large electric field E_{PV} , and the photoexcited free electron density n .

3.7. Phenomenological formulation of the BPV current

Photo-excitation of the donor centers Fe^{2+} gives rise to the electrical dipole moment $\mathbf{p}_{PV} = q\mathbf{l}_{PV}$, whose time variations strongly depend on the relative direction with respect to the polarization of the light. In the vector formalism, the PV current density \mathbf{J} for a linearly (L) and circularly (C) polarized light can be described as^{20,40,41},

$$\mathbf{J}_i = \sum_{jk} G_{ijk}^L \mathbf{e}_j \mathbf{e}_k^* I + i \sum_s G_{is}^C [\hat{\mathbf{e}} \times \hat{\mathbf{e}}^*]_s I \quad (3.9)$$

where G (G_{ijl}^L and G_{il}^C) represent the photovoltaic tensor (: Glass tensor) of third and second rank for linearly and circularly polarized light, respectively, I is the light intensity, and e_j is the j 'th component of the polarization unit vector e , correspondingly. The coefficient i and asterisk denote the imaginary unit and the complex conjugate, respectively. Equation (3.9), known as the phenomenological expression of the BPV effect, gives the relation of the photocurrent with the light intensity and polarization. All effective parameters, such as material, temperature and wavelength were conventionally taken into account in the determination of the BPV tensor^{20,40}. The symmetric G_{ijk}^L is the same as the conventional piezoelectric tensor d_{ijk} , where the non-zero elements were determined from the crystal symmetry. For example, for Fe:LN^{20,38} and LiTaO₃²⁰ (belonging to the point symmetry group C_{3v}), the non-zero elements are G_{333} , $G_{311} = G_{322}$, $G_{222} = -G_{112} = -G_{121} = -G_{211}$, $G_{113} = G_{223}$. The latter term in relation (3.9), (i.e. G_{is}^C) is a non-zero tensor only for gyrotropic non-centrosymmetric crystals, with only one independent element $G_{21}^C = -G_{12}^C$ ⁴⁰. In general, the non-zero values of the Glass tensor obey $G_{333} \approx G_{311} \gg G_{222}$ and G_{113} ²⁹. For example, the Glass elements for the Fe:LN³⁷ are $G_{333} = 40 \times 10^{-9}$ 1/V equal to the G_{311} value, $G_{222} = 2 \times 10^{-9}$ 1/V, and $G_{113} = 0.8 \times 10^{-9}$ 1/V for an excitation wavelength of $\lambda = 500$ nm (corresponding to a photon energy of 2.48 eV) and an iron doping concentration of $6 \times 10^{18}/\text{cm}^3$.

3.8. One-center charge transport scheme and rate equations

Charge carrier transportation in the BPV effect can be described based on the 'one-center model' picture, where the photo-excited electrons (one type of free charge carrier) are transported between one single donor center (i.e., Fe^{2+}) and its ionized state as the only acceptor center (i.e., Fe^{3+}), as schematically presented in Figure 3.8. The total concentration of active centers N (: $N = N_D + N_A$) stays constant in this scheme. The temporal evolution of the system under an arbitrary light intensity $I(r, t)$, can be described by the rate equations, as^{20,29,42},

$$\frac{\partial n}{\partial t} = sIN_D - \gamma nN_A - \frac{1}{q} \nabla \cdot \mathbf{J} \quad (3.10)$$

$$\frac{\partial N_D}{\partial t} = -\frac{\partial N_A}{\partial t} = -sIN_D + \gamma nN_A \quad (3.11)$$

$$\mathbf{J} = qsIN_D l_{PV} \mathbf{u}_{PV} + q\mu n \mathbf{E} - qD \nabla n \quad (3.12)$$

where \mathbf{J} and \mathbf{E} are total current density and electric field, respectively, and D is the diffusion coefficient (accordingly to the Einstein relation: $D = \mu K_B T / q$), \mathbf{u}_{PV} is the unit vector in the direction of the polar axis. The total current density \mathbf{J} results from photovoltaic, drift, and diffusion contributions²⁵ corresponding to the first, second and third term in relation (3.12), respectively ($\mathbf{J} = \mathbf{J}_{PV} + \mathbf{J}_{drift} + \mathbf{J}_{diff}$). The diffusion current density J_{diff} (: with the associated relation in one-dimension (1D) as $J_{diff} = qD \frac{dn}{dz}$) can result from a spatially nonuniform illumination, where the drift current J_{drift} is triggered by the present electric field E as the summation of the induced space-charge (photovoltaic) along the crystallographic \mathbf{c} -axis (supposed in the z -direction) and the external electric field ($E = E_{PV} + E_{ext}$). This model is suitable for the moderate light intensity regime, where the thermal ionization of donors is negligible²⁹.

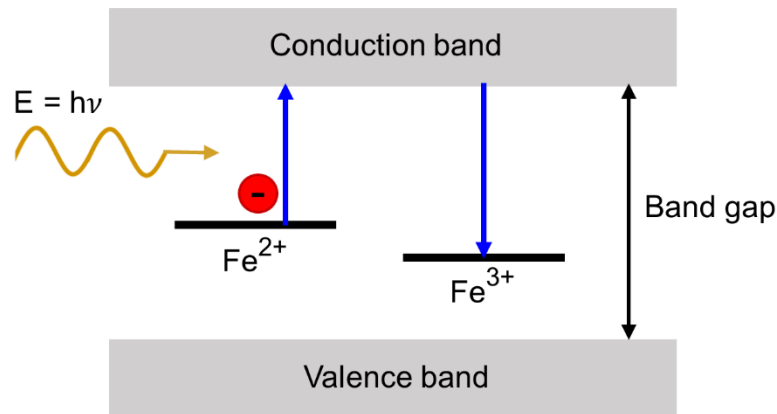


Figure 3.8. Schematic presentation of charge transition in a one-center model composed of filled and empty electron traps, i.e., Fe^{2+} and Fe^{3+} , respectively.

The space-charge field can be obtained from Poisson's equation, as²⁹,

$$\nabla \cdot \mathbf{E} = \frac{q}{\epsilon_0 \epsilon} (n + N_D - N_{D0}) = \frac{q}{\epsilon_0 \epsilon} (n - N_A + N_{A0}) \quad (3.13)$$

where N_{D0} and N_{A0} are thermal equilibrium densities of donor and acceptor centers, respectively, ϵ is the relative dielectric constant of the crystal. From the continuity equation governing the current density \mathbf{J} , it can be shown that²⁹,

$$\nabla \cdot \left(\epsilon_0 \epsilon \frac{\partial \mathbf{E}}{\partial t} + \mathbf{J} \right) = 0. \quad (3.14)$$

From the above mentioned equations, the space-charge field and the corresponding current density can be obtained for any arbitrary light illumination.

3.9. Light spectrum and optical response of LiNbO₃ and Fe:LiNbO₃ (Fe:LN)

The efficiency of the BPV effect measured at the photoionization cross section (s) of the crystal can be determined from the absorption spectrum (optical response of the crystal). In the absorption spectrum of LiNbO₃ (Figure 3.9a), there are two broad peaks³⁹ (of the order of ≈ 1 eV) centered at 310 nm and 628 nm, corresponding to the photon energy of 4 and 1.97 eV, respectively. Since the energy required for the transition between the deep center (dominated by bipolarons) and the conduction band is about 2.0 ~ 2.5 eV, a large amount of electrons can be excited at 310 nm from the deep center into the conduction band³⁹. At 628 nm, only a limited amount of electrons can be excited by this amount of photon energy³⁹.

The absorption peak at 310 nm is mainly associated with band to band absorption (: transition between the deep center and the conduction band), while the absorption peak at 628 nm is an additional result of the absorption between the shallow center (attributed to the small polarons) and the conduction band, as well. For LiNbO₃, an optical response and a photovoltaic current is expected from 3.0 to 0.5 eV⁴³.

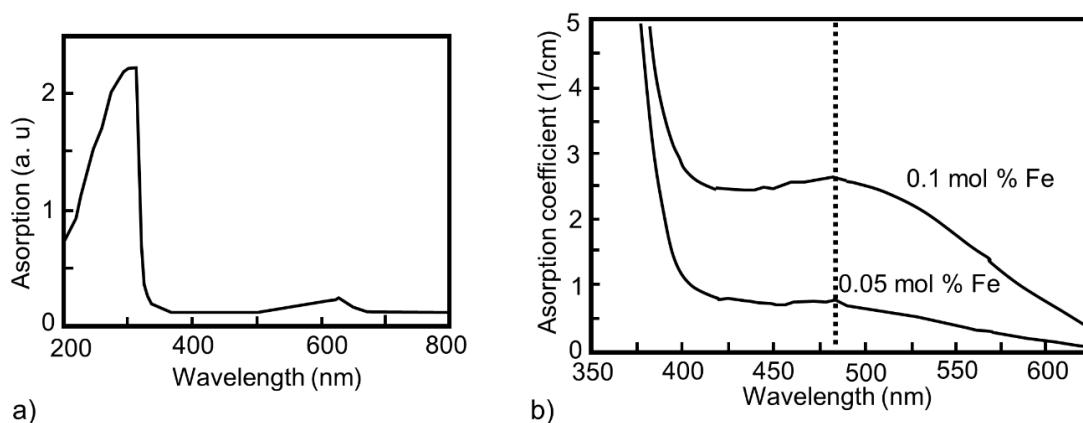


Figure 3.9. a) The absorption spectra of LiNbO₃³⁹. b) The absorption spectrum of two Fe:LN samples with Fe concentrations of 0.1 and 0.05 % for unpolarized light⁴⁰. The absorption peak at 484 nm due to the intervalence transition $Fe_{Li}^{2+}-Nb_{Nb}^{5+}$ is shown with a dotted line. {The graphs a and b were taken from Ref. 39 and Ref. 40, respectively}.

Doping a crystal with transition-metal impurities, such as iron modifies the absorption spectrum, which is extended from 350 nm to 600 nm^{38,40} (seen in Figure 3.9b). Among potential dopants, iron impurities give rise to the highest PV effect⁴⁴. The absorption spectrum is specified with a broad absorption band centered at 484 nm^{38,40} (2.56 eV), shown with a dotted line in Figure 3.9b. The absorption band is attributed to the small polaron transition from Fe_{Li}^{2+} to Nb_{Nb}^{5+} at neighboring sites^{38,45,46}. The Iron impurities enhance the photovoltaic response because of the high photovoltaic drift length, together with the low electron mobility³⁸ (see equation (3.8)).

3.10. Permittivity and refractive indices

Due to the structural polar symmetry, the electric displacement field in the LiNbO₃ can be described based on a diagonal, second-rank relative permittivity tensor

$$\varepsilon_{ij},$$

$$\varepsilon_{ij} \equiv \begin{pmatrix} \varepsilon_{11} & 0 & 0 \\ 0 & \varepsilon_{22} & 0 \\ 0 & 0 & \varepsilon_{33} \end{pmatrix} \quad (3.15)$$

as introduced $\mathbf{D}_i = \varepsilon_{ij} \mathbf{E}_j$ (\mathbf{E}_j : electric field elements)⁴⁷. Non-zero elements of the dielectric constant $\varepsilon_{ij} = \varepsilon_{ij}/\varepsilon_0$ at 25°C are^{20,48} $\varepsilon_{11}^T = 84$ and $\varepsilon_{33}^T = 30$ (for an unclumped crystal), $\varepsilon_{11}^S = 44$ and $\varepsilon_{33}^S = 29$ (for a clumped crystal), respectively, while the dielectric constant has the same value for any electric direction perpendicular to the crystal polar \mathbf{c} -axis (assumed in the z-direction), which means $\varepsilon_{11} = \varepsilon_{22}$.

The optical (light beam frequency dependent) relative permittivity can be described in terms of the refractive indices (n_o and n_e), where the associated values can be manipulated by means of introducing optical-damage-resistant ions (such as Mg, Zn, and In) or [Li]/[Nb] concentration ratio variation²⁰. The LiNbO₃ is transparent in the optical range of 320 nm to 5000 nm (with optical transmission more than 60%). According to Schlarb et al.⁴⁹⁻⁵⁴ the refractive index n for different compositions of LiNbO or doped with optical damage-resistant impurities can be obtained in the range of 400-1200 nm (with an accuracy of about 2×10^{-3}) with respect to the intrinsic defects on the basis of the Sellmeier formalism²⁰. The empirical approach of Jundt et al.⁵⁵ can give the refractive index for laser wavelengths up to 5000 nm with an improved accuracy of 2×10^{-4} , but restricted to the pure LiNbO₃ crystal or doped with Mg ions²⁰.

References

- ¹ Rothwarf, A., & Böer, K. W. (1975). Direct conversion of solar energy through photovoltaic cells. *Progress in Solid State Chemistry*, 10, 71-102.
- ² Würfel, P., & Würfel, U. (2016). *Physics of solar cells: from basic principles to advanced concepts*. John Wiley & Sons.
- ³ Klatt, G., Hilser, F., Chao, W., Gebbs, R., Bartels, A., Huska, K., ... & Faist, J. (2010). Intense terahertz generation based on the photo-Dember effect. In *CLEO/QELS: 2010 Laser Science to Photonic Applications* (pp. 1-2). IEEE.
- ⁴ Becquerel, A. E. (1839). Recherches sur les effets de la radiation chimique de la lumiere solaire au moyen des courants electriques. *CR Acad. Sci*, 9, 145-149.
- ⁵ Green, M. A. (1990). Photovoltaics: coming of age. In *IEEE Conference on Photovoltaic Specialists* (pp. 1-8). IEEE.
- ⁶ Adams, W. G., & Day, R. E. (1877). The action of light on selenium. *Proceedings of the Royal Society of London*, 25(171-178), 113-117.
- ⁷ Agrawal, B., & Tiwari, G. N. (2010). *Building integrated photovoltaic thermal systems: for sustainable developments*. Royal Society of Chemistry.
- ⁸ Fritts, C. E. (1883). On a new form of selenium cell, and some electrical discoveries made by its use. *American Journal of Science*, (156), 465-472.
- ⁹ R.S. Ohl. (1941). Light-sensitive electric device including silicon. US Patent No. 2,402,622.
- ¹⁰ Aazou, S., Ibral, A., White, M. S., Kaltenbrunner, M., Glowacki, E. D., Egbe, D. A., ... & Assaid, E. M. (2013). Organic Bulk Heterojunction Solar Cells Based on P3HT and Anthracene-Containing PPE-PPV: Fabrication, Characterization and Modeling. *Journal of optoelectronics and Advanced Materials*, 13(5-6), 395-404.
- ¹¹ Chapin, D. M., Fuller, C. S., & Pearson, G. L. (1954). A new silicon p-n junction photocell for converting solar radiation into electrical power. *Journal of Applied Physics*, 25(5), 676-677.
- ¹² Reynolds, D. C., Leies, G., Antes, L. L., & Marburger, R. E. (1954). Photovoltaic effect in cadmium sulfide. *Physical Review*, 96(2), 533.
- ¹³ Jenny, D. A., Loferski, J. J., & Rappaport, P. (1956). Photovoltaic effect in GaAs p-n junctions and solar energy conversion. *Physical Review*, 101(3), 1208.
- ¹⁴ Green, M. A., Dunlop, E. D., Levi, D. H., Hohl-Ebinger, J., Yoshita, M., & Ho-Baillie, A. W. (2019). Solar cell efficiency tables (version 54). *Progress in Photovoltaics: Research and Applications*, 27(NREL/JA-5K00-74116).
- ¹⁵ Moorthy, S. B. K. (Ed.). (2015). *Thin film structures in energy applications*. Springer.

-
- ¹⁶ Liu, D., Han, D., Huang, M., Zhang, X., Zhang, T., Dai, C., & Chen, S. (2018). Theoretical study on the kesterite solar cells based on Cu₂ZnSn (S, Se) 4 and related photovoltaic semiconductors. *Chinese Physics B*, 27(1), 018806.
- ¹⁷ Neamen, D. A. (2012). *Semiconductor physics and devices: basic principles*. New York, NY: McGraw-Hill.
- ¹⁸ Breitenstein, O. (2013). Understanding the current-voltage characteristics of industrial crystalline silicon solar cells by considering inhomogeneous current distributions. *Opto-Electronics Review*, 21(3), 259-282.
- ¹⁹ Korkishko, Y. N., & Fedorov, V. A. (1999). *Ion exchange in single crystals for integrated optics and optoelectronics*. Cambridge Int Science Publishing.
- ²⁰ Volk, T., & Wöhlecke, M. (2008). *Lithium niobate: defects, photorefraction and ferroelectric switching* (Vol. 115). Springer Science & Business Media.
- ²¹ Matthias, B. T., & Remeika, J. P. (1949). Ferroelectricity in the ilmenite structure. *Physical Review*, 76(12), 1886.
- ²² Ballman, A. A. (1965). Growth of piezoelectric and ferroelectric materials by the Czochralski technique. *Journal of the American Ceramic Society*, 48(2), 112-113.
- ²³ Fedulov, S. A., Shapiro, Z. I., & Ladyzhin, P. B. (1965). Growth of crystals of LiNbO₃ LTAO₃ and NANBO₃ by czochralski method. *SOVIET PHYSICS CRYSTALLOGRAPHY, USSR*, 10(2), 218.
- ²⁴ Fradkin, V. M., & Magomadov, R. M. (1979). Anomalous photovoltaic effect in LiNbO₃: Fe in polarized light. *JETP Letters*, 30, 686-688.
- ²⁵ A. M. Glass, D. von der Linde, & T. J. Negran. (1974). High-voltage bulk photovoltaic effect and the photorefractive process in LiNbO₃. *Applied Physics Letter*, 25, 233-235.
- ²⁶ Glass, A. M., Linde, D. V. D., & Negran, T. J. (1995). High-voltage bulk photovoltaic effect and the photorefractive process in LiNbO₃. In *Landmark Papers On Photorefractive Nonlinear Optics* (pp. 371-373).
- ²⁷ Villarroel, J., Burgos, H., García-Cabañes, Á., Carrascosa, M., Blázquez-Castro, A., & Agulló-López, F. Photovoltaic versus optical tweezers. *Optics express*, 19(24), 24320-24330, 2011.
- ²⁸ Carns, J. L., Cook, G., Saleh, M. A., Serak, S. V., Tabiryan, N. V., & Evans, D. R. (2006). Self-activated liquid-crystal cells with photovoltaic substrates. *Optics letters*, 31(7), 993-995.
- ²⁹ Agulló-López, F., Calvo, G. F., & Carrascosa, M. (2006). Fundamentals of photorefractive phenomena. In *Photorefractive Materials and Their Applications 1* (pp. 43-82). Springer, New York, NY.
- ³⁰ Arizmendi, L. (2004). Photonic applications of lithium niobate crystals. *physica status solidi (a)*, 201(2), 253-283.
- ³¹ Nadupalli, S., Kreisel, J., & Granzow, T. (2019). Increasing bulk photovoltaic current by strain tuning. *Science advances*, 5(3), eaau9199.

-
- ³² Cancellieri, C., & Strocov, V. N. (2018). *Spectroscopy of Complex Oxide Interfaces*. Springer International Publishing, Cham.
- ³³ Byrnes, S. J. (2008). Basic theory and phenomenology of polarons. *Department of Physics, University of California at Berkeley, Berkeley, CA, 94720*.
- ³⁴ Vittadello, L., Bazzan, M., Messerschmidt, S., & Imlau, M. (2018). Small Polaron Hopping in Fe: LiNbO₃ as a Function of Temperature and Composition. *Crystals*, 8(7), 294.
- ³⁵ Schirmer, O. F., Imlau, M., Merschjann, C., & Schoke, B. (2009). Electron small polarons and bipolarons in LiNbO₃. *Journal of Physics: Condensed Matter*, 21(12), 123201.
- ³⁶ Sanson, A., Zaltron, A., Argiolas, N., Sada, C., Bazzan, M., Schmidt, W. G., & Sanna, S. (2015). Polaronic deformation at the Fe 2+/3+ impurity site in Fe: LiNbO₃ crystals. *Physical Review B*, 91(9), 094109.
- ³⁷ Schirmer, O. F., Imlau, M., & Merschjann, C. (2011). Bulk photovoltaic effect of LiNbO₃: Fe and its small-polaron-based microscopic interpretation. *Physical Review B*, 83(16), 165106.
- ³⁸ Carrascosa, M., García-Cabañes, A., Jubera, M., Ramiro, J. B., & Agulló-López, F. (2015). LiNbO₃: A photovoltaic substrate for massive parallel manipulation and patterning of nano-objects. *Applied Physics Reviews*, 2(4), 040605.
- ³⁹ Lu, Z., Zhao, K., & Li, X. (2011). Photovoltaic effect in ferroelectric LiNbO₃ single crystal. In *Ferroelectrics-Physical Effects*. IntechOpen.
- ⁴⁰ Dam-Hansen, C. (1996). Magnetophotorefractive effect and interference filters in lithium niobate.
- ⁴¹ Fridkin, V. M. (2001). Bulk photovoltaic effect in noncentrosymmetric crystals. *Crystallography Reports*, 46(4), 654-658.
- ⁴² Arregui, C., Ramiro, J. B., Alcázar, Á., Méndez, Á., Burgos, H., García-Cabañes, Á., & Carrascosa, M. (2014). Optoelectronic tweezers under arbitrary illumination patterns: theoretical simulations and comparison to experiment. *Optics express*, 22(23), 29099-29110.
- ⁴³ Brüning, H., Dieckmann, V., Schoke, B., Voit, K. M., Imlau, M., Corradi, G., & Merschjann, C. (2012). Small-polaron based holograms in LiNbO₃ in the visible spectrum. *Optics express*, 20(12), 13326-13336.
- ⁴⁴ Krätzig, E., & Kurz, H. (1977). Spectroscopic investigation of photovoltaic effects in doped LiNbO₃. *Journal of The Electrochemical Society*, 124(1), 131-134.
- ⁴⁵ Clark, M. G., DiSalvo, F. J., Glass, A. M., & Peterson, G. E. (1973). Electronic structure and optical index damage of iron-doped lithium niobate. *The Journal of chemical physics*, 59(12), 6209-6219.
- ⁴⁶ Hush, N. S. (1968). Homogeneous and heterogeneous optical and thermal electron transfer. *Electrochimica Acta*, 13(5), 1005-1023.

-
- ⁴⁷ Nye, J. F. (1985). *Physical properties of crystals: their representation by tensors and matrices*. Oxford university press.
- ⁴⁸ Tomeno, I., & Matsumura, S. (1988). Dielectric properties of LiTaO₃. *Physical Review B*, 38(1), 606.
- ⁴⁹ Schlarb, U., Wöhlecke, M., Gather, B., Reichert, A., Betzler, K., Volk, T., & Rubinina, N. (1995). Refractive indices of Zn-doped lithium niobate. *Optical Materials*, 4(6), 791-795.
- ⁵⁰ Schlarb, U., Matzas, B., Reichert, A., Betzler, K., Wöhlecke, M., Gather, B., & Volk, T. (1996). Refractive indices of Zn/In-co-doped lithium niobate. *Ferroelectrics*, 185(1), 269-272.
- ⁵¹ Schlarb, U., & Betzler, K. (1993). Refractive indices of lithium niobate as a function of temperature, wavelength, and composition: A generalized fit. *Physical Review B*, 48(21), 15613.
- ⁵² Schlarb, U., & Betzler, K. (1993). Refractive indices of lithium niobate as a function of wavelength and composition. *Journal of applied physics*, 73(7), 3472-3476.
- ⁵³ Schlarb, U., & Betzler, K. (1994). A generalized sellmeier equation for the refractive indices of lithium niobate. *Ferroelectrics*, 156(1), 99-104.
- ⁵⁴ Schlarb, U., & Betzler, K. (1994). Influence of the defect structure on the refractive indices of undoped and Mg-doped lithium niobate. *Physical Review B*, 50(2), 751.
- ⁵⁵ D.H. Jundt. (2002). Properties of Lithium Niobate, ed. by K.K. Wong, no. 28 in EMIS datareviews series; 28 (INSPEC, Institution of Electrical Engineers), pp. 115–118.

Chapter 4: Photorefractive Effect in NLC Cells Caused by Anomalous Electrical Properties of ITO Electrodes*

4.1. Abstract

In a neat nematic liquid crystal (NLC) cell, optically-induced charge carriers followed by transports in double border interfaces of orientant/LC and ITO/orientant (or LC) can cause removal of screening of the static electric field inside the LC film. This is called **surface photorefractive effect** (SPR) which induces director field reorientation at a low DC electric field beyond the threshold at a reduced Fréedericksz transition and, as a result, a modulation of the LC effective refractive index.

The studies conducted on the photoinduced opto-electrical responses in pure nematic LC cells biased with uniform static DC electric fields support the SPR effect (attributed to the photoelectric activation of the double interfaces). The SPR effect was further studied in LC cells with photoresponsive substrates which act as a source of a bell-shaped electric field distribution in the LC film if no ITO electrode was employed. In equipped cell with ITO, the photovoltaic electric field induces charge carrier redistribution in the ITO film, hence the SPR effect.

* **INVITED:** Habibpormoghadam, A. (2020). Photorefractive Effect in NLC Cells Caused by Anomalous Electrical Properties of ITO Electrodes. *Crystals*, 10(10), 900. (<https://doi.org/10.3390/cryst10100900>)

This chapter is aimed at highlighting all the evidences supporting ITO film as one of the fundamental sources of the SPR effect in neat NLC cells under the condition of applying low optical power and low DC voltage. An optically-induced fringe electric field stemming from inhomogeneous photo-charge profiles near the electrode surfaces is expected in the LC film due to the semiconducting behavior of the ITO layer.

4.2. Introduction

The surface photorefractive (SPR) effect describes a change in refractive index near the surface of a material owing to an optically induced redistribution of electrons and holes. An optically-induced refractive index modulation due to nonuniformly photoinduced-charge carriers generation and migration was first discovered in ferroelectric materials at a laser beam focus region^{1,2}. In inorganic materials, the photorefractive index change is associated with an internal space-charge electric field, E_{SC} , known as **Pockels effect**³.

In neat (undoped) NLC cells, the SPR effect is realized as a director field reorientation driven by a nonuniform electric field of photo-generated charge carriers under the action of a visible light beam which was for example manifested in aberrational patterns formation and characterizations^{4,5}. In liquid crystal (LC) cells, it is typically specified by the tangent element of the modulated electric field at the LC interfaces with the cell surfaces⁵. Indium-Tin-oxide ([In₂O₃:Sn], ITO) coating of the glass plates of LC sandwich cells is often used as a conducting transparent electrode for electro-optic switching. The related conductivity of ITO normally excludes tangential components of a static electric field, which are easily compensated by mobile charge carriers that redistribute in the conducting layer. It is thus puzzling, at first glance, that ITO layers can nevertheless serve as semiconducting photosensitive layers producing tangential electric field components that may lead to specific local reorientations of the nematic LC director. Thanks to the photosensitive semiconducting behavior of the ITO layer, the SPR effect can be exploited for beneficial applications in electro-optics. In this review, the physical background that solves this apparent paradox is discussed.

The SPR effect in the NLCs was first attributed to the bulk photogenerated-charge carriers separation (due to the bulk drift and diffusion of the photogenerated-charge carriers in the static electric field) leading to a photoconductivity at moderate light intensities. The mechanism was suitably intensified in doped NLCs⁶⁻⁸ supplied with photo-charge producing agents, where the lifetime of the optically excited states of ionic carriers (generated from bimolecular dissociation) was desirably enhanced⁶.

The static nature of the space-charge field was verified in the self-diffraction investigations of nematic cells^{6,7}. Later on, the theory of the bulk SPR effect in NLC cells was modified by taking the strong anchoring condition at the cell surfaces into account⁹.

Diffraction grating studies in the cells filled with homeotropically aligned NLC suggested that the observed SPR effect is most likely due to the photo-induced charge carriers' modulation at the interfaces of the orientants (aligning layers) and the LC rather than being dominated by the ions' separations and migrations in the undoped LC bulk¹⁰. The hypothesis was developed as the modified electric field can rotate the director field from initial (homeotropic) alignment in the bulk, as well as at the aligning surface, hence tuning the easy axis of anchoring (being initially normal to the cell surfaces)¹⁰. This hypothesis was developed as the modified electric field can rotate the director field from initial (homeotropic) alignment in the bulk, as well as at the aligning surface (despite the pre-defined anchoring condition as being initially normal to the cell surfaces). The speculation was that the tangent element of the surface-charge field is able to change the anchoring properties of the aligning surface, and hence the easy axis of the anchoring¹⁰.

Further investigations confirmed the dominance of the surface charge modulation in the photorefractive effect observed in neat NLCs while rejecting the hypothesis of anchoring tuning at the LC cell surfaces¹¹. It was understood from a diminished threshold voltage verified selectively at the anode in the laser on state, and hence decreasing the effective operating DC voltage¹¹⁻¹³. This effect was realized at the double layers of polymer-LC and transparent electrode (ITO)-polymer in neat LC cells^{11,13} illuminated with an appropriate wavelength. The AC mode does not support charge carriers accumulation in the ITO electrode, hence SPR effect¹⁴. An optically-induced reduction of the surface charge carriers densities contributing to the screening of the biased DC electric field was confirmed at laser on-state¹³ due to the photo-generation of charge carriers. On the other hand, in photocurrent measurements, the key role of the transparent conducting oxide (TCO) electrode, i.e., ITO, was verified where the SPR effect was seen in all types of undoped LC cells treated or non-treated with an alignment layer¹³. In doped NLCs with dye, the director field alignment in the SPR effect can be controlled by dye deposition on a nonphotosensitive aligning surfaces (of UV-irradiated para-PVCN-F orientant)¹⁵. In doped NLCs mixtures (despite undoped matrices), the asymmetry of the aberrational patterns induced by the self-action of the light beam are decreased due to the interaction of the light field with the LC director field¹⁶.

It was also experimentally shown that equipping a photoresponsive NLC cell with an ITO electrode can change the entity of the formed topological defects at the laser exposure spot from hyperbolic¹⁷ to radial (with and without polymer coating as an anchoring agent)¹⁸, while the impact of the ITO layer on modifying the electric field distribution in such LC test cells as a result of the induced space-charge field, E_{SC} was verified and simulated in an alternative work¹⁹.

In this chapter, importance of the TCO electrode, i.e., ITO, for the SPR effect is discussed. Since this effect exists independent of the LC mixtures and orientation layers, one has to draw the attention to the relevant optical and semiconducting properties of the ITO layer participating in the SPR effect, as will be discussed in the following.

4.3. ITO electrode as the SPR effect source in the neat NLC cells

Photocurrent measurements in the neat liquid crystal cells addressed with a DC voltage verified the SPR effect in the ITO thin film¹³ acting as a semiconducting electrode lit by an appropriate optical wavelength. Test cells filled with an NLC (i.e., ZhKM-1277 nematic matrix) with a thickness of $d = 50 \mu\text{m}$ confined by ITO equipped glass plates were exposed to a laser beam (a solid state laser ($\lambda = 473 \text{ nm}$)) with a beam waist of about $100 \mu\text{m}$. The charge flow in the external circuit driven by the laser beam illumination on the LC cell was obtained as $Q_{ph} \approx 7.5 \times 10^{-11} \text{ C}$, whereas the screening charges in the laser exposure region estimated as $Q_{sc} \approx 2 \times 10^{-14} \text{ C}$. If Q_{ph} was associated solely to the photo-generated mobile charges due to optical transitions. Since pair-production happens, the value of Q_{ph} indicates that the photogenerated charge carriers are large enough to neutralize the screening charges in the beam spot¹³.

Here, the photo-induced current density flow in the external circuit is dominated by the photo-generated electrons transported under the action of the modified static electric field, (see section 3), as $J_{drift} = Q_{ph}\mu E = 3.9 \text{ nA/m}^2$ (where the reduced electric field E was obtained from the reduced voltage V (equal to 0.65 V)¹³ divided by the cell thickness d . Here, μ is the charge carrier mobility assumed equal to $40 \text{ cm}^2\text{V}^{-1}\text{s}^{-1}$). With the assumption of a Gaussian profile for the screening charges at the anode (photo-generated holes) with the same full width at half maximum (FWHM) as the beam width, for example, the diffusion current can be calculated from $J_{diff} = -D \frac{\partial Q_{sc}}{\partial x}$

in one dimension (1D), supposed along the x -direction, where D is the diffusion constant ($= \mu K_B T / q$, K_B is the Boltzmann constant, T is the temperature, and q is the electric unit charge), in a cross section through the beam center, which gives the maximum diffusion current with the same order of magnitude as the drift current for the photo-generated positive charge carriers before going to the recombination process.

Charge carrier photogeneration can happen in the ITO layer when shone by a laser beam with an appropriate wavelength in the visible range, as discussed in section 2.1. Since ITO is an n-type semiconductor, the PR effect is more effective at the ITO electrode connected to the anode (positive) polarity of the battery. The SPR effect can be further enhanced by a charge carrier photogeneration and diffusion in the alignment layers^{11,13}.

Photoinduced modulation of the conductivity of the ITO electrodes, as discussed in section 2.2, can support the occurrence of the SPR effect. While the **Burstein–Moss (B–M) effect** (explained in section 2.3) can be an important factor in the low effective voltage regime (in the ITO layer) by controlling the conductivity of the ITO as for example explained for the NLC cells with photoresponsive substrate¹⁹.

4.3.1. Opto-electronic behavior of ITO thin films

In NLC cells, LC films are commonly confined between ITO-equipped glass covers (ITO film had a thickness in the range of a few hundred nm). In static electric fields, photo-induced charge carriers' accumulation and redistribution can happen at the border thin double layers (i.e., the ITO and the orientant). This mechanism can modify the electric field profile in the LC cell, for example in a planar cell, from being uniform and normal to the cell surfaces at the illumination off state to fringe distributions near to the interfaces when shone by a laser beam with an inhomogeneous profile⁵. As a result, understanding the electrical properties of the thin ITO layer seems critical.

Based on their classification, semiconductors are introduced as “a group of materials having conductivities between those of metals and insulators”²⁰. In general ITO is classified as an n-type semiconductor with a wide bandgap in a range of $\sim 3.5 - 4.4$ eV²¹ (increasing from the intrinsic absorption edge ~ 3.5 eV by increasing charge carrier concentration²² known as the **Burstein–Moss shift**²³), which accounts for the transparency of 80% – 95% in the visible and near-infrared ranges of light.

An ITO thin film has a conductivity in a range of $0.01 - 1 \mu\Omega^{-1}\text{m}^{-1}$. This is usually in a reduced range of $0.01 - 0.1 \mu\Omega^{-1}\text{m}^{-1}$ when deposited on glass substrate²⁴⁻²⁷. The electrical conductivity²⁸ of semiconductors is in a range of $10^{-11} - 0.1 \mu\Omega^{-1}\text{m}^{-1}$,

while metals have higher electrical conductivities $> 1 \mu\Omega^{-1}\text{m}^{-1}$. Besides the deposition technique, the conductivity of the ITO film depends on the film thickness and type of substrate. For example, ITO with film thicknesses of 100, 300 nm deposited on glass substrates by electron-beam evaporation and ion-assisted deposition (IAD) has electrical conductivities of²⁹ 0.15 and 0.1 $\mu\Omega^{-1}\text{m}^{-1}$, respectively. In comparison, copper (Cu) thin films with the same thicknesses have conductivities of³⁰ $\sigma = 40, 56 \mu\Omega^{-1}\text{m}^{-1}$ (measured at room temperature by filtered cathodic vacuum arc (FCVA) technique), respectively, being more than two orders of magnitude larger than that of ITO.

Doped charge densities in the ITO lie in the range of $\sim 10^{19} - 10^{21} \text{ cm}^{-3}$, where below the lower limit, ITO acts as a **Mott** insulator suppressing free electron behavior³¹. According to the **Ioffe-Regel criterion**^{32,33}, the metallic regime can be described by the condition of $k_F l \gg 1$, where $k_F (= 1/\lambda_e)$ and l are the Fermi wave number (λ_e : Fermi electron wavelength) and the mean free path, respectively. This quantity gives the degree of metallic behavior. The metal-insulator (M-I) transition happens when $k_F l < 1$ (**Mott** criterion)^{33,34}. In general, the degree of metallic behavior of an ITO thin film is about $k_F l \sim 1$ which means ITO is moderately disordered classified as degenerate semiconductor³⁵. In a high-quality ITO³⁶ with a bulk carrier density of $n = 1 \times 10^{21} \text{ cm}^{-3}$ in the ohmic operating mode, resistivity of $R = 1.5 \mu\Omega\text{m}$, and an electron mobility of $\mu_e = 42 \text{ cm}^2\text{V}^{-1}\text{s}^{-1}$ (which can be obtained from Hall relation), the degree of conducting $k_F l$ can be calculated from a free electron model; hence, the Fermi wave number can be obtained from $k_F = (3\pi^2 n)^{1/3} = 3.06 \times 10^9 \text{ m}^{-1}$, the electron mean free path is formulated as $l = v_F \tau$, where the Fermi velocity v_F and the electron mean free time τ can be calculated from $v_F = \hbar k_F / m^*$ and $\tau = m^* / (ne^2 R)$ (or in other words, $\tau = m^* \mu_e / e$), respectively. Here, m^* is the electron effective mass which is equal to $0.35m_e$ at the low charge densities near the Mott density, and $m_e = 9.11 \times 10^{-31} \text{ kg}$ is the electron rest mass, which give $v_F = 1 \times 10^6 \text{ m/s}$ and $\tau = 8.3 \times 10^{-15} \text{ s}$, correspondingly. Substituting the values of v_F and τ in the relation of the mean free path gives $l = 8.3 \times 10^{-9} \text{ m}$. Then, the metallic degree for ITO can be obtained equal to³⁶ $k_F l = 25.73$ which is much more smaller than a good conductors'. For example for copper the metallic degree in room temperature is $k_F l = 538.21$, where $k_F = 13.24 \times 10^9 \text{ m}^{-1}$ and $l = 39.9 \times 10^{-9} \text{ m}$, respectively. Then it would be expected that ITO acts as a semiconductor to some degree.

According to the electronic band structure of ITO, there is a direct wide optical band gap with a value in a range of $\sim 3.5 \text{ eV}$ (typical value attributed to the direct

bandgap of ITO) – 4.3 eV causing the strong optical absorption (zero transparency) in the UV spectrum. As mentioned, depending on the charge density magnitude, the band gap energy can be elevated from ~ 3.5 eV to ~ 4.4 eV by a value of ΔE_g^{B-M} (known as B–M shift^{23,37}). The B–M shift, ΔE_g^{B-M} , (as schematically shown³⁸ in Figure. 9, Ref. 38) can be obtained from^{21,22,26,39,40},

$$\Delta E_g^{B-M} = (\hbar^2/2m_{cV}^*)(3\pi^2N_0)^{2/3} \quad (4.1)$$

where m_{cV}^* ($= m_c^* \times m_v^*/(m_c^* + m_v^*)$, here m_c^* and m_v^* are the carriers effective mass in conduction and valence bands, respectively) is the electron reduced effective mass about $0.65m_e$ ²¹ for ITO. If the photon energy is equal to the B–M energy, the electron intra-band transition can take place⁴¹ in the conduction band over the B–M barrier, which makes the ITO film to act as an ohmic conductor.

Since the energy of many-body interaction for the electron–electron and electron–ionized impurities causing narrowing of band gap is minor, the band gap energy E_g for an electron transition from the top state in the valence band (with a parabolic structure^{22,42}) to the lowest empty state in the semi–parabolic conduction band⁴¹ can be obtained disregarding of this minor energy change, as^{21,22,26},

$$E_g = E_{g0} + \Delta E_g^{B-M} \quad (4.2)$$

where E_{g0} is the intrinsic band gap ~ 3.5 eV. As can be seen from relation (4.1) and as discussed in Ref. 26, the band gap energy of ITO is directly proportional to $(N)^{2/3}$, determining the absorption coefficient. From the B–M energy, ΔE_g^{B-M} , electron density occupying all low lying energy states up to the Fermi level (now located in the conduction band) in the conduction band can be calculated, for example for a band gap shift of 0.8 eV, N can be obtained as $1.72 \times 10^{21} \text{ cm}^{-3}$.

Regarding the electronic structure of the ITO, there is an indirect band gap with an edge ~ 2.8 eV which can shift to higher values around ~ 3.4 eV as a result of the B–M mechanism^{22,43}. Additionally, a weak absorption was observed for photons with energy $h\nu$ around 2.3 ± 0.1 eV (~ 500 nm) associated with an indirect bandgap in the ITO electronic band structure⁴⁴ which can cause a weak charge carriers generation in the ITO film in the light beam spot, for example with interesting applications briefly discussed in section 3 in the LC engineering part. Also, ITO exhibits another indirect band gap approximately around 1.9 eV (at $\lambda = 652$ nm) formed by the oxygen

deficiencies (acting as defects) known as orange emission⁴⁵. The latter gives a strong emission, as a result probe beam with such a wavelength is not able to induce SPR effect. A typical absorption spectrum of the ITO thin film is shown in Figure 4.1.

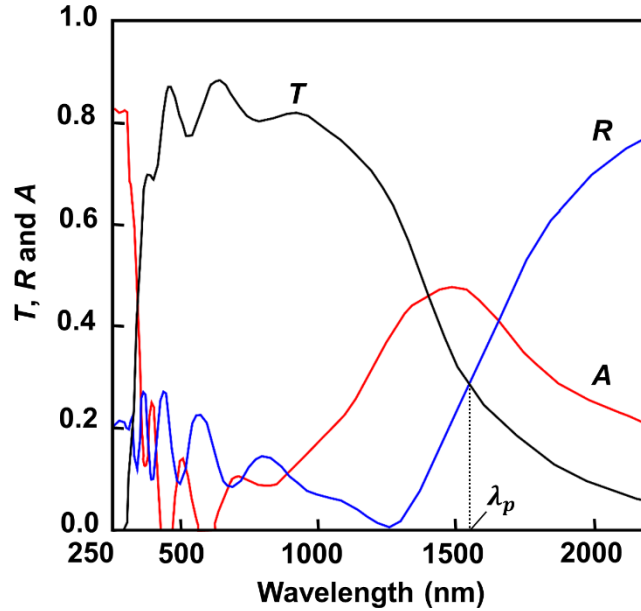


Figure 4.1. Graph of the particular ITO transmission T , reflectance R , and absorption A spectrum for a thin film with thickness of $d \sim 300$ nm shown in enhanced resolution²⁶. The plasma (cut-off) wavelength is shown.

{Adapted from [Kim, H., Gilmore, A. C., Pique, A., Horwitz, J. S., Mattoussi, H., Murata, H., ... & Chrisey, D. B. (1999). *Journal of applied physics*, 86(11), 6451-6461, (<https://doi.org/10.1063/1.371708>).], with the permission of AIP Publishing}.

4.3.2. Frequency dependent-conductivity of ITO thin films

Opto-electrical properties of ITO films can be investigated based on the classical **Drude model**. In ITO, the charge density N_0 almost exclusively (independent of charge mobility) determines the plasma frequency ϑ_p ⁴⁶ (if the electron effective mass was kept constant²⁶) which in turn determines the reflectance edge. In the low charge density regime (i.e. $N_0 < 10^{21} \text{ m}^{-3}$), the plasma frequency ϑ_p , at which the electrons undergo a resonance, is defined as^{26,47},

$$\vartheta_p^2 = N_0 e^2 / \varepsilon_0 m^* \quad (4.3)$$

where e , m^* , and ε_0 are the electron unit charge, the electron effective mass, and the vacuum permittivity, respectively. In the high charge density regime where $\omega_p \tau \gg 1$ (ω_p is the plasma angular frequency) is fulfilled, the plasma frequency ϑ_p is modified as $\vartheta_p^* = \vartheta_p / \sqrt{\varepsilon_\infty}$ (ε_∞ is the high frequency permittivity being ~ 4 for ITO). For example for ITO thin film, by a nonlinear change of the electron effective mass from $m^* = 0.35m_e$ to $0.53m_e$ corresponding to the charge densities of $N_0 = 6.2 \times 10^{19} \text{ cm}^{-3}$, $1.4 \times 10^{21} \text{ cm}^{-3}$, respectively⁴⁸, the plasma frequency can be obtained equal to $\vartheta_p = 375 \text{ THz}$, 1449 THz . In this case, the plasma (cut-off) wavelength λ_p , where the transmission equals the reflectance $T = R$, can be obtained from²⁶,

$$\lambda_p = 1.24 \times 10^3 \text{ e} / h \vartheta_p \quad (4.4)$$

where h is the **Planck** constant, which gives $\lambda_p = 798 \text{ nm}$, 207.1 nm , correspondingly. Apparently, these values show the plasma frequency shift from near IR (for charge densities in the range of $N_0 \sim 10^{19} \text{ cm}^{-3}$) to UV (for $N_0 \sim 10^{21} \text{ cm}^{-3}$) range⁴⁹. ITO is highly reflective at optical frequencies $\vartheta < \vartheta_p$, whereas, highly transparent at $\vartheta > \vartheta_p$ ^{50,51}. As a result, for exhibiting transparency in the visible range of the light, the charge density would be tuned carefully in order to lead to a plasma frequency in the near IR or IR regions. High free charge density in conventional metals such as Cu or Ag ($6 \times 10^{22} \text{ cm}^{-3} - 8 \times 10^{22} \text{ cm}^{-3}$) hampers electrical manipulation of their optical properties.

It can be concluded that ITO as a transparent electrode in NLC cells has unavoidably semiconducting properties in the visible light beam, which allows diffusion and redistributions of the photogenerated charge carriers along the ITO interface, which in turn supports the SPR effect.

Conductivities of metal oxides such as tin oxide or indium–tin oxide (ITO) are frequency dependent⁵². Generally speaking, there is a duality in the electro-optical behavior of the ITO thin film as it acts metallic in the microwave band exhibiting high conductivity, while semiconducting in the visible spectrum exhibiting much lower conductivity.

When an ITO film is shone by a light beam with an angular frequency ω , the effective conductivity can be obtained from Drude model⁵⁰ as,

$$\sigma_{eff}(\omega) = \frac{\sigma}{1 - j\omega\tau} \quad (4.5)$$

where ω is the angular frequency, τ is the electron relaxation/scattering time which has an effective value about 3.3×10^{-15} s for ITO thin films⁴⁷, and $\sigma (= N_0 e^2 \tau / m^*)$ is the Drude DC conductivity.

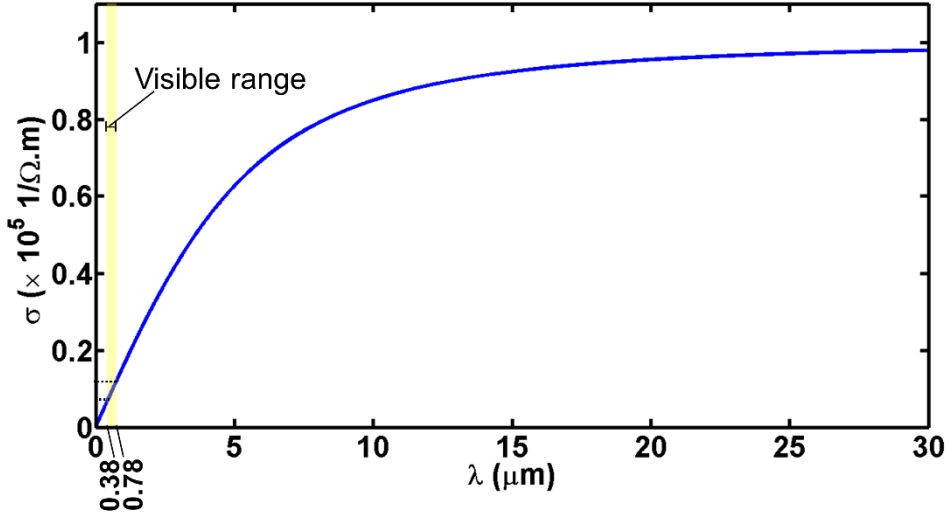


Figure 4.2. Simulated ITO conductivity as a function of light beam wavelength ranging from the UV to near-IR spectrum. For an ITO thin film deposited on glass, the DC conductivity was supposed $\sim \sigma = 0.1 \mu\Omega^{-1}\text{m}^{-1}$.

The effective conductivity is a complex quantity with real and imaginary parts, i.e., $\text{Re}\sigma_{eff}$ and $\text{Im}\sigma_{eff}$, of:

$$\text{Re}\sigma_{eff} = \frac{\sigma}{1+\omega^2\tau^2}, \quad \text{Im}\sigma_{eff} = \frac{\sigma\omega\tau}{1+\omega^2\tau^2}. \quad (4.6)$$

From above the relations, it can be deduced that in the low-frequency limit (i.e., $\omega\tau \ll 1$), when the input beam is in the IR region, ITO shows the maximum conductivity as $\sigma_{eff}(\omega) \rightarrow \sigma$, where $\text{Im}\sigma_{eff} \ll \text{Re}\sigma_{eff}$, $\text{Re}\sigma_{eff} \rightarrow \sigma$ (see in Figure 4.2). By increasing the frequency ω , the imaginary part of the effective conductivity, $\text{Im}\sigma_{eff}$, grows beyond the real part, $\text{Re}\sigma_{eff}$, as both quantities are kept lower than the DC conductivity σ . For example for a visible light beam with a wavelength of $\lambda = 500$ nm, and the associated angular frequency $\omega = 3768 \times 10^{12}$ rad/s (counting for $\omega\tau = 12.43$ rad), the real and imaginary parts of effective conductivity read $\text{Re}\sigma_{eff} = 6.4 \times 10^{-3}\sigma$ and $\text{Im}\sigma_{eff} = 8 \times 10^{-2}\sigma$ which give the effective conductivity equal to $\sigma_{eff} = 8.01 \times 10^{-2}\sigma$. In the high-frequency regime (i.e., $\omega\tau \gg 1$), both terms go to zero but $\text{Re}\sigma_{eff}$ with a faster rate, as ITO acts as an insulator with almost zero conductivity when lit by a very high frequency light beam (seen in Figure 4.2).

4.3.3. ITO conductivity in very low DC operating regime

If the electrostatic potential, eU , in the ITO thin film is much smaller than the Fermi energy E_F , the ITO layer can be approximated as being in the equilibrium state. In general, the electrochemical potential in the Fermi level located in the conduction band, i.e. ξ , can be approximated as $\xi = \Delta E_g^{B-M} - eU \approx \Delta E_g^{B-M}$ ⁵³ which implies that $\xi = E_F$, where E_F is the Fermi energy. For instance, the electrochemical potential ξ is about 0.7 eV for an ITO thin film with a thickness of $d = 200$ nm grown on the glass²⁶. Because of the B–M shift, at an equilibrium state, only the charge carriers above the Fermi level are free to move and contribute to the conductivity. Since ITO is a degenerate n-type semiconductor, the thermally available free charge density at equilibrium state ($|eU| \ll \Delta E_g^{B-M} = E_F$) above the B–M barrier at temperature T , can be estimated as^{54,55},

$$N = N_C \exp(-E_F/K_B T) \quad (4.7)$$

where N_0 is referred to as the effective density of states in the conduction band, the term $K_B T$ (the product of Boltzmann constant K_B and temperature T) is 25.7 meV at room temperature. Hence, for example if $N_0 = 10^{26} \text{ m}^{-3}$ and $\xi = 0.6$ eV, then the maximum available (thermally excited) free charge density can be obtained as $N \approx 10^{16} \text{ m}^{-3}$. The DC electric field screening by this amount of mobile charge density is infinitesimal. The so-called **Thomas–Fermi** screening length, λ^{T-F} , can be obtained from⁵⁶,

$$\lambda^{T-F} = \left[\frac{2\epsilon_0 \epsilon_{ITO} E_F}{3e^2 N} \right]^{1/2} \quad (4.8)$$

where m^* is the electron effective mass, \hbar is the plank constant divided by 2π . For the $N = 10^{16} \text{ m}^{-3}$, λ^{T-F} is 147 μm which shows the minor damping of the static electric field in the ITO thin film in the near equilibrium condition. If ITO acts metallic, then $\lambda^{(T-F)}$ is of the order of several nm; In this condition, it would be expected that electric field is completely screened in the ITO film which implies the suppression of the fringe electric field formation specified with tangent element to the interface. As a result, in the metallic operating regime of ITO, the SPR effect cannot occur.

In the non-equilibrium condition when $|eU| \leq E_F$, N reads⁵⁷,

$$N = N_0 \exp(-(E_F - eU)/KT). \quad (4.9)$$

Due to the irregularity in the band structure of the ITO film, a minimum energy equal to ΔE_g^{B-M} is required in order to make ITO cut through its conduction band, giving rise to the free charge carriers, hence, behaving in a quasi-metallic manner. This amount of energy can be provided for example by an optical stimulus⁴¹ or an electrostatic field.

In the low DC voltage operating regime when the ITO thin film is lit by a visible light beam, hence operating with low conductivity, hot photo-generated charge carriers in the beam spot can be swept away by the DC electric field. This leaves behind regions with very low charge densities of opposite charge carriers (densities diminished due to recombination process with the residing ions) which locally induces semiconducting behavior in the ITO thin film in the beam spot. The self-action of the light beam in some applications will be discussed in the next section.

4.4. A brief review of the self-action of a visible light beam in the NLC cells biased with a DC electric field

In the experimental investigations conducted on the NLC cells with initial planar alignment, it was verified that treating the LC cell surfaces with non-photoconducting polymer layer (such as LQ1800 polyimide) could weaken or disable (depending on the cell configuration and light beam incidence direction) the SPR effect in cells filled with pure E7 LC by means of decreasing the degree of the electric field modulation inside the LC film⁵⁸. However, the use of an alkyne compound LC (such as BL001) caused effective director field realignments to take place due to a higher sensitivity of the director field realignment in the electric field. Hence, by suppressing charge carriers photo-generation inside the aligning layer and bulk LC, photo-induced charge carriers' redistributions in the ITO layers were verified. The mechanism was highly sensitive to the applied optical wavelength⁵⁸.

In the NLC cells filled with E7 LC and equipped with an ITO thin film coated with polyvinyl alcohol (PVA) - a polymeric film exhibiting photoconductivity⁵⁹ - as a common anchoring agent in the LC cells, the DC voltage drop was verified on the double thin layers (i.e., polymer/LC and ITO/LC interfaces) when shone by a homogeneous laser beam profile in a planar cell¹¹. It was attributed to the neutralization of the accumulated ions by the photo-induced charge carriers under the recombination

process. Minority charge carriers, i.e., holes, dominate in both the ITO and polymer layers, forming barriers at the interfaces. Therefore, the DC voltage locally drops (which can be understood from the physics of a plane capacitor resembling the LC cell)¹¹. Biased low DC voltages ($V_{DC} < 2$ V in test cells with thickness of 30 μm) were completely screened at the LC film interfaces, while by increasing the voltage magnitude, the screening degree decreased reaching a constant value¹¹.

In sum, all evidences imply that ITO can contribute in the SPR effect independent of the LC mixture and the orientation layers due to the semiconducting operation mode in the visible light which is correlated with its specific optical characteristics. Thanks to the SPR effect, stronger director field realignments and control can be achieved.

The impact of SPR effect on the electro-optical behavior of the neat NLC cells is discussed further in the following sections.

4.4.1. The SPR effect manifested in the formation of the aberration patterns

Aberrational patterns are specified with concentric ring structure in the far diffraction zone. They have asymmetric shapes⁶⁰ with a kink at the corner seen in symmetric LC cell designs subject to a DC electric field^{4,5,61}.

From the aberration pattern, information regarding director field reorientation^{60,62-63} and the ratio of elastic constants⁶⁴ can be extracted. In the case of director field reorientation by the light electric field \mathbf{E} , information regarding self-focusing or self-defocusing can be obtained from the investigation of the aberrational patterns⁶³. If director field tends to take alignment along the light field \mathbf{E} , refractive index change of the LC is positive categorized as self-focusing. A negative change in refractive index can cause self-defocusing of the light beam attributed to an opposite trend of director field reorientation.

Aberrational patterns with specific orientational properties can form in neat NLC cells illuminated by a visible light beam due to the SPR effect^{4,5,61}. The efficiency of the SPR effect depends on the light wavelength^{4,61}. Studies on the asymmetry (the horizontal divergence) of the aberrational patterns and the number of rings in the far-field diffraction zone were conducted on transparent NLC cells equipped with ITO electrodes and biased with low DC voltage. They showed that with increasing the wavelength within a spectral range of 458 – 647 nm (corresponding to the photon energy range of 2.7 – 1.92 eV) the efficiency decreased to zero (the phenomenon was

not seen at $\lambda = 647$ nm). The orientational SPR effect became manifest in the aberrational patterns formation independent of the light beam polarization^{4,5,61}. It was effectively exploited at very low optical power irradiation (few milliwatt (mW)) and low biased DC voltage (a few volts) in the visible range of the light beam^{4,5,61} before smoothing of the director field reorientation happened (when the maximum possible realignment was achieved)¹⁶.

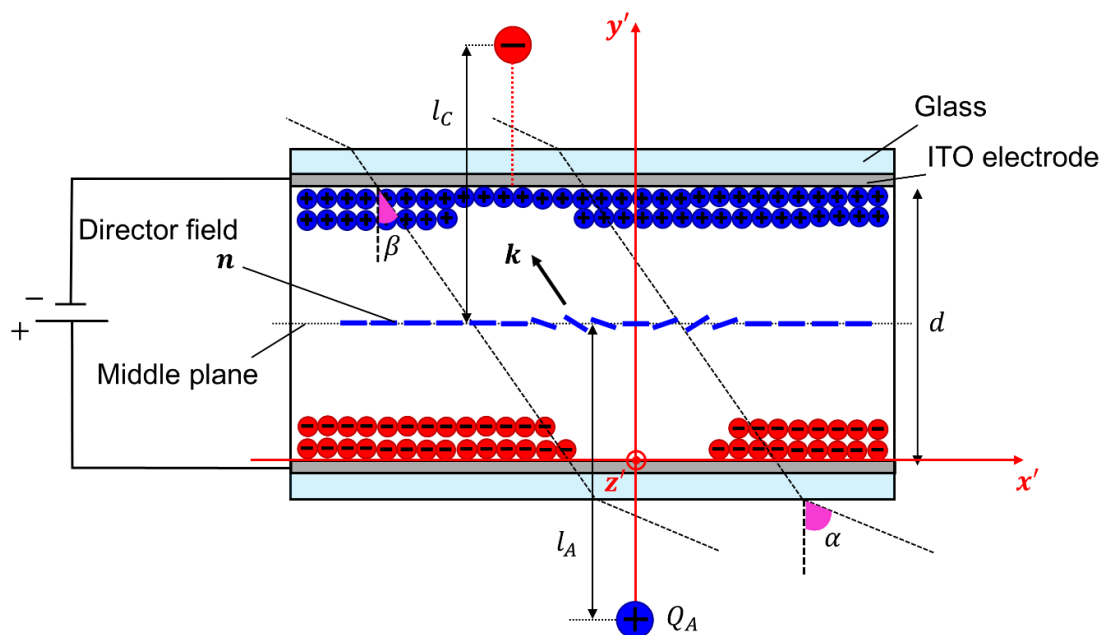


Figure 4.3. Removal of the DC electric field-screening by the light beam in a NLC cell filled with a nematic LC with positive dielectric anisotropy, $\Delta\epsilon > 0$, causing a hyperbolic umbilic caustic. The redistribution of surface electric charges at the semiconductor (ITO) electrodes was modeled by two point charges Q_A and Q_C adjusted at distances l_A and l_C relative to the cell middle plane, respectively. The director field deflection from initial planar alignment in the induced fringe electric field is shown in the cell middle plane. k is the light beam wave vector. {This Figure was inspired from Figure 6 in Ref 4 and Figure 3 in Ref 5}.

In Figure 4.3, in the electrode connected to the battery anode, the photo-generated charge carriers (electron-hole pairs) can get spatially separated more effectively^{4,5,61}. The fast photo-generated electrons participate in the photo-induced current density under the drift mechanism, whereas the slow photo-generated holes diffuse in the beam spot along the electrodes hence neutralizing the static negative charge ions residing in this region¹³.

For simulating the electric field in the LC for a planar test cell made from ITO electrodes and filled in with neat NLC, the redistribution of the surface charges

responsible for the screening of the electric field under the self-action of light were modeled by assumption of two point charges (with signs opposite to the screening charges at the corresponding surfaces), i.e., Q_A and Q_C , induced at the electrodes connected to the anode and cathode polarities of the battery, respectively, with opposite signs as the surface charges sit on corresponding surfaces⁵ (see Figure 4.3). The photo-induced charges can be determined from measuring the photo-induced external current through the circuit¹³. The electric field has a fringe profile at the ITO surface characterizing the semiconducting nature of the ITO layer (associated with an electric potential gradient) under visible laser beam illumination⁵.

In electric field modeling, the point charges Q_A and Q_C were adjusted out of the ITO planes at distances l_A and l_C (along the beam propagation axis) relative to the cell midplane, in order to give a suitable model of the fringe electric field profile in the LC cell⁵. By considering the Gaussian profile of the laser beam, these point charges located out the electrode surfaces can provide a good approximation of the real electric field profile induced by redistributed surface charge densities (with Gaussian profiles) at the beam spot⁵. Hence, the electric field inside the LC volume for example in the central plane located at $y = d/2$, where d is the cell thickness, can be obtained from⁵,

$$\mathbf{E} = \frac{Q_A(i\mathbf{x}' + j\mathbf{l}_A + k\mathbf{z}')}{\varepsilon_{dc}(x'^2 + l_A^2 + z'^2)^{3/2}} + \frac{Q_C(i(x' + d \tan \beta) + j\mathbf{l}_C + k\mathbf{z}')}{\varepsilon_{dc}((x' + d \tan \beta)^2 + l_C^2 + z'^2)^{3/2}} + j\eta E_0 \quad (4.10)$$

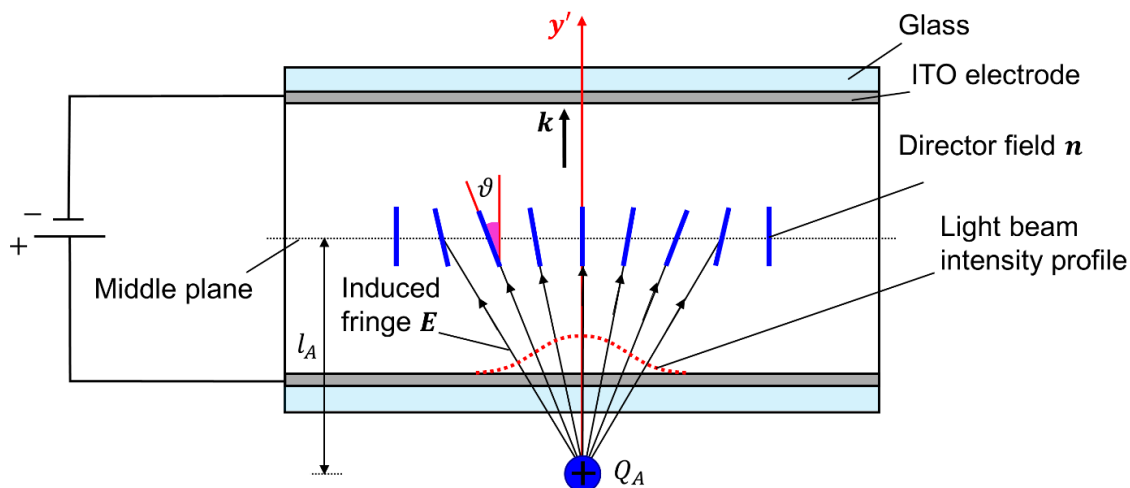
where the unit vectors i , j and k are along the Cartesian coordinate axes x' , y' , and z' , ε_{dc} is the dielectric permittivity in the DC field, β is the refraction angle at the LC boundary with the substrate which can be approximated as $\beta = \sin^{-1}(\sin \alpha / n_{\text{eff}})$, α is the incident angle of the light beam with respect to the y' axis and n_{eff} is the LC effective extraordinary refractive index. In relation (4.10), the term ηE_0 gives the reduced electric field in the LC cell in the laser-off state when the electric field $E_0 = U_0/d$ is screened by the surface charges by a factor η ⁵.

4.4.2. Generation of optical vortices in the NLC context due to the SPR effect

In the NLCs, umbilical defects (in short “umbilics”)^{65,66} can act as a topological matter context for the generation of the optical vortices (OVs). In Laguerre–Gauss beams, OVs carry orbital angular momentum (OAM). They are characterized by phase

singularity along their beam propagation axis⁶⁷. OVs have found application in efficient optical tweezers to trap low- and high-index particles with low optical intensities^{68,69}, in high-resolution astronomical imaging⁷⁰, in optical coronagraph with 95% intensity contrast⁷¹, and in classical⁷² and quantum⁷³ optical communication systems.

a) Surface photorefractive effect in a NLC cell with $\Delta\epsilon > 0$



b) Surface photorefractive effect in a NLC cell with $\Delta\epsilon < 0$

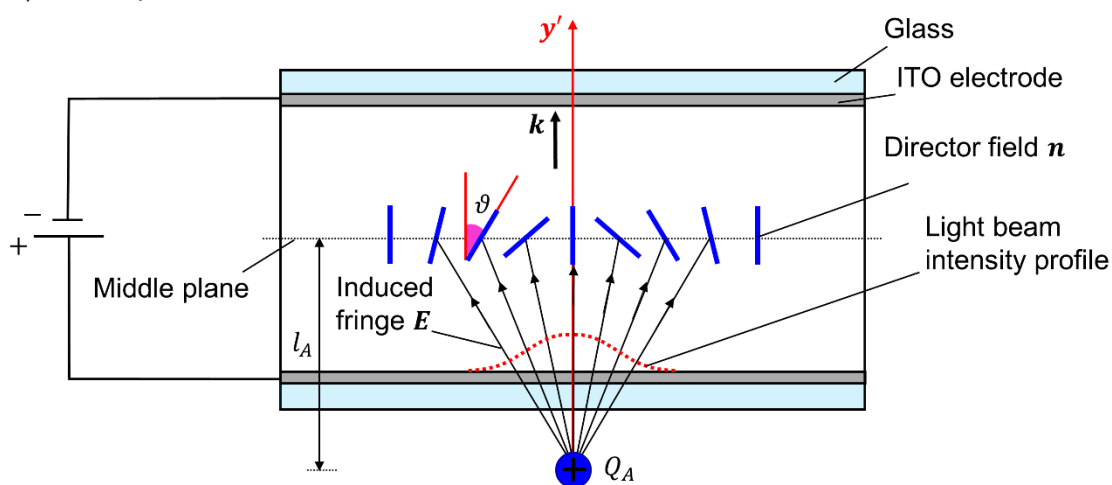


Figure 4.4. Director field reorientation in NLCs from initial homeotropic alignment with a) positive, b) negative dielectric anisotropy, respectively, as a result of the SPR effect leading to formation of the optical vortices. The light beam is normally incident onto the anode electrode and the beam profile is shown by a red dashed curve.

{This figure was inspired from Figure 1 in Ref 61}.

Electric field in the illuminated NLC cell by a light beam at normal incident to the surfaces can have a fringe profile in the planar configuration as a result of the SPR effect. The induced fringe electric field inside the LC volume is capable to realign NLCs

(with positive and negative dielectric anisotropies) from initial homeotropic alignment when shone by a low laser power (of a few mW) at a reduced threshold voltage, as schematically shown in Figure 4.4⁷⁴⁻⁷⁷. Independent of the sign of the dielectric anisotropy, radial director field distributions in the transverse plane were seen as a result of director realignments from initial homeotropic alignment induced by the SPR effect⁷⁴⁻⁷⁷. This leads to the formation of OVs⁷⁸⁻⁸⁰ from an incident plane wave.

As discussed, according to the beam profile, the electric field screening can be removed under the self-action of a light beam. Since this mechanism is more effective at the anode electrode connected to the positive polarity of the DC voltage (verified from the elongation direction of the aberrational patterns⁶¹), the modeling of the induced electric field was roughly simplified here by assuming only one positive point charge located near the anode at a distance l_A relative to the cell midplane. It represents the redistributed surface electric charges at the corresponding electrode⁷⁴⁻⁷⁷. The simplified model was able to describe the generation of OVs in the corresponding test cells well⁷⁴⁻⁷⁷.

At the first attempts, OVs were generated with low efficiency (with a maximum value of about 30% for NLC with negative anisotropy)⁷⁴. However, high conversion efficiency (of incident plane wave to the helical waves) of above 95% was theoretically predicted in NLC with negative dielectric anisotropy by defining small LC film thickness (about 25 μm) and low optical birefringence (about 0.1) where a high degree of director field realignment was attained⁷⁶. The technique developed by Kravets and co-workers⁷⁷ based on the optimum application of the DC electric field in the common NLC cells leads to a low optical phase delay of π . Then, the OVs are generated with high efficiency (>90%) and purity since the NLC template acts as a half-wave plate providing the maximum conversion efficiency⁷⁷.

According to the literature, the SPR effect was verified under the condition of “low electric field and low optical power” in all cases studied. It was found that the DC voltage drop is usually between 0.5 to 1 in the pure NLC¹¹, which means an addressed voltage $\sim 2\text{V}$ can usually compensate the voltage drop and drive the LC realignment above the Fréedericksz threshold. On the other hand, the photo-induced electric field (originated from the photogenerated charge carriers) in low optical powers would be above the Fréedericksz threshold field as being able to induce the director field reorientation.

4.4.3. SPR effect-assisted formation of umbilical defects in a NLC cell made from a photoresponsive substrate

The photorefractive effect⁸¹ was verified in the ITO electrode due to the charge carriers' accumulation at the boundary of the ITO with an insulator in the presence of a static electric field⁸²⁻⁸⁵. The induced charge redistribution, in addition to the modulation of the ITO refractive index and voltage drop, can also induce a secondary refractive index modulation in the LC film through the SPR effect in the low power laser beam regime.

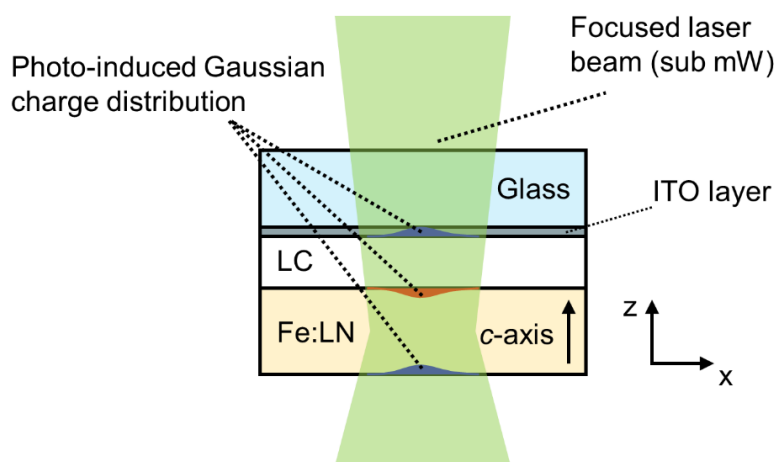


Figure 4.5. Schematic of a hybridized LC test cell equipped with an ITO coated glass¹⁹.

The SPR effect can generate and support umbilical defects (characterized as non-singular topological defects) in the NLC cells with photoresponsive substrate of a z-cut ferroelectric material, i.e., iron-doped lithium niobate (Fe:LiNbO₃ or in short Fe:LN) covered with an ITO-equipped glass slab as schematically shown in Figure 4.5. They act as context for the generation of OVs¹⁹. Here, photoresponsive substrate acts as a source of nonuniform photovoltaic electric field present in the LC film. In such test cells, the director field reorientation from an initial homeotropic alignment (provided by an anchoring agent) can take place under the action of an optically-assisted fringe electric field distribution in the LC film (Figure 4.6)¹⁹. The fringe structure of the induced electric field is provided from both the photo-induced charge carriers' accumulation at the surfaces of the ferroelectric slab, as well as in the ITO layer in the beam spot¹⁹.

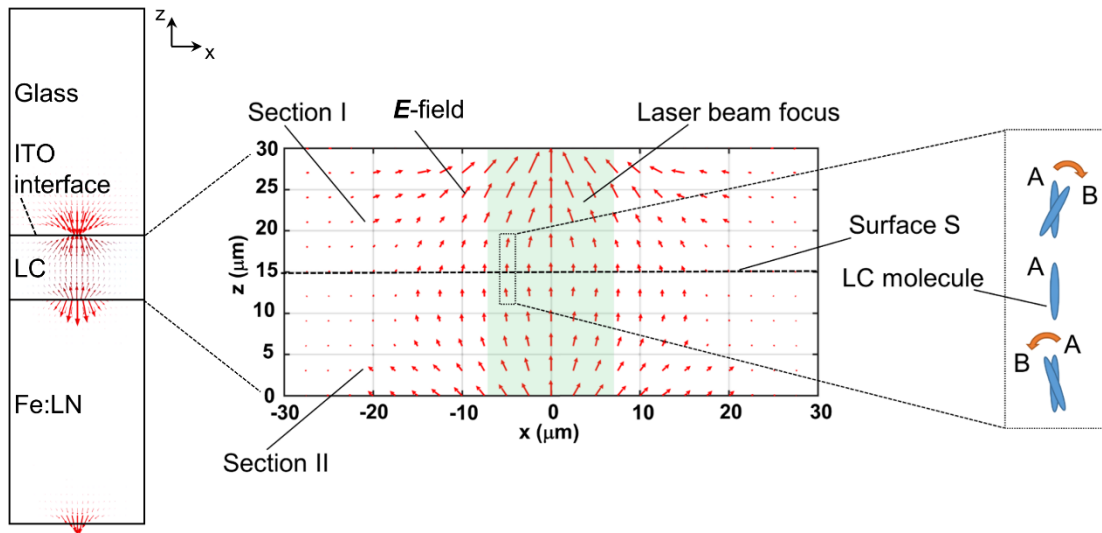


Figure 4.6. Electric field distribution in the hybridized LC test cell made from a ferroelectric substrate and an ITO coated cover slab. The fringe electric field distribution inside the LC film is capable to induce splay umbilical defects in the initial homeotropic configuration¹⁹.

As seen, the fringe electric field stemming only from the photo-induced charge carriers distributions in the ferroelectric substrate is not capable to induce the umbilical defects with spatial structure in the LC media as introduced by Rapini⁶⁶ in the cells without ITO equipment (the topological defects were formed only at the boundary surfaces of the LC layer)¹⁷. The umbilics are characterized by topological phase singularities extended along the test cell at the beam exposure center where the initial homeotropic alignment of the LC was kept fixed¹⁹. They can form when the electric field structure is effectively modified due to the induced fringe electric field distribution near to the LC border with the coated glass slab equipped with the ITO¹⁹. The radial realignment of the LC director field in the transverse plane comparable to an optical q-plate with radial geometry⁸⁶ can be supported in the whole LC volume¹⁹.

4.5. Conclusions

The very common electrode in the LC cells, i.e. ITO, is well known for its refractive index modulation property. In the regimes of low addressed electrostatic potential and visible optical power, it can act quite semiconducting due to the charge carriers' redistributions with a low density in the laser beam spot. As a result, the screening of the electric field on the LC film can be effectively removed by the action of the light beam when initially (at the laser off state) no realignment was observed even at voltages well above the threshold. This was attributed to the action of ions sitting at the border interfaces of the LC film while the B–M effect at the transparent electrode can be speculated as a cause.

The photorefractive effect in the ITO-equipped NLC cells was reported and utilized in the diffraction gratings in wave-mixing studies, the creation of hyperbolic umbilic caustics, and OVs through umbilical defects generation in NLC cells in optically-assisted modified electric field profiles from initial uniform and fringe-shape profiles, respectively.

A challenge was the understanding of the sources of the SPR effect in the NLC cells; it was found that the electron-hole pair production and subsequent transport can happen in the ITO thin layer in addition to the orientant, where the residing charge carriers in the beam spot can be effectively neutralized due to the photo-induced low conductivity. In the semiconducting operating mode of the ITO layer, a fringe electric field with its tangent element to the LC confining surfaces (equipped with ITO) was induced which results in the LC director field realignment parallel to the cell surfaces (irrespective of the sign of the dielectric anisotropy), hence the SPR effect.

This chapter was aimed to track some of the efforts that were made to realize and utilize the photorefractive effect in NLC cells in the static electric field while emphasizing the key supporting role of the transparent electrode, i.e., ITO.

References

- ¹ Ballman, A. A. (1965). Growth of piezoelectric and ferroelectric materials by the Czochralski technique. *Journal of the American Ceramic Society*, 48(2), 112-113.
- ² Nassau, K., Levinstein, H. J., & Loiacono, G. M. (1966). Ferroelectric lithium niobate. 2. Preparation of single domain crystals. *Journal of Physics and Chemistry of Solids*, 27(6-7), 989-996.
- ³ Yariv, A., & Yeh, P. (1984). *Optical waves in crystals* (Vol. 5). New York: Wiley.
- ⁴ Zolot'ko, AS, Budagovsky, IA, Kitaeva, VF, Ochkin, VN, Shakun, AV, Smayev, MP, & Barnik, MI (2006). Orientational interaction of a light beam and NLCs subjected to external DC field. *Molecular Crystals and Liquid Crystals*, 454 (1), 407-809.
- ⁵ Budagovsky, I. A., Zolot'ko, A. S., Smayev, M. P., & Barnik, M. I. (2010). Self-action of a light beam in nematic liquid crystals in the presence of a DC electric field. *Journal of Experimental and Theoretical Physics*, 111(1), 135-145.
- ⁶ Rudenko, E. V., & Sukhov, A. V. (1994). Optically induced spatial charge separation in a nematic and the resultant orientational nonlinearity. *JETP*, 105, 1621-1634.
- ⁷ Rudenko, E. V., & Sukhov, A. V. (1994). Photoinduced electrical conductivity and photorefractive effect in a nematic liquid crystal. *JETP Letters*, 59(2), 142-146.
- ⁸ Rudenko, E. V., & Sukhov, A. V. (1996). Photorefractive Effect in Nematic Liquid Crystals: Ion-Diffusion Approach. *Molecular Crystals and Liquid Crystals Science and Technology. Section A. Molecular Crystals and Liquid Crystals*, 282(1), 125-137.
- ⁹ Zhang, G., Montemezzani, G., & Günter, P. (2000). Orientational photorefractive effect in nematic liquid crystal with externally applied fields. *Journal of Applied Physics*, 88(4), 1709-1717.
- ¹⁰ Zhang, J., Ostroverkhov, V., Singer, K. D., Reshetnyak, V., & Reznikov, Y. (2000). Electrically controlled surface diffraction gratings in nematic liquid crystals. *Optics letters*, 25(6), 414-416.
- ¹¹ Pagliusi, P., & Cipparrone, G. (2003). Extremely sensitive light-induced reorientation in nondoped nematic liquid crystal cells due to photoelectric activation of the interface. *Journal of applied physics*, 93(11), 9116-9122.
- ¹² Khoo, I. C., Chen, K., & Williams, Y. Z. (2006). Orientational photorefractive effect in undoped and CdSe nanorods-doped nematic liquid crystal—bulk and interface contributions. *IEEE Journal of selected topics in quantum electronics*, 12(3), 443-450.
- ¹³ Budagovsky, I. A., Zolot'ko, A. S., Lobanov, A. N., Smayev, M. P., Tskhovrebov, A. M., Averyushkin, A. S., & Barnik, M. I. (2010). Study of the photocurrent in liquid crystal cells exhibiting the photorefractive effect. *Bulletin of the Lebedev Physics Institute*, 37(2), 49-55.

-
- ¹⁴ Habibpournmoghadam, A., Wolfram, L., Jahanbakhsh, F., Mohr, B., Reshetnyak, V. Y., & Lorenz, A. (2019). Tunable Diffraction Gratings in Copolymer Network Liquid Crystals Driven with Interdigitated Electrodes. *ACS Applied Electronic Materials*, 1(12), 2574-2584.
- ¹⁵ Ouskova, E., Reznikov, Y., Shiyanovskii, S. V., Su, L., West, J. L., Kuksenok, O. V., ... & Simoni, F. (2001). Photo-orientation of liquid crystals due to light-induced desorption and adsorption of dye molecules on an aligning surface. *Physical Review E*, 64(5), 051709.
- ¹⁶ Budagovsky, IA, Ochkin, VN, Smayev, MP, Zolot'ko, AS, Bobrovsky, AY, Boiko, NI, ... & Barnik, MI (2009). Interaction of light with a NLC-dendrimer system. *Liquid Crystals*, 36 (1), 101-107.
- ¹⁷ Habibpournmoghadam, A., Jiao, L., Reshetnyak, V., Evans, D. R., & Lorenz, A. (2017). Optical manipulation and defect creation in a liquid crystal on a photoresponsive surface. *Physical Review E*, 96(2), 022701.
- ¹⁸ Habibpournmoghadam, A., Jiao, L., Omairat, F., Evans, D. R., Lucchetti, L., Reshetnyak, V., & Lorenz, A. (2017). Confined photovoltaic fields in a photo-responsive liquid crystal test cell. In *Liquid Crystals XXI* (Vol. 10361, p. 1036112). International Society for Optics and Photonics.
- ¹⁹ Habibpournmoghadam, A. (2019). Theoretical Prediction of Umbilics Creation in Nematic Liquid Crystals with Positive Dielectric Anisotropy. *ACS omega*, 4(25), 21459-21468.
- ²⁰ Neaman, D. A. *Semiconductor Physics and Devices* (IRWIN, Chicago, 2003). Chap, 10, 457.
- ²¹ Ray, S., Banerjee, R., Basu, N., Batabyal, A. K., & Barua, A. K. (1983). Properties of tin doped indium oxide thin films prepared by magnetron sputtering. *Journal of Applied Physics*, 54(6), 3497-3501.
- ²² Ohhata, Y., Shinoki, F., & Yoshida, S. (1979). Optical properties of r.f. reactive sputtered tin-doped In₂O₃ films. *Thin Solid Films*, 59(2), 255-261.
- ²³ Burstein, E. (1954). Anomalous optical absorption limit in InSb. *Physical Review*, 93(3), 632.
- ²⁴ Her, S. C., & Chang, C. F. (2017). Fabrication and characterization of indium tin oxide films. *Journal of applied biomaterials & functional materials*, 15(2), 170-175.
- ²⁵ Mazur, M., Kaczmarek, D., Domaradzki, J., Wojcieszak, D., Song, S., & Placido, F. (2010, October). Influence of thickness on transparency and sheet resistance of ITO thin films. In *The Eighth International Conference on Advanced Semiconductor Devices and Microsystems* (pp. 65-68). IEEE.
- ²⁶ Kim, H., Gilmore, A. C., Pique, A., Horwitz, J. S., Mattoussi, H., Murata, H., ... & Chrisey, D. B. (1999). Electrical, optical, and structural properties of indium-tin-oxide thin films for organic light-emitting devices. *Journal of applied physics*, 86(11), 6451-6461.

- ²⁷ Alam, M. J., & Cameron, D. C. (2002). Investigation of annealing effects on sol-gel deposited indium tin oxide thin films in different atmospheres. *Thin Solid Films*, 420, 76-82.
- ²⁸ Hosono, H., & Ueda, K. (2017). Transparent conductive oxides. In *Springer Handbook of Electronic and Photonic Materials* (pp. 1-1). Springer, Cham.
- ²⁹ Farhan, M. S., Zalnezhad, E., Bushroa, A. R., & Sarhan, A. A. D. (2013). Electrical and optical properties of indium-tin oxide (ITO) films by ion-assisted deposition (IAD) at room temperature. *International Journal of Precision Engineering and Manufacturing*, 14(8), 1465-1469.
- ³⁰ Shi, J. R., Lau, S. P., Sun, Z., Shi, X., Tay, B. K., & Tan, H. S. (2001). Structural and electrical properties of copper thin films prepared by filtered cathodic vacuum arc technique. *Surface and Coatings Technology*, 138(2-3), 250-255.
- ³¹ Edwards, P. P., Porch, A., Jones, M. O., Morgan, D. V., & Perks, R. M. (2004). Basic materials physics of transparent conducting oxides. *Dalton transactions*, (19), 2995-3002.
- ³² Ioffe, A. F., & Regel, A. R. (1960). Non-crystalline, amorphous and liquid electronic semiconductors. *Prog. Semicond*, 4(89), 237-291.
- ³³ Heeger, A. J. (2002). The critical regime of the metal-insulator transition in conducting polymers: experimental studies. *Physica Scripta*, 2002(T102), 30.
- ³⁴ Mott, N. F., & Davis, E. A. (2012). *Electronic Processes in Non-crystalline Materials*. Oxford University Press, UK.
- ³⁵ Kaushik, D. K., Kumar, K. U., & Subrahmanyam, A. (2017). Metal-insulator transition in tin doped indium oxide (ITO) thin films: Quantum correction to the electrical conductivity. *AIP Advances*, 7(1), 015109.
- ³⁶ Lin, J. J., & Li, Z. Q. (2014). Electronic conduction properties of indium tin oxide: single-particle and many-body transport. *Journal of Physics: Condensed Matter*, 26(34), 343201.
- ³⁷ Moss, T. S. (1954). The interpretation of the properties of indium antimonide. *Proceedings of the Physical Society. Section B*, 67(10), 775.
- ³⁸ Fan, J. C., & Goodenough, J. B. (1977). X-ray photoemission spectroscopy studies of Sn-doped indium-oxide films. *Journal of Applied Physics*, 48(8), 3524-3531.
- ³⁹ Hamberg, I., Granqvist, C. G., Berggren, K. F., Sernelius, B. E., & Engström, L. (1984). Band-gap widening in heavily Sn-doped In₂O₃. *Physical Review B*, 30(6), 3240.
- ⁴⁰ Hamberg, I., & Granqvist, C. G. (1986). Evaporated Sn-doped In₂O₃ films: Basic optical properties and applications to energy-efficient windows. *Journal of Applied Physics*, 60(11), R123-R160.

-
- ⁴¹ Guizzardi, M., Bonfadini, S., Moscardi, L., Kriegel, I., Scotognella, F., & Criante, L. (2020). Large scale indium tin oxide (ITO) one dimensional gratings for ultrafast signal modulation in the visible spectral region. *Physical Chemistry Chemical Physics*, 22(13), 6881-6887.
- ⁴² Klein, A., Körber, C., Wachau, A., Säuberlich, F., Gassenbauer, Y., Harvey, S. P., ... & Mason, T. O. (2010). Transparent conducting oxides for photovoltaics: Manipulation of fermi level, work function and energy band alignment. *Materials*, 3(11), 4892-4914.
- ⁴³ El Hichou, A., Kachouane, A., Bubendorff, J. L., Addou, M., Ebothe, J., Troyon, M., & Bougrine, A. (2004). Effect of substrate temperature on electrical, structural, optical and cathodoluminescent properties of In₂O₃-Sn thin films prepared by spray pyrolysis. *Thin Solid Films*, 458(1-2), 263-268.
- ⁴⁴ Matino, F., Persano, L., Arima, V., Pisignano, D., Blyth, R. I. R., Cingolani, R., & Rinaldi, R. (2005). Electronic structure of indium-tin-oxide films fabricated by reactive electron-beam deposition. *Physical Review B*, 72(8), 085437.
- ⁴⁵ Lee, M. S., Choi, W. C., Kim, E. K., Kim, C. K., & Min, S. K. (1996). Characterization of the oxidized indium thin films with thermal oxidation. *Thin Solid Films*, 279(1-2), 1-3.
- ⁴⁶ Palik, E. D. (Ed.). (1998). *Handbook of optical constants of solids* (Vol. 3). Academic press.
- ⁴⁷ Porch, A., Morgan, D. V., Perks, R. M., Jones, M. O., & Edwards, P. P. (2004). Electromagnetic absorption in transparent conducting films. *Journal of Applied Physics*, 95(9), 4734-4737.
- ⁴⁸ Liu, X., Park, J., Kang, J. H., Yuan, H., Cui, Y., Hwang, H. Y., & Brongersma, M. L. (2014). Quantification and impact of nonparabolicity of the conduction band of indium tin oxide on its plasmonic properties. *Applied Physics Letters*, 105(18), 181117.
- ⁴⁹ Lee, H. W., Papadakis, G., Burgos, S. P., Chander, K., Kriesch, A., Pala, R., ... & Atwater, H. A. (2014). Nanoscale conducting oxide PlasMOS₂. *Nano letters*, 14(11), 6463-6468.
- ⁵⁰ Chen, C. W., Lin, Y. C., Chang, C. H., Yu, P., Shieh, J. M., & Pan, C. L. (2010). Frequency-dependent complex conductivities and dielectric responses of indium tin oxide thin films from the visible to the far-infrared. *IEEE Journal of Quantum Electronics*, 46(12), 1746-1754.
- ⁵¹ Levy, D., & Castellón, E. (Eds.). (2018). *Transparent Conductive Materials: Materials, Synthesis, Characterization, Applications*. John Wiley & Sons.
- ⁵² Neelakanta, P. S. (1995). *Handbook of electromagnetic materials: monolithic and composite versions and their applications*. CRC press.
- ⁵³ Bechstedt, F. (2016). *Many-Body Approach to Electronic Excitations*. Springer-Verlag Berlin An.

-
- ⁵⁴ Leonard, Regis. F. (1991-1992). *Solid state technology branch of Nasa Lewis research center fourth annual digest, +NASA Technical Memorandum (V. 105752)*. Lewis Research Center, USA.
- ⁵⁵ Panda, S. (2009). *Microelectronics and optoelectronics technology*. Laxmi Publications Pvt. Ltd, New Delhi.
- ⁵⁶ Hamaguchi, C. (2010). *Basic semiconductor physics* (Vol. 9, pp. 443-510). Berlin: Springer-Verlag.
- ⁵⁷ Brennan, K. F. (1999). *The physics of semiconductors: with applications to optoelectronic devices*. Cambridge University Press, USA.
- ⁵⁸ Pagliusi, P., & Cipparrone, G. (2002). Surface-induced PR-like effect in pure liquid crystals. *Applied physics letters*, *80*(2), 168-170.
- ⁵⁹ Lafemina, J. P. (1989). Photoconduction in polyimide. *Chemical physics letters*, *159*(4), 307-309.
- ⁶⁰ Zolot'ko, AS, Kitaeva, VF, Sobolev, NN, & Sukhorukov, AP (1981). Self-focusing of laser radiation in the course of the Fréedericksz transition in the nematic phase of a liquid crystal. *Zh. Eksp. Teor. Fiz.* , *81* , 933-941.
- ⁶¹ Budagovsky, I. A., Ochkin, V. N., Smayev, M. P., Zolot'ko, A. S., & Barnik, M. I. (2007, July). Asymmetric aberrational patterns at light beam self-action in nematic liquid crystals. In *ICONO 2007: Coherent and Nonlinear Optical Phenomena* (Vol. 6729, p. 67293E). International Society for Optics and Photonics. Proc. of SPIE, USA.
- ⁶² Zel'dovich, BY, & Tabiryan, NV (1985). Orientational optical nonlinearity of liquid crystals. *Soviet Physics Uspekhi* , *28*(12), 1059.
- ⁶³ Kitaeva, VF, Zolot'ko, AS, & Barnik, MI (2000). Orientational optical nonlinearity of absorbing nematic liquid crystals. *Molecular Materials*, *12*(4), 271-293.
- ⁶⁴ Zolot'ko, AS, Kitaeva, VF, Kroo, N., Sobolev, NN, Sukhorukov, AP, & Csillag, L. (1982). Nature of the aberration pattern formed as the result of self-focusing of a light beam caused by reorientation of the director in liquidcrystals. *Zh. Eksp. Teor. Fiz*, *83*, 1368-1375 [J. Exp. Theor. Phys (Sov. Phys. JETP). **83**(4), 786 (1982)].
- ⁶⁵ Brasselet, E. (2012). Tunable optical vortex arrays from a single nematic topological defect. *Physical review letters*, *108*(8), 087801.
- ⁶⁶ Rapini, A. (1973). Umbilics: static properties and shear-induced displacements. *Journal de Physique*, *34*(7), 629-633.
- ⁶⁷ Basistiy, IV, Soskin, MS, & Vasnetsov, MV (1995). Optical wavefront dislocations and their properties. *Optics Communications* , *119* (5-6), 604-612.
- ⁶⁸ Gahagan, KT, & Swartzlander, GA (1996). Optical vortex trapping of particles. *Optics Letters*, *21*(11), 827-829.

-
- ⁶⁹ Gahagan, KT, & Swartzlander, GA (1999). Simultaneous trapping of low-index and high-index microparticles observed with an optical-vortex trap. *JOSA B*, 16(4), 533-537.
- ⁷⁰ Tamburini, F., Anzolin, G., Umbriaco, G., Bianchini, A., & Barbieri, C. (2006). Overcoming the Rayleigh criterion limit with optical vortices. *Physical review letters*, 97(16), 163903.
- ⁷¹ Lee, JH, Foo, G., Johnson, EG, & Swartzlander Jr, GA (2006). Experimental verification of an optical vortex coronagraph. *Physical review letters*, 97(5), 053901.
- ⁷² Gibson, G., Courtial, J., Padgett, MJ, Vasnetsov, M., Pas'ko, V., Barnett, SM, & Franke-Arnold, S. (2004). Free-space information transfer using light beams carrying orbital angular momentum. *Optics express*, 12(22), 5448-5456.
- ⁷³ Mair, A., Vaziri, A., Weihs, G., & Zeilinger, A. (2001). Entanglement of the orbital angular momentum states of photons. *Nature*, 412(6844), 313-316.
- ⁷⁴ Budagovsky, I. A., Shvetsov, S. A., & Zolot'ko, A. S. (2016). Optical vortex generation in homeotropic NLCs in the presence of DC electric field. *Molecular Crystals and Liquid Crystals*, 637(1), 47-52.
- ⁷⁵ Budagovsky, IA, Zolot'ko, AS, Smayev, MP, & Shvetsov, SA (2015). Formation of the light beam with wavefront screw dislocation at the photorefractive effect in nematic liquid crystal. *Bulletin of the Lebedev Physics Institute*, 42(11), 319-322.
- ⁷⁶ Budagovsky, IA, Zolot'ko, AS, & Shvetsov, SA (2016). On the formation of vortex light beams at the surface photorefractive effect in NLC. *Bulletin of the Lebedev Physics Institute*, 43(11), 340-344.
- ⁷⁷ Kravets, N., Podoliak, N., Kaczmarek, M., & Brasselet, E. (2019). Self-induced liquid crystal q-plate by photoelectric interface activation. *Applied Physics Letters*, 114(6), 061101.
- ⁷⁸ Curtis, J. E., & Grier, D. G. (2003). Structure of optical vortices. *Physical review letters*, 90(13), 133901.
- ⁷⁹ Maleev, I. D., & Swartzlander, G. A. (2003). Composite optical vortices. *JOSA B*, 20(6), 1169-1176.
- ⁸⁰ Yao, A. M., & Padgett, M. J. (2011). Orbital angular momentum: origins, behavior and applications. *Advances in Optics and Photonics*, 3(2), 161-204.
- ⁸¹ Zhang, Y., Burzynski, R., Ghosal, S., & Casstevens, M. K. (1996). PR polymers and composites. *Advanced Materials*, 8(2), 111-125.
- ⁸² Feigenbaum, E., Diest, K., & Atwater, H. A. (2010). Unity-order index change in transparent conducting oxides at visible frequencies. *Nano letters*, 10(6), 2111-2116.
- ⁸³ Melikyan, A., Lindenmann, N., Walheim, S., Leufke, P. M., Ulrich, S., Ye, J., ... & Freude, W. (2011). Surface plasmon polariton absorption modulator. *Optics Express*, 19(9), 8855-8869.

-
- ⁸⁴ Yi, F., Shim, E., Zhu, A. Y., Zhu, H., Reed, J. C., & Cubukcu, E. (2013). Voltage tuning of plasmonic absorbers by indium tin oxide. *Applied Physics Letters*, 102(22), 221102.
- ⁸⁵ Sorger, V. J., Lanzillotti-Kimura, N. D., Ma, R. M., & Zhang, X. (2012). Ultra-compact silicon nanophotonic modulator with broadband response. *Nanophotonics*, 1(1), 17-22.
- ⁸⁶ Marrucci, L. (2008). Generation of helical modes of light by spin-to-orbital angular momentum conversion in inhomogeneous liquid crystals. *Molecular Crystals and Liquid Crystals*, 488(1), 148-162.

Chapter 5: Theoretical Prediction of Umbilics Creation in NLCs with Positive Dielectric Anisotropy*

5.1. Abstract

Optically-assisted electrical generation of umbilic defects, arising in homeotropically aligned nematic liquid crystal cells and known as topological templates for generation of optical vortices, are reported in nematic liquid crystals with positive dielectric anisotropy in detail. It is shown that such nematic LCs can serve as a stable and efficient medium for optical vortex generation from both linearly and circularly polarized Gaussian input beams. Hybrid cells made from a thin layer of nematic liquid crystal confined between a photoresponsive slab of iron-doped lithium niobate and a glass plate coated with an active material, i.e., indium tin oxide (ITO), were studied. Exposure to a laser beam locally induces a photovoltaic field in the iron-doped lithium niobate substrate, which can penetrate into the liquid crystal film and induce realignment of molecules. The photovoltaic field drives charge carrier accumulation at the interface of ITO with the liquid crystal, which effectively modifies the shape and symmetry of the electric field.

* Habibpournmoghadam, A. (2019). Theoretical Prediction of Umbilics Creation in Nematic Liquid Crystals with Positive Dielectric Anisotropy. *ACS omega*, 4 (25), 21459-21468. (<https://doi.org/10.1021/acsomega.9b03158>, Copyright © 2019 American Chemical Society)

The photovoltaic field has a continuous radial distribution in the transverse xy -plane, weakening with increasing distance from the light irradiation center, where the electric field is normal to the cell plane. Umbilics are created as a result of the liquid crystal tendency to realign parallel to the electric field. Numerical studies of the transmitted intensity profiles between linear polarizers reveal optical vortex patterns (of 4 or 8 optical lobes) characteristic for umbilical defects. The application of crossed circular polarizers results in annular-shaped intensity patterns as a result of spin-to-orbital angular momentum conversions, which give rise to the optical vortices.

5.2. Introduction

Dynamical rotation of the electromagnetic field of light with respect to the axis of propagation is described by a vector quantity called angular momentum associated with a spin angular momentum (SAM) and an orbital angular momentum (OAM). While the SAM is attributed to the light beam polarization being elliptical or circular, the OAM corresponds to the twisting of the beam wavefront around the propagation axis (coincident with a topological phase singularity); such a beam is called an optical vortex (OV)¹⁻⁶. The intensity profiles of OVs consist of donut-shaped concentric rings with zero-intensity at the center¹⁻⁶ associated with the beam phase singularity. At a given wavelength λ , the phase front of an OV beam is composed of $|l|$ intertwined helices along the propagation axis, where the integer azimuthal index l gives the amount of OAM carried by the wave per photon as $l\hbar$ ^{6,7}.

OVs are structurally stable in homogeneous, isotropic media due to an invariant OAM⁸. In nonlinear media (characterized with third-order nonlinear optical susceptibility $\chi(3) > 0$), the lensing property imposes vortex solitons generation as self-trapped spatially localized beams keeping their structural shape during propagation^{9,10}. During the past decades, OVs have found tremendous applications in different fields such as coronagraphy in astronomy^{11,12}, cryptography based on OAM states of photons in telecommunication systems¹³⁻¹⁵, micromanipulation techniques in biological systems¹⁶⁻¹⁸, and as depletion beams in stimulated-emission-depletion (STED) microscopy¹⁹.

Different methods were developed for generating OVs, such as employing a pair of cylindrical lenses²⁰, spiral phase plates²¹⁻²³, segmented deformable mirrors²⁴, computer-generated holograms (CGHs) in the form of spatial light modulators (SLMs)²⁵, forked diffraction gratings²⁵⁻²⁷ or spiral Fresnel lenses²⁸. Nematic liquid crystals (LCs), as outstanding candidates, have found applications in electro-optical

systems aimed at spin-orbit manipulation of light²⁹⁻³¹ because of their self-organization properties, ease of controlling their optical axis, exhibiting a long-range orientational order, and exhibiting high optical anisotropy and birefringence as well.

OVs can be generated in nematic liquid crystals by means of different mechanisms such as q-plates³², nematic droplets³³, and umbilical defects (in short “umbilics”)^{34,35}. The topological structures of umbilics were described by Rapini in 1973⁶, resembling string-like objects in three-dimensions (3D)^{35,36}. In the LC, umbilics act as topological matter templates, which are able to convert an incoming circularly polarized light beam into a helical (vortex) light beam, so-called photonic spin-to-orbital momentum couplers³⁷. Umbilics have been extensively studied in nematic LCs with negative dielectric anisotropy ($\Delta\epsilon < 0$), where the LCs tend to realign perpendicular to the applied electric field. Here, it is shown how nematic LCs with positive dielectric anisotropy ($\Delta\epsilon > 0$), as initially aligned homeotropically, can be successfully employed for the purpose of umbilics generation as well confined and without formation of any line or wall defect. In our recent experimental study³⁸, it was shown that the planar anchoring condition on the cell walls can lead to the formation of wall defects in LC cells with a similar structure to the one studied here.

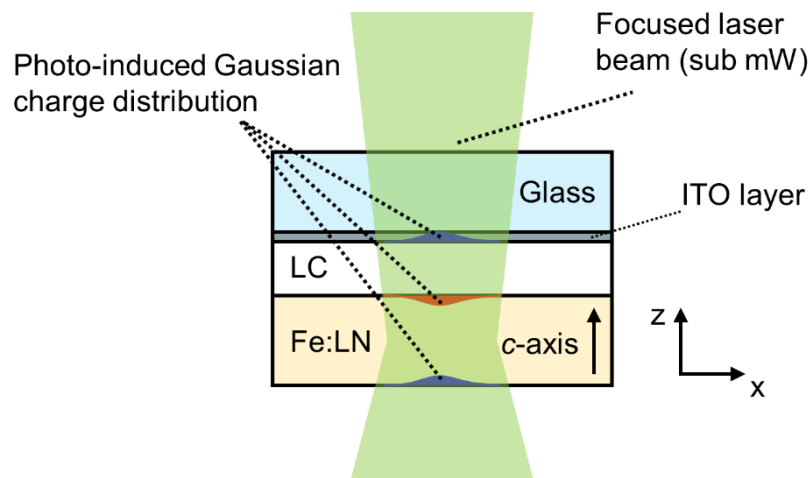


Figure 5.1. Schematic of a hybridized LC test cell exposed to a laser beam with sub-milliwatt (mW) power.

Hybridized LC cells made from a thin film of LC confined between an ITO-coated glass slab and a z-cut ferroelectric-substrate iron-doped lithium niobate (Fe:LiNbO₃ or in short Fe:LN) were studied (Figure 5.1). Treating the cell walls with an orientant, such as lecithin, (both ITO-coated glass and the interface of Fe:LN with the LC) can provide a homeotropic anchoring condition for the LC, corresponding to an

unperturbed condition. In the recent experimental work of N. Kravets and co-workers³⁹, it was shown that the photoassisted dc-electric field can induce spin-orbit optical vortex generation with high purity and efficiency (> 90%). The light induced photovoltaic (PV) field in the Fe:LN has a distribution in the LC medium capable to induce the LC reorientation^{38,40-42}. Here, photoinduced charge carrier accumulation in the single active ITO layer reshape the electric field profile in a promising way for optical vortex generation. In the work reported by Barboza et al⁴³, a liquid crystal light valve (LCLV) was made by employing a $\text{Bi}_{12}\text{SiO}_{20}$ (BSO) slab as a photosensible wall, which acts as an optical tunable impedance, if illuminated properly, by means of tuning the effective voltage in the LC media.

The umbilics in the nematic LC with positive dielectric anisotropy ($\Delta\epsilon > 0$) are created as the result of the competition between the elastic torque and electric torque applied by the optically assisted PV field. Previously, they were studied both experimentally and theoretically in a situation where the external applied torque on the LC was of purely optical nature^{44,45}.

For comparison, umbilics generated in an LCs with negative dielectric anisotropy, referred as model umbilics, were studied. The simulation results showed that the topological defects generated in the nematic liquid crystal with positive dielectric anisotropy possess all fundamental features of the model umbilics.

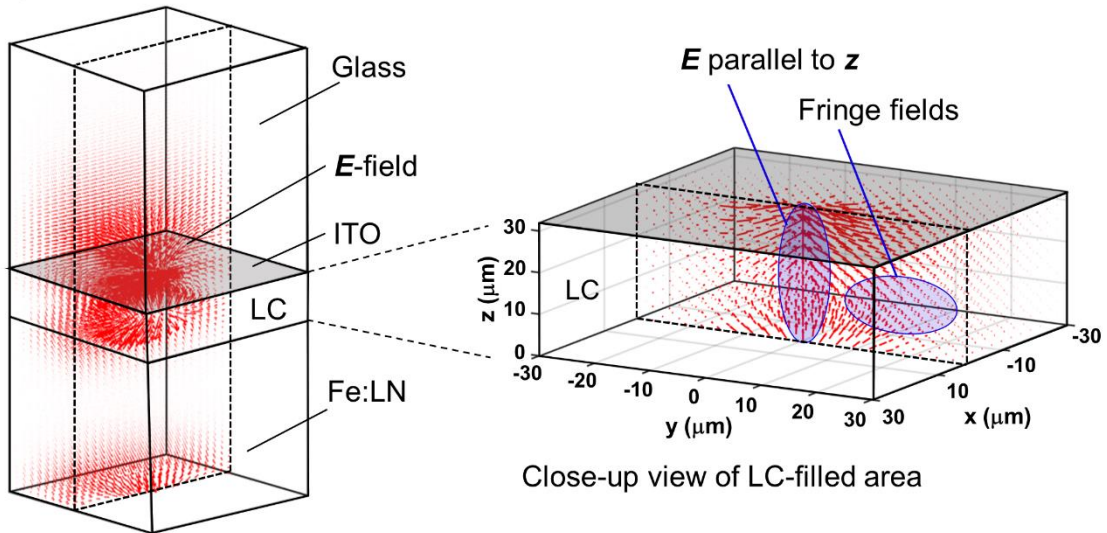
5.3. Simulation of the photo-generated electric field in the hybridized LC cells equipped with an ITO layer

Studies were conducted for the nematic LC of MLC-2087^{38,40} with the positive dielectric anisotropy of $\Delta\epsilon = 13.31$ at zero frequency associated with the DC electric field, a birefringence of $\Delta n = 0.076$, and an average elastic constant of $K = 14.7$ pN (in one-constant approximation). To obtain a visualization of the photovoltaic field distribution in the LC, the simulation was conducted in a test cell filled with an isotropic medium with a dielectric constant of $\epsilon^{iso} = 10.16$ (equal to the average dielectric constant of MLC-2087), shown in Figure 5.2. LC realignments were studied by taking into account the anisotropy of media as discussed in the following sections. The simulation geometry can also be seen in Figure 5.2. As described⁴⁰, irradiation of the LC test cell with Fe:LN substrate gives rise to a photoinduced charge carrier separation that can be described by a two-dimensional Gaussian distribution $\sigma = \sigma_0 e^{-(x^2+y^2)/w^2}$ of positive charge carriers at the top surface of the Fe:LN substrate and a similar

distribution of negative charge carriers at the base. The full width at half maximum (FWHM) w of the Gaussian charge carriers distributions was set equal to the FWHM (14 μm) of the exposure beam focus. The thickness of the Fe:LN substrate was set to 100 μm and its dielectric constant was considered anisotropic ($\epsilon_{\parallel z} = 29$ and $\epsilon_{\perp z} = 85$).

Simulated \mathbf{E} -field in the Fe:LN test cell equipped with ITO

a)



b)

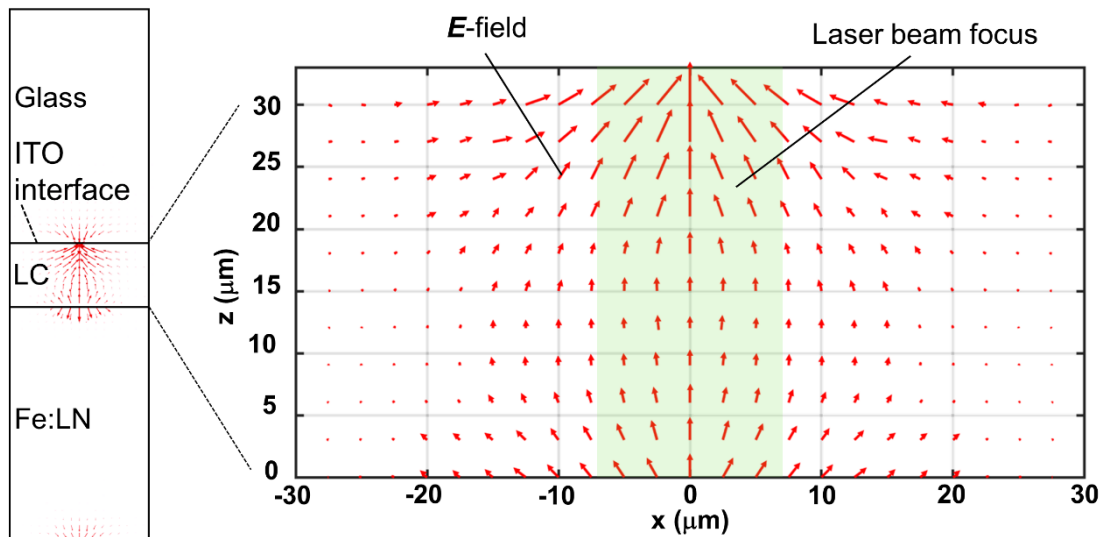


Figure 5.2. Schematic of photogenerated electric field distribution in a hybridized LC test cell with Fe:LN substrate and ITO-coated glass plate a) in three-, b) two-dimensions. The electric field generated within the Fe:LN substrate induces a charge carrier accumulation in the active ITO layer. As a result, modeling was done by placing a Gaussian charge carrier distributions in the upper and lower plane (xy -plane) of the Fe:LN substrates, as well as in the LC/ITO interface. In three-dimensional modeling,

the \mathbf{E} -field is shown in the rear half of the volume to give a clear view of the center area in magnification.

The simulation geometry had a footprint of $x \times y = 60 \times 60 \mu\text{m}^2$ in the transverse xy -plane.

The test cell was set up from an ITO-coated cover glass with a relative permittivity of about $\epsilon_S^{\text{ITO}} = 9^{46-48}$ in the static electric field. The thickness of the ITO layer deposited at the glass surface was much smaller than both the LC layer and the Fe:LN substrate; it was supposed in the range of 100-300 nm in the simulations: A Gaussian charge distribution, with negative sign and the same FWHM as the ones attributed to the Fe:LN crystal, was supposed at the boundary of the ITO with the LC, as a result of charge accumulation induced via photovoltaic field within the ITO layer (the reasons are explained in more detail in the sections 5. 4 and 5. 6). In modeling, the photovoltaic field was considered as the only source of the static electric field in the cell. The electric field exhibits a distribution inside the glass plate because of the limited permittivity and negligible thickness of the ITO film. The charge density amplitudes σ_0 of the Gaussian charge carrier distributions, and thus the magnitude of the static electric fields inside the LC layer, were increased stepwise in the simulations.

The field distribution obtained in this model is seen in Figure 5.2. It shows that the local electric field is normal to the sample plane (parallel to the z -direction) at the exposure spot center. One can thus expect that the initial homeotropic alignment of the LC (in the LC with positive dielectric anisotropy, provided by coating with lecithin as anchoring agent) is maintained here locally, which—for transmitted polarized light—presents a virtual continuous phase singularity: this region appears as a dark spot in the intensity distribution of transmitted light. Moreover, fringe fields are seen around the exposure spot center (the center of the Gaussian charge carrier distribution) and the electric field decays in radial direction. As can be seen in Figure 5.2, the electric field distribution has a continuous radial distribution in the transverse xy -plane. Such a field distribution can be expected to induce a radial distribution of the LC director in the cell corresponding to the director realignment in a splay umbilic. If so, the polarization of the light incident in the area surrounding the local phase singularity can be modulated, since the optical axis is no longer oriented parallel to the propagation direction. In the umbilics with transverse distribution of the local optical axis, this leads to the creation of optical vortices^{35,49}.

5.4. Discussion on the charge carrier accumulation in the ITO thin film

The static electric field is capable to induce charge accumulation^{50,51} in the ITO film near the interface with the LC (as an insulator media). In the visible light, ITO behaves as an active n-type semiconductor⁵¹. For a single source of electric field, the accumulated charge density is equal to the source's⁵⁰. In our system, photo-induced Gaussian-distributed charge densities were supposed at the top and bottom surfaces of the Fe:LN substrate, respectively (with positive sign at the top, and negative sign at the bottom surface, accordingly), which both contributed in the effective electric field in the ITO layer. Here, the expected emerged accumulated charge density was numerically calculated in a straightforward approach.

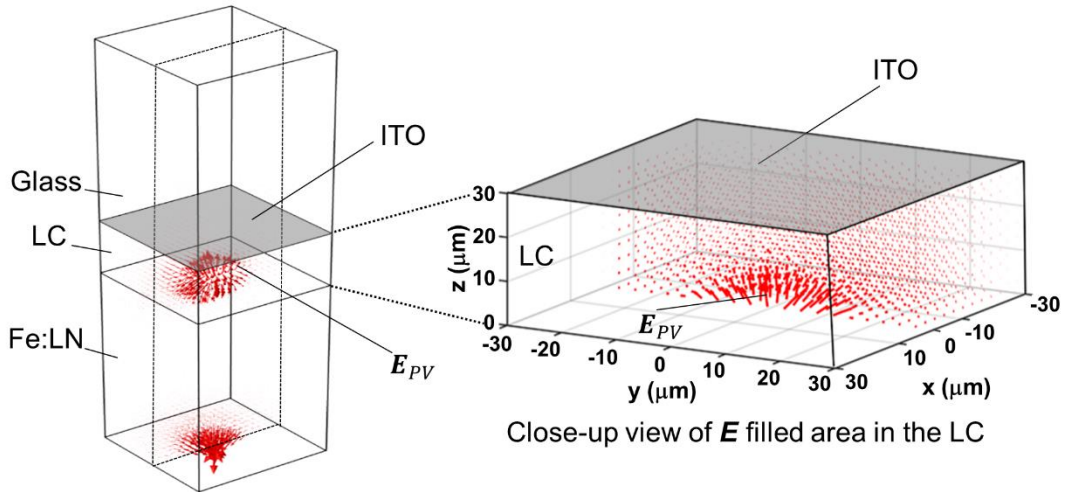


Figure 5.3. The photovoltaic electric field (E_{PV}) responsible for the charge accumulation in the ITO layer is shown in the LC cell in magnification.

Since the average thickness of the accumulation layer (about 0.9 nm^{48}) is ignorable compared to the size of device, the induced carrier density N_i within the ITO layer can be assumed in two-dimensions (2D). In one-dimension (1D), the excess carrier density δN induced in the accumulation layer in a cross section through the beam center along the x -axis supposed at $y = 0 \text{ } \mu\text{m}$, and $z_i = 30 \text{ } \mu\text{m}$ relative to the Fe:LN interface with LC (as seen in Figure 5.3) can be calculated from⁵²,

$$\Delta U(x)|_{y=0 \text{ } \mu\text{m}, z_i=30 \text{ } \mu\text{m}} = U_i - U_\infty = \frac{e\delta N(x)}{\epsilon_0 \epsilon_{ITO}} \quad (5.1)$$

where e is the unit charge, ϵ_0 and $\epsilon_{\text{ITO}} = 9.3^{48,52}$ are the vacuum and the relative static permittivity of ITO, respectively. Voltage at the ITO surface was determined relative to $z_f \rightarrow \infty$. Considering radial symmetry of the system, excess carrier density in two dimensions (2D) can be obtained from $\delta N \times \delta N$.

The electric potential in the ITO layer (in 1D) placed at $z_i = 30 \mu\text{m}$ (Figure 5.3) was numerically obtained from:

$$\Delta U = - \int_i^f \mathbf{E} \cdot d\mathbf{l} = - \int_{z_i}^{\infty} E_z dz, \quad (5.2)$$

which was calculated with respect to the outer surface of glass ($f \rightarrow \infty$), where the electric field goes to zero because of the high thickness of glass (more than $100 \mu\text{m}$), hence $U_{\infty} = 0$, and as a result $\Delta U = U$ (U : electric potential at ITO surface $U = U_i$) holds. The electric potential was numerically calculated from the electric field distribution stemming only from the photo-induced charge densities in the Fe:LN substrate (seen in Figure 5.3).

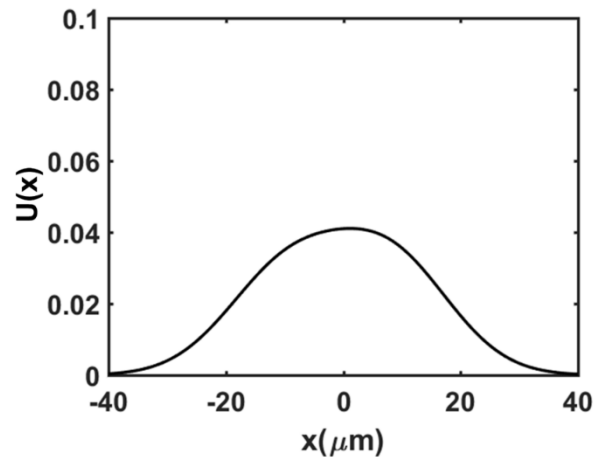


Figure 5.4. Numerically obtained electric potential (in volts) distribution in the ITO thin film in the cross section through the beam center.

From equation (5.2), the electric potential distribution in the ITO layer was obtained by means of Matlab. In Figure 5.4, the result is shown for the induced charge density equal to $\sigma_0 = 40 \mu\text{Cm}^{-2}$ corresponding to the emerged charge distribution of $\sigma = |\sigma_0| e^{-(x^2+y^2)/w^2}$ at the top and bottom surfaces of Fe:LN in two-dimensions (2D). The electric potential has a larger width than the optical width due to the divergence of the photovoltaic electric field responsible for the charge carrier accumulation.

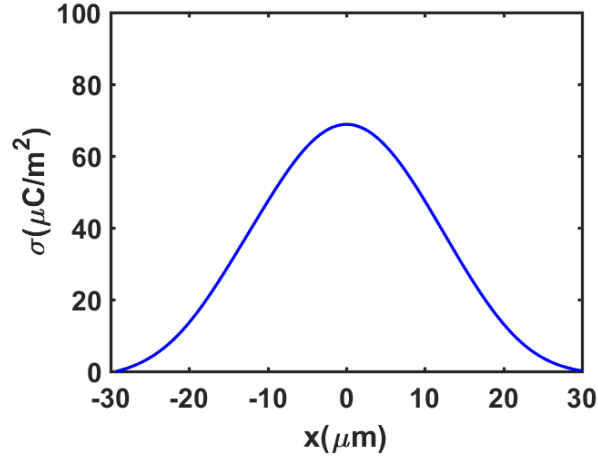


Figure 5.5. Charge carrier density accumulated at the boundary of ITO with the LC in the cross section through the beam center.

By substituting the numerical values obtained for U , the excess carrier density δN was obtained from Equation (5.1), where the excess electric charge density was calculated from $\sigma = e\delta N$, with e the unit charge. The corresponding induced charge density in 2D is shown in Figure 5.5.

5.5. Modeling of the director field in a splay umbilic observed in NLC with negative anisotropy (model umbilic)

Umbilics appear in the LC cell at voltages U higher than a threshold $U > U_t$ ($U_t = \pi (K_3/\epsilon_0 |\Delta\epsilon|)^{1/2}$ ^{35,36}, where K_3 is the bend elastic constant and $\Delta\epsilon = \epsilon_{||}^\Omega - \epsilon_{\perp}^\Omega$ is the dielectric anisotropy at a frequency Ω , defined as the difference between the relative permittivities along and across the director, i.e., $\epsilon_{||}^\Omega$ and ϵ_{\perp}^Ω , respectively. Continuity in the structure is in fact the main difference between an umbilical and a **Frank** defect³⁶. The structure of an umbilic is specified by a continuous core $a(r)$ called reduced amplitude, which is numerically obtained from³⁶:

$$\frac{d^2a}{dr^2} + \frac{1}{r} \frac{da}{dr} + \left(\chi^2 - \frac{1}{r^2}\right)a = \left(\frac{\chi}{a_\infty}\right)^2 a^3 \quad (5.3)$$

where a_∞ is the core reduced amplitude at infinity approaching the value of one³⁵, and the parameter χ is inversely proportional to the core radius r_c , defined as³⁶,

$$\chi = r_c^{-1} = \frac{\pi}{d} \left(\frac{K_3}{K} \right)^{1/2} (\tilde{U}^2 - 1)^{1/2} \quad (5.4)$$

where d is LC film thickness, K is the effective elastic constant determined from the nature of the defect (for example, $K = K_1$ for splay umbilics)³⁶, and $\tilde{U} = U/U_t$ is called the reduced voltage.

The local orientation of a nematic liquid crystal is represented by a dimensionless director field \mathbf{n} , where \mathbf{n} and $-\mathbf{n}$ are physically equivalent due to the lack of polarity of the director field. The director field \mathbf{n} (described as $\mathbf{n} = (n_x, n_y, n_z)$) can be introduced based on the projections in the transverse xy -plane (i.e., \mathbf{n}_\perp) and along the z -axis (i.e., n_z), respectively, as $\mathbf{n} = (\mathbf{n}_\perp, n_z)$. The director field in any transverse plane, \mathbf{n}_\perp , reads $\mathbf{n}_\perp = |\mathbf{n}_\perp| \mathbf{C}(\varphi)$, where $|\mathbf{n}_\perp|$ is its amplitude and \mathbf{C} is a unit vector giving the local direction in the transverse xy -plane as a function of the angle φ ($\varphi = s\phi + \varphi_0$, where s gives the topological strength of the defect, ϕ is the azimuthal angle, and φ_0 is a constant value equal to zero for the case of a splay umbilic, shown in Figure 5.6a). In the splay umbilic, $\mathbf{C}(\varphi)$ gives a radial distribution in the transverse xy -plane (Figure 5.6). According to Rapini³⁶, \mathbf{n}_\perp can be obtained from,

$$\mathbf{n}_\perp = a(r) \cos\left(\frac{\pi z}{d}\right) \mathbf{C}(\varphi) \quad (5.5)$$

where $a(r)$ ($: 0 \leq a(r) \leq 1$) has the minimum value of zero at the center of the defect. By considering \mathbf{n} as an unit vector field, $|\mathbf{n}_z|$ (or n_z) can be obtained from the tilt angle ϑ with respect to the z -direction (\mathbf{k} -vector supposed parallel to the z -direction), as $|\mathbf{n}_z| = \cos(\vartheta)$. The angle ϑ can be calculated from³⁶,

$$\vartheta(r, z) = \vartheta_\infty a(r) \sin(\pi z/d) \quad (5.6)$$

where ϑ_∞ is the value of ϑ at large r , defined as³⁶:

$$\vartheta_\infty = [2(\tilde{U}^2 - 1)/(K_1/K_3 - \tilde{U}^2 \Delta\epsilon/\epsilon_{||}^0)]^{1/2}. \quad (5.7)$$

The parameters K_1 and K_3 are elastic constants corresponding to the splay and bend configurations, respectively.

The director field of the model umbilic in the LC with negative dielectric anisotropy (based on the model described in the literature³⁵) projected in the xy -plane represented by \mathbf{n}_\perp distribution in three and two dimensions, 3D and 2D, is shown in Figures 5.6c, d, respectively. The director field \mathbf{n} distribution in 3D and 2D is

demonstrated in Figure 5.7a and b, respectively. The LC cell is addressed with a homogenous electric field. The simulations were done for the nematic MLC-2079³⁵ with the negative dielectric anisotropy of $\Delta\epsilon = -6.1$ at a frequency $\Omega = 1$ kHz, a birefringence of $\Delta n = 0.15$ at 589 nm wavelength, and the elastic constants of $K_1 = 15.9$ pN and $K_3 = 18.3$ pN. At the center of the model umbilic, $|\mathbf{n}_\perp|$ has the minimum value of zero (Figure 5.6c, d): because of no preferential orientation in this spot, the LC keeps its homeotropic alignment along the LC film conventionally associated with a topological phase singularity. In a planar cell applied by a uniform external electric field, the magnitude of $|\mathbf{n}_\perp|$ increases in the radial direction and reaches its maximum value far from the center of the laser focus³⁵ where $\lim_{r \rightarrow \infty} a(r) = 1$ under the dominance of the reduced amplitude a .

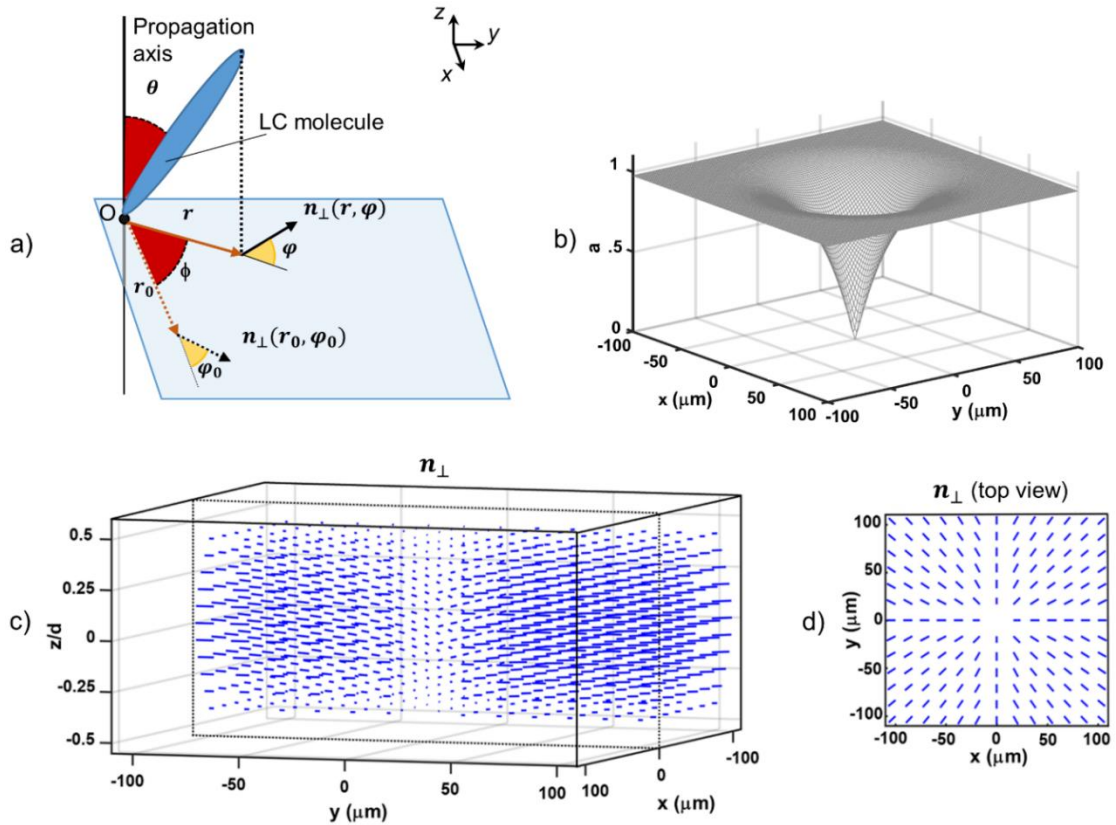


Figure 5.6. a) Demonstration of the coordinate system elements. b) Simulated reduced amplitude a at a relative voltage of $U/U_t = 1.12$. Projection of the model director field in the xy -plane (\mathbf{n}_\perp): c) side-on view, d) top view. The parameter d corresponds to the cell gap.

The distribution of the local optical axis is comparable to an optical q -plate with radial geometry⁵³ suitable for vortex generation. Such a director pattern can generate

optical vortices in a thin sample or if the LC has a low birefringence. Then, diffraction effects (which are unwanted in a q -plate) are negligible for light propagating perpendicular to the sample plane^{53,54}.

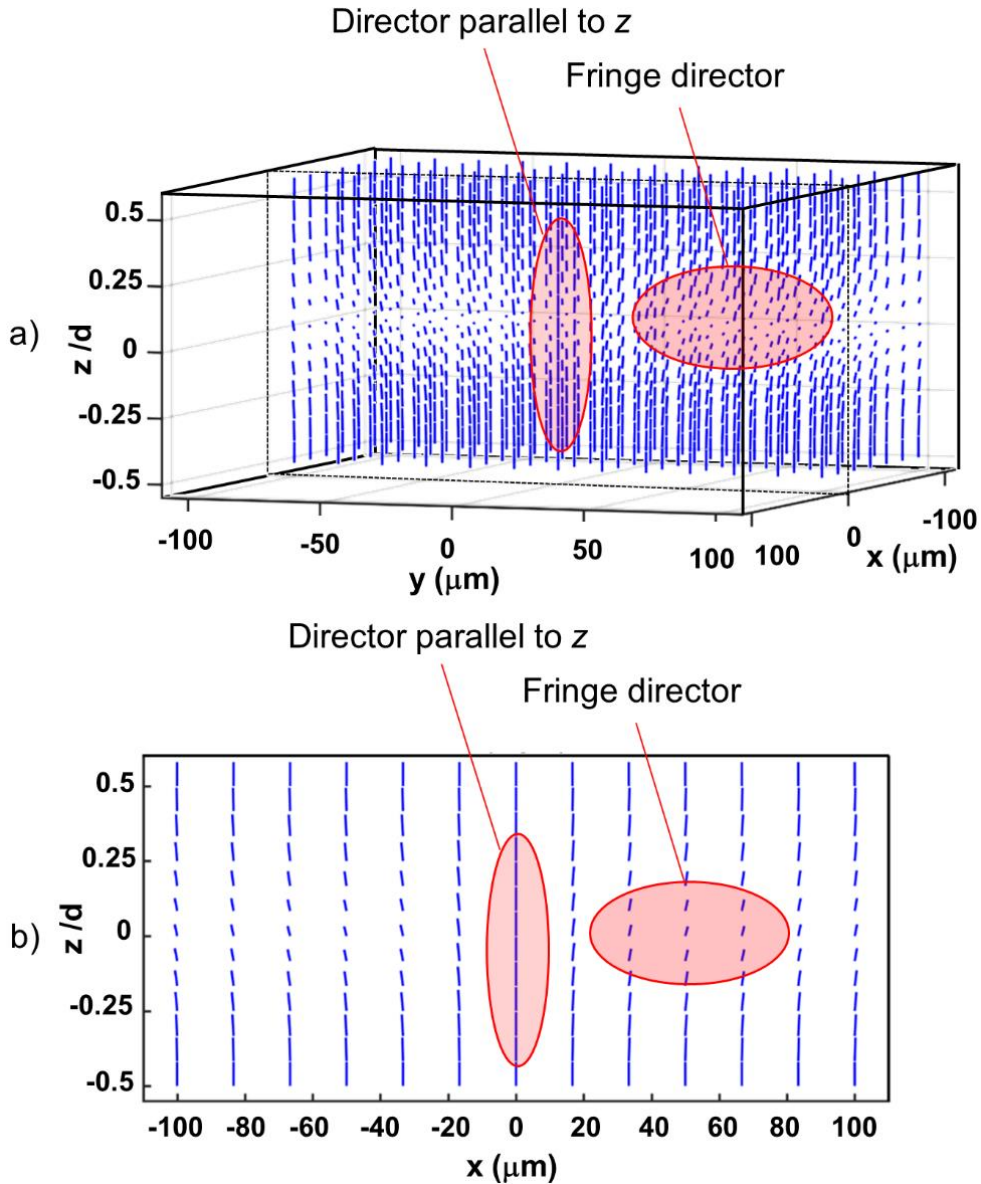


Figure 5.7. Simulated director field of the model umbilic defect in an homeotropically aligned LC cell in a) three-dimensions (3D), and b) two-dimensions (2D). The umbilic shows rotational symmetry around the z -axis.

5.6. Formation of a splay umbilic in NLC with positive dielectric anisotropy

In the second step, the field-induced LC realignment was simulated in the MLC-2087 filled sample with an Fe:LN substrate by using a \mathbf{Q} -tensor approach, by fully considering the anisotropic dielectric constant of the LC (MLC-2087) with $\epsilon_{||}^0 = 16.81$ and $\epsilon_{\perp}^0 = 3.50$ at zero frequency and using one-constant approximation (this approach was described earlier⁴⁰ in detail). For the simulation of the electric field³⁸, the following modification was necessary: charge accumulation is considered in the ITO layer induced by the photovoltaic voltage (discussed in the section 5.4). In addition, the anchoring conditions were defined based on the test cells conditions: at both the ITO and Fe:LN surfaces (covering the LC), homeotropic anchoring was considered.

The LC director field as $\mathbf{n} = (n_x, n_y, n_z)$ was obtained from numerically calculating the \mathbf{Q} -tensor^{40,55-60}:

$$\mathbf{Q}_{ij} = \frac{S}{2}(3n_i n_j - \delta_{ij}) \quad (5.8)$$

where S and δ_{ij} are the scalar order parameter and the Kronecker delta function, respectively. The energy of the LC volume in the static configuration can be described in terms of the \mathbf{Q} -tensor elements and their spatial derivatives, i.e., \mathbf{Q}_{ij} and $\nabla\mathbf{Q}_{ij}$. According to the Landau-de Gennes expansion, in the absence of any external electrical or optical stimuli, the energy density of the LC can be considered as summation of Landau-de Gennes potential and elastic energy, i.e., $E_{LdG}^P(\mathbf{Q}_{ij})$ and $E_{LdG}^e(\nabla\mathbf{Q}_{ij})$, respectively^{40,57}:

$$E_{LdG}(\mathbf{Q}_{ij}, \nabla\mathbf{Q}_{ij}) = E_{LdG}^P(\mathbf{Q}_{ij}) + E_{LdG}^e(\nabla\mathbf{Q}_{ij}) \quad (5.9)$$

where,

$$E_{LdG}^P(\mathbf{Q}_{ij}) = -\frac{A}{2} \mathbf{Q}_{ij} \mathbf{Q}_{ij} + \frac{B}{3} \mathbf{Q}_{ij} \mathbf{Q}_{jk} \mathbf{Q}_{ki} + \frac{C}{4} (\mathbf{Q}_{ij} \mathbf{Q}_{ij})^2 \quad (5.10)$$

$$E_{LdG}^e(\nabla\mathbf{Q}_{ij}) = \frac{L}{2} (\partial_k \mathbf{Q}_{ij})(\partial_k \mathbf{Q}_{ij}). \quad (5.11)$$

Here, A , B , and C are material constants (where A is temperature dependent) and $L/2$ is the effective elastic constant K . Since the LC had a positive dielectric anisotropy, the director field was locally rotated toward the electric field direction, which leads to elastic torques in the LC. Anisotropic dielectric properties of the LC were considered by the relative permittivity tensor^{40,57}:

$$\epsilon_{ij} = \bar{\epsilon}\delta_{ij} + \Delta\epsilon\mathbf{Q}_{ij} \quad (5.12)$$

where $\bar{\epsilon} = \frac{1}{3}(\epsilon_{\parallel}^0 + 2\epsilon_{\perp}^0)$ and, as mentioned before, $\Delta\epsilon = (\epsilon_{\parallel}^0 - \epsilon_{\perp}^0)$, with ϵ_{\parallel}^0 and ϵ_{\perp}^0 being the relative permittivity along and across the director direction at dc field, respectively. As discussed in Chapter 1, the electric energy density stored in the system E_E could be retrieved in terms of the electric potential U and \mathbf{Q} -tensor elements as^{40,55-58},

$$E_E = -\left(\frac{1}{2}\epsilon_0\bar{\epsilon}\delta_{ij}(\partial_i U)(\partial_j U) + \frac{1}{3}\epsilon_0\Delta\epsilon(\partial_j U)(\partial_k U)\frac{Q_{jk}}{S}\right) \quad (5.13)$$

The total free energy in the whole volume of the LC V was calculated from^{40,57},

$$E = \int_V d^3r (E_{LdG}^P(\mathbf{Q}_{ij}) + E_{LdG}^e(\nabla\mathbf{Q}_{ij}) + E_E). \quad (5.14)$$

By minimizing the total free energy, the Euler-Lagrange equation⁴⁰ was obtained, which yields the director field distributions in the static condition,

$$\frac{L}{2}\nabla^2\mathbf{Q}_{ij} + \epsilon_0\epsilon_{ij}\mathbf{E}_i\mathbf{E}_j = 0 \quad (5.15)$$

where $L/2 = K$ is the effective elastic constant of the LC in the one elastic constant approximation. In this approach, the distribution of Q was numerically calculated using finite elements (COMSOL Multiphysics 5.2a). The data obtained were analyzed in Matlab in a mesh of $x \times y \times z = 124 \times 124 \times 124$ data points.

The boundary conditions for the LC director field alignment at the confining surfaces of ITO and Fe:LN were supposed homeotropic with infinite anchoring energy. Q^b at these boundaries was locally set as:

$$\mathbf{Q}^b = \left(\frac{1}{2}S\right)(-\mathbf{e}_1 \otimes \mathbf{e}_1 - \mathbf{e}_2 \otimes \mathbf{e}_2 + 2\mathbf{e}_3 \otimes \mathbf{e}_3), \quad (5.16)$$

where \mathbf{e}_x , \mathbf{e}_y and \mathbf{e}_z are unit vectors of the Cartesian coordinate system (x, y, z) ⁶¹.

The distribution of the optically-assisted electric field is shown in Figure 5.8. As seen in this figure, the magnitude of the static electric field is higher in the upper region of the sample (near to the ITO-coated glass plate, section I) than in the lower part of the sample (near Fe:LN interface, section II), and had a minimum value in the vicinity of the (virtual) surface S (Figure 5.8) at the center of the LC layer.

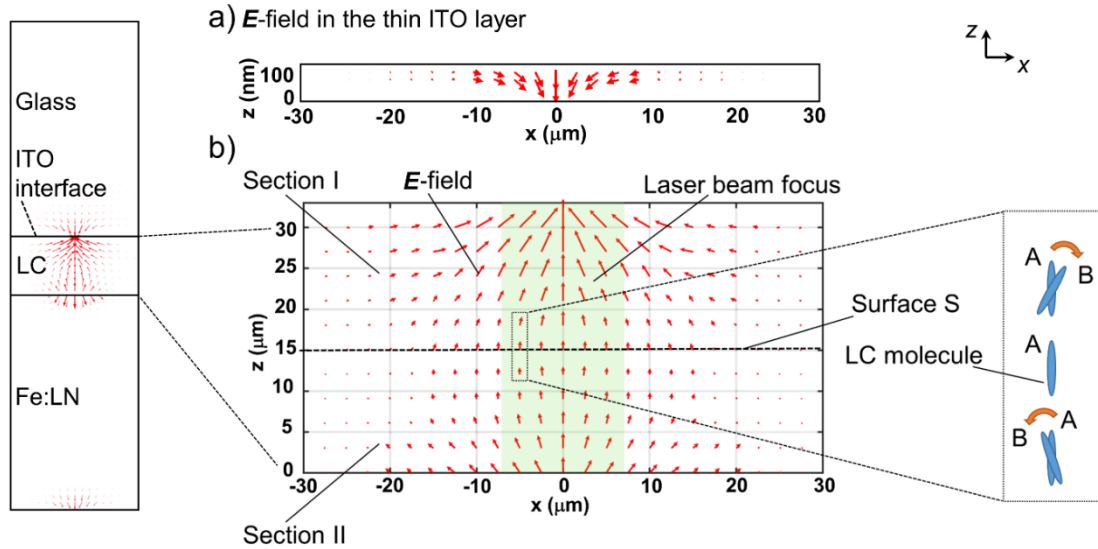


Figure 5.8. Optically-assisted electric field distribution in the xz -plane of the simulated test cell. a) shown in the thin ITO layer. b) The LC filled-area is shown selectively. This area is divided into two sections (section I near the ITO surface, section II near the field generating Fe:LN slab), which are separated by a virtual surface S. A possible tendency to locally realign the director from the initial homeotropic alignment A to a reoriented state B is indicated for each section.

At a photovoltaic voltage ($U > 0$), ITO acts as an active n-type semiconductor in contact with the LC as an insulator medium. The structure of the cell is comparable to a metal-insulator-semiconductor (MIS)⁵⁰ structure. As a result, it can be expected that the charge accumulation happens at the boundary of ITO with the LC. In detail, the mechanism can be explained as near to the ITO/LC interface, the ITO conduction band (E_c) bends downward toward the Fermi level (E_f) as it was kept flat. Since the carrier density in the semiconductor is proportional to $\exp(-(E_c - E_f)/K_B T)$ (where K_B is the Boltzmann constant and T is the temperature), this reduction drives electron accumulation⁵⁰ near the ITO/LC interface. According to the literature⁵¹, the induced charge density can reach an order of magnitude larger than the bulk-free carrier density of the ITO, if biased properly. Since this mechanism can strongly affect the real and imaginary parts of the refractive index of ITO (exploited with a thickness in the

range of some tens to hundreds nanometer), it has found applications in the phase and absorption modulation of surface plasmon polaritons (SPP) in the visible⁵¹ and infrared⁴⁸ (specifically in telecommunication^{52,62}) wavelength ranges. Here, charge accumulation in the ITO layer desirably affects the structure of the electric field in the LC cell, making it suitable for umbilics formation.

The charge carrier density supposed in the accumulation at the ITO/LC interface results in the convergence of the electric field in the LC medium with rotational symmetry, which in fact provides the vital condition for the generation of the fringe director field (shown in Figure 5.7) corresponding with the umbilical realignments. Since ITO has a relatively small relative permittivity in the static electric field⁴⁶⁻⁴⁸, the tangent element of the electric field at the boundary of the ITO with LC is seen (Figure 5.8a). However, as expected, the electric field strength decreases in the ITO thin film as it goes to zero, far away from the charge carrier accumulation⁵² in the glass (Figures 5.2 and 5.8).

In the laser-on state, when the induced voltage exceeds the threshold, the director field is locally realigned from the initial homeotropic alignment (A) to a realigned state (B) parallel (or antiparallel) to the electric field vector in sections I and II. Since the director has no polarity, it is deflected by the electric field in a way to minimize the energy, which means that it always prefers to rotate with the smallest possible angle from its initial to its final alignment. For example, in the left region (Figure 5.8, at $x < 0$) of the LC-filled area, the electric field tends to realign the LC director clockwise (section I, $x < 0$), and counterclockwise in section II. The static condition is maintained, because at every point, the electric torque exerted on the LC director is compensated by the net elastic torque exerted by the neighboring director field. As a result, the director field is realigned in the cell, giving rise to the umbilical configuration corresponding to minimum total free energy of the LC.

The electric field distribution has rotational symmetry in the xy -plane and it is therefore able to induce a continuous radial (Figure 5.9c) realignment of the LC director in this plane. In the area surrounding the exposure spot center, where the photovoltaic field is vertical, the radial alignment is supported by the elastic interactions in the LC imposed by the neighboring director field realignment in the radial direction. As seen in Figure 5.9, the simulated director field has rotational symmetry, as expected. The alignment in the xz -plane (Figure 5.9b) shows all the characteristics of a splay umbilic^{35,36} configuration: as in the model umbilic (Figures 5.6 and 5.7). Homeotropic alignment is preserved at the defect center ($x = 0$). Moreover, the director field has splay deformations, which is seen in Figures 5.9a and b (in the xz -plane). The radial distribution of the LC director is best seen in a top view (Figure 5.9c). In addition to

giving the LC director distribution, the simulation is also capable of explaining the generation of optical vortices in the samples (as discussed in the following section).

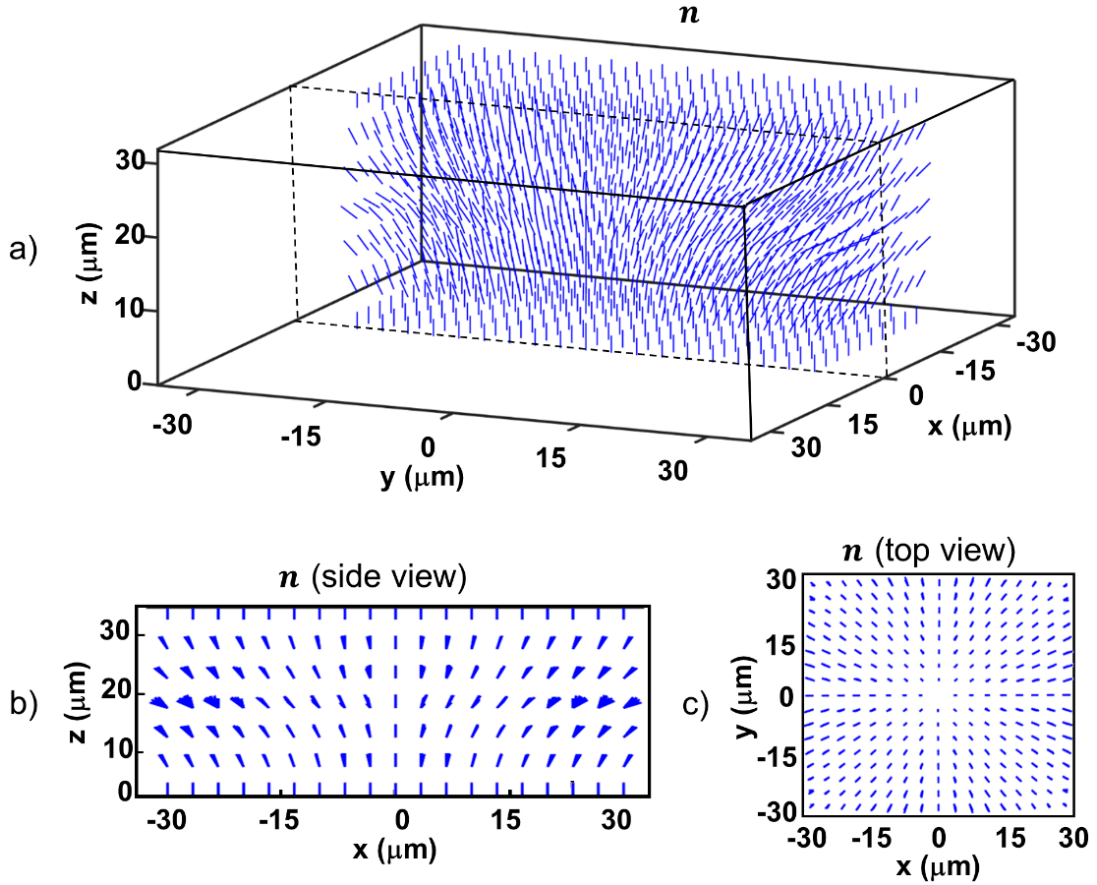


Figure 5.9. Simulated splay umbilic director field, obtained in the one-constant approximation, for a LC test cell with Fe:LN substrate and ITO-coated cover glass, which was filled with MLC-2087. Homeotropic anchoring at the confining surfaces was provided by an anchoring agent, i.e., lecithin. The amplitude of the Gaussian charge density distribution was set to $\sigma_0 = 40 \mu\text{Cm}^{-2}$. a) Simulated director field. For clarity, half the volume of the LC layer is shown to give a clear view of the center of the realigned director field. b) Director pattern in the xz -plane. c) Top view.

5.7. Simulation of the output intensity patterns

The intensity distributions of the optical transmissions between linear and circular polarizers were calculated. The local effective refractive index for probe light passing (propagating in the z -direction) through the LC was obtained from^{37,49,63,64}:

$$n_{\text{eff}}(\vartheta) = \frac{n_o n_e}{\sqrt{n_e^2 \sin^2(\vartheta) + n_o^2 \cos^2(\vartheta)}} \quad (5.17)$$

where $\vartheta(x, y, z)$ is the tilt angle of the director with respect to the z -direction, n_o and n_e are ordinary and extraordinary refractive indices equal to 1.48 and 1.55 for MLC-2087 (simulations, positive dielectric anisotropy) at a wavelength of $\lambda = 589$ nm, respectively. Data was provided from ‘Technical data sheet’ from ‘Merck KGaA’.

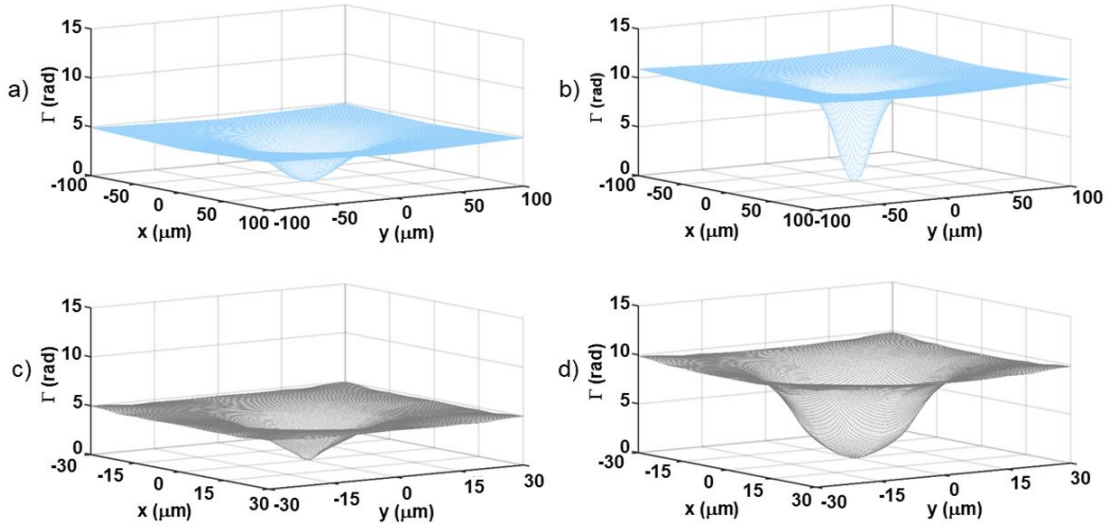


Figure 5.10. Simulated phase change profiles Γ a) and b) in the model umbilical defect at the reduced voltages \tilde{U} equal to 1.1235 and 1.25. c, d) in the umbilics observed in the nematic LC with positive anisotropy corresponding to the induced charge-densities equal to $\sigma_0 = 40 \mu\text{Cm}^{-2}$ and $\sigma_0 = 60 \mu\text{Cm}^{-2}$, respectively.

The total optical phase difference $I(x, y)$ between ordinarily and extraordinarily polarized light was obtained for each point in the xy -plane by calculating the optical phase change accumulated by transmission through the LC layer^{35,37,49,64} as:

$$I(x, y) = \frac{2\pi}{\lambda} \int_0^d (n_{\text{eff}}(\vartheta(x, y)) - n_o) dz, \quad (5.18)$$

where d is the cell gap ($30 \mu\text{m}$). Optical phase changes I were numerically obtained and compared to the corresponding results for umbilic defects (referred to as model umbilics) generated in the LC (MLC-2079³⁵) with negative dielectric anisotropy reported by Brasselet (in Ref 35) in conventional LC cells^{35,36} under static electric fields (at the reduced voltages $\tilde{U} = U/U_t$ equal to 1.12³⁵ and 1.25³⁵, respectively). Numerical studies were performed with the assumption of the same LC film thickness of $30 \mu\text{m}$ and irradiation by a laser beam with the same $\lambda = 589$ nm wavelength. Both models revealed continuous Gaussian-like phase change profiles³⁷ for both types of LCs, where I always has the minimum value of zero at the center of defects (Figure 5.10),

driven by the homeotropic alignment, as it provides an isotropic spot for the light propagation in the LC. Although the size of the defect core in the model umbilic is a function of the applied voltage (as by increasing the voltage it decreases significantly)³⁵, the core radius of the umbilic generated in the LC with positive anisotropy depends only on the FWHM of the incident laser spot.

The polarization modulation properties of the director patterns were studied by Jones calculus. The local Jones matrices $M(x, y)$ ⁵³ were obtained by considering the Jones matrix for an oriented (azimuth angle $\varphi(x, y)$) waveplate inducing an optical phase change $\Gamma(x, y)$, where in general Γ was free to take arbitrary and locally varying values,

$$M(x, y) = \begin{bmatrix} 1 & 0 \\ 0 & 1 \end{bmatrix} \cos\left(\frac{\Gamma}{2}\right) + i \begin{bmatrix} \cos(2\varphi) & \sin(2\varphi) \\ \sin(2\varphi) & -\cos(2\varphi) \end{bmatrix} \sin\left(\frac{\Gamma}{2}\right). \quad (5.19)$$

The Jones electric field vector notation for \mathbf{x} -polarized input light is $\mathbf{E}_{in}(x) = E_0 \begin{bmatrix} 1 \\ 0 \end{bmatrix}$, which describes a linearly polarized plane wave, polarized in the x -direction ($\mathbf{E}_{in}(x) = E_0 e^{-i(\omega t - k_0 z)} \mathbf{x}$), with angular frequency ω and wave vector \mathbf{k}_0 . The Jones vector of the transmitted light can be obtained from $\mathbf{E}_{out}(x, y) = M\mathbf{E}_{in}(x)$,

$$\mathbf{E}_{out}(x, y) = E_0 \cos\left(\frac{\Gamma}{2}\right) \begin{bmatrix} 1 \\ 0 \end{bmatrix} + iE_0 \cos(2\varphi) \sin\left(\frac{\Gamma}{2}\right) \begin{bmatrix} 1 \\ 0 \end{bmatrix} + iE_0 \sin(2\varphi) \sin\left(\frac{\Gamma}{2}\right) \begin{bmatrix} 0 \\ 1 \end{bmatrix}. \quad (5.20)$$

The algebraic relations $\cos(2\varphi) = \frac{1}{2}(e^{i2\varphi} + e^{-i2\varphi})$ and $\sin(2\varphi) = \frac{1}{2i}(e^{i2\varphi} - e^{-i2\varphi})$, where $\varphi = s\phi$, can be applied to recast equation (5.20) as³⁵,

$$\mathbf{E}_{out}(x, y) = E_0 \cos\left(\frac{\Gamma}{2}\right) \begin{bmatrix} 1 \\ 0 \end{bmatrix} + i \left(\frac{E_0}{2}\right) e^{i2s\phi} \sin\left(\frac{\Gamma}{2}\right) \begin{bmatrix} 1 \\ -i \end{bmatrix} + i \left(\frac{E_0}{2}\right) e^{-i2s\phi} \sin\left(\frac{\Gamma}{2}\right) \begin{bmatrix} 1 \\ i \end{bmatrix}, \quad (5.21)$$

where $c_{\mp} = \frac{1}{\sqrt{2}} \begin{bmatrix} 1 \\ \mp i \end{bmatrix}$ is the Jones matrix for circular polarizations ($-$ for the right handed circularly polarized light, $+$ for left handed circularly polarized light). This calculation showed^{34,35,65} that x -polarized input light was partially converted into two contra-circularly polarized helical fields (optical vortices) with the phase factor of $e^{i2s\phi}$ and $e^{-i2s\phi}$ through an equal conversion factor of $\left|\frac{1}{2} \sin\left(\frac{\Gamma}{2}\right)\right|^2$ ³⁵. Since in the case of splay umbilic the topological strength is $s = 1$ ^{35,36}, the phase fronts in each optical vortex had a topological charge of $|l| = 2s = 2$ corresponding to $|l|\hbar$ orbital angular momentum (OAM) per photon⁶, which was also suggested for the optical vortex generation in the

nematic LC with negative dielectric anisotropy in the literature^{34,35,37,65}. In the spin-orbit space $S \otimes L_2$ with quantum orbital number $|l| = 2$, the circularly polarized vortex photons can be expressed as $| -1 \rangle_S \otimes | +2 \rangle_{L_2}$ and $| +1 \rangle_S \otimes | -2 \rangle_{L_2}$, respectively, where $| -1 \rangle_S$ and $| +1 \rangle_S$ stand for the right (spin down)- and left (spin up)-circular polarization bases and $| +2 \rangle_{L_2}$ and $| -2 \rangle_{L_2}$ for the orbital angular momentum bases with the quantum orbital number ± 2 , respectively. As a result, the output beam can be characterized as an entangled state of the two vortex photons as $(| -1 \rangle_S \otimes | +2 \rangle_{L_2} + | +1 \rangle_S \otimes | -2 \rangle_{L_2})/2^{34}$, which appear as annular-shaped beams if no analyzer is used because of the inherent singularity along the propagation axis where the intensity distribution goes to zero, and as optical lobes if a linear polarizer is employed as the analyzer^{34,65}. For the case of circularly polarized input light, a similar analytical approach can be employed^{35,37,49,53,54}: The input circularly polarized beam ($| \mp 1 \rangle_S$) can be converted to a single vortex beam with opposite helicity ($| \pm 1 \rangle_S \otimes | \mp 2 \rangle_{L_2}$)³⁴.

A quick check in the amount of momentum carried by the photons shows that if the input beam was linearly polarized, the output total angular momentum per photon is expected to be zero because of the axisymmetry of the system (“ $q = 1$ ” case). For the case of a circularly polarized input beam, a conversion of the spin angular momentum (SAM) to the orbital angular momentum (OAM) happens while the net exchanged momentum is zero^{49,54}. Therefore, when a photon passes through such a q-plate, regardless of the polarization, the total angular momentum is conserved, which indicates zero torque on the matter defect and maintenance of the defect stabilization.

The output intensity patterns between crossed and parallel polarizers (referred to as π_{\perp} and π_{\parallel} , respectively) were obtained from Equation (5.20) as:

$$I_{out}^{\pi_{\perp}}/I_0 = \sin^2(2\phi) \sin^2\left(\frac{\Gamma(x)}{2}\right), \quad (5.22)$$

$$I_{out}^{\pi_{\parallel}}/I_0 = \cos^2\left(\frac{\Gamma(x)}{2}\right) + \cos^2(2\phi) \sin^2\left(\frac{\Gamma(x)}{2}\right), \quad (5.23)$$

where I_0 corresponds to the input intensity. Considering energy conservation, the relation $I_{out}^{\pi_{\perp}} + I_{out}^{\pi_{\parallel}} = I_0$ is always maintained, as expected.

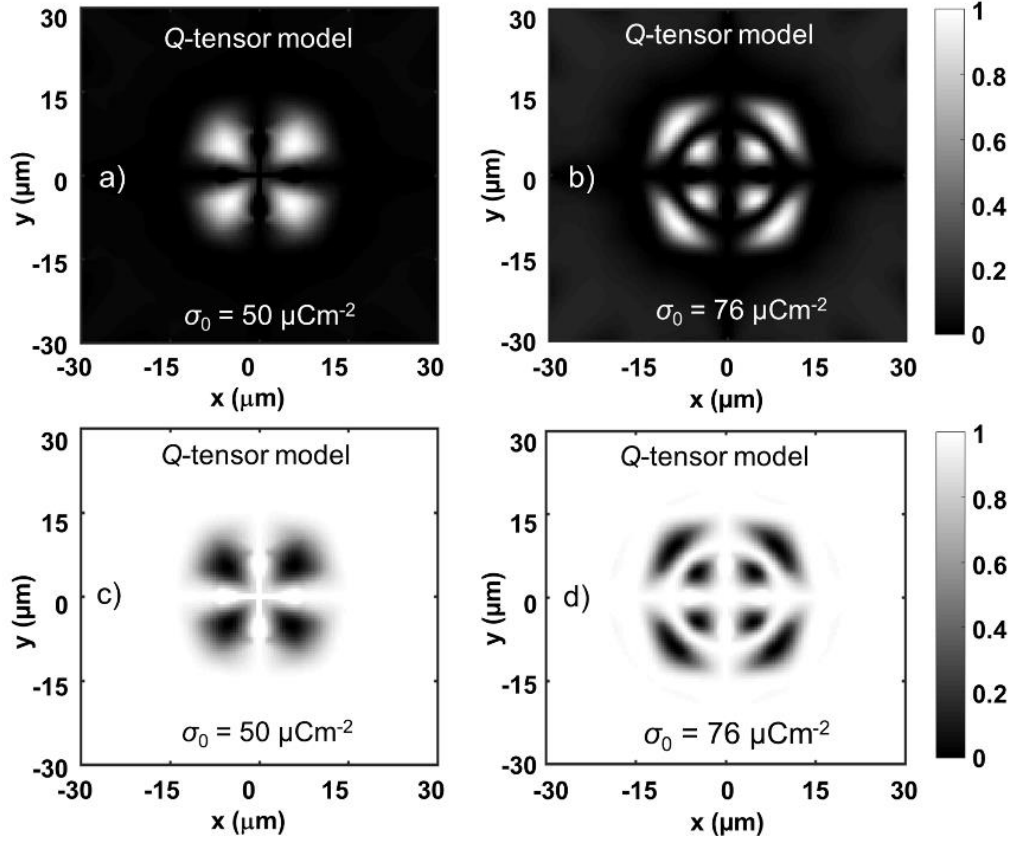


Figure 5.11. Simulated output intensities (at $\lambda = 589$ nm) between a, b) cross- c, d) parallel linear polarizers for the umbilics generated in the LC (MLC-2087) at a, c) $\sigma_0 = 50 \mu\text{Cm}^{-2}$, and b, d) $\sigma_0 = 76 \mu\text{Cm}^{-2}$, respectively.

The output intensity distributions numerically calculated for the umbilic defect (Figure 5.9) are shown in Figure 5.11. Patterns of four and eight optical lobes are seen between linear polarizers at $\sigma_0 = 50 \mu\text{Cm}^{-2}$ and $\sigma_0 = 76 \mu\text{Cm}^{-2}$, respectively. The intensity distributions calculated for crossed linear polarizers are shown in Figure 5.11a for $\sigma_0 = 50 \mu\text{Cm}^{-2}$ and in Figure 5.11b for $\sigma_0 = 76 \mu\text{Cm}^{-2}$, respectively. The patterns obtained for parallel linear polarizers are shown in Figures 5.11c and d. The patterns of OVs are well defined and clearly distinguishable, which are frequently seen^{35,65} and reported for umbilics³⁵: the first and second quadruple of OVs (numbered relative to the center of defect) are made from four identical elongated and flattened patterns, respectively, as seen in Figures 5.11a, c and Figures 5.11b, d, respectively.

The annulus-shaped intensity distributions for the umbilic director reorientations were obtained for completeness: between crossed circular polarizers, the output intensity was calculated by³⁵:

$$I_{out}^{\sigma_{\perp}}/I_0 = \sin^2\left(\frac{I}{2}\right), \quad (5.24)$$

where σ_{\perp} indicates crossed circular polarizers. The calculated output patterns are shown in Figure 5.12. Here, the LC film acts as a spin-orbit coupler (q-plate), which creates a phase singularity along the propagation axis of incident nonsingular light beams, which appeared as the central dark spot.

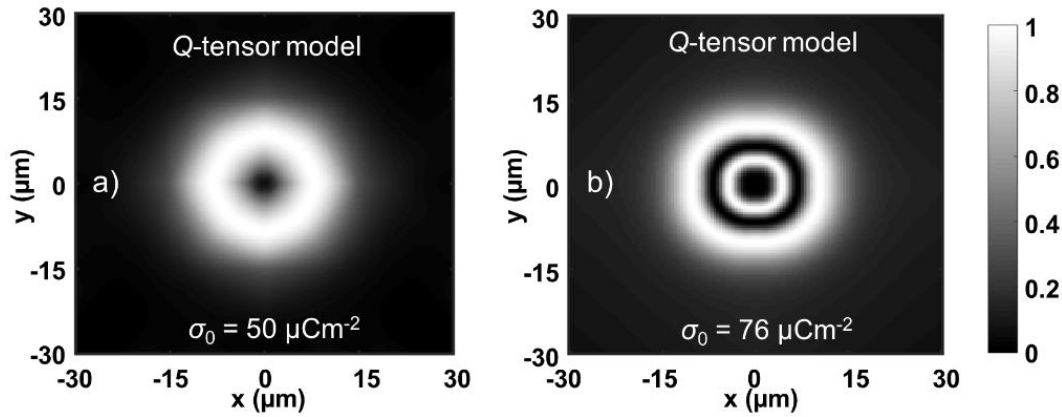


Figure 5.12. Transmitted intensity profiles (at $\lambda = 589$ nm) between crossed circular polarizers simulated for the umbilics induced in the LC (MLC-2087) corresponding to a) $\sigma_0 = 50 \mu\text{Cm}^{-2}$ and b) $\sigma_0 = 76 \mu\text{Cm}^{-2}$, respectively.

In the recent work by Calisto and co-workers⁶⁶, the theoretical studies indicate the possibility of generation of optical vortices in a LC media with positive elastic anisotropy ($\delta > 0$), defined as $\delta = (K_1 - K_2)/(K_1 + K_2)$. In another work⁶⁷, it was shown that in the liquid crystal light valves (LCLVs), competition between the forcing of the external electric field-induced by the inhomogeneous light profile and the elastic anisotropy can result in the swirling of the vortex arms. Here, although the numerical modeling was made with the assumption of one elastic constant approximation, the model can well describe the structure of umbilics. The induced electric field is of the order of 10 kV/m, which prevails a phase jump angle in the core of the vortex as the observed structure with no bending and quite stretched in the radial direction in the core region, and characteristic straight lines between linear polarizers are expected (Figure 5.11).

5.8. Conclusions

Optically assisted electrical formations of the umbilical defects in the LC with positive dielectric anisotropy are reported. The generation of umbilics was observed in the hybridized LC cells made from a plane-parallel z-cut Fe:LN substrate and an ITO-coated covering glass. The photovoltaic field induced in the Fe:LN substrate upon light irradiation has a distribution in the LC-filled region, as suitable for the formation of the umbilical defects. The intensity profiles in the nematic LC with positive dielectric anisotropy were obtained from simulations based on the Q -tensor method. The local exposure to a tightly focused Gaussian laser beam can lead to the generation of umbilics with four- and eight-lobes textures (depending on the induced charge densities in the Fe:LN) between linear polarizers. Investigating the output intensity profiles suggests that the shape of lobes well resembles those seen in a splay umbilic. Annulus-shaped intensity profiles were obtained by investigating the light transmission between crossed circular polarizers, typically characterizing the output intensity patterns of OVs.

Simulations revealed that the proper electric field (photovoltaic field) distribution in the LC film enhanced by the SPR effect was responsible for the creation of umbilics. Comparison of the director field profiles (in three-dimensions (3D) and in the transverse plane), as well as the phase change profiles with the corresponding profiles associated with the model umbilics (observed in the nematic LC with negative anisotropy) confirm the accuracy of the prediction.

The generation of OVs induced by the umbilics was first discovered in the discussed theoretical studies and simulations⁶⁸. The theory predictions were checked experimentally for a test cell (with the same geometry as discussed) filled with the nematic LC of MLC-2087, and the high efficiency formation of umbilics inducing OVs were verified.

This finding can lead to new efficient techniques based on the OVs generation in the self-engineered and controllable LC cells with tremendous applications. Thanks to the locally confined topological defects, the generation of an array of OVs from a single LC cell is promising. Since the size of the defect core is determined from the full width at half maximum (FWHM) of the laser beam, it enables the generation of OVs with desired structures.

References

¹ Boyd, R. W., & Padgett, M. J. (2016). Quantum Mechanical Properties of Light Fields Carrying Orbital Angular Momentum. In *Optics in Our Time* (pp. 435-454). Springer, Cham.

² Bekshaev, A. Y., Vasnetsov, M. V., & Soskin, M. S. (2006). Description of the morphology of optical vortices using the orbital angular momentum and its components. *Optics and spectroscopy*, 100(6), 910-915.

³ Pismen, L. M., & Pismen, L. M. (1999). *Vortices in nonlinear fields: from liquid crystals to superfluids, from non-equilibrium patterns to cosmic strings* (Vol. 100). Oxford University Press.

⁴ Bezryadina, A., Neshev, D. N., Desyatnikov, A. S., Young, J., Chen, Z., & Kivshar, Y. S. (2006). Observation of topological transformations of optical vortices in two-dimensional photonic lattices. *Optics express*, 14(18), 8317-8327.

⁵ Maleev, I. D., & Swartzlander, G. A. (2003). Composite optical vortices. *JOSA B*, 20(6), 1169-1176.

⁶ Yao, A. M., & Padgett, M. J. (2011). Orbital angular momentum: origins, behavior and applications. *Advances in Optics and Photonics*, 3(2), 161-204.

⁷ Allen, L., Beijersbergen, M. W., Spreeuw, R. J. C., & Woerdman, J. P. (1992). Orbital angular momentum of light and the transformation of Laguerre-Gaussian laser modes. *Physical review A*, 45(11), 8185.

⁸ Nye, J. F. (1999). *Natural focusing and fine structure of light: caustics and wave dislocations*. CRC Press.

⁹ Kivshar, Y. S., & Luther-Davies, B. (1998). Dark optical solitons: physics and applications. *Physics reports*, 298(2-3), 81-197.

¹⁰ Desyatnikov, A. S., Torner, L., & Kivshar, Y. S. (2005). Optical vortices and vortex solitons. *arXiv preprint nlin/0501026*.

¹¹ Foo, G., Palacios, D. M., & Swartzlander, G. A. (2005). Optical vortex coronagraph. *Optics letters*, 30(24), 3308-3310.

¹² Swartzlander, G. A. (2001). Peering into darkness with a vortex spatial filter. *Optics Letters*, 26(8), 497-499.

¹³ Mair, A., Vaziri, A., Weihs, G., & Zeilinger, A. (2001). Entanglement of the orbital angular momentum states of photons. *Nature*, 412(6844), 313-316.

¹⁴ Wang, J., Yang, J. Y., Fazal, I. M., Ahmed, N., Yan, Y., Huang, H., ... & Willner, A. E. (2012). Terabit free-space data transmission employing orbital angular momentum multiplexing. *Nature photonics*, 6(7), 488.

¹⁵ Gibson, G., Courtial, J., Padgett, M. J., Vasnetsov, M., Pas'ko, V., Barnett, S. M., & Franke-Arnold, S. (2004). Free-space information transfer using light beams carrying orbital angular momentum. *Optics express*, 12(22), 5448-5456.

-
- ¹⁶ Grier, D. G. (2003). A revolution in optical manipulation. *nature*, 424(6950), 810-816.
- ¹⁷ Fazal, F. M., & Block, S. M. (2011). Optical tweezers study life under tension. *Nature photonics*, 5(6), 318-321.
- ¹⁸ Jeffries, G. D., Edgar, J. S., Zhao, Y., Shelby, J. P., Fong, C., & Chiu, D. T. (2007). Using polarization-shaped optical vortex traps for single-cell nanosurgery. *Nano letters*, 7(2), 415-420.
- ¹⁹ Farahani, J. N., Schibler, M. J., & Bentolila, L. A. (2010). Stimulated emission depletion (STED) microscopy: from theory to practice. *Microscopy: science, technology, applications and education*, 2(4), 1539-1547.
- ²⁰ Wang, S., Zhang, S. L., Li, P., Hao, M. H., Yang, H. M., Xie, J., ... & Zhou, S. H. (2018). Generation of wavelength-and OAM-tunable vortex beam at low threshold. *Optics express*, 26(14), 18164-18170.
- ²¹ Turnbull, G. A., Robertson, D. A., Smith, G. M., Allen, L., & Padgett, M. J. (1996). The generation of free-space Laguerre-Gaussian modes at millimetre-wave frequencies by use of a spiral phaseplate. *Optics communications*, 127(4-6), 183-188.
- ²² Oemrawsingh, S. S. R., Van Houwelingen, J. A. W., Eliel, E. R., Woerdman, J. P., Verstegen, E. J. K., & Kloosterboer, J. G. (2004). Production and characterization of spiral phase plates for optical wavelengths. *Applied optics*, 43(3), 688-694.
- ²³ Sueda, K., Miyaji, G., Miyanaga, N., & Nakatsuka, M. (2004). Laguerre-Gaussian beam generated with a multilevel spiral phase plate for high intensity laser pulses. *Optics express*, 12(15), 3548-3553.
- ²⁴ Tyson, R. K., Scipioni, M., & Viegas, J. (2008). Generation of an optical vortex with a segmented deformable mirror. *Applied optics*, 47(33), 6300-6306.
- ²⁵ BAZHENOV, V., Vasnetsov, M. V., & Soskin, M. S. (1990). Laser beams with wave front screw dislocations (Lazernye puchki s vintovymi dislokatsiiami volnovogo fronta). *Pis'ma v Zhurnal Eksperimental'noi i Teoreticheskoi Fiziki*, 52, 1037-1039.
- ²⁶ Bazhenov, V. Y., Soskin, M. S., & Vasnetsov, M. V. (1992). Screw dislocations in light wavefronts. *Journal of Modern Optics*, 39(5), 985-990.
- ²⁷ Heckenberg, N. R., McDuff, R., Smith, C. P., Rubinsztein-Dunlop, H., & Wegener, M. J. (1992). Laser beams with phase singularities. *Optical and Quantum Electronics*, 24(9), S951-S962.
- ²⁸ Heckenberg, N. R., McDuff, R., Smith, C. P., & White, A. G. (1992). Generation of optical phase singularities by computer-generated holograms. *Optics letters*, 17(3), 221-223.
- ²⁹ Matsumoto, N., Ando, T., Inoue, T., Ohtake, Y., Fukuchi, N., & Hara, T. (2008). Generation of high-quality higher-order Laguerre-Gaussian beams using liquid-crystal-on-silicon spatial light modulators. *JOSA A*, 25(7), 1642-1651.
- ³⁰ Aleksanyan, A., & Brasselet, E. (2016). Vortex coronagraphy from self-engineered liquid crystal spin-orbit masks. *Optics letters*, 41(22), 5234-5237.

³¹ Soskin, M. S., & Vasnetsov, M. V. (2001). Singular optics. *Progress in optics*, 42(4), 219-276.

³² Marrucci, L., Manzo, C., & Paparo, D. (2006). Optical spin-to-orbital angular momentum conversion in inhomogeneous anisotropic media. *Physical review letters*, 96(16), 163905.

³³ Brasselet, E., Murazawa, N., Misawa, H., & Juodkazis, S. (2009). Optical vortices from liquid crystal droplets. *Physical review letters*, 103(10), 103903.

³⁴ Brasselet, E., & Loussert, C. (2011). Electrically controlled topological defects in liquid crystals as tunable spin-orbit encoders for photons. *Optics letters*, 36(5), 719-721.

³⁵ Brasselet, E. (2012). Tunable optical vortex arrays from a single nematic topological defect. *Physical review letters*, 108(8), 087801.

³⁶ Rapini, A. (1973). Umbilics: static properties and shear-induced displacements. *Journal de Physique*, 34(7), 629-633.

³⁷ Barboza, R., Bortolozzo, U., Clerc, M. G., Residori, S., & Vidal-Henriquez, E. (2015). Optical vortex induction via light-matter interaction in liquid-crystal media. *Advances in Optics and Photonics*, 7(3), 635-683.

³⁸ Habibpourmoghadam, A., Jiao, L., Omairat, F., Evans, D. R., Lucchetti, L., Reshetnyak, V., & Lorenz, A. (2017, August). Confined photovoltaic fields in a photo-responsive liquid crystal test cell. In *Liquid Crystals XXI* (Vol. 10361, p. 1036112). International Society for Optics and Photonics.

³⁹ Kravets, N., Podoliak, N., Kaczmarek, M., & Brasselet, E. (2019). Self-induced liquid crystal q-plate by photoelectric interface activation. *Applied Physics Letters*, 114(6), 061101.

⁴⁰ Habibpourmoghadam, A., Jiao, L., Reshetnyak, V., Evans, D. R., & Lorenz, A. (2017). Optical manipulation and defect creation in a liquid crystal on a photoresponsive surface. *Physical Review E*, 96(2), 022701.

⁴¹ Lucchetti, L., Kushnir, K., Zaltron, A., & Simoni, F. (2016). Light controlled phase shifter for optofluidics. *Optics letters*, 41(2), 333-335.

⁴² Habibpourmoghadam, A., Lucchetti, L., Evans, D. R., Reshetnyak, V. Y., Omairat, F., Schafforz, S. L., & Lorenz, A. (2017). Laser-induced erasable patterns in a N* liquid crystal on an iron doped lithium niobate surface. *Optics express*, 25(21), 26148-26159.

⁴³ Barboza, R., Bortolozzo, U., Assanto, G., Vidal-Henriquez, E., Clerc, M. G., & Residori, S. (2012). Vortex induction via anisotropy stabilized light-matter interaction. *Physical review letters*, 109(14), 143901.

⁴⁴ Brasselet, E. (2009). Singular optical manipulation of birefringent elastic media using nonsingular beams. *Optics letters*, 34(20), 3229-3231.

⁴⁵ Brasselet, E. (2010). Singular optical reordering of liquid crystals using Gaussian beams. *Journal of Optics*, 12(12), 124005.

-
- ⁴⁶ Hamberg, I., & Granqvist, C. G. (1986). Evaporated Sn-doped In₂O₃ films: Basic optical properties and applications to energy-efficient windows. *Journal of Applied Physics*, 60(11), R123-R160.
- ⁴⁷ Gao, Q., Li, E., & Wang, A. X. (2018). Comparative analysis of transparent conductive oxide electro-absorption modulators. *Optical Materials Express*, 8(9), 2850-2862.
- ⁴⁸ Yi, F., Shim, E., Zhu, A. Y., Zhu, H., Reed, J. C., & Cubukcu, E. (2013). Voltage tuning of plasmonic absorbers by indium tin oxide. *Applied Physics Letters*, 102(22), 221102.
- ⁴⁹ Barboza, R., Bortolozzo, U., Assanto, G., & Residori, S. (2013). Optical vortex generation in nematic liquid crystal light valves. *Molecular Crystals and Liquid Crystals*, 572(1), 24-30.
- ⁵⁰ Sze, S. M., & Ng, K. K. (2006). *Physics of semiconductor devices*. John Wiley & sons., 197-200.
- ⁵¹ Feigenbaum, E., Diest, K., & Atwater, H. A. (2010). Unity-order index change in transparent conducting oxides at visible frequencies. *Nano letters*, 10(6), 2111-2116.
- ⁵² Melikyan, A., Lindenmann, N., Walheim, S., Leufke, P. M., Ulrich, S., Ye, J., ... & Freude, W. (2011). Surface plasmon polariton absorption modulator. *Optics express*, 19(9), 8855-8869.
- ⁵³ Marrucci, L. (2008). Generation of helical modes of light by spin-to-orbital angular momentum conversion in inhomogeneous liquid crystals. *Molecular Crystals and Liquid Crystals*, 488(1), 148-162.
- ⁵⁴ Barboza, R., Bortolozzo, U., Assanto, G., Vidal-Henriquez, E., Clerc, M. G., & Residori, S. (2013). Harnessing optical vortex lattices in nematic liquid crystals. *Physical review letters*, 111(9), 093902.
- ⁵⁵ Lee, G. D., Bos, P. J., Ahn, S. H., & Kim, K. H. (2003). Fast Q-tensor method for modeling the dynamics of defects in a liquid crystal director field. *Physical Review E*, 67(4), 041715.
- ⁵⁶ James, R., Willman, E., Fernandez-Fernandez, F. A., & Day, S. E. (2006). Finite-element modeling of liquid-crystal hydrodynamics with a variable degree of order. *IEEE Transactions on Electron Devices*, 53(7), 1575-1582.
- ⁵⁷ Tovkach, O. M., Conklin, C., Calderer, M. C., Golovaty, D., Lavrentovich, O. D., Vinals, J., & Walkington, N. J. (2017). Q-tensor model for electrokinetics in nematic liquid crystals. *Physical Review Fluids*, 2(5), 053302.
- ⁵⁸ Anderson, J. E., Watson, P., & Bos, P. J. (2001). Comparisons of the vector method and tensor method for simulating liquid crystal devices. *Liquid Crystals*, 28(1), 109-115.
- ⁵⁹ Kralj, S., Virga, E. G., & Žumer, S. (1999). Biaxial torus around nematic point defects. *Physical Review E*, 60(2), 1858.
- ⁶⁰ Mottram, N. J., & Newton, C. J. (2014). Introduction to Q-tensor theory. *arXiv preprint arXiv:1409.3542* [Cond-Mat. Soft].

⁶¹ Kralj, S., & Majumdar, A. (2014). Order reconstruction patterns in nematic liquid crystal wells. *Proceedings of the Royal Society A: Mathematical, Physical and Engineering Sciences*, 470(2169), 20140276.

⁶² Sorger, V. J., Lanzillotti-Kimura, N. D., Ma, R. M., & Zhang, X. (2012). Ultra-compact silicon nanophotonic modulator with broadband response. *Nanophotonics*, 1(1), 17-22.

⁶³ Pavlin, J., Vaupotič, N., & Čepič, M. (2013). Direction dependence of the extraordinary refraction index in uniaxial nematic liquid crystals. *European Journal of Physics*, 34(2), 331.

⁶⁴ Pereira, A. C., & Rosato, A. (1975). Transmission of nematic liquid crystals in electric fields. *Revista Brasileira de Fisica*, 5(2), 237-241.

⁶⁵ Basselet, E. (2018). Tunable high-resolution macroscopic self-engineered geometric phase optical elements. *Physical review letters*, 121(3), 033901.

⁶⁶ Calisto, E., Clerc, M. G., Kowalczyk, M., & Smyrnelis, P. (2019). On the origin of the optical vortex lattices in a nematic liquid crystal light valve. *Optics letters*, 44(12), 2947-2950.

⁶⁷ Barboza, R., Bortolozzo, U., Clerc, M. G., Residori, S., & Vidal-Henriquez, E. (2014). Light-matter interaction induces a single positive vortex with swirling arms. *Philosophical Transactions of the Royal Society A: Mathematical, Physical and Engineering Sciences*, 372(2027), 20140019.

⁶⁸ Habibpormoghadam, A. (2019). Theoretical Prediction of Umbilics Creation in Nematic Liquid Crystals with Positive Dielectric Anisotropy. *ACS omega*, 4 (25), 21459-21468.

Chapter 6: Topological Defect Creation in NLC Cells with Photoresponsive Substrates

6.1. Introduction

Topological defects appear as a consequence of broken continuous symmetry in a system¹. They arise in many different fields of physics, such as cosmological models², crystalline solids³, superconductors^{4,5}, and liquid crystals^{6,7}. They can be generated as a response to the applied electric or magnetic field, as well as a quench in order to reorganize the system from a disordered into an ordered phase⁸. In addition, defects can be suitably created in a system by means of geometrical and proper boundary conditions⁸.

Since 2016, the topological defects in the nematic LCs were treated as point-like objects, Vromans and Giomi showed that disclinations can possess orientational and polar properties, which can strongly affect the dynamic of the system^{9,10,11}.

In this chapter, the generation of disclinations as a result of the LC interaction with the photovoltaic field together with geometrical impacts is studied in static conditions as observed under microscope between linear polarizers.

Hybridized nematic LC test cells assembled with photosensitive ferroelectric, iron-doped LiNbO₃ (Fe:LN) substrates were studied. In these samples, the Fe:LN surface in contact with LC was rubbed unidirectionally to provide parallel anchoring of the LC, while an application or treatment of the other confining surface was optional. The test cells were filled with MLC-2087, a nematic LC with positive dielectric anisotropy ($\Delta\epsilon = \epsilon_{||} - \epsilon_{\perp} = 13.31$) and a desirably low birefringence of $\Delta n = 0.076$,

which was ideal to study birefringent stripes and light induced defect textures in various kinds of samples. Open and covered film samples are investigated in this chapter. In the former, the LC film was confined either with a non-coated glass plate or an indium tin oxide (ITO) coated glass plate. When the samples were exposed to a tightly focused laser beam ($\approx 14 \mu\text{m}$ FWHM), local modulations of the effective refractive index were observed at the exposure spot, and as a result, the formation of reconfigurable defects^{12,13}.

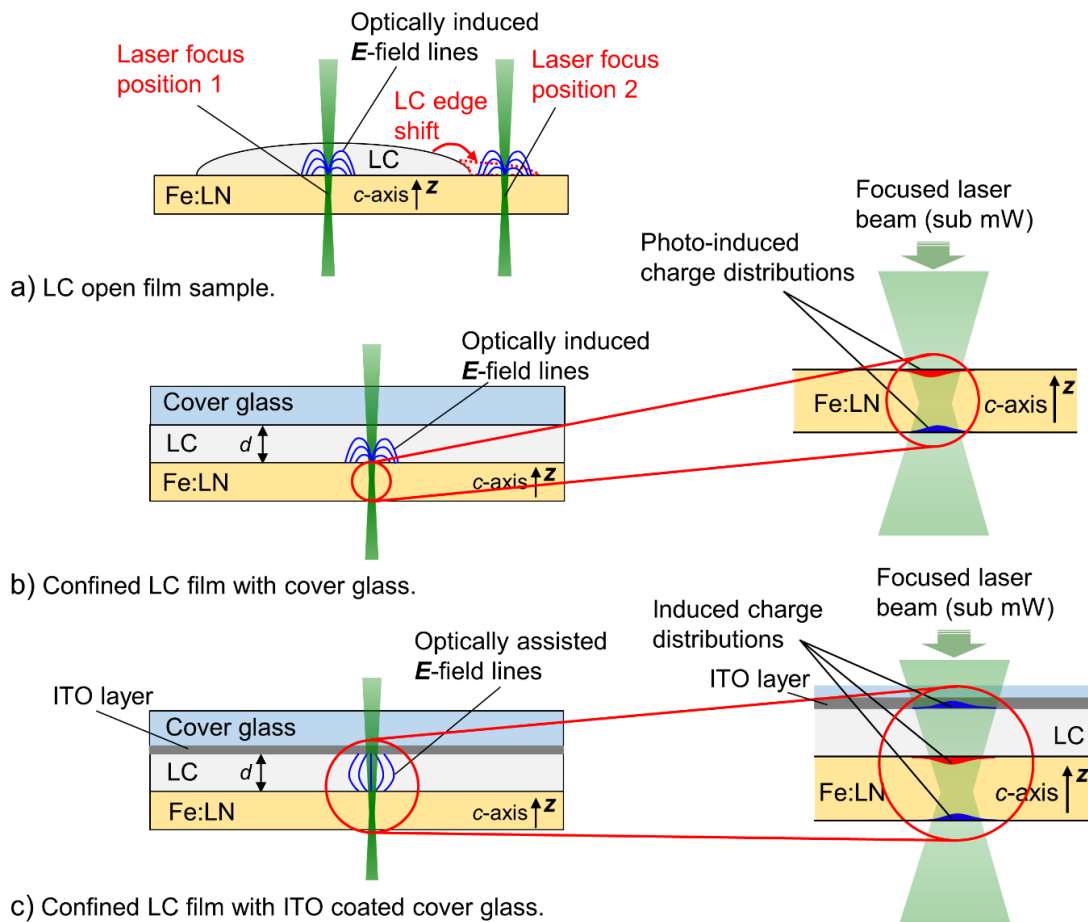


Figure 6.1. Schematic of LC cells where unidirectionally rubbed Fe:LN layer was used as substrate. a) An open LC film sample exposed to a focused laser beam near the film center (focus position 1) and the film edge (focus position 2). b) A confined LC cell with two film spacers and a cover glass, and c) when cover glass was coated with ITO.

In an open film sample or covered with a non-coated glass slip, the formation of disclinations as non-singular (: seen only as a distorted, without any discontinuity in the director field) and singular point defects, respectively, line and wall defects (in short, 'walls') was observed. The central defect created at the exposure spot center

was always located at the Fe:LN/LC interface which caused the creation of characteristic Maltese cross patterns in the imaging plane. In the case of formation of two point defects, they were located at the upper and lower boundaries of the LC film interconnected by a wall. In addition, the generation of inversion walls separating reverse tilt domains was seen¹².

In LC cells confined with ITO coated glass plates¹³, non-singular defects (umbilical defects) with topological charge of +1 constructed from (deformed because of the imposed anchoring condition at the Fe:LN interface) ring patterns were revealed at the center of the laser exposure spot. The topological defects had a thickness of a few microns, which could be expanded in dimensions by increasing the exposure intensity ($\approx 56 \mu\text{m}$ at 0.71 mW, and $\approx 100 \mu\text{m}$ at powers > 1.1 mW, for the case of non-treated ITO-covered cell).

LC realignments were induced in the samples by means of a bulk photovoltaic field E_{pV} generated in Fe:LN, and additionally assisted by the field stemming from the charge carrier accumulation in the thin ITO layer if the cover glass was coated with ITO. The electric field had a strong distribution in the LC film. The formation of field-induced topological defects as hyperbolic (in an open LC sample) and radial (in a confined LC sample with ITO coated cover glass) were modeled in numerical simulations. The LC director field $\mathbf{n}(x, y, z)$ was numerically studied using the Q -tensor method (explained in Chapter 1) dealing with the coupling of the director field with the induced electric field. The applied simulation approaches were highly useful to understand and reproduce the behavior of the studied LC cells.

6.2. Nematic disclinations in two-dimensions (2D)

A Schlieren texture^{14,15}- due to the birefringence, and typically observable in a thin planar LC cell without any rubbing treatment - is characterized by formation of disclinations (defined as a discontinuity in the director field¹⁶) as singular point defects (also, called point disclinations or hedgehogs in the case of nematic) and disclination lines (in some applications called disclinations in short) as a result of broken symmetry, as well as inversion walls (Figure 6.2¹⁷). Point defects appear as hedgehogs and boojums¹⁴ (generating only at the boundary of the medium) in the nematic phase. In the Schlieren texture, dark brushes appear between crossed polarizers in the regions where the director field aligns in the direction of either polarizer or analyzer. Dark brushes meet in the point defects - where a discontinuity in the director field is seen -

in a group of two or four lines (Figure 6.2). In walls, the director field has a continuous reorientation between two symmetric equivalent configurations¹⁶.

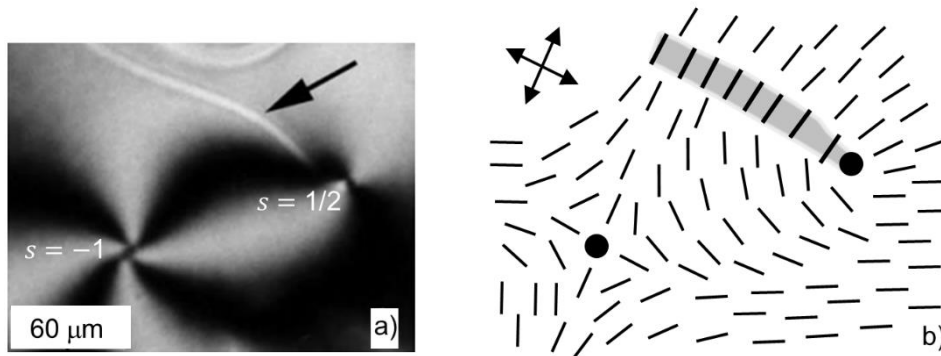


Figure 6.2. (a) Schlieren texture of a thin nematic LC film between crossed linear polarizers, and (b) diagram of the associated director field¹⁷. Point disclinations (with strengths of $s = -1, 1/2$) are seen at the centers of the dark brushes between crossed polarizers. A polar horizontal wall is indicated by a black arrow. The LC film has a thickness of about $1 \mu\text{m}$. {The image was taken from Ref. 17}.

The director \mathbf{n} has a continuous reorientation around a defect which costs elastic energy. If a defect had a planar structure in the xy -plane, the director \mathbf{n} can be described as $\mathbf{n} = (\cos(\varphi), \sin(\varphi), 0)$, where φ is the angle between the director \mathbf{n} and x -axis^{8,10}. The point defects are characterized by their topological charge q or topological strength s ¹⁸. The topological strength s can be obtained by assuming an arbitrary contour enclosing the defect, as⁸:

$$\oint d\theta = 2\pi s. \quad (6.1)$$

In uniaxial nematics, the lowest energy defect configurations correspond to the topological strength of $s = \pm 1/2$ ⁸. The topological strength s can be determined from the number of dark brushes (seen in-between linear polarizers) that cut an imaginary circle surrounding the point defect as $|s| = \text{number of brushes}/4$ ¹⁹. The sign of s depends on the behavior of the brushes between rotating linear polarizers. The plus sign is assigned if the brushes rotate in the same direction as the linear polarizers do, and minus is employed, if the rotation of dark brushes is in opposite direction. This approach of determining s is valid only if the rate of director rotation keeps a fixed sign. Examples of schematic diagrams of the director field distribution around defects with different strengths s are shown in Figure 6.3²⁰.

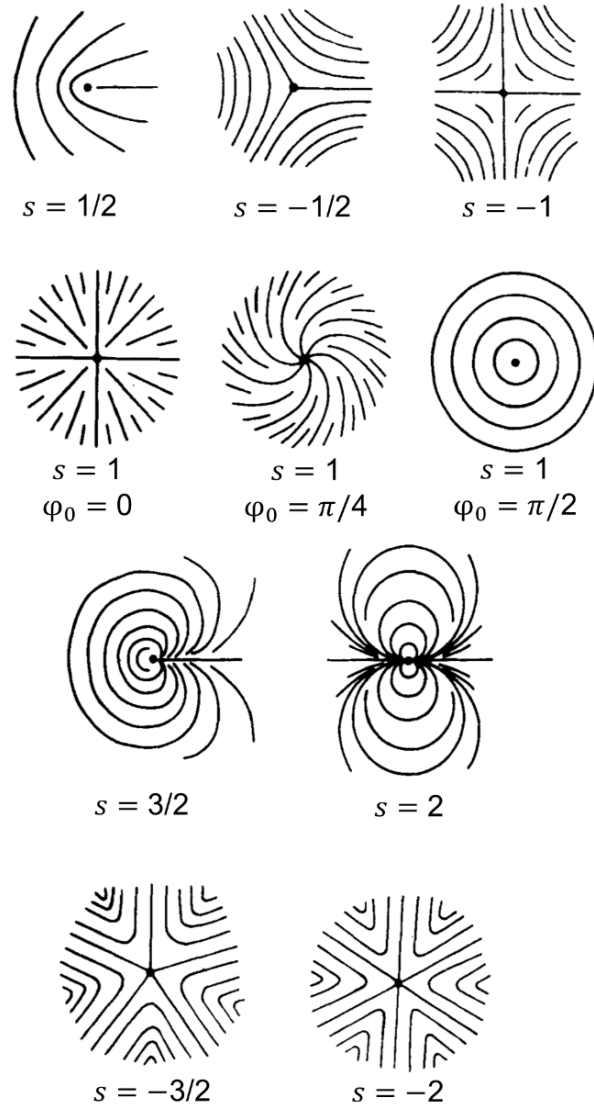


Figure 6.3. Director profiles of different disclinations with topological strength s are shown in the transverse xy -plane²⁰. {This image was taken from Ref. 20}.

In the one constant approximation for the Frank elastic constants ($K = K_{11} = K_{22} = K_{33}$), the elastic energy is^{9,10},

$$F = \frac{K}{2} \int d^2r |\nabla\varphi|^2, \quad (6.2)$$

minimizing F near a topological defect leads to a solution^{8,10,20} $\varphi = s\phi + \varphi_0$, where s gives the topological strength of defect, and $\phi = \tan^{-1}(y/x)$ is the azimuthal angle made by the radius vector connecting the center of the defect to a given point, and φ_0 is a constant value specifying the defect structure. Since φ is multiple valued at the

center of defect, there is a singularity there. The energy of the defect was described as^{8,14,20}:

$$W = \pi K s^2 \log \frac{R}{a} + W_c \quad (6.3)$$

where R is the size of the system, a is the core radius, and W_c is the core energy owing to the isotropic alignment.

6.3. Experimental procedures

Different types of hybrid samples were investigated (schematically shown in Figure 6.1) as the open LC film (Figure 6.1a) and the covered LC cells (Figures 6.1b, c) where the LC film was confined with film spacers and a specific cover plate. In all confined cells, the LC film had a thickness of 30 μm . The Fe:LN slabs (Fe doping concentration of 0.05 mol %, optical quality polished surfaces, obtained from Deltronic Crystal Industries) were used in all samples as substrates. The Fe:LN slabs had dimensions of $25 \times 25 \times 1 \text{ mm}^3$ along x -, y -, and z -axis, respectively. They were z -cut as their crystallographic c -axis was normal to the xy -plane. The surface of the Fe:LN slab in contact with the LC was rubbed unidirectionally with Kimwipes 80 times to provide parallel anchoring of the LC at the substrate interface with the LC corresponding with planar alignment^{12,13}.

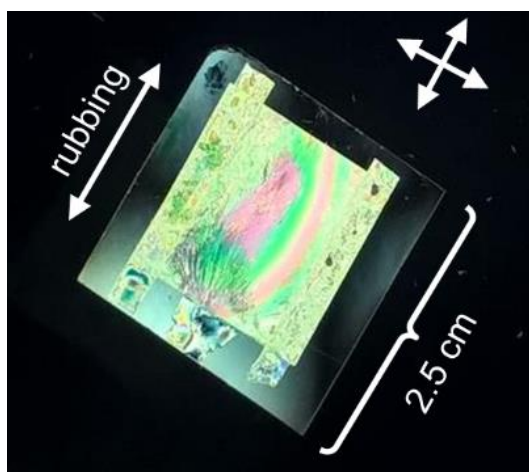


Figure 6.4*. Photograph of a covered film sample with a plain microscopy cover slip at laser off state between crossed linear polarizers. Rubbing directions predefining the LC alignments at the confining surfaces are the same as shown by a single double arrow. {The image was taken from Ref. 12 (see Declarations and Acknowledgments)}.

In an open film sample (Figure 6.1a), a small droplet of LC (about 0.5 μl , and with 0.5–1 mm diameter,) was spread out upon the rubbed Fe:LN substrate with a spatula¹². At the boundary of the LC with the air, the director took homeotropic alignment²¹. In confined film samples, the LC was confined between film spacers (Mylar film) on a rubbed Fe:LN substrate either with an unidirectionally rubbed (in the same direction as substrate) plain microscopy cover slip made from glass, or an ITO coated cover glass. In the confined film samples with plain cover glass¹², the LC had a uniform alignment at laser-off state in whole volume (Figure 6.4).

In confined film samples with ITO equipped-glass plates¹³, two different types of cover plates, coated with polyimide and uniaxially rubbed to provide planar alignment (obtained from commercial (EHC) LC test cells) and non-coated with polyimide were investigated.

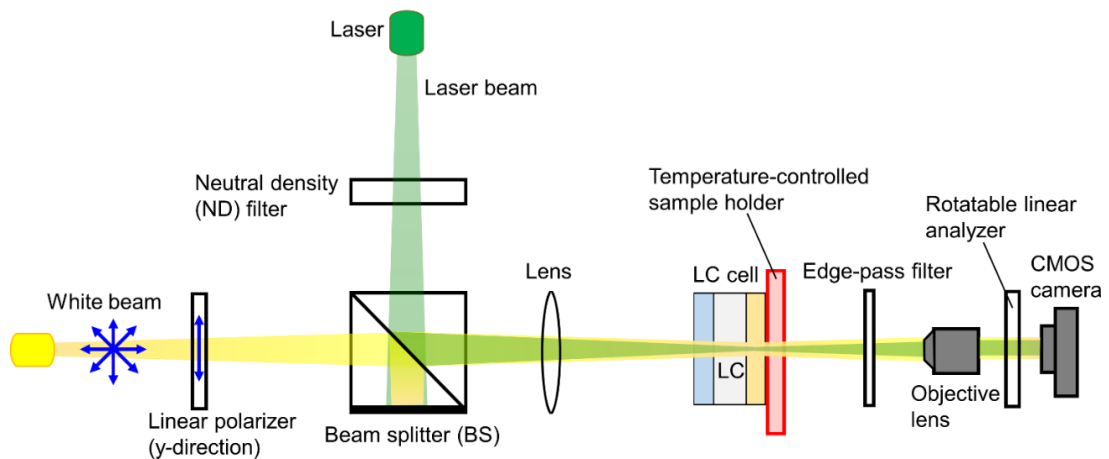


Figure 6.5. Schematic of the experimental setup. Samples were exposed to a focused green diode laser and investigated between a fixed linear polarizer and a rotatable linear analyzer.

Optical responses of the test cell upon radiation by a diode laser (Thorlabs CPS 532: 532 nm wavelength, circular beam profile, 14.3 and 42.5 μm full width at half maximum, 4.5 mW) were studied in a microscopic imaging setup (Figure 6.5) with micron resolution. The experimental setup was supplied with crossed linear polarizers and an inverted polarizing optical microscope (Olympus PMG3). A beam profiler (Spiricon SP620U) was assembled in the image plane of the microscope where a 20 \times objective lens was used in order to investigate the beam profile of the focused beam. A Gaussian intensity distribution with a full width at half maximum of 14.3 μm and full width of 42.5 μm was measured. A CMOS color camera (The Imaging Source, DFK MKU120-10x22, supplied with a 10 x zoom objective lens) was employed to record

images. LC test cells were studied at temperatures between room temperature and 45 °C. The experimental and imaging setup is explained in more detail in Ref. 12.

6.4. Electric fields in the studied LC cells

The Fe:LN was employed as the source of the electric field to induce optical and electrical responses in hybridized LC samples by using low energy cw laser light. As discussed in Chapter 3, the bulk photovoltaic effect is responsible for the electric field generation in optically responsive ferroelectric materials such as Fe:LN. The bulk photovoltaic effect can cause generation of photovoltaic fields: Upon exposure to a laser beam, charge carriers separation happens along the polar crystallographic *c*-axis of Fe:LN, which results in large photovoltaic fields E_{PV} (of the order of 100 kV/cm^{22,23,24}). The presence of the E_{PV} above the ferroelectric substrate surfaces was utilized as the source of the electric field in the thin layer of LC placed on top of the substrate, which induced reorientation of the LC director and defects creations. The electric field was assisted by the charge carrier accumulation in the thin layer of the ITO when the cover slab was coated with ITO (the mechanism was explained in Chapter 4). In all types of samples, the LC relaxes back to its initial alignment when the laser shutter is closed, because of the disappearance of the electric field. Obviously, one would expect no optical responses in blank test cells, where the Fe:LN substrate is absent.

Simulated electric field distributions in test cells filled with a medium with an isotropic dielectric constant of 7.93¹³ (corresponding to the average dielectric constant measured in the LC) are shown for comparison in Figure 6.6, where the LC cells were covered with plain and ITO coated glass plates, respectively. When the LC samples were exposed to a Gaussian laser beam, charge carrier separation in the z-cut Fe:LN substrate stemmed from the bulk photovoltaic effect. Simply, as discussed before this behavior was modeled (via COSOL Multiphysics 5.2a) by considering Gaussian charge carriers distribution densities with opposite signs and of the form $\sigma = \sigma_0 \exp(-(x^2 + y^2)/w^2)$ at the upper and lower surfaces of the Fe:LN substrates. In the sample where the LC is in contact with the thin ITO electrode (Figure 6.6b), a charge density was additionally accumulated in the ITO film, which resulted in convergence of the electric field near the ITO surface since ITO film acts semiconducting in the visible light and low voltage operating regime. The present electric fields in both LC films have highly non-uniform distributions throughout the samples with fringe profiles, as shown in Figure 6.6. The magnitude of the electric field was always high at the center of

illumination and had a bell-shape distribution near interfaces of the LC with confining walls, if a charge density was attributed to the corresponding interfaces.

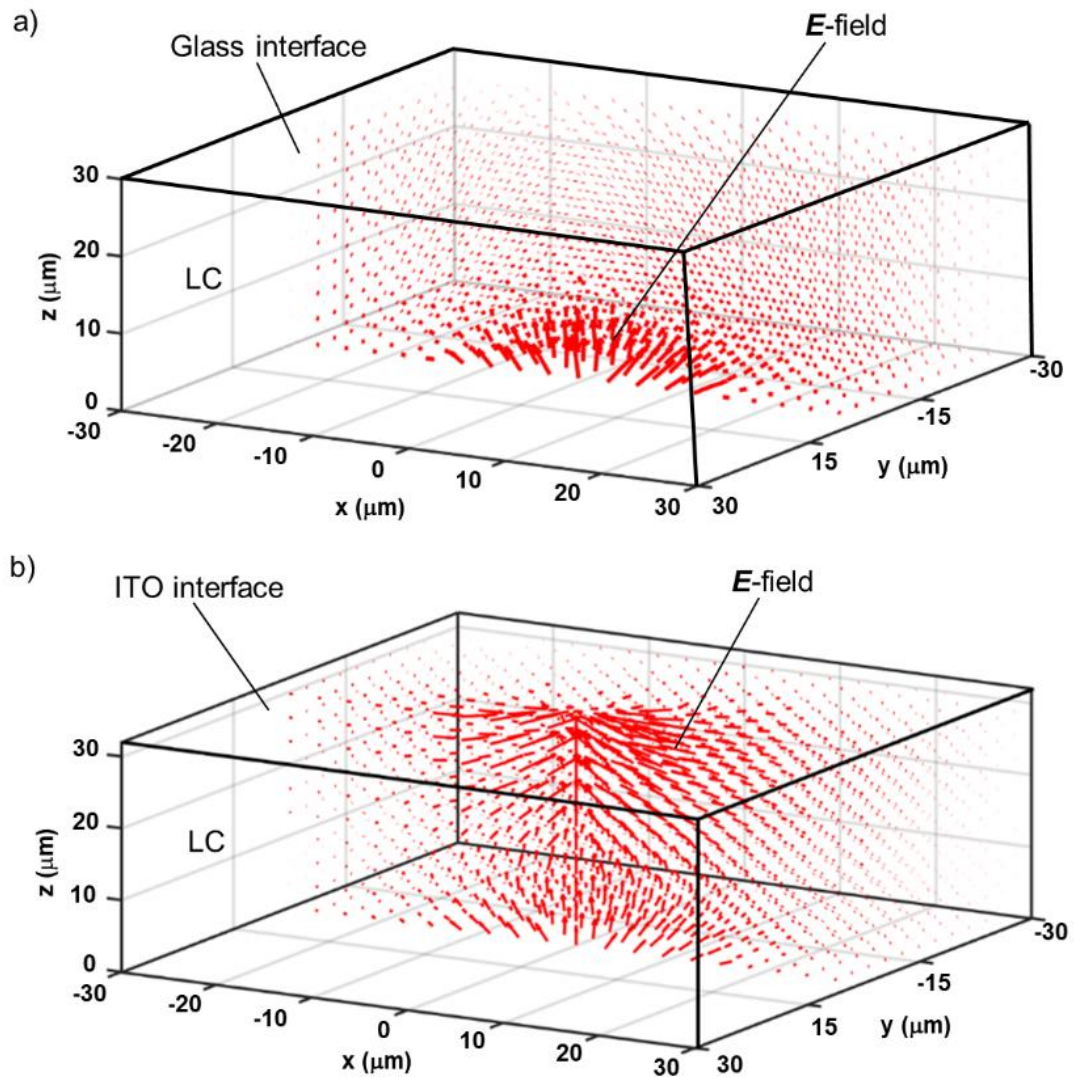


Figure 6.6. Simulated electric-field distributions inside hybridized LC test cells where charge densities (with opposite sign) with amplitude of $|\sigma_0| = 40 \mu\text{C}/\text{m}^2$ were induced at the Fe:LN planar surfaces when, (a) a plain glass was used to cover the LC, (b) the LC was covered with an ITO coated glass plate which changes the E -field distribution because of the charge carriers accumulated at the LC/ITO interface. The E -field is shown in half of the volumes to give a clear view of the center area in magnification.

If the glass plate was equipped with the thin ITO layer, homeotropic alignment was found around the center between crossed linear polarizers where the alignment of the LC was almost homogenous¹³, at laser off state. In this investigation, various test cells appeared dark around the beam center where the homeotropic alignment was considerably dominant. Deviation from homeotropic alignment resulted in brighter

colors near the cell edges.

As explained in the following, defect formations with two- and four-fold symmetries were seen in the LC cells without ITO coated cover¹². In contrast, defect-free reorientations with radial symmetry were found in the samples with ITO-coated cover glass¹³. The electric field distribution determines the reorientation of the LC director field \mathbf{n} from its initial alignment. Since a nematic LC with positive dielectric anisotropy was studied, the director field \mathbf{n} tends to realign parallel to the photo-generated electric fields. Therefore, the simulated E -field distributions can already be very helpful to understand the director realignment observed in the experiments.

6.5. Defect formation in LC samples without ITO application

A photovoltaic (PV) electric field was generated in the photoresponsive substrate exposed to a tightly focused cw laser beam with micron resolution and at low powers. The PV electric field can induce localized responses within the LC layer (without any need of an external electric field supply) such as formation of the topological charge defects (i.e., single defects, connected defects), which can be displaced by scanning the laser beam across the LC in an open film sample causing expansion of the LC surface¹². The field-induced optical responses were investigated with polarized probe light and application of microscopic imaging techniques.

6.5.1. Defects formation in open LC samples

Open film samples¹² were exposed to a focused laser beam at two different positions; near the film center (focus position 1) and near the film edges (focus position 2) between crossed linear polarizers, as schematically shown in Figure 6.1a. The LC film is shown in the initial state (in the Figure 6.7a), where a colorful texture of relatively broad red and green stripes was observed because of the LC film thickness (of a few dozens of micrometers at the center) variations in an open film sample without any confinement; this is pronounced near the film edges (Figures 6.7e).

Laser beams with optical power greater than approximately 0.20 μW can induce LC realignment from its initial alignment which resulted in defect formations¹² (as point and line defects), as seen in Figure 6.7b. Close-up views of the image shown in Figure 6.7b are shown in Figures 6.7c, d as colorful and desaturated (gray-scale), respectively. In the desaturated image, concentric rings forming the pattern are

highlighted in red, where the number of rings depends on both the film thickness h and the birefringence of the LC. Point defects or topological charges with Maltese cross textures were created as a result of locally induced director field realignment which causes a spatially distribution of the optical phase retardation. The sign of topological charges induced in the LC film was investigated with application of a pair of rotatable polarizers. It was revealed that Maltese cross pattern always rotates in opposite direction of polarizers rotation direction while it keeps its fourfold symmetry and right angles between adjacent brushes¹². As a result, a strength of -1 was attributed to this defect being characteristics for a hyperbolic defect¹². An image sequence of investigations is shown in Figures 6.7a-c¹². The field-induced defect was theoretically studied and discussed in the following section.

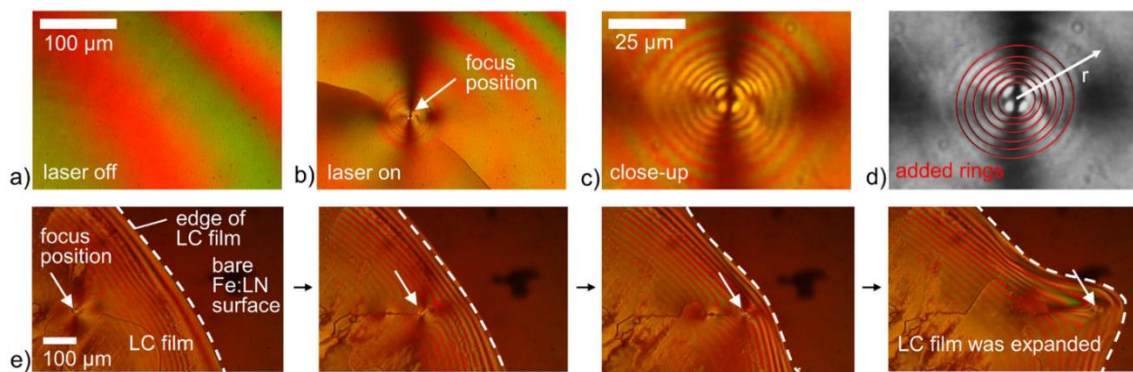


Figure 6.7*. Photographs of the open film samples upon laser beam exposure between crossed linear polarizers. a) LC cell in the initial state. b) Induced topological defect coupled with a line defect formed perpendicular to the rubbing direction imposing the anchoring. c) Close-up image of the topological defect, and d) shown as desaturated (gray-scale). e) Evolution of the LC edge under scanning the laser focus position (within a few seconds). {The image was taken from Ref. 12}.

Walls were also induced in the LC open film samples. In the case of the formation of the second point defect (with slightly deformed structure and of -1 strength) located near to the open surface of the LC, it was connected by a wall to the first point defect pinned to the laser focus position at the Fe:LN surface referred to as central defect (Figures 6.8a-c¹²).

Walls can be generated because of the surface treatment, because of flow^{25,26,27}, and by the interaction of LC with a nonhomogeneous electric field^{28,29}. They usually end in surface generated defects²⁷ and are pinned by point defects. The simultaneous formation of two walls was also observed¹² (Figure 6.8d), where the first wall is pinned to the center of the central defect connected to the surface-near defect,

while the second wall extends from this defect to the edge of the central defect. In addition, four dark brushes were seen as two of them were extended from the central defect toward the surface-near defect (Figure 6.8d).

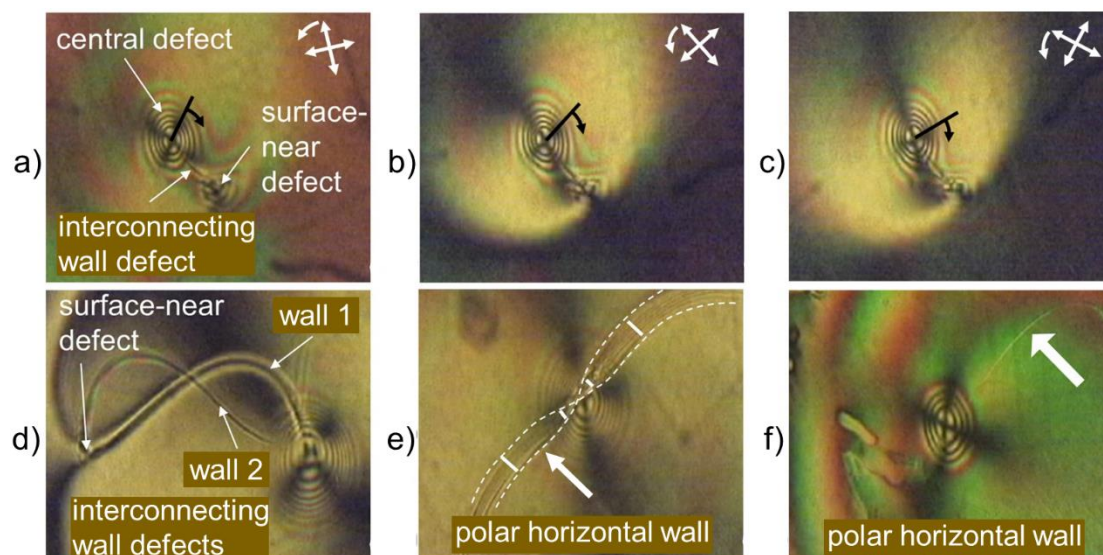


Figure 6.8*. Images of the defects created in the open film samples between crossed linear polarizers. (a)–(c) The central defect was figured out by rotating the crossed polarizers counterclockwise, which caused rotation of the corresponding Maltese cross pattern clockwise. A black line along one of the dark brushes was used as guide to the eye. (d)–(f) Additional defect structures detected in the sample. The planar anchoring at the LC/Fe:LN interface was provided by unidirectional rubbing of the interface. {The image was taken from Ref. 12}.

A formation of inversion walls (also known as reverse-tilt-domain (RTD) walls) can be induced by the fringe fields (electric or magnetic) above a threshold in planar cells treated for uniform azimuthal orientation, where the director field slowly changes its inclination azimuthally by a large angle, often by π , across the wall. The director field can be described by the same polar angle θ in both regions adjacent to the wall but different azimuthal angles as φ and $\varphi + \pi$, accordingly²⁷. Walls were seen as “polar vertical” in Figures 6.8a-d, and “polar horizontal” in Figures 6.8e, f, respectively. The polar vertical walls (interconnecting wall) in Figures 6.8a-d appear as a single dark stripe (between crossed linear polarizers)²⁷. The polar horizontal defect in Figure 6.8e is broader in width and possesses a birefringent striped texture when compared with Figure 6.8f. Approximately midway through the wall, the director has a planar orientation through a polar horizontal wall (if appearing as a single stripe), while it has a vertical alignment along a polar vertical wall²⁷ (appearing as a single dark stripe).

Furthermore, a polar horizontal defect is topologically stable while the stability of a polar vertical defect depends on the anchoring.

In addition, the formation of defects was studied by scanning the laser beam stepwise across an open film sample towards the film edge¹² (Figure 6.7e). It is seen that the LC film or droplets can be moved and expanded beyond the edges. As seen in Figure 6.7e, scanning the laser beam results in the expansion of the induced defect along the scanning direction near to the LC edges (Figure 6.1a) in a time interval of 1 s between the formation of a new defect and the annihilation of the advanced defect caused by the electric field decay in the advanced position. In fact, the temporarily generated empty gap of LC (between the former and new defects) caused that the dielectric force pushes the LC towards the new defect location because of the higher dielectric energy (the LC possessing higher electric relative permittivity than air).

6.5.2. Theoretical investigations and simulation of an induced topological defect localized at the laser beam spot

The formation of field-induced defects was simulated (COMSOL MULTIPHYSICS 5.2a, post-processed in MATLAB). These simulations were challenging because a three-dimensional model was required. A hybrid aligned sample, which resembled the open film samples, turned out to be a very good approximation to numerically study the properties of the induced defect. A three-dimensional (3D) model with a footprint of $x \times y = 60 \times 60 \mu\text{m}^2$ was simulated with three layers (Fe:LN, LC, and air). The substrate layer was a 90 μm -thick Fe:LN layer with dielectric constants of $\epsilon_{\perp} = 85$ and $\epsilon_{\parallel} = 29$ with respect to the crystallographic c -axis. The c -axis was parallel to the z -direction. The Fe:LN layer was covered with a layer of LC with a thickness of $h = 30 \mu\text{m}$, where the LC was supposed in contact with a 90 μm -thick layer of air ($\epsilon = 1$). A schematic of the three-layered model is shown in Figure 6.9a. The formation of the point defects was studied in the LC cell based on the \mathbf{Q} -tensor approach^{30,31,32,33} explained in detail in Chapter 1. Local \mathbf{Q} -tensor data Q_{ij} in the LC cell were numerically modeled corresponding to director field configuration in 3D. LC alignment was visualized by converting the local \mathbf{Q} -tensor data Q_{ij} into the corresponding LC director $\mathbf{n}(x, y, z)$ by means of Equation (1.16). The local \mathbf{Q} -tensor data Q_{ij} were obtained from numerically solving the **Euler-Lagrange** equation (5.15) by predefining appropriate boundary conditions on the LC alignment (anchoring conditions) at the Fe:LN- and air-LC interfaces, as well as the boundary conditions for

induced electric field.

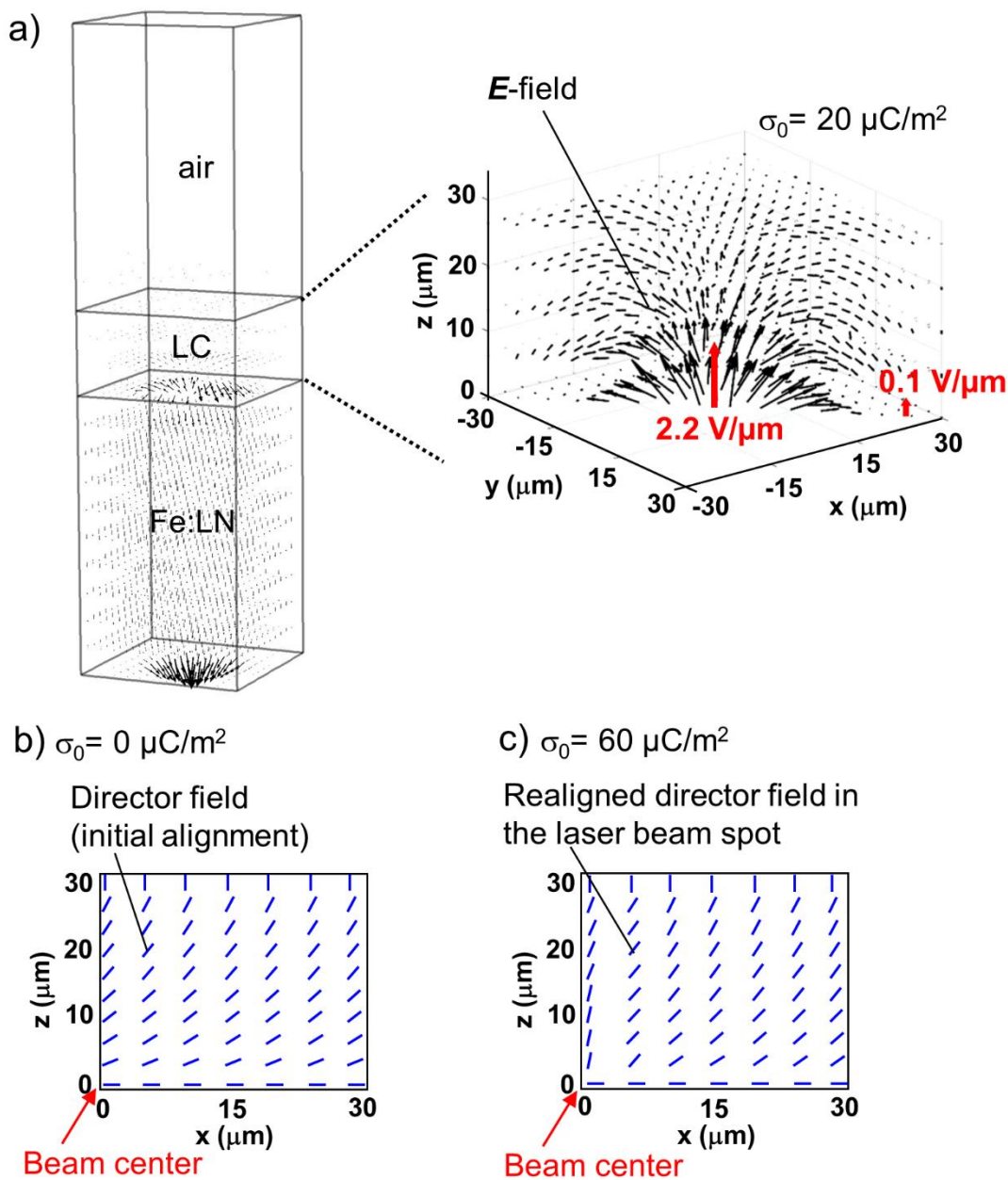


Figure 6.9. a) The electric field distribution shown in the simulated three-dimensional (3D) geometry. Director fields are shown in the half xz -plane at the cross-section of the LC cell; b) Director field orientation in the initial (laser-off) state corresponding to the planar anchoring conditions at the Fe:LN surface (parallel to the x -direction) and homeotropic at the LC-air boundary. d) Director field reorientation in the induced electric field above threshold. The electric field is shown in one half of the cell for clarity.

In order to investigate the electric field-induced realignment of the LC, a light-induced charge carrier separation along the crystallographic c -axis of the Fe:LN

substrate was assumed²³. The laser beam had a Gaussian intensity profile, and therefore a centrosymmetric Gaussian distribution of charge densities σ with opposite signs were assumed ($\sigma = \sigma_0 e^{-(x^2+y^2)/w^2}$) at both the upper and lower surfaces of the Fe:LN layer. A width of $w = 10 \mu\text{m}$, and values of $\sigma_0 = 20, 60 \mu\text{C}/\text{m}^2$ were found to yield strong enough fringe fields within the LC layer being capable to realign LC from its initial alignment. These Gaussian distributions were centered within the respective surfaces. The obtained electric field distribution inside the LC layer is shown (in magnification in Figure 6.9a in half of the LC cell). The electric field obtained was highly divergent (fringe fields) and had a magnitude of $\approx 2.2 \text{ V}/\mu\text{m}$ at the center of the charge density distribution and decayed to $\approx 0.1 \text{ V}/\mu\text{m}$ in the area nearby the center.

At the air-LC interface, homeotropic LC alignment was imposed²¹. At the Fe:LN-LC interface, two different alignment conditions were studied. This approach was useful to see if the model was capable to result in LC realignments corresponding with the induced birefringent patterns. First, uniform alignment parallel to the x -direction (rubbing direction) was simulated. The director field of the LC is shown in its initial state (no photo-induced electric fields) (Figure 6.9b) and with field present (Figure 6.9c). It is clearly seen that the director field was realigned by the fringe electric fields, which was decaying and divergent along the z -direction. The strictly uniform anchoring at the Fe:LN surface (parallel to the x -direction) resulted in a director field pattern with twofold symmetry (as seen in the confined LC cells with two confining walls). Since in open film samples, a defect texture with fourfold symmetry and a negative topological charge was experimentally observed, the surface anchoring at the Fe:LN surface was varied to resemble a hyperbolic defect pattern in the second simulation approach (Figure 6.10). A negative topological charge of strength -1 , as identified in the experiments¹², was modeled. It has the structure of a hyperbolic pattern (Figures 6.10a, b). Consequently, the hyperbolic director realignment was assumed in approximation as the boundary condition at the back-surface (the LC/Fe:LN interface) of the LC cell. This was in agreement with the experimental observation of a field-induced hyperbolic defect. This approximation turned out to yield a promising model of the experimentally observed defect texture. As expected, the output optical pattern with fourfold symmetry between linear polarizers was obtained (Figure 6.10c).

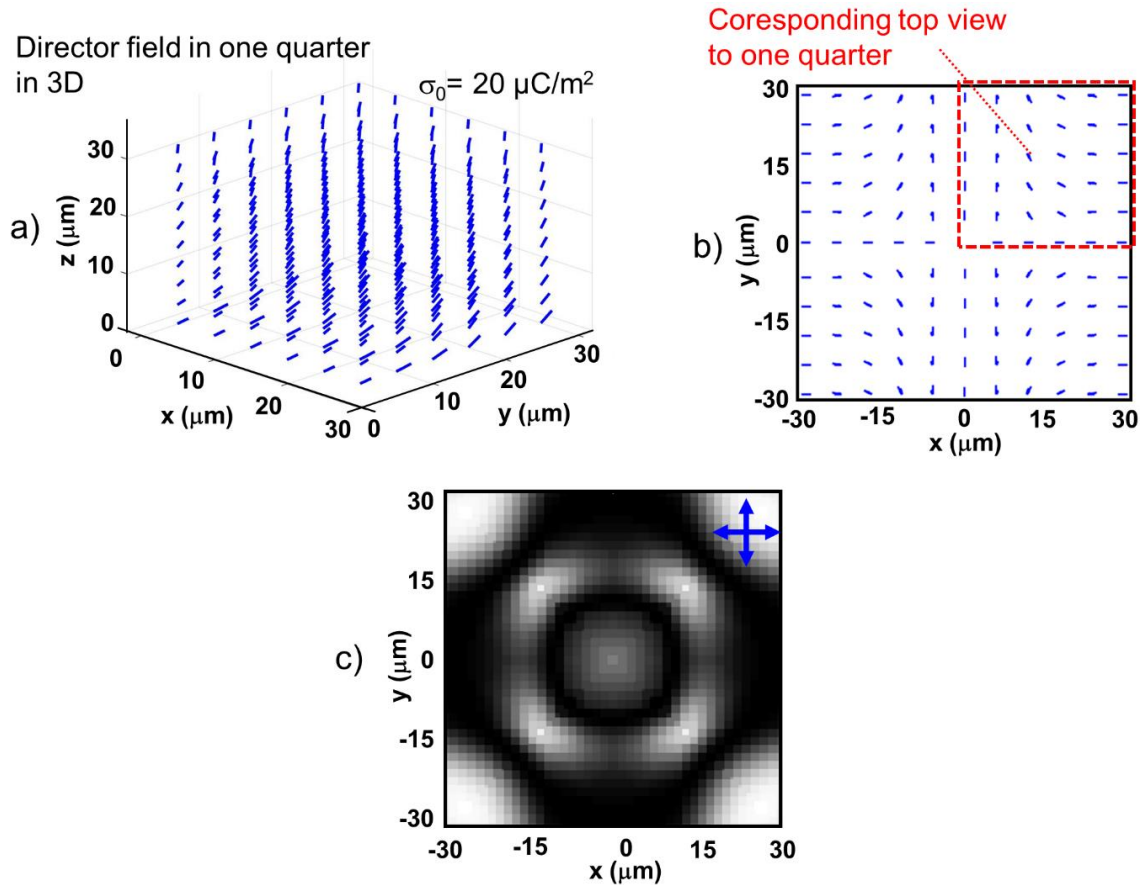


Figure 6.10. Demonstration of the hyperbolic defect induced at the Fe:LN-LC interface and pinned at the laser exposure spot. a) The associated director field realignment in three-dimensions (3D) shown in one quarter, and b) in transverse xy -plane corresponding with the top view of the whole cell. c) Simulated birefringent pattern corresponding with transmission of the monochromatic light (589 nm) between crossed polarizers.

The simulated director field¹² in one quadrant of the exposure area is shown in three-dimensions (3D) in Figure 6.10b, which provides a view of the defect center and the local director reorientation at a charge carrier density of $\sigma_0 = 20 \mu\text{C}/\text{m}^2$. In addition, the modulation of the transmittance of monochromatic polarized light (589 nm in wavelength, crossed polarizers) was numerically obtained from relation (5.22) using the Jones method explained in Chapter 5³⁴. The obtained pattern associated with the full area of simulation (Figure 6.10c) had fourfold symmetry and resembled the experimentally observed pattern: In addition to four dark brushes, ring patterns were seen. Since the output intensity is proportional to $\sin^2\left(\frac{\Gamma(x)}{2}\right)$, the bright and dark rings can be associated with a phase change Γ (measured at the center of each ring) equal to $(2i - 1)\pi$ and $2i\pi$ where i is a positive integer, respectively, which correspond to a

birefringence equal to $\Delta n = (2i - 1)(\lambda/2h)$ and $\Delta n = (2i)(\lambda/2h)$ at the center of bright and dark rings, respectively. Several neighboring rings are caused by a continuous variation of the optical retardation, which is low at the center of the pattern and increases continually with increasing radius. For nonpolarized light, this resembles a continuous variation of the optical path length as in a lens.

6.5.3. Defect formation in confined LC samples

In a confined LC cell with film spacers or additionally a plain cover slip, point defects and walls were induced simultaneously at optical powers above threshold (Figures¹² 6.11 and 6.12, respectively). Induced point defects were seen as well-separated birefringent ring patterns, where two walls were pinned to the central defect with tendency to form perpendicular to the rubbing direction (provided by unidirectionally rubbing treatment of the Fe:LN surface in contact with the LC film, as explained earlier, which determines the initial homogeneous LC alignment at laser off state).

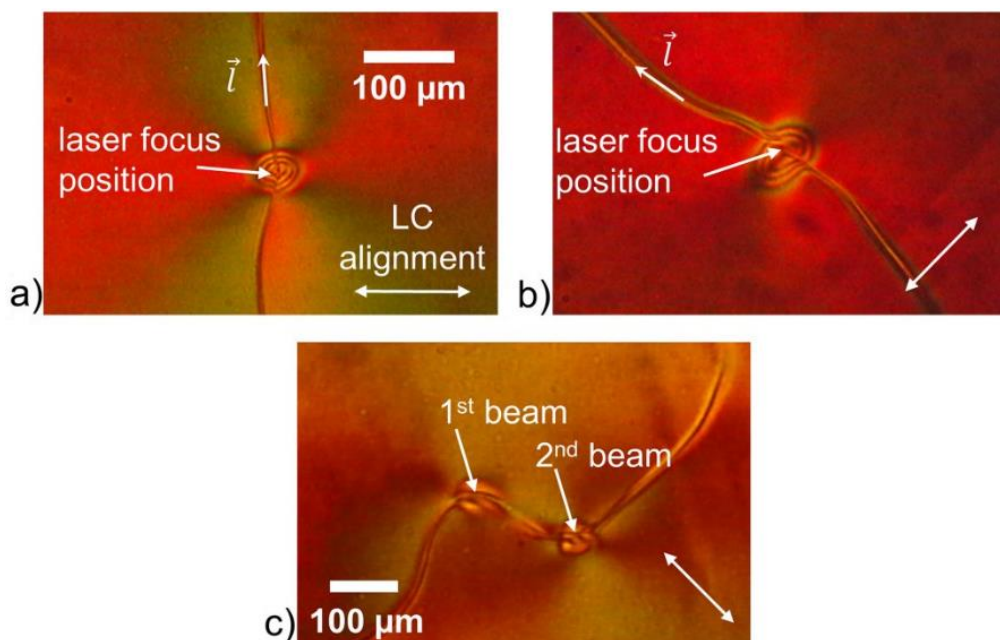


Figure 6.11*. Formation of defects in a confined LC cell with film spacers observed between crossed linear polarizers. a) and b) The LC cell was rotated and it was exposed to a single focused laser beam at different positions. c) The sample upon exposure of a pair focused laser beams. The alignment direction at confining surfaces (of the Fe:LN substrate and the cover slip) is shown by a white double arrow. The wall pinned to the single point defect is shown by vector l . {The image was taken from Ref.

12}.

The formation of the walls influenced the symmetry of the defect texture as seen twofold (Figure 6.11). If compared with the structure of patterns observed in the open film samples, fewer stripes were seen as tuned by film thickness (in average of $h \approx 30 \mu\text{m}$), as seen in Figure 6.11. The number of stripes can vary between one to five depending on the exposure location thickness and intensity.

When the laser shutter is closed, the LC relaxes back to its initial defect free alignment¹². By increasing exposure intensity, the length of the wall can increase. Figure 6.11c is corresponding with the creation of two point defects where the exposure beam was divided into two adjacent focused beams with an inserted wedge cell beam splitter (with small angular splitting) in the beam path. As a result, two circular defects were created at the positions of the laser spots on the sample, which were accompanied by the formation of the walls pinned to their centers. The walls were joined forming a single wall with open ends interconnecting the centers of defects (Figure 6.11c). The generation of interconnecting defect walls can open a new path to reconfigurable microstructures of a series of interconnected field-induced defects.

A fully enclosed film sample with film spacers and a glass cover slip was studied at different exposure intensities (Figure 6.12)¹². At low exposure intensities beyond threshold, at first a defect-free director reorientation occurred, as seen in Figure 6.12b. By increasing the exposure intensity (Figure 6.12c), this reorientation evolved into a pair of point defects of central and secondary defects interconnected by a wall, while the secondary point defect (generated near the glass surface) pinned additionally two other walls with open ends, as well. The formation of interconnected point defects is comparable to the behavior seen in Figure 6.8a corresponding to the formation of the defects in the open film sample. As can be seen from Figure 6.12c and the inset, desaturated image of the generated defects, the pair of singular defects is connected with a wall, which has a length of $35 \mu\text{m}$, slightly larger than the film thickness.

At higher exposure intensities, the secondary defect and the interconnecting wall with the central defect were annihilated as the system evolved to a single defect pinning to the extended wall (Figure 6.12d). By increasing the laser intensity and strengthening the induced electric field, the elastic energy is mainly confined to the central defect which acts as a trap for the permanent walls. The size of the central defect could reach a maximum value of $40 \mu\text{m}$ in diameter (tuned by the PV field strength), while the length of the permanent wall could significantly increase to $200 \mu\text{m}$ by varying the exposure intensity.

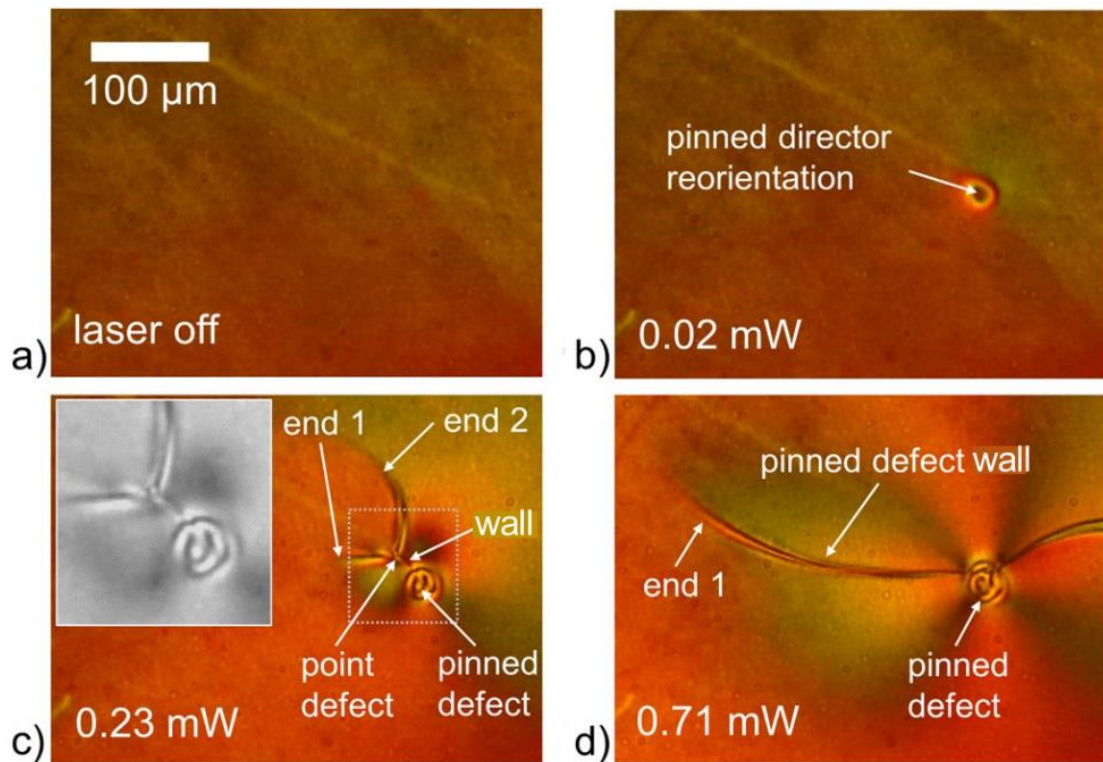


Figure 6.12*. Studying defect formation in a confined film sample with the glass slip between crossed linear polarizers. a) Laser-off state. b) Defect-free reorientation of the LC at a low laser power of 0.02 mW. (c) Defects generation at moderate laser power of 0.23 mW as a collection of the central defect (formed at the laser exposure focus) connected by a wall to the secondary defect (formed near the glass surface) which is coupled with an extended wall. In the inset, the magnified region of the defects is shown. d) Relocation of the extended wall from being pinned to the secondary defect now to the central defect after merging of the two point defects at high laser power of 0.71 mW. {The image was taken from Ref. 12}.

6.6. Defects formation in LC cells covered with glass plates and equipped with ITO layers (without coating)

A photograph of the LC cell in the initial state (laser-off state) is shown¹³ in the polarizing optical microscope (Figure 6.13a). The colorful background of the image can be referred to the residual birefringence in the thick Fe:LN substrate.

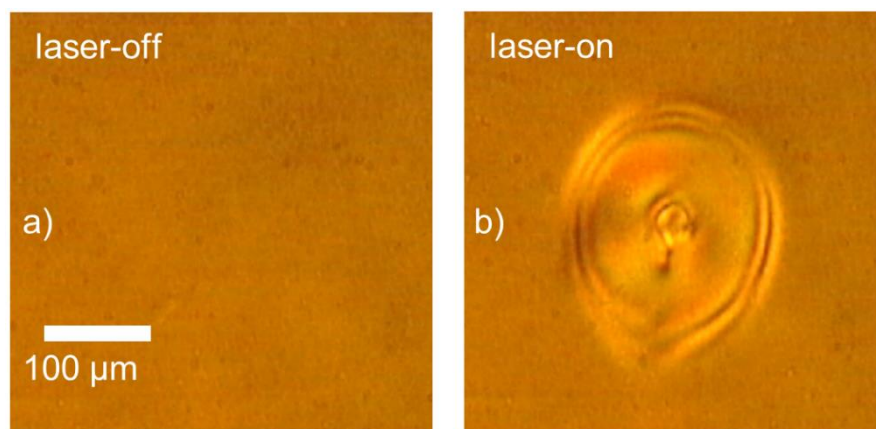


Figure 6.13[&]. Images recorded in the ITO-equipped nematic (i.e, MLC 2087) LC cell between crossed linear polarizers. a) Laser off state. b) Exposed with a Gaussian laser beam (schematically shown to the scale) with optical power of 0.9 mW. The cell gap is 30 μm . {The image was taken from Ref. 13}.

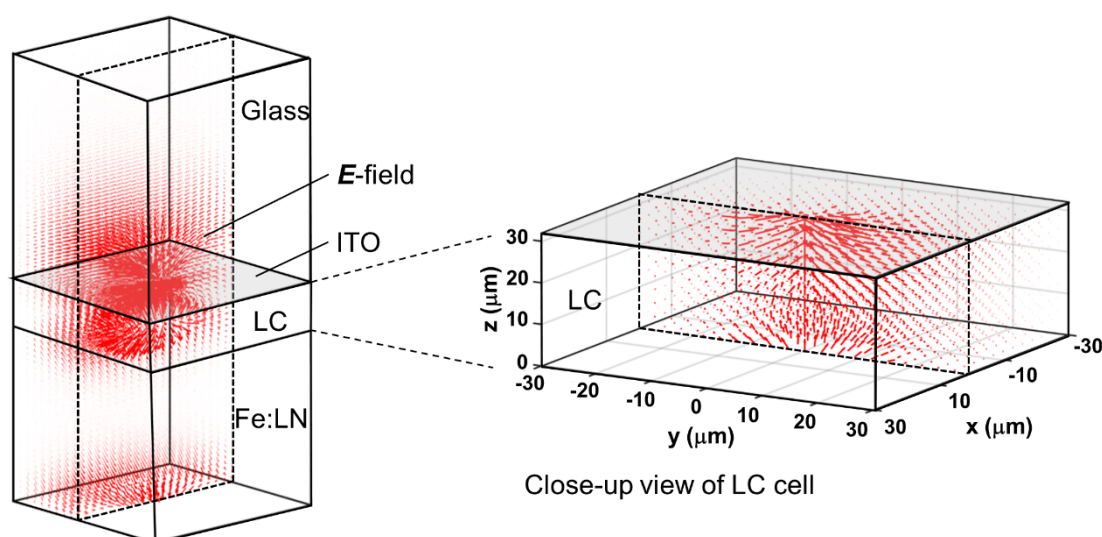


Figure 6.14. Simulated electric field distribution in the hybridized LC test cell with the Fe:LN substrate and the ITO-coated glass plate (Figure 5.2). The \mathbf{E} -field is shown in the rear half of the volume to give a clear view of the center area in magnification.

When the sample is exposed to a high (i.e, above threshold) power laser beam focused at the central region of the test cell where the LC has almost homogenous alignment, the photo generated fringe electric field (shown in Figure 6.6b and Figure 6.14) is capable to realign the LC director, and thereby results in spatial creation of nonsingular topological defects with strength $s = +1$ in the LC volume. The topological defects had a thickness of a few microns as their dimensions could be tuned by the variation of the exposure optical power¹³.

For simulating the director field, it was supposed that the strong electric field with radial distribution in the transverse plane is capable to locally induce a radial topological defect at the laser spot location, as the first approach. On the other hand, since preferential homeotropic alignment was seen at the laser-off state, it was supposed that near the ITO interface, the LC tends to keep homeotropic alignment. Near the Fe:LN interface, the radial realignment is imposed by the strong electric field at the laser spot location. At the laser-on state, this assumption is valid if the charge carrier accumulation in the ITO layer has a large radius compared to the FWHM of the incident laser beam which is supposed to be equal to the width of the induced charge carriers distribution in the Fe:LN substrate. Then, at the ITO boundary, the electric field has a vertical alignment in a larger area surrounding the center compared to the exposure spot focused on the substrate, which can preserve weak homeotropic alignment.

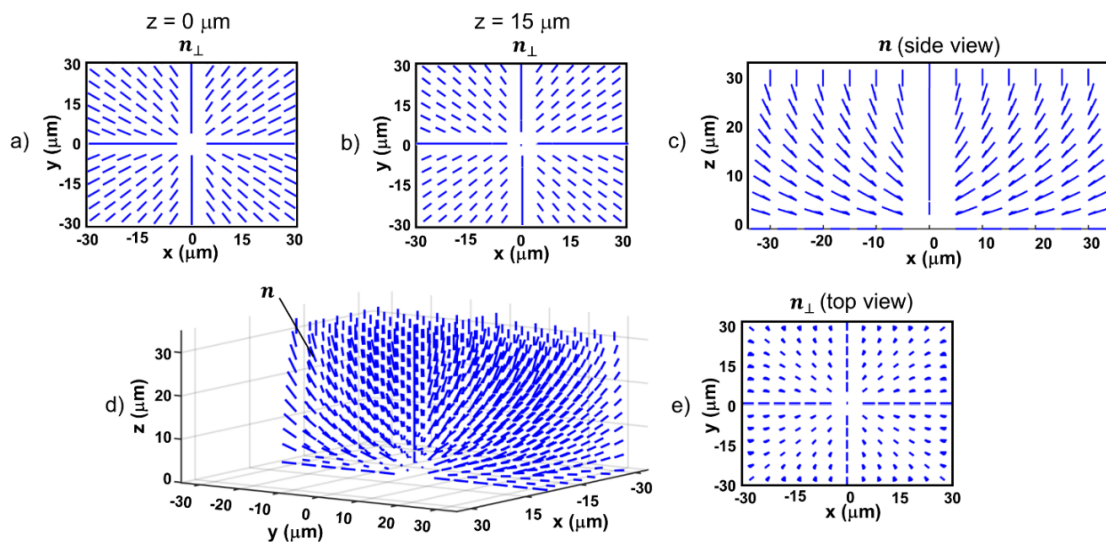


Figure 6.15. The director field \mathbf{n} distribution in the LC cell confined with untreated ITO coated cover glass: a) and b) in the transverse xy -plane shown at $z = 0, 15 \mu\text{m}$, c) side-view, d) in three-dimensions (3D), and e) top view. The induced charge densities were supposed equal to $\sigma = 7 \mu\text{C}/\text{m}^2$ in the Fe:LN slab.

The modeled topological defect is shown in Figure 6.15. As can be seen from this figure, director field has a radial distribution at the transverse plane in the LC film. For a better observation, the director field at the transverse plane n_{\perp} is shown at $z = 0 \mu\text{m}$ and $15 \mu\text{m}$ in Figures 6.15a, b. Additionally, a top view of the director field is shown in Figure 6.16e, corresponding to the director field distribution in 3D in the whole LC volume, which is shown in half of the LC volume in Figure 6.15d for clarity.

In comparison with the formation of a single topological defect formed at the Fe:LN interface, the simulations are done with the assumption of a radial defect formed at the Fe:LN interface (seen in the Figure 6.15a), while homeotropic alignment is supposed as the boundary condition at the ITO interface with the LC film (seen in Figure 6.15c). This is a rough assumption on how the director field realigns from its initial alignment. The simulation approach is modified by speculating that the radial alignment would be dominant at the cell middle thickness rather than at the Fe:LN interface. To prove this, new test cells were prepared by additionally coating the cell confining walls with lecithin, providing the homeotropic alignments as the boundary conditions on the director field distribution. The new model was successful; it revealed the real nature of the topological nonsingular defect as umbilical defect. The modeling results are discussed and shown in Chapter 5.

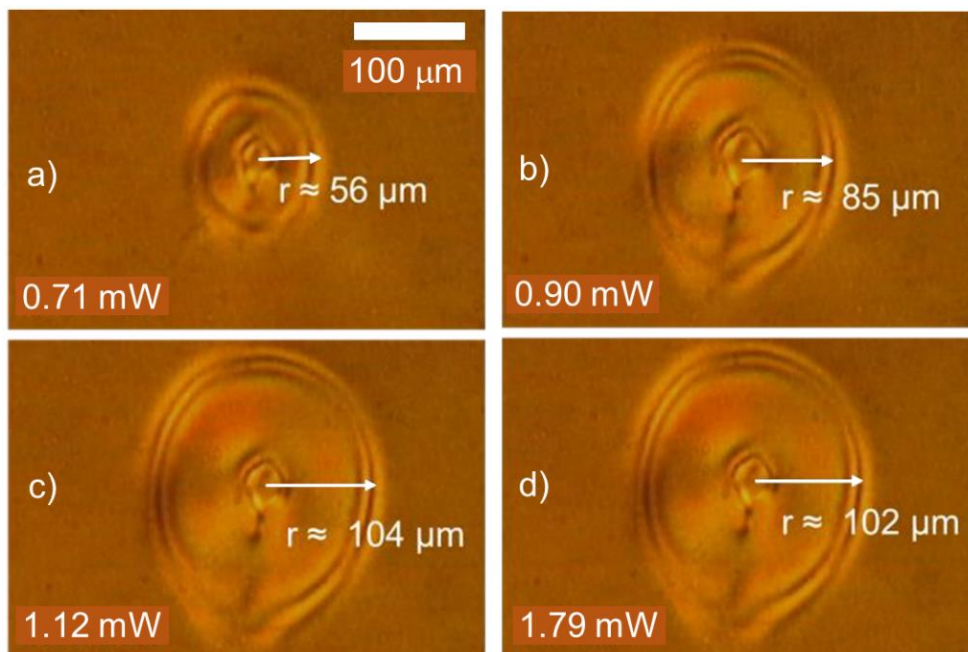


Figure 6.16[&]. Photo-induced non-singular radial defects created in the ITO-equipped LC cells seen between crossed linear polarizers at different exposure intensities. {The image was taken from Ref. 13}.

At low laser powers, the output intensity pattern of optical transmission is seen as a bright ring with a diameter equal to the full width at half maximum (FWHM) of the laser spot. At higher laser powers, after formation of the first ring, the second ring appears in the position of the first ring which grows in radius (while the system is evolving toward a stable state) and reaches a maximum value dependent on the applied optical power. It was found¹³ that the outer ring can reach a maximum value of $\approx 100 \mu\text{m}$ at power $> 1.1 \text{ mW}$ (Figures 6.16 and 6.18). This behavior can be understood by knowing that an increase in the induced charge carrier amplitudes can cause the creation of a stronger electric field with larger spatially expanded profile. It can affect the radius of the outer ring, while the first ring is always located inside the laser waist. The internal ring has a deformed structure, i.e., a lozenge-like shape, because of the formation of a weak wall (perpendicular to the rubbing direction) which affects the symmetry axis. It is characterized by a diameter being equal to the FWHM of the laser beam (Figure 6.16). When the laser shutter is closed, the LC realigns back to its initial state by annihilation of the induced electric field. Modeled output patterns associated with the LC sample with ITO-equipped cover glass are shown in Figure 6.17. They are in good agreement with the experimental observations¹³.

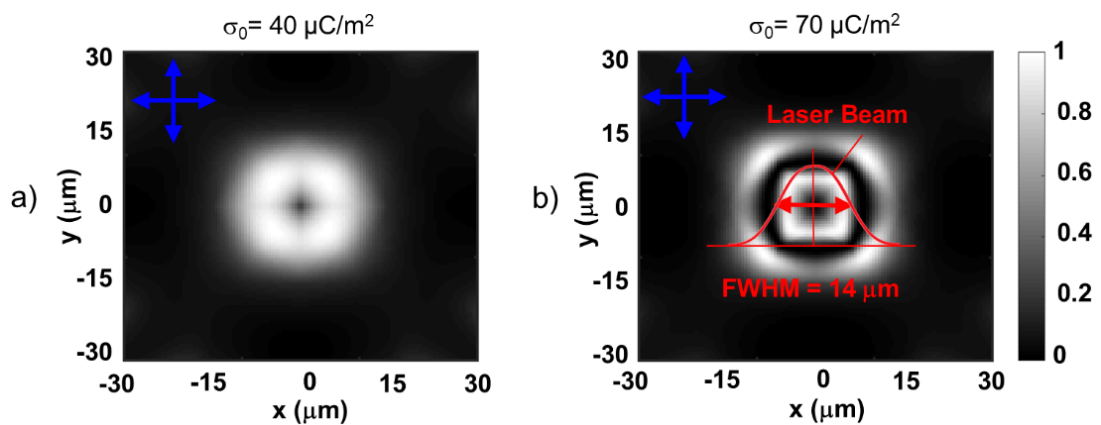


Figure 6.17. Modelling results of the transmitted intensity between crossed linear polarizers of the test cell covered with ITO equipped-glass plate corresponding to the induced charge carriers' amplitude of: a) $\sigma_0 = 40 \mu\text{C}/\text{m}^2$ and b) $\sigma_0 = 70 \mu\text{C}/\text{m}^2$. The exposure beam waist (FWHM) was assumed to be $14 \mu\text{m}$. Light beam focusing was not considered here.

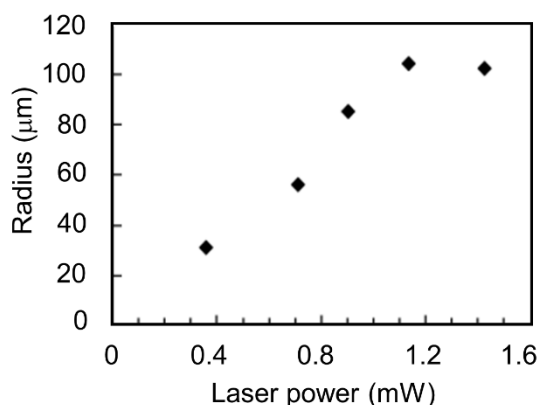


Figure 6.18[&]. Radius of the electrically induced non-singular optical patterns observed in the ITO-equipped LC cells at varying laser powers. {The image was taken from Ref. 13}.

The response times corresponding to the laser on and off states, i.e., t_{on} and t_{off} , respectively, were measured as a function of the laser power (Figure 6.19)¹³. The response time t_{on} defined as the time interval from opening the laser shutter to the stabilization of the optical pattern, which was measured equal to $t_{\text{on}} \approx 16$ seconds (s) is independent of the exposure intensity, while the second response time t_{off} , i.e., the time needed by the LC to relax back to its initial state after the laser shutter was closed, is linearly proportional to the optical power: By increasing optical power from 0.36 mW to 1.42 mW, it was increased linearly from 3 s to 20 s. It can be explained that by increasing optical power, the induced charge carrier density amplitudes are enhanced. This drives a stronger electric field E with a broader spatial profile. As a result, the LC deformation takes place in a larger region, which in turn increases the relaxation time of the LC when the laser beam is shut down.

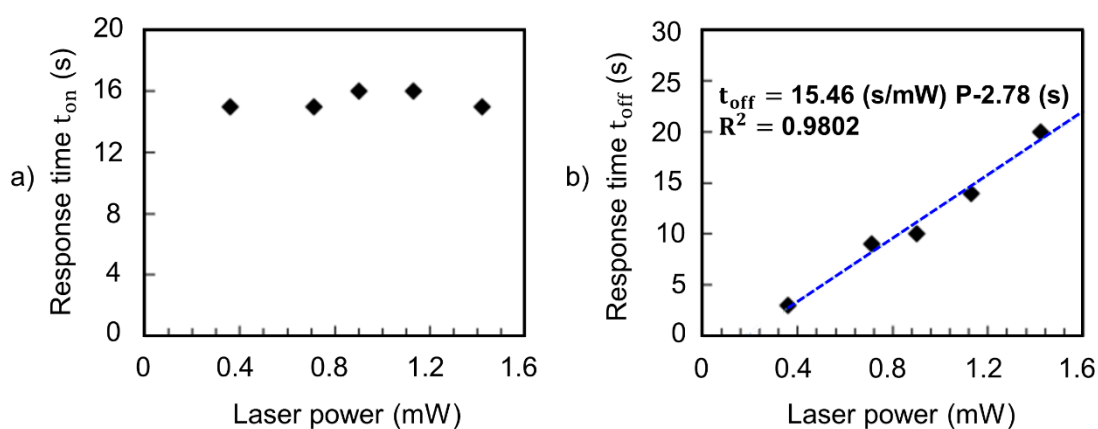


Figure 6.19[&]. The response times t_{on} and t_{off} of the ITO-equipped LC cells at various optical powers shown in a) and b), respectively. {The image was taken from Ref. 13}.

6.7. Defects formation in LC test cells covered with uniaxially rubbed polyimide coated, ITO-equipped glasses

If the ITO cover glass is replaced with a polyimide alignment coating, and uniaxially rubbed ITO electrode (obtained from commercial (EHC) LC test cells), the modified optical ring patterns are generated as a result of tuning the director field realignments¹³, Figure 6.20. Here, the wall (detected perpendicular to the rubbing direction as before) appearing at optical powers higher than 0.9 mW, is more pronounced because of the strong anchoring condition provided at the polyimide surface (if compared with a non-polyimide-coated ITO surface) in addition to the Fe:LN/LC interface.

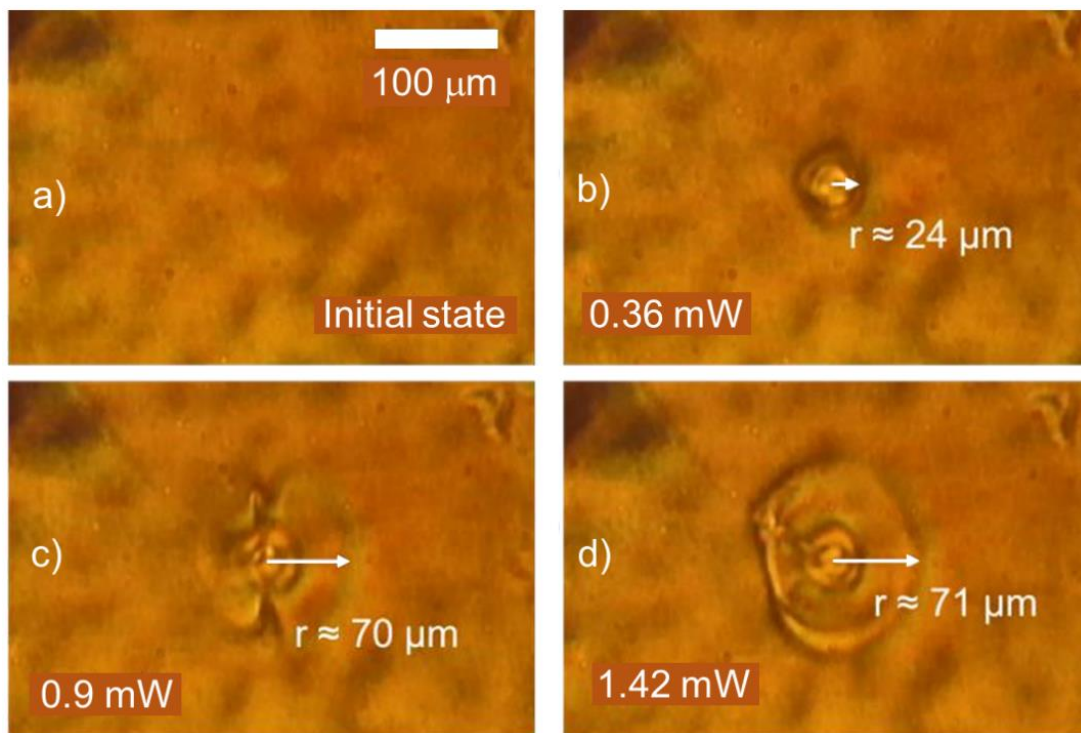


Figure 6.20^a. Micrographs of the photo-induced optical ring patterns observed in the polyimide coated ITO-cover glass at different optical powers between crossed polarizers. A wall formed at optical power of 0.9 mW. {The image was taken from Ref. 13}.

The modulation of the director field realignment led to the change of the response properties of the LC cells. The threshold optical power and the maximum radius measured in the centrosymmetric ring patterns were now reduced by 36% to a magnitude of 0.23 mW, and 20 % to a value of $\approx 80 \mu\text{m}$ (at optical power $\approx 1.1 \text{ mW}$), respectively (Figure 6.21)¹³ in comparison with the corresponding values measured in

non-coated ITO-equipped cell at the optical power ≈ 1.1 mW.

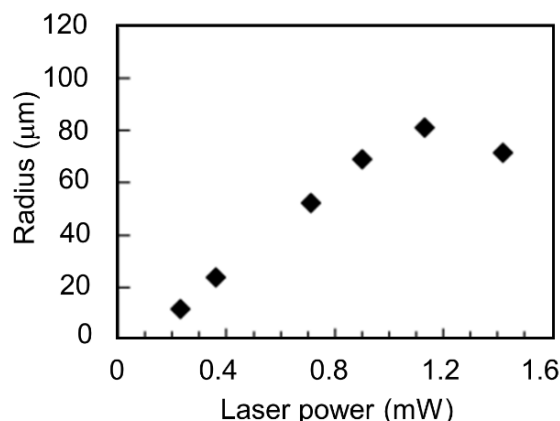


Figure 6.21[&]. Variation of the maximum radius associated to the optical ring patterns seen in the LC cells confined with polyimide coated ITO-equipped glass as a function of the optical power. {The image was taken from Ref. 13}.

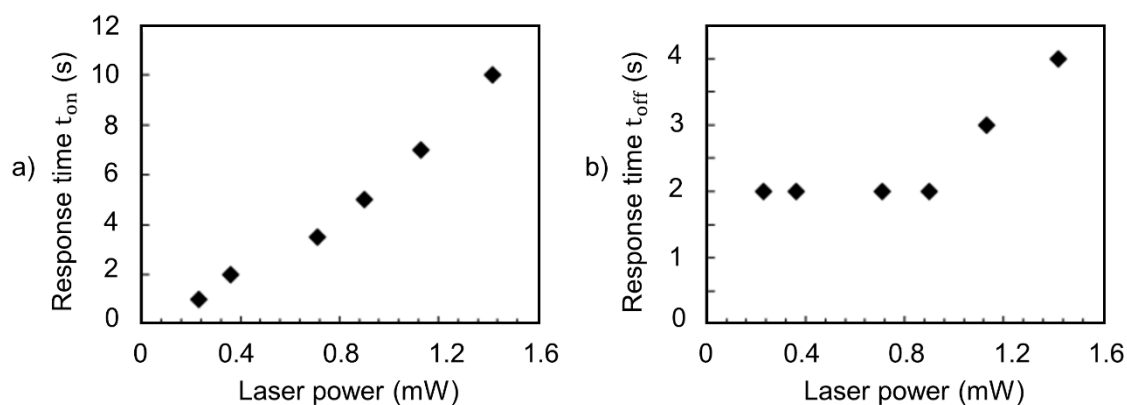


Figure 6.22[&]. The response times of the LC cells confined with polyimide coated ITO-equipped glass as a function of the optical powers; a) the response time t_{on} , and b) the response time t_{off} . The formation of the wall significantly affects the response times. {The image was taken from Ref. 13}.

In polyimide coated cells, the response time t_{on} is not constant. In contrast to the non-coated cells, it grows linearly with increasing optical power from 1 s corresponding to the threshold power of 0.23 mW to the maximum value of 10 s associated with the optical power of 1.42 mW (Figure 6.22a)¹³. The relaxation time t_{off} is almost constant equal to 2 s for optical powers lower than 0.9 mW (: where the wall appears), while at higher powers it linearly grows up to a maximum value of 4 s (which is less than the values measured in the non-coated cells), Figure 6.22b¹³. The response times are now controlled by the formation of the pronounced wall and the planar anchoring at both cell walls. In summary, polyimide coating at the ITO-equipped cover

glass can speed up the optical responses of the LC cells due to the contribution of surface photorefractive effect as discussed in Chapter 4.

6.8. Conclusions

The electric field-induced optical responses in the hybridized LC cells were studied, where the LC reorientation from initial alignment was driven by the photovoltaic electric field generated in the ferroelectric substrates i.e., Fe:LN, and assisted by the charge carrier accumulation in the thin ITO layer. The optical responses to a focused low power cw laser beam were investigated in the microscopic imaging setup with micron resolution.

In the absence of the ITO layer, the transmitted intensities were observed as Maltese textures with birefringent stripes coupled with line or wall(s). In open LC cells (in contact with air), the point defects with the topological strength of -1 corresponding to hyperbolic configuration were induced; the central defect was always observed at the position of the exposure spot, while located at the Fe:LN/LC interface.

In the LC cells equipped with the ITO layer, the modified electric field was able to induce non-singular defects with topological strength of $+1$ associated with radial reconfiguration in the transverse xy -plane. The optical responses appeared as ring patterns spatially distributed in the LC volume instead of being pinned to any planar walls of the cell (unlike the topological defects observed in the non-ITO equipped LC cells where they are pinned to the Fe:LN surfaces).

Additionally, defect formation was explored under different conditions. In the open film samples, displacement of the induced defect within the sample was found by scanning the laser beam across the film plane. By providing two adjacent focused beams of equal intensities, the generation of two singular defects interconnected via a wall was observed (in a confined film sample covered with a plain glass slip). This is promising for creating a lattice of interconnected point defects, using an appropriate the local laser beam distribution.

In the test cells studied, line and walls always formed perpendicular to the rubbing direction and pinned to the defect localized at the exposure spot (; referred to as the central defect). In the confined LC cells, an interesting behavior was seen in both types of ITO-equipped cells (with or without polyimide coating); the deformation of the director field extended to a maximum value only by increasing the optical power.

Induced topological defects were simulated in the open film samples, as well as in the ITO-equipped confined cells by taking the experimental observations into

consideration. Director fields were simulated utilizing the Q -tensor approach by numerically solving the Euler-Lagrange equation giving the evolution of the Q -tensor elements with the electric field. Director field distributions, associated with the topological defects, correspond to local modulations of the effective refractive index which effectively induces phase delay between ordinary and extraordinary waves of the incoming light beam. The optical transmissions between crossed linear polarizers were obtained (as discussed in Chapter 4) giving rise to the characteristics optical patterns seen in samples with induced defects.

Declarations

" Figures 6.4, 6.7-12 reprinted with permission from the associated journal for the publication of {Habibpournoghadam, A., Jiao, L., Reshetnyak, V., Evans, D. R., & Lorenz, A. (2017). Optical manipulation and defect creation in a liquid crystal on a photoresponsive surface. *Physical Review E*, 96(2), 022701}. Copyright © 2017 American Physical Society. "

" Figures 6.13, 6.16, 6.18-22 reprinted with permission from the corresponding journal publishing {Habibpournoghadam, A., Jiao, L., Omairat, F., Evans, D. R., Lucchetti, L., Reshetnyak, V., & Lorenz, A. (2017, August). Confined photovoltaic fields in a photoresponsive liquid crystal test cell. In *Liquid Crystals XXI* (Vol. 10361, p. 1036112). International Society for Optics and Photonics}. © (2017) COPYRIGHT Society of Photo-Optical Instrumentation Engineers (SPIE)). "

Acknowledgments

* Experimental Figures 6.4, 6.7, 6.8, 6.11, 6.12 were provided by Dr. Alexander Lorenz (University Paderborn, Germany) which are highly appreciated.

& Figures 6.13, 6.16, 6.18-22 were provided by Mr. Faisal Omairat (University Paderborn, Germany) and Dr. Alexander Lorenz which are well acknowledged.

References

- ¹ Stark, H. (2001). Physics of colloidal dispersions in nematic liquid crystals. *Physics Reports*, 351(6), 387-474.
- ² Chuang, I., Durrer, R., Turok, N., & Yurke, B. (1991). Cosmology in the laboratory: Defect dynamics in liquid crystals. *Science*, 251(4999), 1336-1342.
- ³ F.R.N. Nabarro, Theory of Crystal Dislocations, The International Series of Monographs on Physics, Clarendon Press, Oxford, 1967.
- ⁴ Blatter, G., Feigel'man, M. V., Geshkenbein, V. B., Larkin, A. I., & Vinokur, V. M. (1994). Vortices in high-temperature superconductors. *Reviews of Modern Physics*, 66(4), 1125.
- ⁵ Abrikosov, A. A. (1957). On the magnetic properties of superconductors of the second group. *Sov. Phys. JETP*, 5, 1174-1182.
- ⁶ Goodby, J. W., Waugh, M. A., Stein, S. M., Chin, E., Pindak, R., & Patel, J. S. (1989). Characterization of a new helical smectic liquid crystal. *Nature*, 337(6206), 449.
- ⁷ Goodby, J. W., Waugh, M. A., Stein, S. M., Chin, E., Pindak, R., & Patel, J. S. (1989). A new molecular ordering in helical liquid crystals. *Journal of the American Chemical Society*, 111(21), 8119-8125.
- ⁸ Giomi, L., Bowick, M. J., Mishra, P., Sknepnek, R., & Cristina Marchetti, M. (2014). Defect dynamics in active nematics. *Philosophical Transactions of the Royal Society A: Mathematical, Physical and Engineering Sciences*, 372(2029), 20130365.
- ⁹ Vromans, A. J., & Giomi, L. (2016). Orientational properties of nematic disclinations. *Soft matter*, 12(30), 6490-6495.
- ¹⁰ Tang, X., & Selinger, J. V. (2017). Orientation of topological defects in 2D nematic liquid crystals. *Soft Matter*, 13(32), 5481-5490.
- ¹¹ Harth, K., & Stannarius, R. (2020). Topological Point Defects of Liquid Crystals in Quasi-Two-Dimensional Geometries. *Frontiers in Physics*, 8, 112.
- ¹² Habibpournmoghadam, A., Jiao, L., Reshetnyak, V., Evans, D. R., & Lorenz, A. (2017). Optical manipulation and defect creation in a liquid crystal on a photoresponsive surface. *Physical Review E*, 96(2), 022701. (<https://doi.org/10.1103/PhysRevE.96.022701>, ©2017 American Physical Society).
- ¹³ Habibpournmoghadam, A., Jiao, L., Omairat, F., Evans, D. R., Lucchetti, L., Reshetnyak, V., & Lorenz, A. (2017, August). Confined photovoltaic fields in a photoresponsive liquid crystal test cell. In *Liquid Crystals XXI* (Vol. 10361, p. 1036112). International Society for Optics and Photonics. (<https://doi.org/10.1117/12.2273990>, © (2017) COPYRIGHT Society of Photo-Optical Instrumentation Engineers (SPIE)).
- ¹⁴ Lavrentovich, O. D. (2001). Nematic liquid crystals: Defects. Elsevier Science Ltd.

-
- ¹⁵ Ohzono, T., Kato, K., Wang, C., Fukazawa, A., Yamaguchi, S., & Fukuda, J. I. (2017). Uncovering different states of topological defects in schlieren textures of a nematic liquid crystal. *Scientific reports*, 7(1), 16814.
- ¹⁶ de Lózar Muñoz, A. (2005). *Liquid Crystal Dynamics: Defects, Walls and Gels*. Cuvillier Verlag.
- ¹⁷ Kleman, M., & Lavrentovich, O. D. (2007). *Soft matter physics: an introduction*. Springer Science & Business Media.
- ¹⁸ Andrienko, D. (2006). Introduction to liquid crystals. *IMPRS school, Bad Marienberg*, 4.
- ¹⁹ Desimpel, C. (2006). Liquid crystal devices with in-plane director rotation. *Dissertation Abstracts International*, 68(01).
- ²⁰ Madhusudana, N. V., & Pratibha, R. (1983). Studies on high strength defects in nematic liquid crystals. *Molecular Crystals and Liquid Crystals*, 103(1-4), 31-47.
- ²¹ Lavrentovich, O. D. (1998). Topological defects in dispersed words and worlds around liquid crystals, or liquid crystal drops. *Liquid crystals*, 24(1), 117-126.
- ²² Glass, A. M., Linde, D. V. D., & Negran, T. J. (1974). High-voltage bulk photovoltaic effect and the photorefractive process in LiNbO₃. *Appl. Phys. Lett.* 25, 233.
- ²³ Villarreal, J., Burgos, H., García-Cabañes, Á., Carrascosa, M., Blázquez-Castro, A., & Agulló-López, F. (2011). Photovoltaic versus optical tweezers. *Optics express*, 19(24), 24320-24330.
- ²⁴ Carrascosa, M., García-Cabañes, A., Jubera, M., Ramiro, J. B., & Agulló-López, F. (2015). LiNbO₃: A photovoltaic substrate for massive parallel manipulation and patterning of nano-objects. *Applied Physics Reviews*, 2(4), 040605.
- ²⁵ Fleury, J. B., Pires, D., & Galerne, Y. (2009). Self-connected 3D architecture of microwires. *Physical review letters*, 103(26), 267801.
- ²⁶ Sengupta, A., Tkalec, U., & Bahr, C. (2011). Nematic textures in microfluidic environment. *Soft Matter*, 7(14), 6542-6549.
- ²⁷ Lee, J. H., Atherton, T. J., Kang, D., Petschek, R. G., & Rosenblatt, C. (2008). Polar-horizontal versus polar-vertical reverse-tilt-domain walls: Influence of a pretilt angle below the nematic-isotropic phase transition. *Physical Review E*, 78(2), 021708.
- ²⁸ Ye, M., Wang, B., & Sato, S. (2004). Liquid-crystal lens with a focal length that is variable in a wide range. *Applied Optics*, 43(35), 6407-6412.
- ²⁹ Hsu, C. J., & Sheu, C. R. (2011). Preventing occurrence of disclination lines in liquid crystal lenses with a large aperture by means of polymer stabilization. *Optics express*, 19(16), 14999-15008.
- ³⁰ Lee, G. D., Anderson, J., & Bos, P. J. (2002). Fast Q-tensor method for modeling liquid crystal director configurations with defects. *Applied physics letters*, 81(21), 3951-3953.

-
- ³¹ Mori, H., Gartland Jr, E. C., Kelly, J. R., & Bos, P. J. (1999). Multidimensional director modeling using the Q tensor representation in a liquid crystal cell and its application to the π cell with patterned electrodes. *Japanese journal of applied physics*, 38(1R), 135.
- ³² Tovkach, O. M., Conklin, C., Calderer, M. C., Golovaty, D., Lavrentovich, O. D., Vinals, J., & Walkington, N. J. (2017). Q-tensor model for electrokinetics in nematic liquid crystals. *Physical Review Fluids*, 2(5), 053302.
- ³³ James, R., Willman, E., FernandezFernandez, F. A., & Day, S. E. (2006). Finite-element modeling of liquid-crystal hydrodynamics with a variable degree of order. *IEEE Transactions on Electron Devices*, 53(7), 1575-1582.
- ³⁴ Marrucci, L. (2008). Generation of helical modes of light by spin-to-orbital angular momentum conversion in inhomogeneous liquid crystals. *Molecular Crystals and Liquid Crystals*, 488(1), 148-162.

Chapter 7: Tunable Diffraction Gratings Driven in In-Plane Switching (IPS) LC Cells

7.1. Abstract

Transmissive diffraction gratings have been numerically studied using a fast Fourier transform (FFT) method utilized in Matlab scripts. It was seen that a rectangular grating can cause both position-dependent phase and transmittance (T) modulations for an incident plane wave as the first step towards studying the impact of grating on the electro-optical behavior of a polymer-enhanced liquid crystal. In an in-plane switching (IPS) test cell, a rectangular grating (supposed as a model grating) stands for electrode and gap areas, where the modulations were solely attributed to the electrode regions, i.e., the area above electrodes. Results obtained from numerical modeling showed that the diffraction patterns of the gratings are influenced by both period and electrode-gap aspect ratio. For specific electrode-gap aspect ratios, diffracted energy can be transferred from zero and second orders of diffraction to first order for a monochromatic plane wave instead of being distributed in all diffraction orders with a Gaussian envelope.

The diffraction behavior of polymer-stabilized liquid crystals was studied in the IPS test cells and compared to the behavior seen in a neat liquid crystal. Since in the studied samples the polymers have a continuous distribution, the samples are also called polymer network liquid crystals (PNLCs). Experiments and simulations were compared to learn about the impact of polymer. PNLCs are composites which possess a specific domain size. The size of such polymer-induced domains was investigated with different

methods such as polarized optical microscopy (POM) and dark field microscopy (DFM) in IPS cells filled with LC, or scanning electron microscopy (SEM) in planar LC cells for comparison. PNLCs are capable to result in a continuous optical phase modulation. If addressed with non-homogenous electric fields, studying the variation of director field and the phase modulation profile as compared to a neat LC is instructive. The diffraction patterns (seen experimentally and modeled) and simulated optical phase change profiles in a NLC influenced by the applied addressing voltage showed some limited tunability already. However, if a PNLC is used, both the diffraction patterns (recorded and modeled) and simulated optical phase change profiles vary drastically as compared to a neat NLC. The gratings show responses localized to the electrodes. Highly responsive PNLC cells provide the possibility of significantly suppressing the 0th diffraction order. Depending on the applied voltage, the diffraction efficiency can be tuned. The presented results are instructive to understand the impact of polymer network on the field-dependent reorientation of the liquid crystal director; If addressed with the same electric field profile, the responses are much more localized in a PNLC cells than in a neat NLC.

7.2. Discussion on the diffraction properties of the model grating

Structures of two phase gratings are schematically shown in Figures 7.1a and b corresponding to grating periods of $\Lambda = 20 \mu\text{m}$ and $12 \mu\text{m}$, respectively.

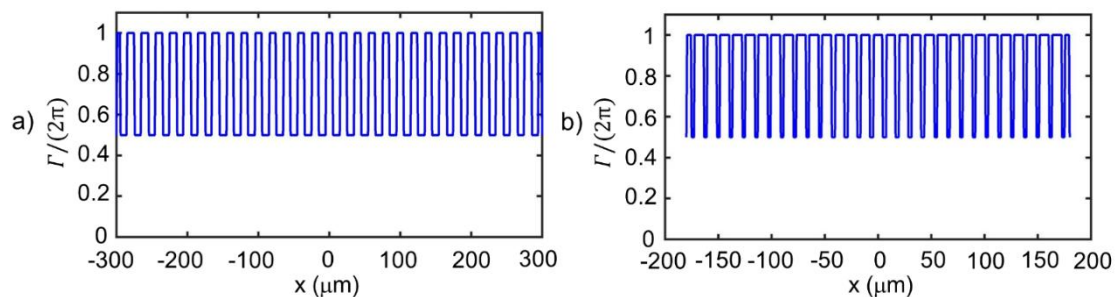


Figure 7.1. Structures of two different phase gratings. Phase delays are equal to $\Gamma^e = \pi$ and $\Gamma^g = 2\pi$ corresponding to the electrode and gap regions, respectively. The electrode length to the gap length, i.e., $w_e : w_g$, is a) $10 \mu\text{m} : 10 \mu\text{m}$, and b) $3 \mu\text{m} : 9$

μm . The supposed number of electrodes is $N = 30$ in both cases. The apertures associated with gap regions are located along the x -axis.

In Figure 7, the phase gratings were modeled as trains of N rectangular pulses ($N = 30$), where phase delays considered for a normally incident monochromatic plane wave shone on the IPS cell were supposed constant over the electrode and gap regions equal to $\Gamma = \pi$ and $\Gamma_0 = 2\pi$, respectively. The overall grating length of each structure is $L = N\Lambda$. The electrode width to the gap size, i.e., $w_e : w_g$, are equal to $10 \mu\text{m} : 10 \mu\text{m}$ and $3 \mu\text{m} : 9 \mu\text{m}$ in the first and second structures, respectively.

The transmission function of an amplitude grating, denoted as $T_A(x)$, can be described as the summation of two transmission functions, i.e., $T_{A,e}(x)$ and $T_{A,g}(x)$, which are the transmitted amplitudes through the electrode and gap regions^{1,2}, respectively,

$$T_A(x) = [T_{A,e}(x) + T_{A,g}(x)] \text{rect}\left(\frac{x}{L}\right) \quad (7.1)$$

where,

$$T_{A,e}(x) = (A_e \text{rect}(x/w_e)) \left(\frac{1}{\Lambda} \text{comb}(x/\Lambda)\right) \quad (7.2)$$

$$T_{A,g}(x) = \left(A_g \text{rect}\left(\left(x - \frac{\Lambda}{2}\right)/w_g\right)\right) \left(\frac{1}{\Lambda} \text{comb}(x/\Lambda)\right) \quad (7.3)$$

where Λ is the grating period, and w_e and w_g are electrode and gap lengths respectively, as introduced earlier. In relation (7.1), the rectangular function, i.e., rect , describes the geometry of the full grating which was extended over the length of L . It has a value of one over the full geometry of the IPS cell in the x -direction, and zero elsewhere (it has an average value of 1/2 at the edges of the structure by mathematical definition). In relations (7.2) and (7.3), the first terms describe the amplitudes attributed to each single electrode and gap area, i.e., A_e and A_g , respectively, while the rect functions give the value of one over the electrode and gap dimensions and zero elsewhere (again they have an average value of 1/2 at the edges of the electrode and gap areas). Two sequences of two different pulses, each pulse describing every single electrode and gap areas, respectively, were obtained from multiplication of the rect functions by comb functions, which consist of sequence of Dirac delta functions considered at the center of electrode and gap regions, respectively.

By considering phase delay, the transmission function of a phase grating³, $T_{Ph}(x)$, can be obtained by modifying the relations (7.1) to (7.3) as,

$$T_{Ph}(x) = [T_{Ph,e}(x) + T_{Ph,g}(x)]rect\left(\frac{x}{L}\right) \quad (7.4)$$

where,

$$T_{Ph,e} = (\exp(-i\Gamma^e)rect(x/w_e))\left(\frac{1}{\Lambda}comb(x/\Lambda)\right) \quad (7.5)$$

$$T_{Ph,g} = (\exp(-i\Gamma^g)rect((x - \frac{\Lambda}{2})/w_g))\left(\frac{1}{\Lambda}comb(x/\Lambda)\right). \quad (7.6)$$

Here, the phase modulation attributed to each single electrode and gap area were described as $\exp(-i\Gamma^e)$ and $\exp(-i\Gamma^g)$, respectively, while the remaining terms in relations (7.5) and (7.6) give the full electrode and gap geometries in the IPS cells, each of them constructed from a sequence of N electrodes and N gaps, respectively. In general speaking, phase delays in the electrode and gap regions can be obtained from $\Gamma^e = 2\pi n^e w/\lambda$ and $\Gamma^g = 2\pi n^g w/\lambda$, where n^e and n^g are effective refractive indices in the electrode and gap regions, w is the thickness of the grating, and λ is the wavelength of the incident wave (which is supposed normal to the cell surface). Fourier transform^{4,5} of the transmission across the grating gives the field distribution of Fraunhofer diffraction in one dimension (1D). Diffraction intensities (patterns) corresponding to the geometries shown in Figure 7.1 (with two different grating periods of $\Lambda = 20 \mu\text{m}$, $12 \mu\text{m}$, respectively) are shown in Figure 7.2, the diffraction angle β corresponding to the diffraction order m can be obtained approximately from $\beta \approx m\lambda/\Lambda$ (when the screen is placed far from the cell). In this figure, diffraction gratings were numerically simulated by neglecting the effect of amplitude modulations, speculating upon the dominance of the phase modulation in the output patterns. The diffraction patterns were considerably affected by both grating periods and the ratio of the electrode to the gap sizes; by choosing the ratio $w_e : w_g = 10 \mu\text{m} : 10 \mu\text{m}$ corresponding to the grating period of $\Lambda = 20 \mu\text{m}$, the zero and second diffraction orders vanish and the diffraction energy is significantly concentrated in the first diffraction order. In general, if $w_e = w_g$. The maximum intensities distributed in the zero and first diffraction orders can be calculated³ from $I_{0,max}/I_{inc} = \cos^2((\Gamma^e - \Gamma^g)/2)$ and

$I_{1,max}/I_{inc} = \text{sinc}^2(1/2)\text{sin}^2((\Gamma^e - \Gamma^g)/2)$, respectively, where I_{inc} is the incident intensity. If $\Gamma^e = \pi$ and $\Gamma^g = 2\pi$ are phase delays in the electrode and gap regions, respectively (corresponding with the grating structure shown in Figure 7.1a). Then it is easy to see that $I_{0,max}/I_{inc} = 0$ and $I_{1,max}/I_{inc} = 0.92$, respectively.

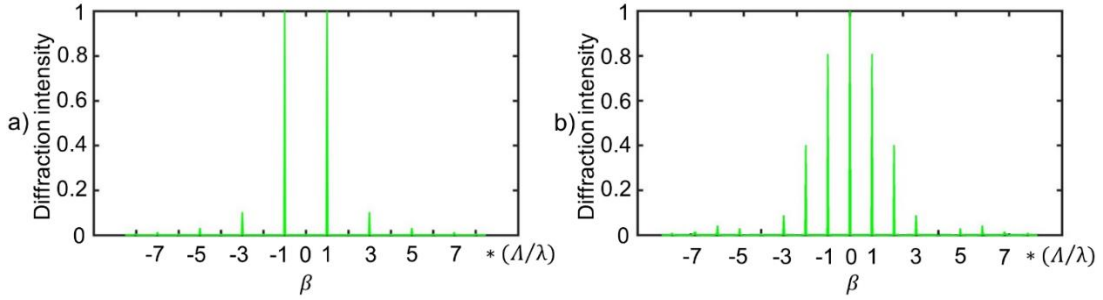


Figure 7.2. a) and b) Normalized diffraction intensity distributions of the phase gratings corresponding to the structures shown in Figure 7.1a, b, respectively.

On the other hand, it was revealed that the intensity modulations have a minor impact on the diffraction patterns. In Figure 7.3, the intensity distributions of the gratings were modeled. Additionally, the transmission modulation of 60% in the electrode regions was imposed. Then, the overall transmission function $T(x)$ was obtained as the multiplication of the transmission functions of the amplitude grating by the phase grating, i.e., $T(x) = T_A(x)T_{Ph}(x)$. Making a Fourier transform of the overall transmission functions $T(x)$ gave the diffraction fields. The corresponding diffraction intensities are shown in Figure 7.3.

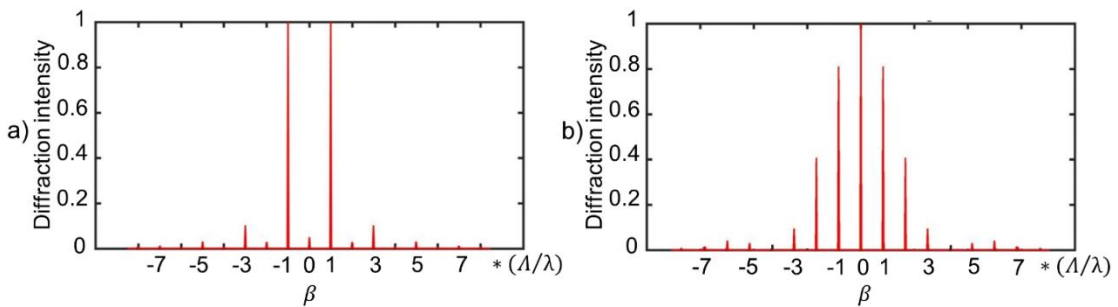


Figure 7.3. Normalized diffraction patterns of the overall grating functions composed from both intensity grating and phase grating functions. The transmission and phase modulations were supposed 60% and π in the electrode regions, respectively.

7.3. Conclusions

As conclusion, a Matlab code was developed to study the effective parameters in the diffraction properties of ideal rectangular gratings attributed to the IPS cells. The code had the capacity to be developed for studying more complex systems such as an IPS cell filled with LC or polymer enhanced LC where the grating has an arbitrary shape of pulses. According to the initial findings, under certain geometrical conditions, the optical power of the monochromatic light beam can be mainly distributed only in the first order (both peaks with the same amplitudes), which can be beneficial in spectrometers. In addition, the transmission grating shows a very minor impact on the diffraction pattern characteristics.

7.4. Tuneable diffraction gratings in copolymer network liquid crystals driven with interdigitated electrodes*

7.4.1. Introduction to the application of PNLCs in diffraction gratings

Tunable liquid crystal (LC) gratings have found exciting applications in various opto-electronic devices such as in beam steering⁶, tunable diffraction^{7,8}, programmable shaping of femtosecond pulses⁹, optical fibers¹⁰, remote sensing¹¹, three-dimensional displays^{12,13}, eye-tracking for emerging virtual reality displays^{14,15}, and beam multiplexing^{16,17}. LC based phase gratings have many desirable properties like straightforward design, ease of fabrication, and low power consumption¹⁸⁻²¹.

Electro-optical properties of such tunable gratings depend on the design of the liquid crystal test cell used (such as cell thickness, shape of electrodes, LC alignment) and also on the electro-optic properties of the LC^{7,8,22}. A NLC is a positive optically uniaxial medium, where the local orientation of the optical axis can be described by the LC director field \mathbf{n} . In an electro-optic experiment, the optical axis can be locally reoriented by applying an electric field. In a NLC, a relatively large layer thickness of the LC can be preferable to achieve high optical phase modulation. However, by increasing the layer thickness, the response times of the LC devices were significantly-

* " Reprinted with permission from {Habibpourmoghadam, A., Wolfram, L., Jahanbakhsh, F., Mohr, B., Reshetnyak, V., & Lorenz, A. (2019). Tuneable Diffraction Gratings in Copolymer Network Liquid Crystals Driven with Interdigitated Electrodes. *ACS Applied Electronic Materials*, 1(12), 2574-2584.}. Copyright © 2019 American Chemical Society. "

delayed²³. To achieve fast response times, LC composites such as polymer-dispersed liquid crystals (PDLCs)²⁴⁻²⁶, polymer-stabilized blue-phase liquid crystals (PS-BPLCs)¹⁵ and polymer network liquid crystals (PNLCs)²³ were investigated.

A PDLC film, which switches from an opaque to a transparent state, has found applications in light control devices because of light-scattering and electro-optical properties²⁴⁻²⁶. However, several trade-offs and drawbacks have limited²⁷ the use of PDLCs for applications in diffraction gratings (low diffraction efficiencies, and depolarization of light makes them inappropriate candidate for this regime).

PS-BPLCs have drawn considerable attention for photonics and displays applications. Fast response times in the submillisecond range and the possibility to waive alignment layers^{18,28} make them desirable candidates. Although drawbacks like hysteresis could be significantly diminished²⁹ (for example by eliminating the usage of photoinitiators and curing BPLC precursors with a high exposure dosage of a long UV wavelength), still PS-BPLCs suffer from side effects of hysteresis which could negatively influence grayscale control²⁸.

Moreover, PS-BPLC gratings require high operating voltages^{18,28}; although the diffraction efficiency may reach the maximum theoretical value of 40%, the driving voltage required can be as high as 160 V¹⁸.

Among these candidates, PNLCs have many desirable properties for diffraction grating applications: The response time of a PNLC can be in the submillisecond-range^{30,31} and they have a large phase modulation depth ($\geq 2\pi$), which can be achieved by controlling polymer density and by using co-polymer network LCs³¹. Undesirable scattering loss can also be avoided by choosing a high viscosity LC host, low temperature UV curing, and controlling domain sizes in the polymer network^{30,31}. High flexibility under an external mechanical pressure was achievable by designing the polymer network in vertical alignment in IPS LC cells³².

In this work, diffraction gratings were investigated in PNLC cells with experiments and simulations and compared correspondingly with the experimental and simulation results obtained for a neat LC cell, respectively. The experiments were done by the coauthors of the paper, whose names are listed and appreciated in the Acknowledgment. The voltage dependent diffraction behavior of such gratings was recorded in IPS test cells (test cells with comb-like, interdigitated electrodes) filled with a NLC and polymer network LCs. Domain sizes in the PNLC samples were investigated with polarized optical microscopy (POM), dark field microscopy (DFM), and

scanning electron microscopy (SEM). Values of $\sim 2.2 \mu\text{m}$ were found for the PNLC domain sizes. The electric field distribution, field induced reorientation of the LC director and diffraction behavior of the investigated test cells were modeled numerically. In the test cells filled with polymer network, the domains were modeled as cuboids with a cross-sectional length of $2.2 \mu\text{m}$. Simulation results were compared to the experiments. Experimental findings and simulation results were in very good agreement: It was found that in such test cells, the PNLC can exploit the spatially variant fields⁷ much more efficiently than would be possible in the neat NLC without the presence of a polymer network.

7.4.2. Materials and Experimental Methods

The prepared IPS test cells (obtained from Instec Inc) had comb-like interdigitated indium-tin-oxide (ITO) stripe electrodes with $w_g = 10 \mu\text{m}$ distance and $w_e = 10 \mu\text{m}$ electrode width and had a uniaxially rubbed polyimide alignment layer to provide initial alignment of the LC director parallel to the electrodes (schematic shown in Figure 7.4). The test cells were biased with ac square wave voltages. The cell thickness of the LC was $d = 10 \mu\text{m}$.

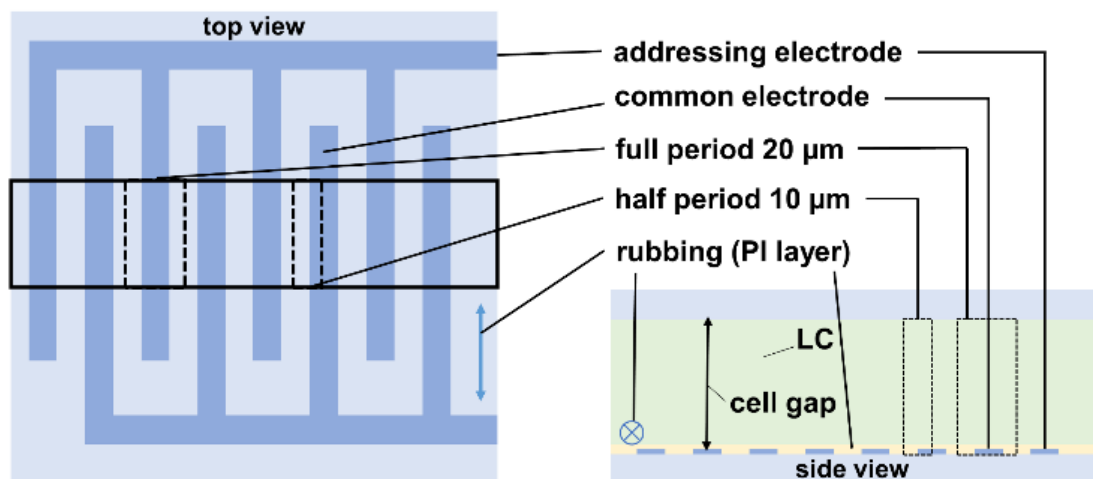


Figure 7.4. Schematic of an IPS test cell investigated.

Test cells were filled with the LC E7 (obtained from Synthon Chemicals GmbH & Co. KG) and two different reactive mixtures. The reactive mixtures consisted of E7 doped with one mesogenic acrylate monomer RM257 (obtained from Synthon Chemicals GmbH & Co. KG), one non-mesogenic acrylate monomer 2-ethylhexyl acrylate (EHA) (Sigma-Aldrich Chemie GmbH), and a photoinitiator phenylbis (2,4,6

trimethylbenzoyl) phosphine oxide (Sigma-Aldrich Chemie GmbH). Two different reactive mixtures were prepared, one with 3 wt% of RM257 and EHA, respectively, and one with 4 wt% of RM257 and EHA, respectively. The concentration of the photoinitiator (1 wt%) was kept constant. The filled test cells were cured with a UV tube source for 12 minutes in order to create PNLC samples, one with an overall polymer content (OPC) of 6% and one with an OPC of 8%³³.

Domain sizes were investigated³³ with POM (crossed polarizers), DFM, and SEM (Hitachi S-4000).

Test cells were biased when studied with POM³³. Rotating the test cell placed between crossed polarizers provides the necessary situation of high color contrasts for evaluation of the domain sizes with adjusted color levels (provided by Gimp software).

Biased test cells were studied³³ with DFM, where the domains appear as bright regions. The recorded photographs were analyzed with the software ImageJ in order to determine the domain sizes.

For the investigation with SEM³³, test cells were assembled from plane electrodes, i.e., ITO-coated glass plates, to have a comparison of polymer domain sizes with the ones formed in the cells with the interdigitated electrode structure. Studying this type of test cells were effortless because of easy access to the generated polymer networks. In this type of cells³³, glass plates were coated with a solution of polyvinyl alcohol (Merck KGaA), heated to 130 °C in a dry lab oven, and subsequently rubbed (uniaxially, 20 times) with clean room tissue. Test cells were assembled with 12 μm spacers, glued with a minimum amount of epoxy glue, filled with the reactive mixture, and exposed to UV light. The test cells were easily reopened (one glass plate was removed with a blade), and the LC was washed out with a solvent (acetone followed by ethanol). The remaining porous polymer layer was sputtered with Au-Pd alloy (4 nm layer thickness).

Target diffraction experiments³³ were performed in the IPS test cells exposed to a non-polarized HeNe laser beam. The LC director field was along the electrodes in the initial voltage-off state. The accumulative realignment induced by the fringe electric field relative to the propagation direction (normal to the LC cell surfaces) directly modulates the effective refractive index changes. The latter, in turn, tune the optical phase delay (relation (7.20)) and the complex phase grating transmission (relation (7.21)). As discussed in Chapter 2, the transmitted light intensity between crossed linear polarizers depends on the azimuthal angle distribution of the director field at the

transverse plane. A comparison between the transmission function of a phase grating in IPS cells filled with LC or PNLC with the transmitted light intensity between crossed linear polarizers revealed that the polarization state of the laser beam has no impact on the dominant mechanism of the phase grating. The experimental diffraction patterns were observed on a screen and recorded with a digital camera calibrated for intensity measurements.

7.4.3. Domain sizes and electro-optic responses

Samples of polymer-network LCs generated in IPS test cells were investigated with POM³³ (illuminated with white light, between crossed polarizers) fitted with a photomultiplier tube detector for the purpose of recording (digital storage oscilloscope) the transmittance vs time. In polymer network LC samples, domains were clearly seen (Figure 7.5³³) if the test cells were addressed with voltages higher than 20 V. In the investigation with POM, color variations in the biased state were used as a guide to identify the subdomain sizes in the PNLC-IPS cells. For this purpose, a test cell with 6% OPC was placed between crossed polarizers (Figure 7.5). In the voltage-off state, when one of the polarizers was placed parallel to the electrodes, the test cells were seen dark because of the orientation of the director field along the electrodes (in this situation, for example by rotating the sample by 45°, it appears in bright colors). By applying a voltage, the subdomains located in the gap regions were identified in some bright colors caused by the reorientation of the director field. This can be seen for example in Figure 7.5c. Since the electric field is very strong near to the electrodes' edges, the director field reorientation extends into the electrode regions. This leads in turn to an increase of the width of bright stripes beyond the gap size, measured to be about 13.5 μm . The domain sizes were measured and an average value of 2.2 \pm 0.3 μm was found.

In Figure 7.5c, the brightness profile of the test cell (6% OPC) between crossed polarizers and addressed with a voltage of 35 V was obtained (Origin Pro, OriginLab Corporation), where the sample was placed parallel to one of the crossed polarizers. From this profile, domains with highest and lowest transmittance can be identified. On average, 3 local maxima and 3 local minima were seen in each bright stripe, which gives a domain size of $13.5 \mu\text{m} / 6 = 2.25 \mu\text{m}$.

Electro-optic responses of two PNLC cells filled with 6% and 8% OPC and biased with 35 V and 45 V are shown³³ in Figures 7.5d and f, respectively. As

expected²³, fast response times of milliseconds (ms) were determined when compared with response times measured in neat NLC cells ($t_{\text{on}} = 74, 26$ ms and $t_{\text{off}} = 73, 80$ ms at $V = 5, 10$ V, respectively³³) probably because of the higher operating voltages, and localized responses.

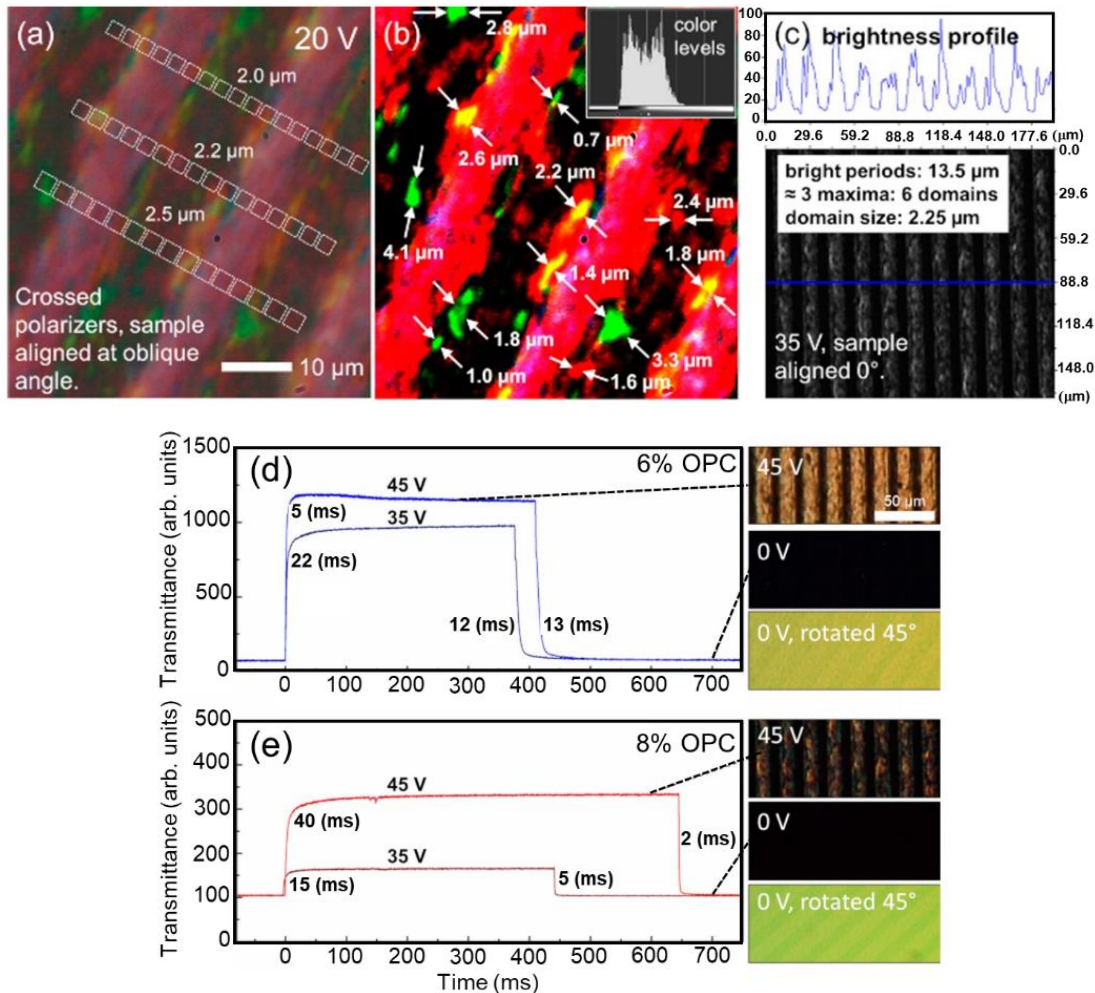


Figure 7.5*. (a) POM image recorded in a PNLC (6% OPC)-IPS test cell at an addressing voltage of 20 V. The sample was aligned at an oblique angle in order to be seen in a better color contrasts. Stacks of squares with different widths were set as guide to the eye. (b) Measured domain sizes in an image with improved color levels. (c) Brightness profile of the test cell (6% OPC) between crossed polarizers (at 0° oblique angle) addressed with 35 V. (d, e) Extract of response times of PNLC samples (6% and 8% OPC) from the electro-optic response curves at voltages of 35 V and 45 V. Supplied with POM images at 45 V and 0 V (at 0° and 45° oblique angles), additionally. {The image was taken from Ref. 33 (see Declarations and Acknowledgments)}.

The size of the subdomains in the PNLC cells were also studied with dark field microscopy³³ (Figure 7.6). The approach is based on the light scattering at the domain boundaries because of the index contrast between the polymer and the LC which is pronounced in the regions occupied with high density of polymer. The subdomains were seen bright as depicted in Figure 7.6. Average domain sizes of 1.36 μm and 1.11 μm were measured at biased voltages of 40 V and 50 V μm , respectively. It was found that this approach can give a rough estimation of the domain sizes since the measured values strongly depend on the applied voltage.

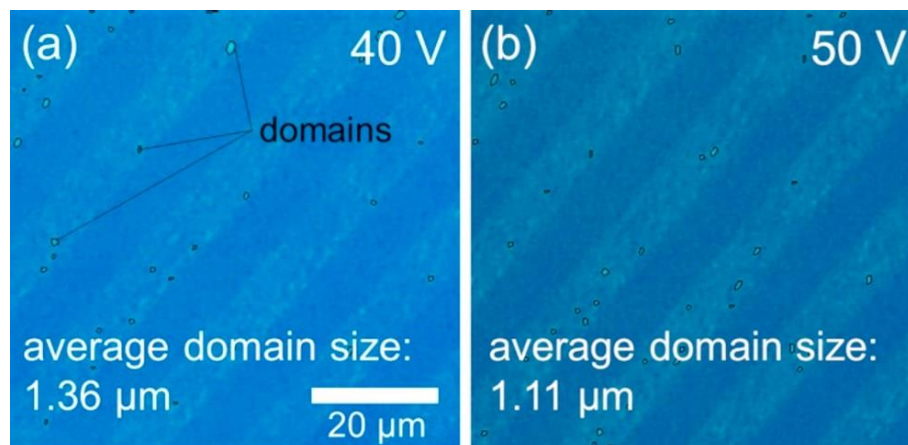


Figure 7.6*. Dark field microscopy images recorded in a PNLC-filled (6% OPC) IPS test cell at various addressing voltages of a) 40 V and b) 50 V. The investigated bright domains were shown with black boundaries. An average domain size of 1.36 μm and 1.11 μm were found, correspondingly. {The image was taken from Ref. 33}.

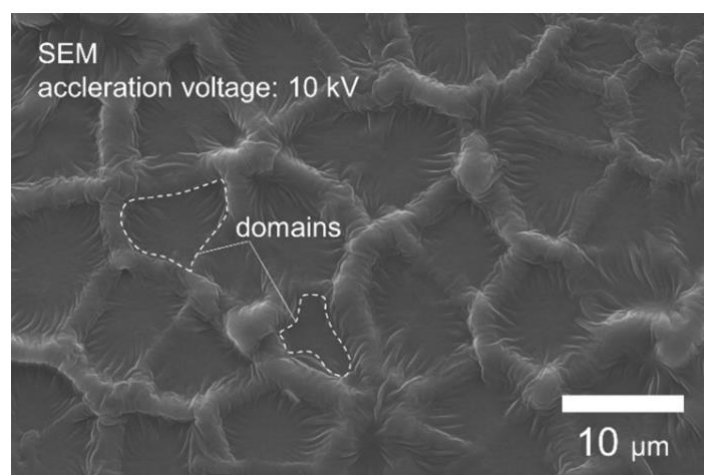


Figure 7.7*. SEM image recorded in a PNLC sample created with 5% RM257 and 5% EHA, washed with acetone and ethanol and sputtered with an Au-Pd alloy. {The image was taken from Ref. 33}.

Additional samples were prepared and studied with SEM³³. Instructive results (Figure 7.7) were obtained by using a reactive mixture that contained 5% EHA and 5% RM257 (overall polymer content 10%); In the washed samples (LC removed), a mesh-like polymer structure was seen. The PNLC had a higher overall polymer content than the mixtures used in IPS test cells. The image shows a smooth polymer mesh surrounding the hollow regions formerly filled with LC. For modeling, the domain sizes found in the IPS test cells with the target doping concentrations were used.

7.4.4. Experimental diffraction behaviour

In the voltage-off state, both types of samples filled with NLC or PNLC showed no diffraction as the intensity was fully transmitted to the position of the 0th-diffraction order, as seen in Figures 7.8a, 7.9a and 7.10a. If addressed with a voltage above threshold, the periodically modulated LC layer acted as a diffraction grating.

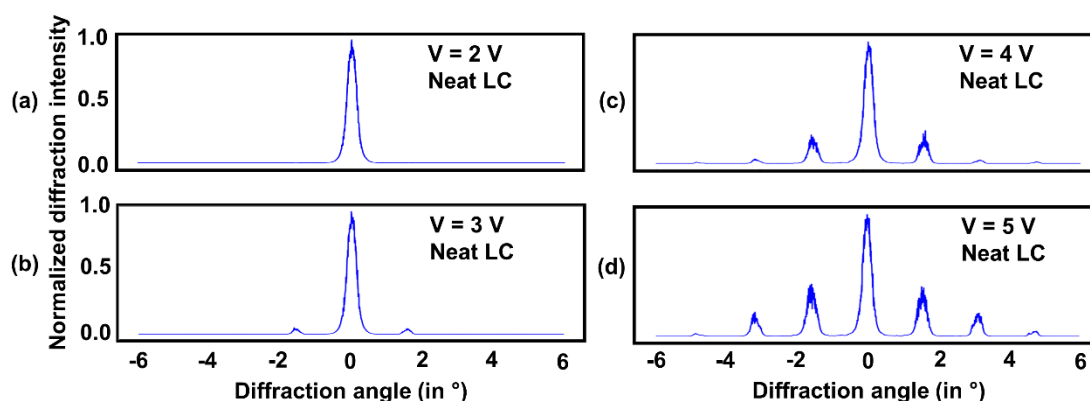


Figure 7.8*. Experimental diffraction patterns recorded at various addressing voltages in the neat NLC sample vs. diffraction angle (in $^{\circ}$). {The image was taken from Ref. 33}.

In the sample filled with a NLC, the minimum voltage to see diffraction patterns was $V_{\min} \approx 3V$ which is approximately equal to the threshold voltage for observing director realignments in a PNLC cell with average domain size of $2.2 \mu\text{m}$, though the accumulative optical phase delay determining the diffraction grating was effective at higher voltages. The diffraction patterns measured in the neat NLC sample are shown in Figure 7.8. At 3 and 4 V, a part of intensity was diffracted in the 1st diffraction order, while the main part of the intensity was still found in the 0th-order peak. Additional

diffraction orders appeared, if the voltage was further increased. However, the highest intensity was always distributed in the 0th-order peak³³.

A comparable behavior with the neat NLC cells was observed in an extended voltage range of 15 V – 35 V in PNLC samples with OPC 6% and 20 V – 60 V in PNLC samples with OPC 8%, as seen³³ in Figures 7.9 and 7.10, respectively, where the intensity was gradually diffracted from the 0th-order (the fundamental diffraction order) to the other orders with almost the same rate. By increasing the voltage beyond 35 V and 60 V in the PNLC cells with OPC 6% and 8%, respectively, the zeroth order intensity was significantly redistributed to the 1st-order peaks as the fundamental energy was seen in these peaks. By increasing the voltage beyond 50 V in the PNLC cells with OPC 6%, the intensity was recovered back to the 0th-order peak at the expense of the 1st diffraction order intensity, which finally leads to a Gaussian redistribution of the diffraction energy among all orders.

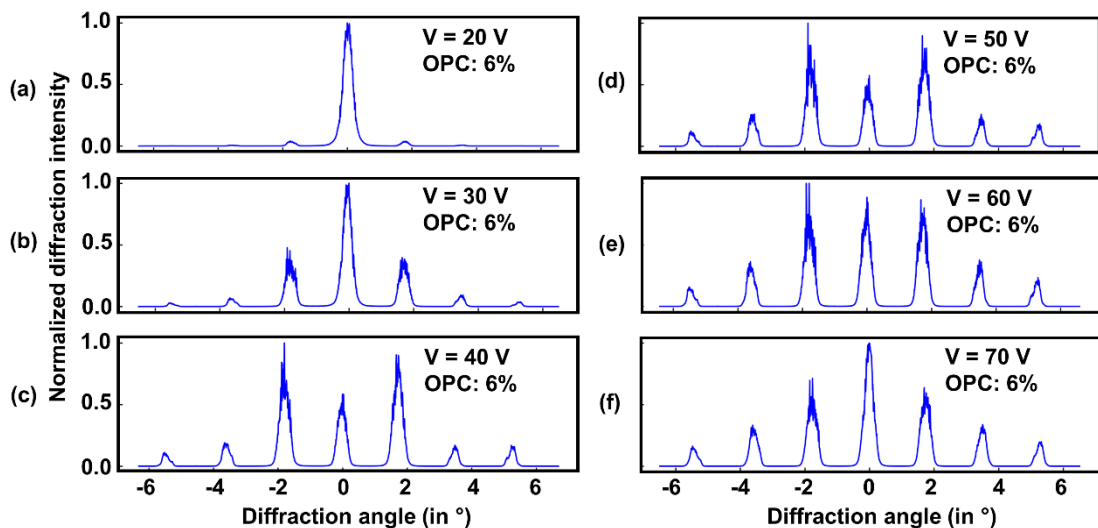


Figure 7.9*. Experimental diffraction patterns recorded at various addressing voltages in PNLC sample with 6% OPC vs diffraction angle (in $^{\circ}$). {The image was taken from Ref. 33}.

The main obstacle for the suppression of the zeroth diffraction order in the NLC is the low operating voltage and early director realignment saturation (at ~ 4 V), as at high voltages the similar behavior would be expected.

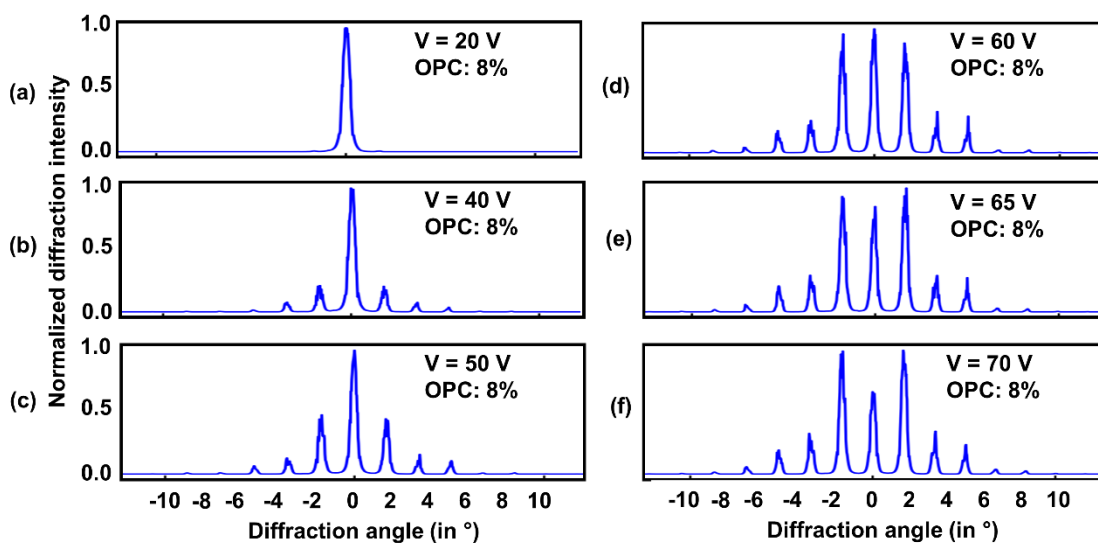


Figure 7.10*. Experimental results of diffraction patterns recorded at various addressing voltages in PNLC sample with 8% OPC vs diffraction angle. {The image was taken from Ref. 33}.

On the other hand, by increasing the voltage, in the PNLC samples with OPC 8%, the 0th order diffraction peak kept diminishing because of the continuous energy transfer to the 1st order peaks (Figures³³ 7.10 and 7.11). Simulation revealed that if the LC director realignment was not saturated at $V = 70$ V in the PNLC cell (OPC 8%) the same behavioral pattern would be seen as in the PNLC cell (OPC 6%) at higher voltages. The diffraction efficiencies extracted from the experimental data are shown in Figure 7.11.

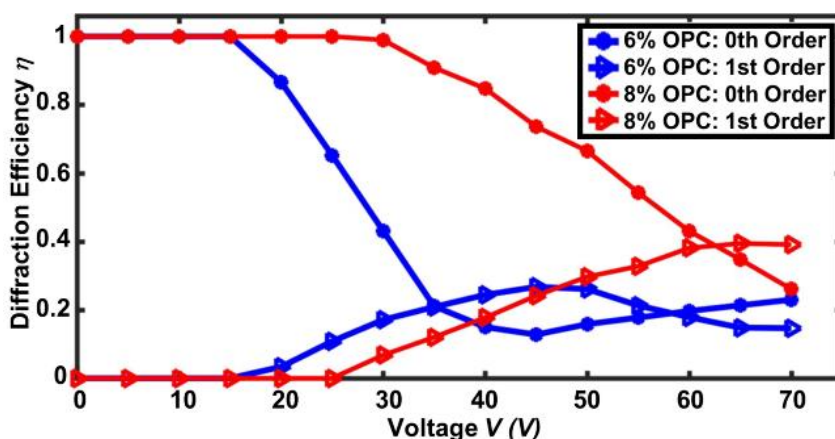


Figure 7.11*. Experimental diffraction efficiencies of 0th and 1st orders recorded in PNLC samples with 6% OPC (blue curves) and 8% OPC (red curves), respectively. {The image was taken from Ref. 33}.

In addition to the experiments performed with non-polarized light beam (results shown in Figures 7.8 to 7.11), the diffraction behavior of the PNLC IPS test cells was additionally studied with linearly polarized light beams. Diffraction patterns of a PNLC IPS cell with 6% OPC addressed with a voltage of 45 V and illuminated with horizontally- and vertically-polarized beams are demonstrated³³ in figures 7.12 b-d and e-g, respectively. The test cell exhibits the same diffraction behavior for all polarization states of the incident light beam if the analyzer was not employed. However, inserting an analyzer (second polarizer) between the test cell and screen resulted in the modulation of the intensity transmission and creation of different diffraction patterns. For example, for an x-polarized laser beam, placing the analyzer at the angle 45° relative to the polarizer caused the redistribution of the diffraction energy from the 0th order diffraction peak to the other orders.

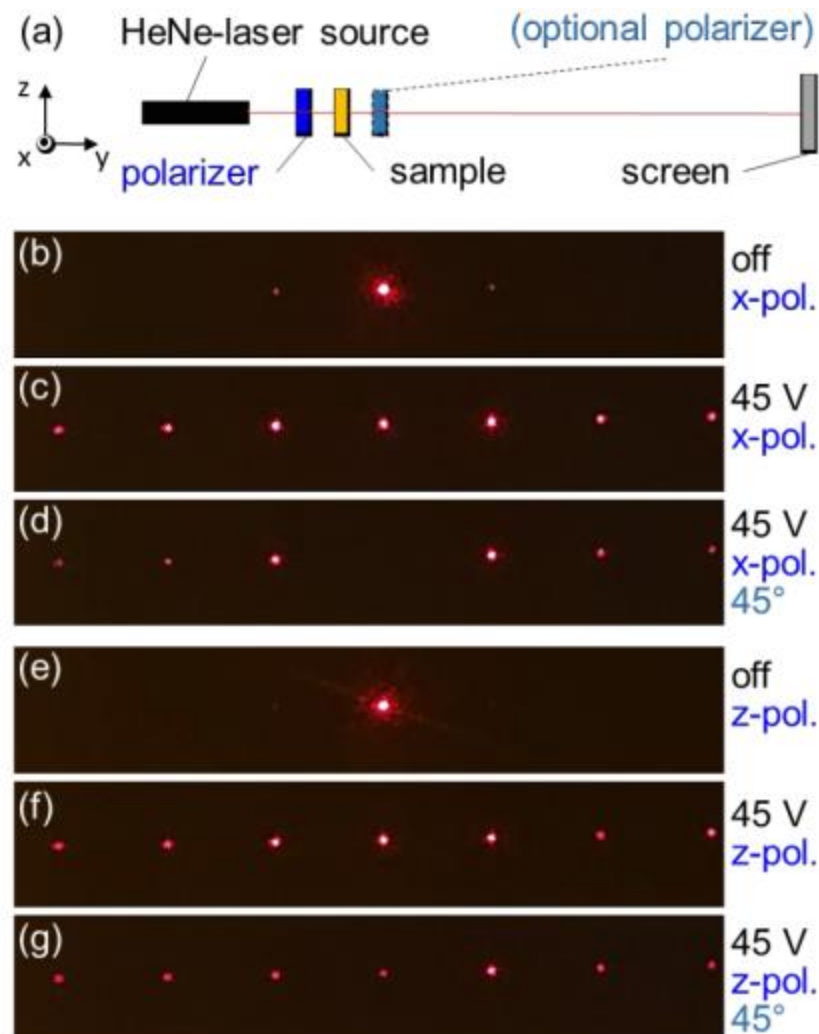


Figure 7.12*. The impact of the analyzer (optional polarizer) on the intensity modulations and diffraction pattern characteristics. a) The experimental set-up is

shown schematically. Diffraction patterns recorded in a PNLC sample (6% OPC) with horizontally (x-) and vertically (z-) polarized beams are shown in figures b) – d), and e) – g), respectively. {The image was taken from Ref. 33}.

7.4.5. Theoretical investigations and simulations

Here, I present the theory and the corresponding simulations which I developed in detail. In the simulations, the Q -tensor was numerically obtained in the modeled IPS test cells with 2D geometries because of the cell symmetry along the electrodes. However, the reorientation of the LC director from initial alignment, i.e., uniform in the z-direction, induced by the fringe electric field present in the test cells (with x- and y-components) was obtained in 3D from the director field components relation with the Q -tensor elements (equation (1.16)). The layer of the LC (or PNLC) had a thickness of $d = 10 \mu\text{m}$, sandwiched between two glass plates. A set of periodic interdigitated stripe-shaped transparent ITO electrodes was placed on the lower glass plate (Figure 7.13). The modeled test cells had a footprint of $x \times y = 0.125 \times 0.125 \mu\text{m}^2$.

In simulations with conventional test cells and fringe electric fields stemming from interdigitated electrodes, it was shown that a polymer network can be modeled by a mesh of cylindrical shaped stretched rods²⁵ forming cuboids. Such a space filling mesh of cuboids was placed inside the test cells: A two-dimensional schematic of the area of calculation is shown (Figure 7.13). These cuboids were assumed to be expanded in the z-direction and had a square cross section of $2.2 \times 2.2 \mu\text{m}^2$ (in the x- and y-direction). The length of $2.2 \mu\text{m}$ was chosen according to the experimentally seen domain size. An overall polymer content of 6% was considered, which was uniformly distributed between the cuboids. Each horizontal row (in x-direction) of cuboids was formed from randomly distributed cuboids. The cuboids were stacked in y-direction (Figure 7.13), which resulted in 4 rows of cuboids with square cross section and one row of thinner cuboids. This row of thin cuboids was placed far away from the electrode plane and thus in a position where the magnitude of the electric field was small.

Placing cuboids is a straight-forward approach to provide a space-filling arrangement of regularly spaced domains, which can provide alignment of the LC in the micro-structured samples. In order to show that the simulations were representative for the behavior of the irregularly spaced domains in the real samples,

simulations were later repeated with alternative structures, where the positions of the cuboids were randomly varied in the x -direction.

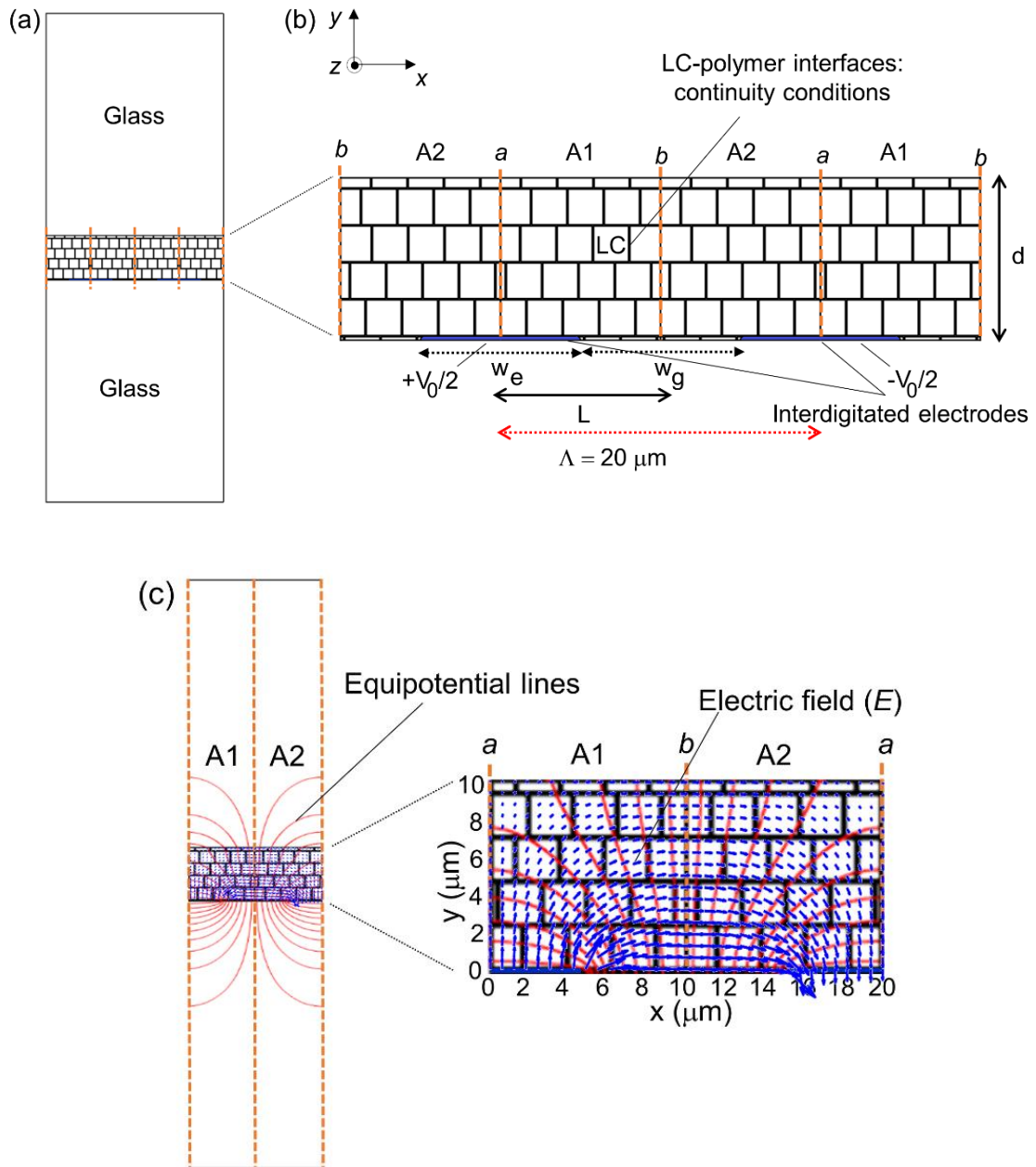


Figure 7.13. (a) and (b) Cross-sectional view of the geometry for the simulation of IPS test cells with electrode width w_e and gap size w_g of $10 \mu\text{m}$. Polymer domains were modeled with cuboids (expanded in z -direction). The cuboid mesh was made by swap transformation of domain A1 (with a length $L = 10 \mu\text{m}$). Additional boundary conditions were imposed on the electric field by placing virtual walls a and b in the IPS test cell. (c) Electric field (blue) and equipotential lines (red) shown in areas A1 and A2, selectively, which correspond to one period $\Lambda = 20 \mu\text{m}$.

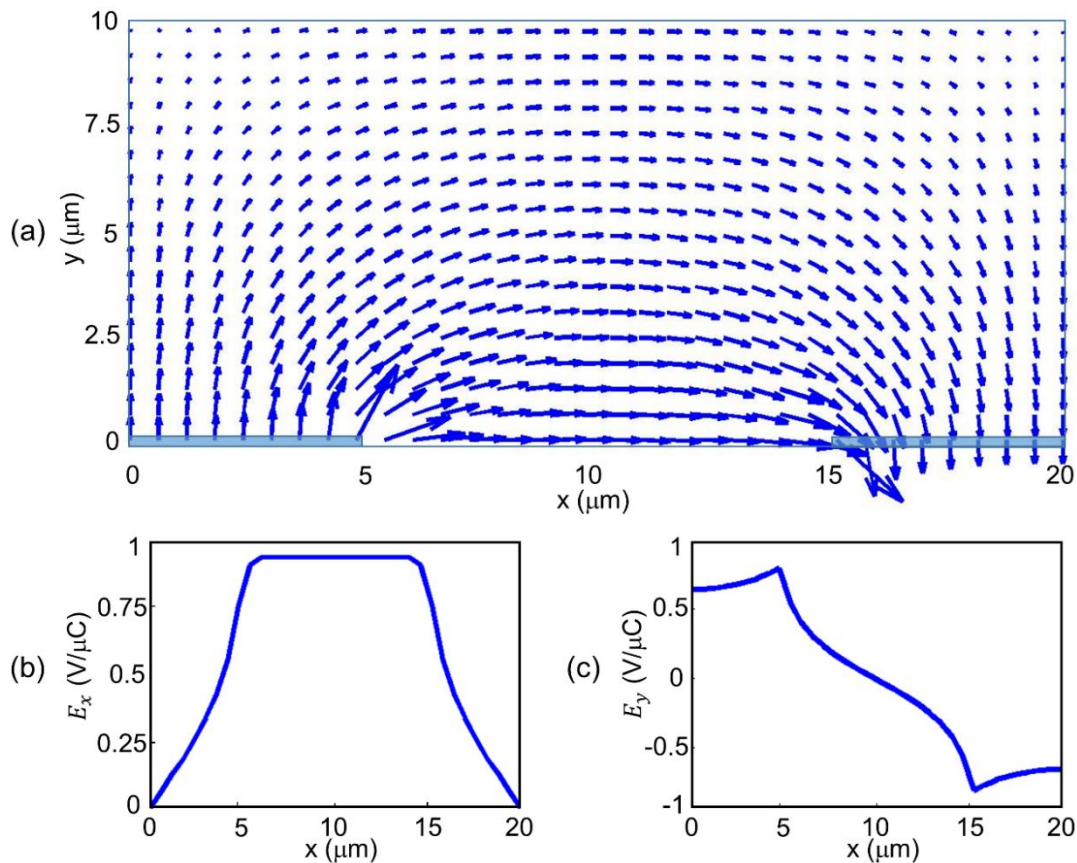


Figure 7.14. (a) The electric field distribution in one period ($\lambda = 20 \mu\text{m}$) is shown. (b) and (c) average values of the x- and y- components of the corresponding electric field are shown, respectively.

First, a single domain (A1, see Figure 7.13) was created and then a test cell with four domains was made from domain A1 through swap translation along the x-direction. An electric potential of $V_1 = +V_0/2$ and $V_2 = -V_0/2$, was placed at the two electrodes, and increased in magnitude, stepwise. Virtual walls (*a* and *b*) were considered as the specific boundary conditions for the electric potential^{34,35}, explained in the following in more detail (these virtual walls result in specific features of the director field configurations in addition to the boundary conditions at the LC cell confining surfaces and polymer network anchoring condition).

Due to the periodic electrode structure, a symmetric, periodic electric field was induced inside the sample with a periodicity of $\lambda = 20 \mu\text{m}$ (Figure 7.13c).

The LC had positive dielectric anisotropy and therefore, the director locally tended to take alignment parallel to the electric field direction³⁶. Competition between the electric field, induced realignment and anchoring at the polymer network can be

expected to imprint domains in the LC filled test cells^{25,37}. In the simulated PNLC, subdomains were formed by the inner regions confined in each polymer cuboid.

The LC can be described by using a tensor order parameter \mathbf{Q} (symmetric and traceless, $\mathbf{Q} = \mathbf{Q}^T$). According to the spectral decomposition theorem, it can be described in terms of eigenvectors $\{\mathbf{e}_1, \mathbf{e}_2, \mathbf{e}_3\}$ and eigenvalues $\{\lambda_1, \lambda_2, \lambda_3\}$, as^{38,39},

$$\mathbf{Q} = \sum_{i=0}^3 \lambda_i \mathbf{e}_i \otimes \mathbf{e}_i. \quad (7.7)$$

The condition of being traceless i.e., $\text{tr}(\mathbf{Q}) = 0$, provides the following constrain on the eigenvalues,

$$\lambda_1 + \lambda_2 + \lambda_3 = 0. \quad (7.8)$$

\mathbf{Q} can be converted to the director-field \mathbf{n} (which describes the orientation of the LC as a pseudo vector field). Since a nematic is a uniaxial state, \mathbf{Q} -tensor elements can be acquired from the simplified form³⁸⁻⁴⁴,

$$Q_{ij} = \frac{3}{2} S \left((\mathbf{n} \otimes \mathbf{n})_{ij} - \frac{\delta_{ij}}{3} \right) \quad (7.9)$$

where \mathbf{n}_i ($i = 1, 2, 3$) are the director-field components representing $(\mathbf{n}_x, \mathbf{n}_y, \mathbf{n}_z)$, the coefficient $\frac{3S}{2}$ with S the scalar order parameter was assumed equal to 0.67 for the NLC E7⁴⁵ at room temperature and δ_{ij} is the Kronecker-delta function.

The electric displacement field $\mathbf{D} = \epsilon_0 \epsilon \mathbf{E}$ (where \mathbf{E} and ϵ are the fringe electric field and the media dielectric constant, respectively, and ϵ_0 is the vacuum permittivity) was obtained by numerically solving the differential form of Gauss' law, with a total free charge density $\rho = 0$ in the entire cell:

$$\nabla \cdot \mathbf{D} = 0. \quad (7.10)$$

The presence of LC and polymer has a distinct influence on the electric field distribution in the sample. The LC dielectric constant ϵ was considered as a second rank tensor $\epsilon_{ij} = \bar{\epsilon} \delta_{ij} + \Delta \epsilon \mathbf{Q}_{ij}$ ^{42,43}, with the average dielectric constant of $\bar{\epsilon} = \frac{1}{3}(\epsilon_{\parallel} + 2\epsilon_{\perp})$ and the dielectric anisotropy $\Delta \epsilon = \epsilon_{\parallel} - \epsilon_{\perp}$, $\epsilon_{\parallel} = 19$, $\epsilon_{\perp} = 5.2$ for the NLC E7⁴⁵. For the polymer cuboids, a value of $\epsilon^{Polymer} = 14.4$ was assumed. The evolution of the

dielectric permittivity induced by the electric voltage variation is discussed in Appendix B.

At the interfaces of the LC with the polymer cuboids, the tangent component of the electric field ($\mathbf{E} = -\nabla V$, where V is the electric potential), and the normal components of the electric displacement field \mathbf{D} fulfilled the continuity conditions; $\mathbf{E}_{\parallel}^{LC} = \mathbf{E}_{\parallel}^{Polymer}$ and $\mathbf{D}_{\perp}^{LC} = \mathbf{D}_{\perp}^{Polymer}$. For the polymer cuboid walls (polymer-LC boundaries) extended in the xz -plane, the following continuity conditions were considered:

$$\frac{\partial V^{LC}}{\partial x} = \frac{\partial V^{Polymer}}{\partial x}, \quad (7.11)$$

$$\left(\epsilon_{21} \frac{\partial V^{LC}}{\partial x} + \epsilon_{22} \frac{\partial V^{LC}}{\partial y} \right) = \left(\epsilon^{Polymer} \frac{\partial V^{Polymer}}{\partial y} \right). \quad (7.12)$$

Similarly, the boundary conditions for the polymer cuboid walls located in the yz -plane were defined as,

$$\frac{\partial V^{LC}}{\partial y} = \frac{\partial V^{Polymer}}{\partial y}, \quad (7.13)$$

$$\left(\epsilon_{11} \frac{\partial V^{LC}}{\partial x} + \epsilon_{12} \frac{\partial V^{LC}}{\partial y} \right) = \left(\epsilon^{Polymer} \frac{\partial V^{Polymer}}{\partial x} \right), \quad (7.14)$$

where ϵ_{11} , ϵ_{12} , ϵ_{21} and ϵ_{22} are components of the LC dielectric tensor ϵ_{ij} . Equations (7.12) and (7.14) can be simplified, if the director field alignment in the z -direction at the cuboid surfaces is known. The boundary condition for the electric potential at the center of electrode regions was assumed $\frac{\partial V}{\partial x} = 0$. Therefore, the in-plane component \mathbf{E}_x had to fulfill the condition $\mathbf{E}_x = 0$ in the virtual walls a (Figure 7.13). At the centers of the electrode gaps, equipotential surfaces with $V = 0$ (equal to the average addressing voltage at the center of the electrode gap) were present (virtual walls b). The glass substrates were considered to be much thicker than the LC slab, therefore we speculate that the electric field produced by the fringe electrodes decays to zero at the outer surfaces of the glass substrates, and so we applied a ground condition at these surfaces.

The interaction of LC and electric field E was described by the electric potential energy density E_E ($E_E = -\frac{1}{2} \mathbf{D} \cdot \mathbf{E}$, with the electric displacement field \mathbf{D} defined as $\mathbf{D}_i = \varepsilon_0 \varepsilon_{ij} \mathbf{E}_j$)^{43,44}:

$$E_E(\mathbf{Q}_{ij}) = -\frac{1}{2} \varepsilon_0 (\bar{\varepsilon} \delta_{ij} (\partial_i V) (\partial_j V) + \Delta \varepsilon (\partial_j V) (\partial_k V) \mathbf{Q}_{jk}). \quad (7.15)$$

In a thermodynamically stable state, the LC realignment induced by the electric field can be numerically simulated by exploiting the Euler–Lagrange equation^{42,43},

$$K \nabla^2 \mathbf{Q}_{ij} + \varepsilon_0 \varepsilon_{ij} (\partial_i V) (\partial_j V) = 0 \quad (7.16)$$

where K is the mean elastic constant obtained from the Franck elastic constants K_{ii} ; In voltage off state, all deformations of splay, twist and bend are zero. A mean elastic constant as $K = (K_{11} + K_{22} + K_{33})/3$ was employed. Hence beyond the threshold, all deformations increase with the same rate. Data for E7⁴⁷ were used ($K_{11} = 11.1$ (pN), $K_{22} = 10.32$ (pN), and $K_{33} = 17.1$ (pN)). Anchoring of the LC at the planar glass cell surfaces and electrodes was supposed infinitely strong (orientation of the director in z -direction). Anchoring at the polymer cuboid surfaces s was taken into consideration by using the surface anchoring energy density f_s , described as^{40,41},

$$f_s^{(i)} = \frac{w^{(i)}}{2} \text{Tr} \left(\mathbf{Q} - \mathbf{Q}_s^{(i)} \right)^2 \quad (7.17)$$

where i denoted the number of lateral surfaces of each cuboid, $w^{(i)}$ was the anchoring strength parameter with the limitation of $w^{(i)} \rightarrow \infty$ for the strong anchoring condition, and $\mathbf{Q}_s^{(i)}$ was used to describe the preferential orientation at each surface.

The cuboids were rectangular, hollow tubes. They provided strong anchoring for the LC, keeping the LC orientation in the initial alignment near their surfaces. Preferential alignment at the polymer cuboid surfaces was described by \mathbf{Q}_s , as,

$$\mathbf{Q}_s = \left(\frac{1}{2} S \right) (-\mathbf{e}_1 \otimes \mathbf{e}_1 - \mathbf{e}_2 \otimes \mathbf{e}_2 + 2\mathbf{e}_3 \otimes \mathbf{e}_3), \quad (7.18)$$

which resulted in the desired director field alignment in the z -direction^{40,48}. Alternative approaches were tested but the reported approach resulted in the correct initial LC orientation parallel to the z -direction (as seen in the experiments) and was feasible to yield field induced LC orientations at the same time.

7.4.6. Director field simulation and observation of disclination walls

The field induced director reorientations in one period Λ (domains A1 and A2 in Figure 7.13) are selectively shown for a sample without polymer (Figure 7.15) and with polymer cuboids (Figure 7.16). Initially (in the voltage-off state), the director field was uniformly aligned along the z-direction, parallel to the electrodes in both type of samples. In all samples, anchoring at the cell confining surfaces (at $y = 0$ and $y = 10 \mu\text{m}$) was supposed along the z-direction. In the voltage-on state (see the electric field distribution shown in Figure 7.14), the LC director tended to reorient parallel to the electric field direction. The in-plane component of the electric field E_x , which caused the rotation of the LC director in the xy -plane, reached its maximum value at the electrode gap center at $x = 10 \mu\text{m}$ (virtual wall b in Figure 7.13).

As seen in Figures 7.15 and 7.16, the LC director fields were continuously reoriented between the electrodes from initial alignment along the z-direction (parallel to the electrodes) toward the xy -plane by the in-plane electric field E_x . The reorientation along the x-direction was most pronounced at the electrode gap region; The maximum rotation of the director field was achieved by E_x at the gap centers, where E_x is maximum.

As seen in Figure 7.16, the realigned director field was clearly influenced by the presence of polymer domains: For example, the responses were much more confined and most pronounced in the first layer of cuboids ($y = 0 \dots 2.2 \mu\text{m}$). The electric field had a higher magnitude in this area than in the upper layers. The impact of the polymer is best seen in the three-dimensional plots Figures 7.16a and c and from the evolution of the azimuthal and polar angles, ϑ and ϕ , (Figure 7.17). The uneven shape of the corresponding profiles of ϑ and ϕ was due to the strong anchoring at the polymer walls with zero impact on the phase grating; It was found that only the overall envelope of each profile determines the output diffraction profile. The simulations clearly revealed how the LC director in different domains of a PNLC can be reoriented independently of the surrounding domains. As expected, this behavior resulted in a severely changed optical behavior of these samples.

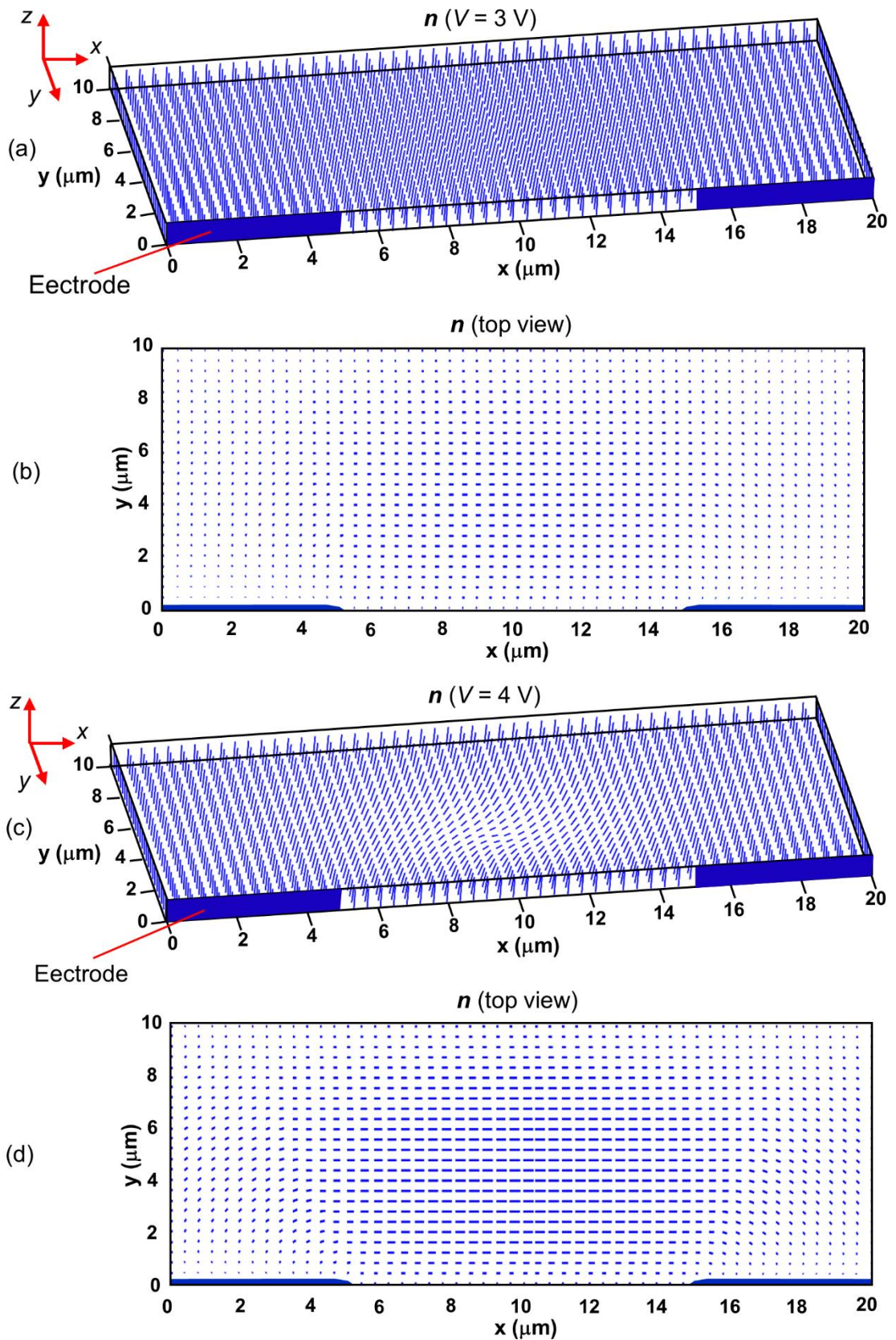
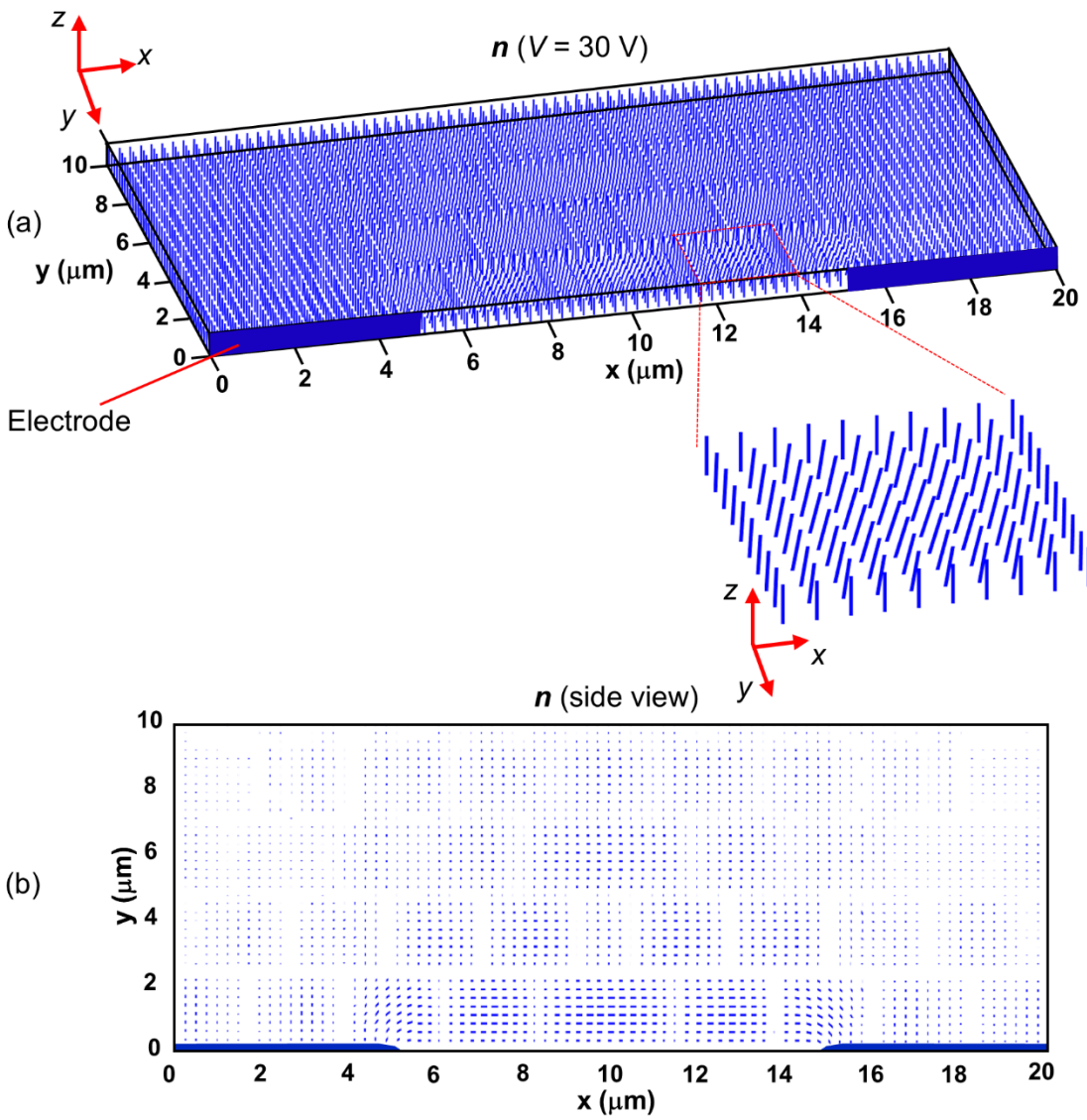


Figure 7.15. Simulated director field in a sample filled with undoped E7. (a, b) At an applied voltage of 3 V, and (c, d) at an applied voltage of 4 V. The electrodes are highlighted in blue color.



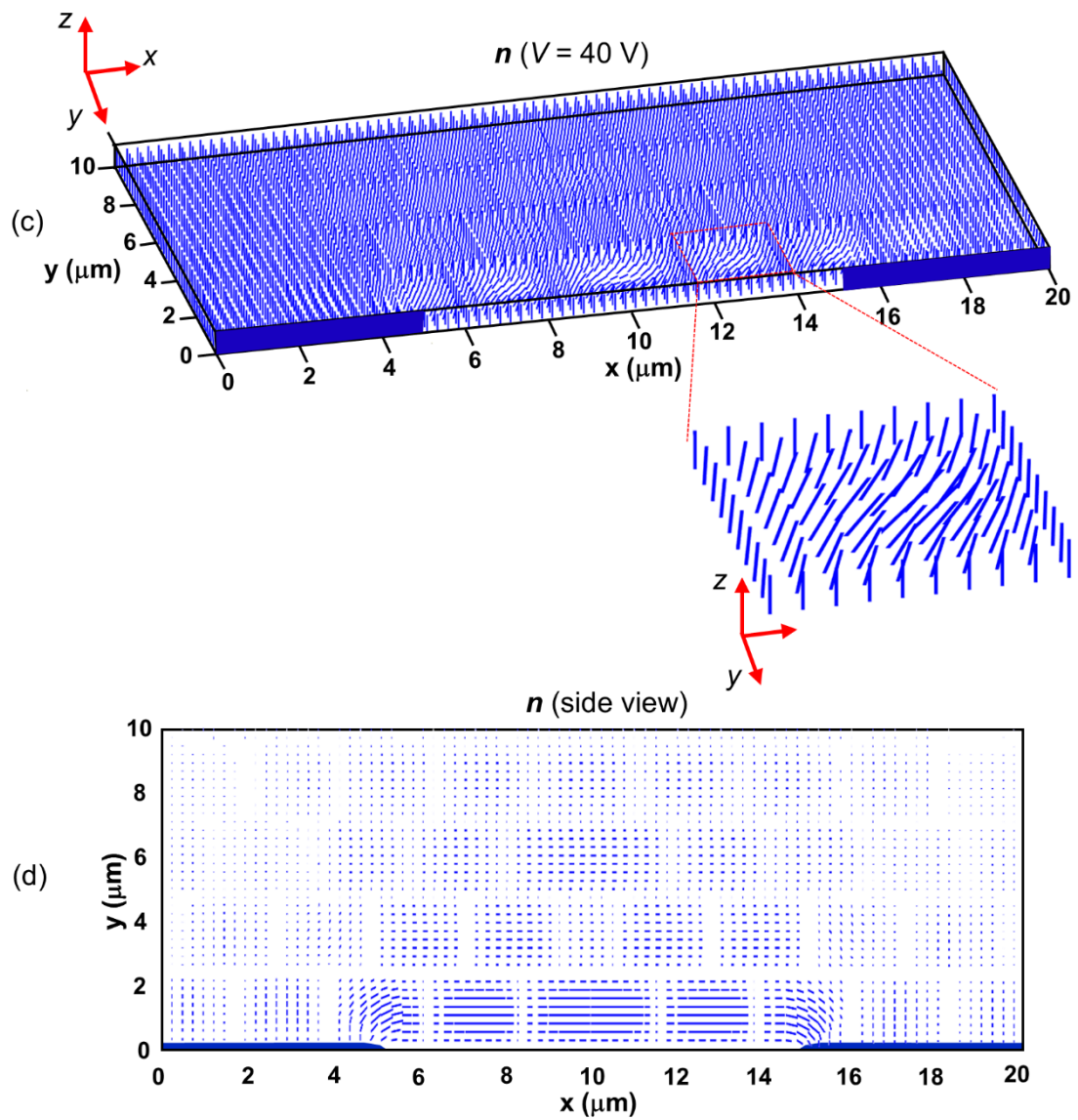


Figure 7.16. Director field distribution in the PNLC: (a, b) At an applied voltage of 30 V, and (c, d) at an applied voltage of 40 V. The electrodes are highlighted in blue color.

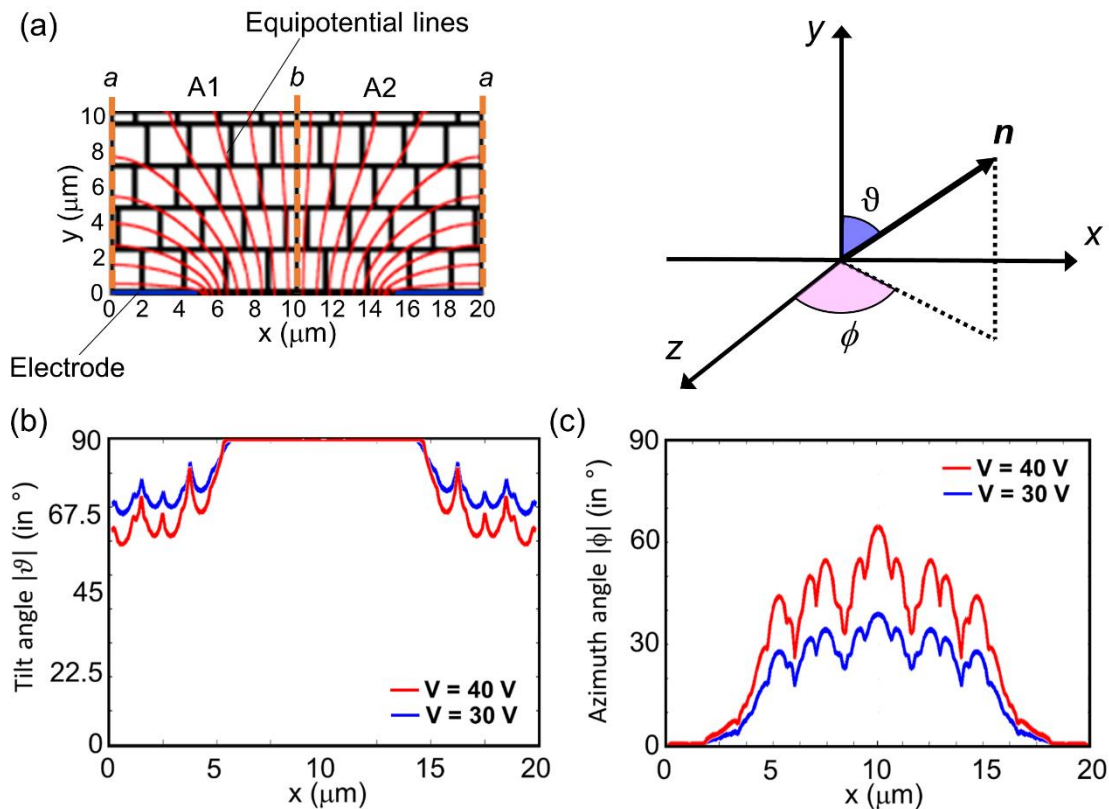


Figure 7.17. Voltage induced evolution of the azimuthal and polar angles, ϑ and ϕ , in the PNLC cell (shown in (a)) in one period, corresponding to the director realignments shown in Figure 7.16, demonstrated in (b), (c), respectively. The profiles of ϑ and ϕ were shown in absolute values.

At the electrode centers (at $x = 0$ and $20 \mu\text{m}$ in Figures 7.13, 7.14 in the place of the virtual walls a), the LC realignment was additionally influenced by the almost vertical electric field E_y residing in this area with the tendency to tilt the director field. Hence, the tilt angle reaches its maximum value at the electrode center (Figure 7.17 b). In the domains A1, by increasing distance from the electrode centers, where the in-plane electric field E_x is zero and the vertical electric field E_y is maximum, there existed a conflict in realigning the director field because of the growing in-plane electric field strength with the tendency to rotate the director field in the xz -plane. However, due to the mirror symmetry of the electric field, the opposite trend is present in the domains A2 as the director field is rotated by the in-plane electric in opposite direction relative to the virtual walls a at the electrode centers.

As seen in Figure 7.14, the electric field fringes, especially in the area around $y = 3 \mu\text{m}$. In the area $x = 0 \dots 5 \mu\text{m}$, these fringe fields are inclining (acute angle). In

the area $x = 15 \dots 20 \mu\text{m}$, the fringe fields are declining (obtuse angle). Accordingly, there is an electrically induced torque in clockwise direction or counterclockwise direction, respectively. Accordingly, disclination walls form above the electrodes. In such disclination walls, the director field continuously changes its orientation in the transverse xz -plane from $-\phi$ to ϕ relative to the electrodes centers. This behavior was seen due to the zero rubbing angle at the electrode surfaces resulting in a symmetric LC director configuration (providing a small pretilt angle less than 3° to avoid unwillingly random domains)³⁴. If rubbing angle was large, then the director field is mainly influenced by the anchoring energy and elastic interactions as the similar realignments, with the same azimuth angle and same sign, with respect to the electrode centers was expected at opposite sides of electrode regions giving rise to director field asymmetric configurations³⁴.

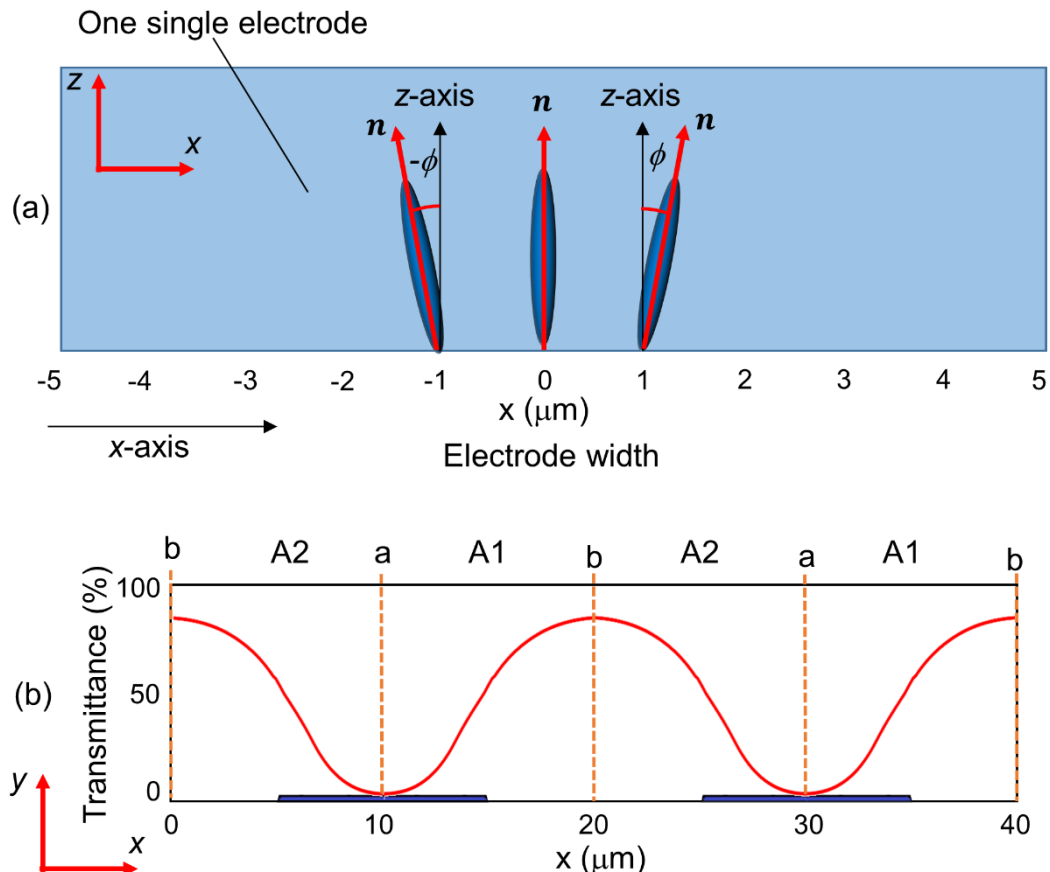


Figure 7.18. Simulated transmittance of an IPS cell filled with neat E7 LC, and biased with a voltage of $V = 4 \text{ V}$ between crossed linear polarizers (the transmission axis of one of the crossed polarizers was supposed parallel to the electrodes direction). Transmittance goes to zero at the locations of the disclination walls formed along the centers of the electrodes.

Since director field keeps its projection along the electrodes at the centers of the electrodes (Figure 7.18a), light transmittance goes to zero along the centers between crossed linear polarizers (Figure 7.18b). The intensity distribution in two periods (Figure 7.18b) clearly shows how these walls would appear between crossed linear polarizers.

The neat LC samples were experimentally checked for the formation of the disclination walls; It was found that the disclination walls can appear along the electrodes in the neat LC cells above the threshold voltage where the transmittance goes to zero between linear crossed polarizers.

7.4.7. Simulated optical phase delays

The simulated LC director field distributions in the domains A1 and A2 (Figure 7.13) were imported to Matlab as three-dimensional data $\mathbf{n}(x, y, z)$ and post-processed; From the director field, a train of four one-dimensional optical phase delay distributions was constructed and the diffraction patterns were obtained by calculating fast Fourier transforms (FFT). Diffraction patterns were obtained by considering effective refractive index distributions⁴⁹. The local optical axis of LC was parallel to the local director. The distortion angle of the director with respect to the light propagation direction (perpendicular to the cell surface oriented in the y -direction), i.e., ϑ , was obtained from $\vartheta = \arcsin n_y$, where n_y can be obtained from the relation $Q_{22} = \frac{3S}{2} \left(n_y n_y - \frac{1}{3} \delta_{22} \right)$. As a result, the position dependent effective refractive index $n_{\text{eff}}(\vartheta(x, y, z))$, defined as^{37,50},

$$n_{\text{eff}}(\vartheta) = \frac{n_o n_e}{\sqrt{n_e^2 \sin^2(\vartheta) + n_o^2 \cos^2(\vartheta)}}, \quad (7.19)$$

was calculated for each lattice point (x, y, z) , where ordinary and extraordinary refractive indices were considered equal to $n_o = 1.52$ and $n_e = 1.75$, respectively.

In a straight-forward approach, the optical phase change profile $\Gamma(x)$ for an optical plane wave at a given wavelength (λ) was calculated by:

$$\Gamma(x) = \left(\frac{2\pi}{\lambda}\right) \int_0^d (n_{\text{eff}}(\vartheta) - n_o) dy, \quad (7.20)$$

where $d = 10 \mu\text{m}$ was the cell thickness³⁷ (this approach is correct for x-polarized light). A laser wavelength of $\lambda = 632 \text{ nm}$ was considered. In the voltage off-state, unpolarized light propagates with maximum optical phase change $\Gamma = 21.84 = 3.48(2\pi)$ (uniform throughout the test cell, no diffraction).

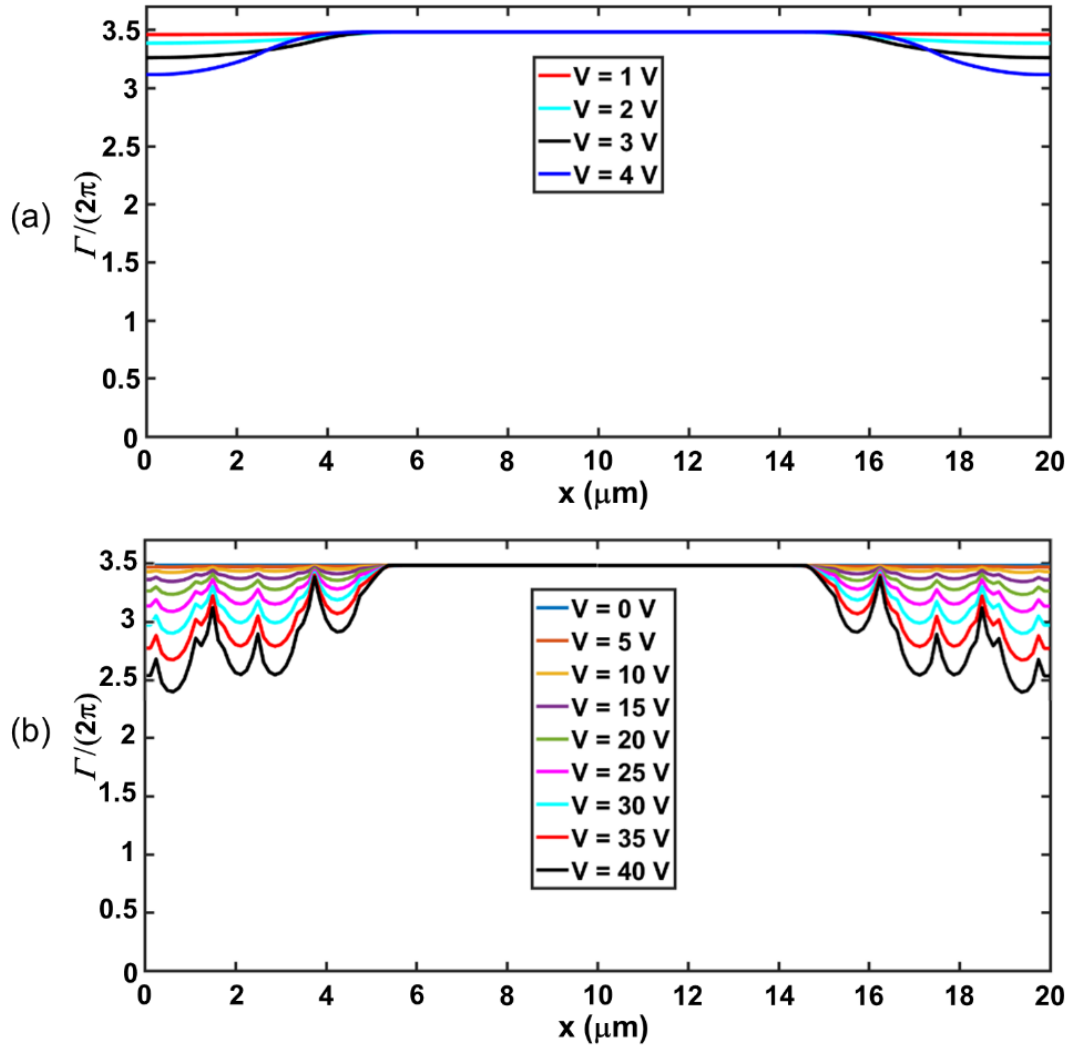


Figure 7.19. Numerically calculated phase change profiles in IPS test cells. (a) NLC in the voltage range of 0 to 4 V in steps of 1 V. (b) PNLC in the voltage range of 0 to 40 V in steps of 5 V.

The voltage dependent optical phase change vs. x is shown in Figure 7.19. For both the neat LC and the PNLC, the phase change profiles were constant in the voltage off-state. In the neat LC, a typical threshold behavior was seen, where the phase change profile could be described by a step-like envelope at voltages exceeding the

threshold ($V_{th} = \pi(K/(\epsilon_0\Delta\epsilon))^{1/2}$)⁴⁶ of 0.78 V (Figure 7.19a). The phase change profile slightly varied by further increasing the addressing voltage near the saturation voltage because of minor reorientations. For the case of a PNLC, higher voltages were required. Here, a continuous response was seen, where the phase change varied continuously with increasing addressing voltages (Figure 7.19b). The presence of the polymer network resulted in a modulation of the phase change profiles, which now showed a number of small pulses approximately 2 μm wide (\approx cuboid size) due to the polymer distributions. However, it was found that only the curve envelopes are determining the output results (after checking many different distributions and comparing their corresponding results). At higher voltages, the phase modulation depth for the PNLC reached 2.2π .

For studying diffraction gratings, the phase change profiles were coalesced (considering mirror symmetry at the half-period edges) to describe a train of grating periods, which is advantageous for applying Matlab's FFT-algorithm. The merged phase change profiles $\Gamma(x')$ were used to determine the complex phase grating transmission function $T(x')$, through^{51,52}:

$$T(x') = \exp(i\Gamma(x')). \quad (7.21)$$

7.4.8. Simulated diffraction patterns

The diffraction patterns were obtained by numerically calculating Fourier transforms of the phase grating transmission function $T(x')$ ⁵³⁻⁵⁵. Finally, the voltage dependent diffraction efficiency $\eta_N(V)$ was calculated from,

$$\eta_N(V) = I_N(V)/I_{tot}(V_0), \quad (7.22)$$

where $I_N(V)$ and $I_{tot}(V_0)$ were the intensities in the diffraction order N ($N = 0, 1, 2, \dots$) at a given voltage V and the total intensity in the initial state, respectively^{11,18}.

The diffraction behavior in the neat LC was straightforward: The maximum intensity was always found in the 0th order at any given voltage. By increasing the addressing voltage beyond threshold, the intensity distribution in the 1st-order gradually increased (Figure 7.20). A comparison of the simulated diffraction patterns

was shown in Figure 7.20. The intensity of the 1st- and 2nd-orders diffraction peaks increased with increasing voltage (at almost the same rate). The diffraction peaks resemble the experimental ones well, because the most important feature of the optical phase modulation profiles was contrast (step like modulation) between the area above the electrodes and between the electrodes.

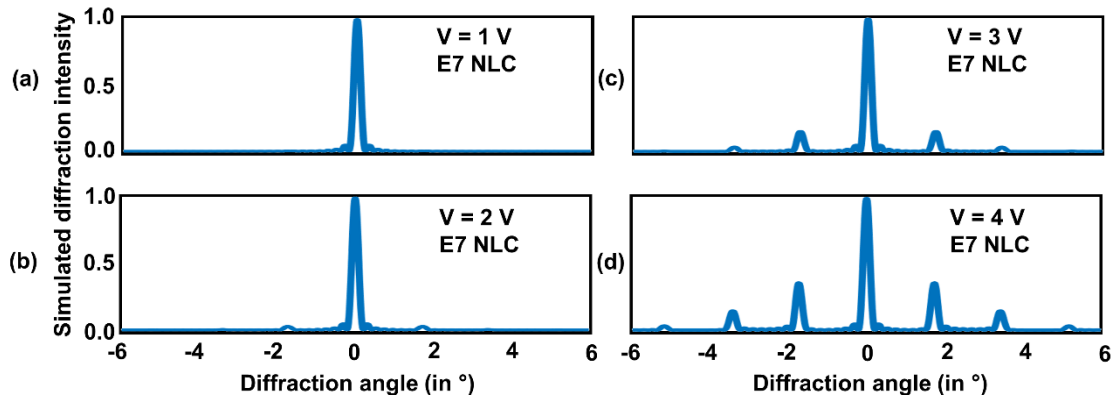


Figure 7.20. Simulated normalized diffraction intensities for the neat NLC addressed with voltages $V = 1, 2, 3$ and 4 V, respectively, for a light beam with the wavelength of $\lambda = 632$ nm. LC initial alignment was supposed being parallel to the electrodes. Saturation in LC realignments happened near to $V = 4$ V.

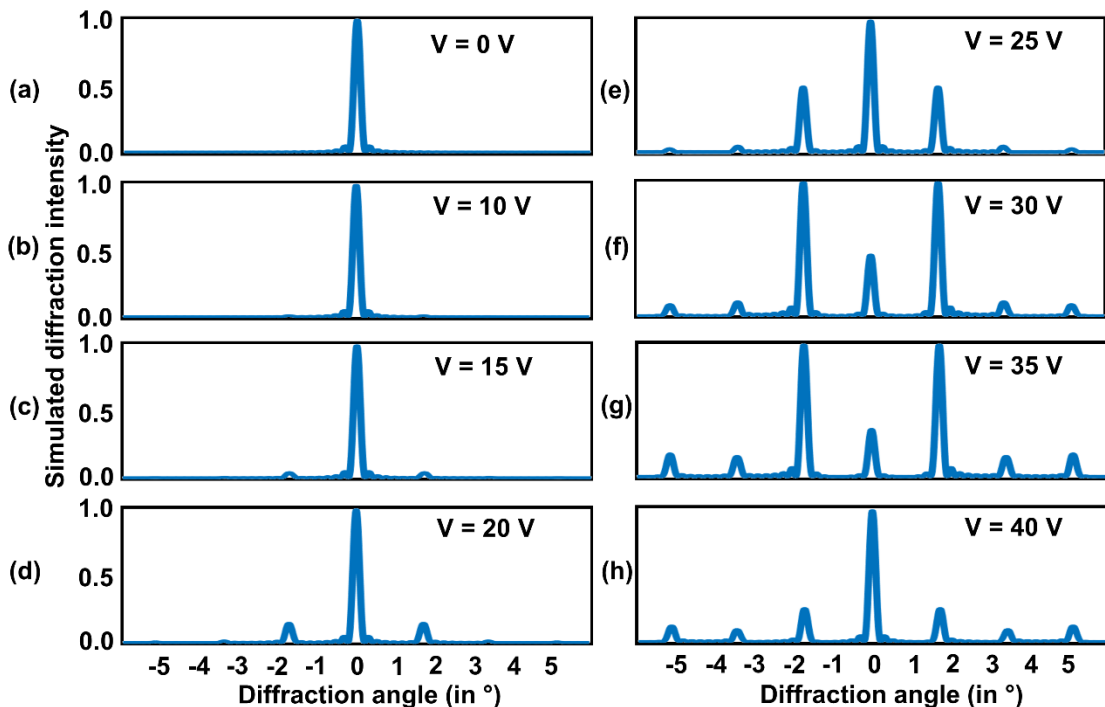


Figure 7.21. Simulated normalized diffraction intensities in the PNLC (with OPC 6%) at selective voltages $V = 0, 10, 15, 20, 25, 30, 35$ and 40 V vs diffraction angle (in degrees) made from a sequence of geometries shown in Figure 7.13.

For PNLC IPS test cells, numerical results show that the realignment of LC molecules started above threshold voltage in regions nearby the electrodes. Here, the local electric field was high enough to change the initial alignment of the LC director field, although the accumulative effect on the average director field and, subsequently, phase change profiles were low until $V = 15$ V. Accordingly, from 0 V to 10 V, almost non-diffracted light was seen (pronounced 0th-order peak), which resulted a diffraction efficiency of 1 for the 0th-order peak. By increasing voltage from zero to 25 V, diffraction energy was gradually transferred from the 0th-order peak to the other peaks specifically 1st-order peaks, however, approximately Gaussian envelopes could be attributed to the diffraction intensity profiles by $V = 25$ V (Figure 7.21c-e). By continuously increasing the addressing voltage, the 0th-order diffraction efficiency decreased to a minimum value less than 0.2, while the first order diffraction efficiency noticeably reached to its maximum value at $V = 35$ V (Figure 7.21g and Figure 7.22). By further increasing the voltage beyond 35 V, intensity was retransferred from the 1st-order peaks back to the 0th-order (Figure 7.21h and Figure 7.22). The simulation geometry (the position of the cuboids in the mesh) was varied (see Appendix C), and similar outcomes were obtained for different random distributions of the cuboids (Figure 7.22).

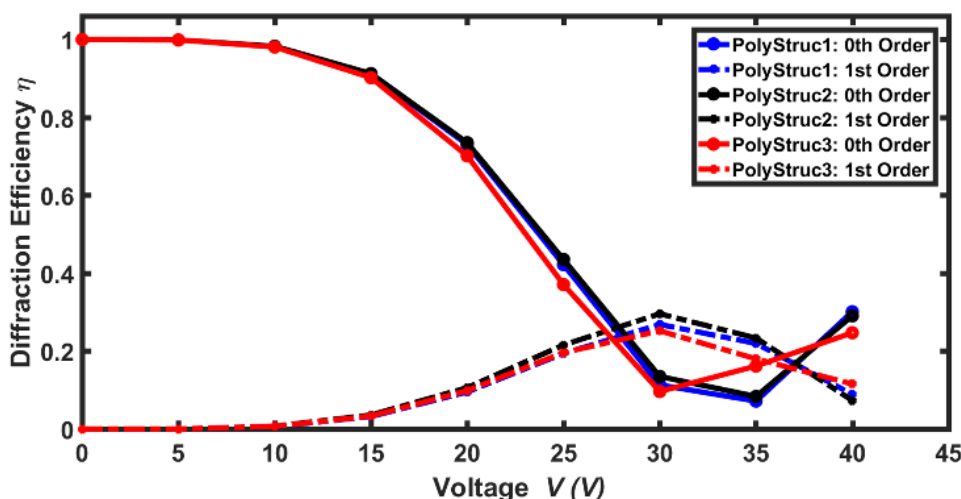


Figure 7.22. Numerically calculated the 0th and 1st diffraction orders efficiencies for three test cells filled with different randomly distributed polymer cuboids with 6% OPC. Polymer structure 1 is shown in Figure 7.13, the alternative structures are included in the Supporting Information.

Interestingly, due to the presence of polymer network, the 0th-diffraction order could be suppressed which can have useful applications for example in quantum spectroscopy. This behavior is in a good agreement with the experimental results.

7.4.9. Conclusions

The diffraction behavior of a PNLC was investigated. Experimental results such as the domain size were used to develop a numerical model. The simulation results were compared with experimental data. In the simulations, the field dependent director fields in the test cells were obtained. From these data, the optical phase modulation profiles were calculated and, subsequently, the corresponding diffraction patterns were simulated by applying the fast Fourier transform (FFT) method.

In the case of a non-doped NLC, the phase modulation profiles can be described with a step-like envelop. Introducing polymer network led to a considerable deformation of the phase modulation profile caused by anchoring torque exerted by the porous polymer network. A continuous modulation was found and understood in detail. The domain size in the samples was also found in the phase modulation profiles. This finding is particularly interesting, since it shows how the electro-optic modulation can be spatially confined and controlled by the presence of a tailored polymer network. The simulated results are in good agreement with experimental findings. Due to the continuous phase modulation, PNLCs can yield a higher variety in diffraction patterns, while it has been possible to suppress the 0th-order peak drastically even in a rather straight forward LC test cell with constant electrode width and gap ratio. We believe that the method of using cuboids of appropriate sizes to model polymer network LCs and copolymer network LCs and their responses in non-homogeneous fields can lead to much more efficient uses of these promising composite materials in optical devices such as tunable gratings and complex diffractive elements, holograms and waveplates. It is impressive how the presence of domains can elastically decouple the elastic interactions of the LC confined in the neighboring domains, which is not possible in an undoped LC.

Declaration

Figures 7.4 – 7.13, 7.15 – 7.16, 7.19 – 7.22 reprinted with permission from the associated journal of the publication " {Habibpournoghadam, A., Wolfram, L., Jahanbakhsh, F., Mohr, B., Reshetnyak, V., & Lorenz, A. (2019). Tuneable Diffraction Gratings in Copolymer Network Liquid Crystals Driven with Interdigitated Electrodes. ACS Applied Electronic Materials, 1(12), 2574-2584.}. Copyright © 2019 American Chemical Society. "

Acknowledgments

Figures 7.5 and 7.6 were provided by Dr. Alexander Lorenz (Uni. Paderborn & Uni. Kassel, Germany) and Ms. Fatemeh Jahanbakhsh (Uni. Kassel, Germany–Uni. Bonab, Iran). Figure 7.7 was made by Ms. Fatemeh Jahanbakhsh, and with Mr. Benedikt Mohr (Uni. Kassel, Germany). Figures 7.8 – 7.10 were obtained by Lukas Wolfram (Uni. Kassel). The figures 7.12 was provided by Dr. Alexander Lorenz. All are highly acknowledged and appreciated.

The Figure 7.11 was obtained from the experimental data reported for the Figures 7.9 and 7.10. The providence is greatly appreciated.

References

- ¹ Steward, E. G. (2004). *Fourier optics: an introduction*. Courier Corporation.
- ² Goodman, J. W. (2005). *Introduction to Fourier optics*. Roberts and Company Publishers.
- ³ Gao, H., Ouyang, M., Wang, Y., Shen, Y., Zhou, J., & Liu, D. (2007). Analysis on diffraction properties of the transmission phase grating. *Optik*, 118(9), 452-456.
- ⁴ Bracewell, R. N. (1986). *The Fourier transform and its applications* (Vol. 31999). New York: McGraw-Hill.
- ⁵ Duffy, D. G. (2016). *Advanced engineering mathematics with MATLAB*. Chapman and Hall/CRC.
- ⁶ Apter, B., Efron, U., & Bahat-Treidel, E. (2004). On the fringing-field effect in liquid-crystal beam-steering devices. *Applied optics*, 43(1), 11-19.
- ⁷ Lorenz, A., Gardiner, D. J., Morris, S. M., Castles, F., Qasim, M. M., Choi, S. S., ... & Wilkinson, T. D. (2014). Electrical addressing of polymer stabilized hyper-twisted chiral nematic liquid crystals with interdigitated electrodes: Experiment and model. *Applied Physics Letters*, 104(7), 071102.
- ⁸ Hyman, R. M., Lorenz, A., & Wilkinson, T. D. (2016). Phase modulation using different orientations of a chiral nematic in liquid crystal over silicon devices. *Liquid Crystals*, 43(1), 83-90.
- ⁹ Weiner, A. M. (2000). Femtosecond pulse shaping using spatial light modulators. *Review of scientific instruments*, 71(5), 1929-1960.
- ¹⁰ James, S. W., & Tatam, R. P. (2003). Optical fibre long-period grating sensors: characteristics and application. *Measurement science and technology*, 14(5), R49.
- ¹¹ Yuan, Y., Li, Y., Chen, C. P., Liu, S., Rong, N., Li, W., ... & Su, Y. (2015). Polymer-stabilized blue-phase liquid crystal grating cured with interfered visible light. *Optics express*, 23(15), 20007-20013.
- ¹² Fattal, D., Peng, Z., Tran, T., Vo, S., Fiorentino, M., Brug, J., & Beausoleil, R. G. (2013). A multi-directional backlight for a wide-angle, glasses-free three-dimensional di. *Nature*, 495(7441), 348-351.
- ¹³ Kang, S. W., Choi, Y. E., Lee, B. H., Lee, J. H., Kundu, S., Jin, H. S., ... & Komitov, L. (2014). Surface polymer-stabilised in-plane field driven vertical alignment liquid crystal device. *Liquid Crystals*, 41(4), 552-557.
- ¹⁴ Kim, J., Oh, C., Serati, S., & Escuti, M. J. (2011). Wide-angle, nonmechanical beam steering with high throughput utilizing polarization gratings. *Applied optics*, 50(17), 2636-2639.
- ¹⁵ Chen, H., Weng, Y., Xu, D., Tabiryan, N. V., & Wu, S. T. (2016). Beam steering for virtual/augmented reality dis with a cycloidal diffractive waveplate. *Optics express*, 24(7), 7287-7298.

-
- ¹⁶ Kang, S. W., & Chien, L. C. (2007). Field-induced and polymer-stabilized two-dimensional cholesteric liquid crystal gratings. *Applied physics letters*, 90(22), 221110.
- ¹⁷ Lin, Y. H., Wang, Y. J., & Reshetnyak, V. (2017). Liquid crystal lenses with tunable focal length. *Liquid Crystals Reviews*, 5(2), 111-143.
- ¹⁸ Yan, J., Li, Y., & Wu, S. T. (2011). High-efficiency and fast-response tunable phase grating using a blue phase liquid crystal. *Optics letters*, 36(8), 1404-1406.
- ¹⁹ Lin, Y. T., Jau, H. C., & Lin, T. H. (2013). Polarization-independent rapidly responding phase grating based on hybrid blue phase liquid crystal. *Journal of Applied Physics*, 113(6), 063103.
- ²⁰ Xu, D., Tan, G., & Wu, S. T. (2015). Large-angle and high-efficiency tunable phase grating using fringe field switching liquid crystal. *Optics Express*, 23(9), 12274-12285.
- ²¹ Stockley, J. E., Subacius, D., & Serati, S. A. (1999, March). Influence of the interpixel region in liquid crystal diffraction gratings. In *Liquid Crystal Materials, Devices, and Applications VII* (Vol. 3635, pp. 127-136). International Society for Optics and Photonics.
- ²² Yang, D. K., & Wu, S. T. (2006). Fundamentals of liquid crystal devices. John Wiley. Chichester, Hoboken, NJ.
- ²³ Huang, S., Li, Y., Zhou, P., Liu, S., & Su, Y. (2017). Polymer network liquid crystal grating/Fresnel lens fabricated by holography. *Liquid Crystals*, 44(5), 873-879.
- ²⁴ Fergason, J. L. (1985). Polymer encapsulated nematic liquid crystals for di and light control applications. *SID Dig. Tech. Paper*, 16, 68-70.
- ²⁵ Doane, J. W., Vaz, N. A., Wu, B. G., & Žumer, S. (1986). Field controlled light scattering from nematic microdroplets. *Applied Physics Letters*, 48(4), 269-271.
- ²⁶ Doane, J. W., Golemme, A., West, J. L., Whitehead Jr, J. B., & Wu, B. G. (1988). Polymer dispersed liquid crystals for di application. *Molecular Crystals and Liquid Crystals*, 165(1), 511-532.
- ²⁷ Fuh, A. Y. G., Chen, W. K., Cheng, K. T., Liu, Y. C., Liu, C. K., & Chen, Y. D. (2015). Formation of holographic gratings in polymer-dispersed liquid crystals using off-resonant light. *Optical Materials Express*, 5(4), 774-780.
- ²⁸ Huang, B. Y., Lin, S. H., Lin, K. C., & Kuo, C. T. (2017). Switchable Two-Dimensional Liquid Crystal Grating in Blue Phase. *Crystals*, 7(6), 182.
- ²⁹ Liu, Y., Xu, S., Xu, D., Yan, J., Gao, Y., & Wu, S. T. (2014). A hysteresis-free polymer-stabilised blue-phase liquid crystal. *Liquid Crystals*, 41(9), 1339-1344.
- ³⁰ Sun, J., Xu, S., Ren, H., & Wu, S. T. (2013). Reconfigurable fabrication of scattering-free polymer network liquid crystal prism/grating/lens. *Applied Physics Letters*, 102(16), 161106.

-
- ³¹ Lorenz, A., Braun, L., & Kolosova, V. (2016). Continuous optical phase modulation in a copolymer network nematic liquid crystal. *ACS Photonics*, 3(7), 1188-1193.
- ³² Lim, Y. J., Choi, Y. E., Lee, J. H., Lee, G. D., Komitov, L., & Lee, S. H. (2014). Effects of three-dimensional polymer networks in vertical alignment liquid crystal di controlled by in-plane field. *Optics express*, 22(9), 10634-10641.
- ³³ Habibpournmoghadam, A., Wolfram, L., Jahanbakhsh, F., Mohr, B., Reshetnyak, V., & Lorenz, A. (2019). Tuneable Diffraction Gratings in Copolymer Network Liquid Crystals Driven with Interdigitated Electrodes. *ACS Applied Electronic Materials*, 1(12), 2574-2584. (<https://doi.org/10.1021/acsaelm.9b00579>, Copyright © 2019 American Chemical Society)
- ³⁴ Choi, T. H., Choi, Y., Woo, J. H., Oh, S. W., & Yoon, T. H. (2016). Electro-optical characteristics of an in-plane-switching liquid crystal cell with zero rubbing angle: dependence on the electrode structure. *Optics express*, 24(14), 15987-15996.
- ³⁵ Choi, T. H., Woo, J. H., Choi, Y., & Yoon, T. H. (2016). Effect of two-dimensional confinement on switching of vertically aligned liquid crystals by an in-plane electric field. *Optics express*, 24(18), 20993-21000.
- ³⁶ Fujieda, I. (2001). Liquid-crystal phase grating based on in-plane switching. *Applied optics*, 40(34), 6252-6259.
- ³⁷ Kossyrev, P. A., Qi, J., Priezjev, N. V., Pelcovits, R. A., & Crawford, G. P. (2002, May). P-79: Model of Freedericksz Transition and Hysteresis Effect in Polymer Stabilized Nematic Liquid Crystal Configurations for Di Applications. In *SID Symposium Digest of Technical Papers* (Vol. 33, No. 1, pp. 506-509). Oxford, UK: Blackwell Publishing Ltd.
- ³⁸ Bisi, F., Gartland Jr, E. C., Rosso, R., & Virga, E. G. (2003). Order reconstruction in frustrated nematic twist cells. *Physical Review E*, 68(2), 021707.
- ³⁹ Kralj, S., Virga, E. G., & Žumer, S. (1999). Biaxial torus around nematic point defects. *Physical Review E*, 60(2), 1858.
- ⁴⁰ Kralj, S., & Majumdar, A. (2014). Order reconstruction patterns in nematic liquid crystal wells. *Proceedings of the Royal Society A: Mathematical, Physical and Engineering Sciences*, 470(2169), 20140276.
- ⁴¹ Mottram, N. J., & Newton, C. J. (2014). Introduction to Q-tensor theory. *arXiv preprint arXiv:1409.3542*.
- ⁴² Habibpournmoghadam, A., Jiao, L., Reshetnyak, V., Evans, D. R., & Lorenz, A. (2017). Optical manipulation and defect creation in a liquid crystal on a photoresponsive surface. *Physical Review E*, 96(2), 022701.
- ⁴³ Tovkach, O. M., Conklin, C., Calderer, M. C., Golovaty, D., Lavrentovich, O. D., Vinals, J., & Walkington, N. J. (2017). Q-tensor model for electrokinetics in nematic liquid crystals. *Physical Review Fluids*, 2(5), 053302.

-
- ⁴⁴ Lee, G. D., Bos, P. J., Ahn, S. H., & Kim, K. H. (2003). Fast Q-tensor method for modeling the dynamics of defects in a liquid crystal director field. *Physical Review E*, 67(4), 041715.
- ⁴⁵ Lorenz, A. (2010). *Switchable waveguiding in photonic liquid crystal microstructures* (Doctoral dissertation). University Paderborn, Germany.
- ⁴⁶ Schadt, M., & Helfrich, W. (1971). Voltage-dependent optical activity of a twisted nematic liquid crystal. *Applied Physics Letters*, 18(4), 127-128.
- ⁴⁷ Decker, M., Kremers, C., Minovich, A., Staude, I., Miroshnichenko, A. E., Chigrin, D., ... & Kivshar, Y. S. (2013). Electro-optical switching by liquid-crystal controlled metasurfaces. *Optics express*, 21(7), 8879-8885.
- ⁴⁸ Stewart, I. W. (2019). *The static and dynamic continuum theory of liquid crystals: a mathematical introduction*. Crc Press.
- ⁴⁹ Bellini, B., Geday, M., Bennis, N., Spadło, A., Quintana, X., Otón, J., & Dąbrowski, R. (2006). Design and simulation of single-electrode liquid crystal phased arrays. *Opto-Electronics Review*, 14(4), 269-273.
- ⁵⁰ Pavlin, J., Vaupotič, N., & Čepič, M. (2013). Direction dependence of the extraordinary refraction index in uniaxial nematic liquid crystals. *European Journal of Physics*, 34(2), 331.
- ⁵¹ Arrizón, V. M., & Lopez, L. A. G. (2005). Encoding fully-complex transmittance with coupled amplitude-phase liquid-crystal modulator. *Optical Engineering*, 44(7), 070502.
- ⁵² Rickenstorff, C., & Ostrovsky, A. S. (2010). Measurement of the amplitude and phase modulation of a liquid crystal spatial light modulator. *Superficies y vacío*, 23, 36-39.
- ⁵³ Gao, H., Ouyang, M., Wang, Y., Shen, Y., Zhou, J., & Liu, D. (2007). Analysis on diffraction properties of the transmission phase grating. *Optik*, 118(9), 452-456.
- ⁵⁴ Goodman, J. W. (2005). *Introduction to Fourier optics*. Roberts and Company Publishers.
- ⁵⁵ Magnusson, R., & Gaylord, T. K. (1978). Diffraction efficiencies of thin phase gratings with arbitrary grating shape. *JOSA*, 68(6), 806-809.

Appendix A: Optical Transparency of ITO Thin Films

For a transparent conductive oxide (TCO) film such as ITO, the optical transparency can be obtained from^{1,2},

$$T/T_0 \approx e^{(-2d/\delta)} \quad (\text{A.1})$$

where d is the ITO film thickness and δ is the skin depth which determines the geometrical length of electromagnetic absorption in the material. The skin depth δ depends on the operating frequency (ω) regime of ITO; If $\omega < \omega_p$ (where ITO is a good conductor but it shows low transparency), the tradeoff between the optical transparency and the conductivity³ can be seen from skin depth, which can be formulated as^{4,5},

$$\delta \approx \sqrt{2/\omega\mu_0\sigma}, \quad (\text{A.2})$$

where, μ_0 is the free space permeability, and σ is the DC conductivity (which can be calculated from sheet resistance R_s and the film thickness d as $\sigma = 1/(R_s d)$). At a specific thickness d , increasing conductivity costs transparency. Therefore, thin films with higher conductivities usually have much lower transparency. For the operating frequency regime of $\omega > \omega_p$, where ITO film has high transparency with low effective conductivity, δ can be approximated as¹,

$$\delta \approx \frac{2m^* \omega^2 \tau}{Z_\infty e^2 N_0} \quad (\text{A.3})$$

where m^* and e are the electron effective mass and electron unit charge, respectively, $Z_\infty (= 377\Omega/\sqrt{\epsilon_\infty})$ is the high frequency wave impedance of ITO, N_0 is the charge density and τ is the electron relaxation/scattering time. Since the charge density N_0 is a limiting factor in determining the plasma frequency, techniques to enhance the skin depth, hence transparency in the visible range, are usually based on tuning the electron effective mass or the electron mobility, since $\tau \propto m^* \mu_e$, which are also limited by the material processing technology.

Appendix B: LC Dielectric Permittivity Study in a Polymer Stabilized IPS Cell

At voltage off-state ($V = 0$ V), director field was homogeneously aligned in the z-direction in whole LC volume. By increasing voltage the director field was mostly tilted (near to the electrode edges) and rotated (around gap centers) as it was realigned from initial orientation in the z-direction. In Figure B.1, for example evolution of ϵ_{11} distribution with voltage was shown at three different voltages $V = 0, 20,$ and 30 V, respectively, in a polymer stabilized IPS cell. By increasing the value of Q_{11} , the magnitude of ϵ_{11} was increased proportionally according to the relation $\epsilon_{11} = \bar{\epsilon} + \Delta\epsilon Q_{11}$ as discussed in Chapter 1.

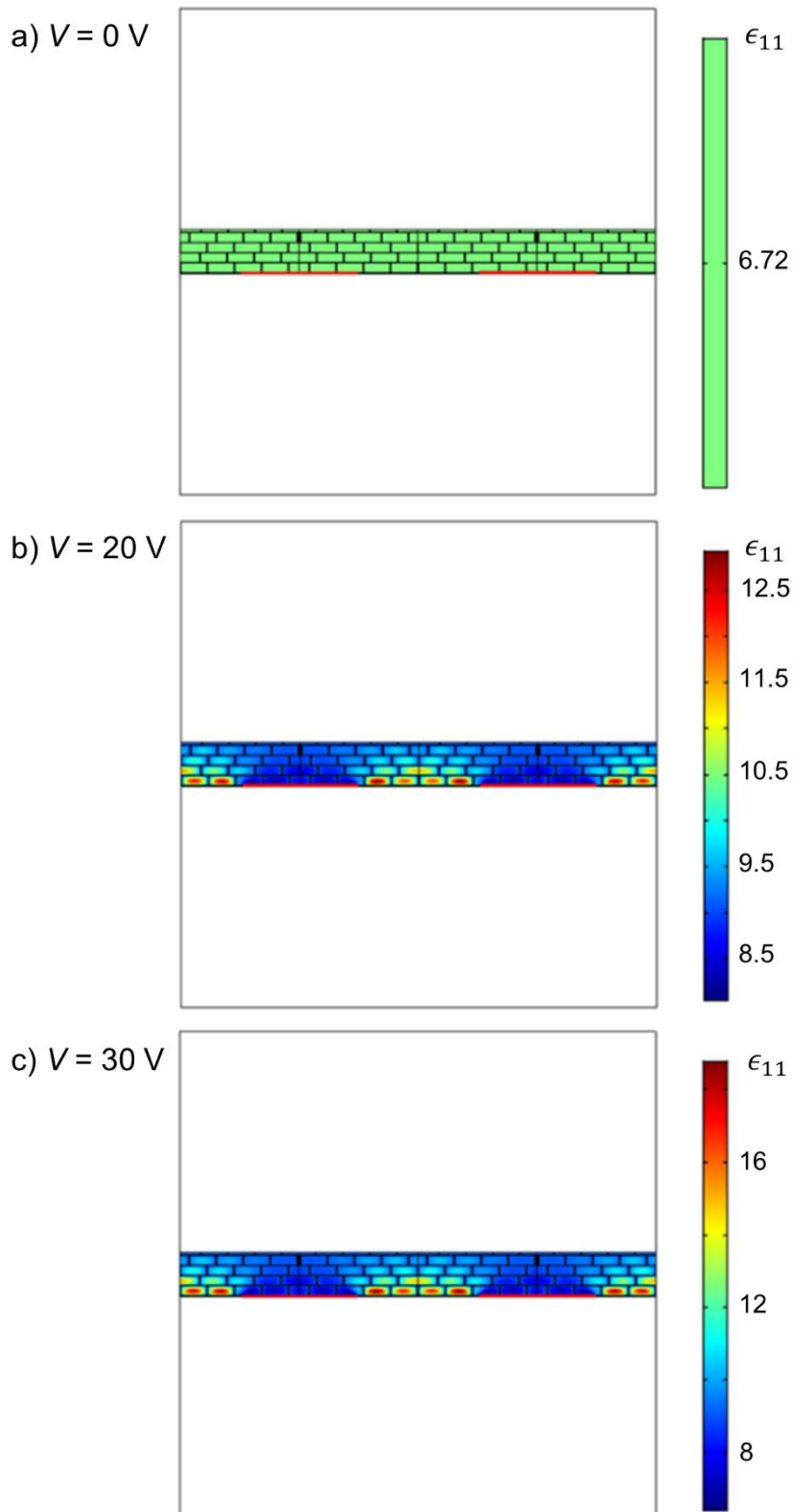


Figure B.1. a)-c): Voltage evolution of ϵ_{11} at the arbitrary voltages $V = 0, 20,$ and 30 V, respectively. The colorbars show the distribution of ϵ_{11} values. For better demonstrations, electrodes were shown in red and larger than their size in simulation.

Appendix C: Alternative Structures of Polymer Stabilized IPS Cells

The simulation geometry (the position of the cuboids in the mesh) was varied. Diffraction gratings were additionally studied for different random distributions of the cuboids. Associated diffraction efficiencies were reported in Chapter 7 as shown in Figure 7.22.

In PNLC IPS Cell, the simulation geometry (the position of the cuboids in the mesh) was varied with imposing different random distributions of the cuboids resembling the polymer structure. In addition to the structure reported in Chapter 7. Associated diffraction efficiencies were reported in Chapter 7 as shown in Figure 7.22.

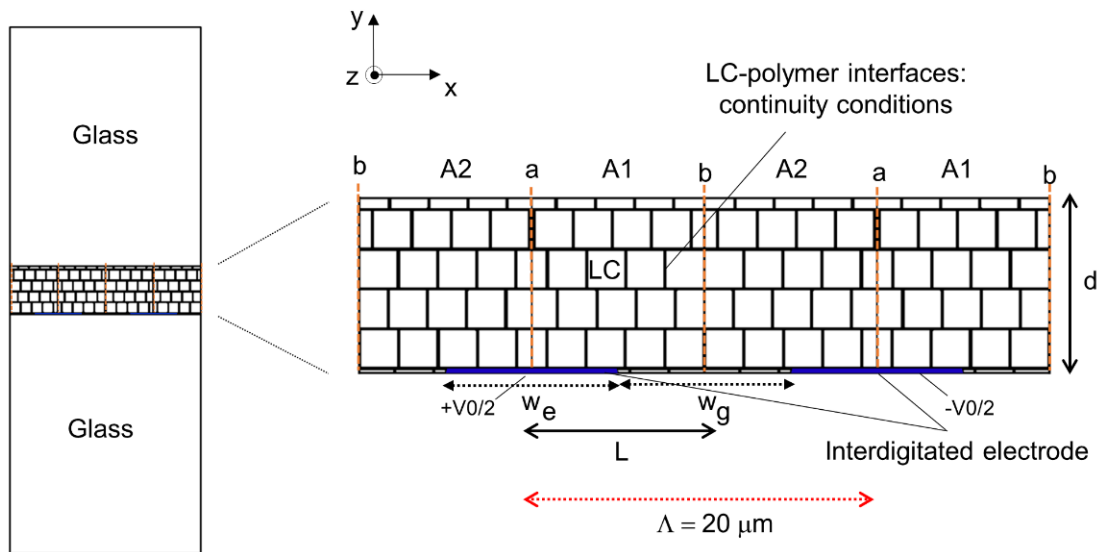


Figure C.1. Geometry of the second supposed polymer structure. The electrode and gap widths i.e., w_e and w_g respectively, both equal to $10 \mu\text{m}$, equal to the cell thickness: $d = 10 \mu\text{m}$.

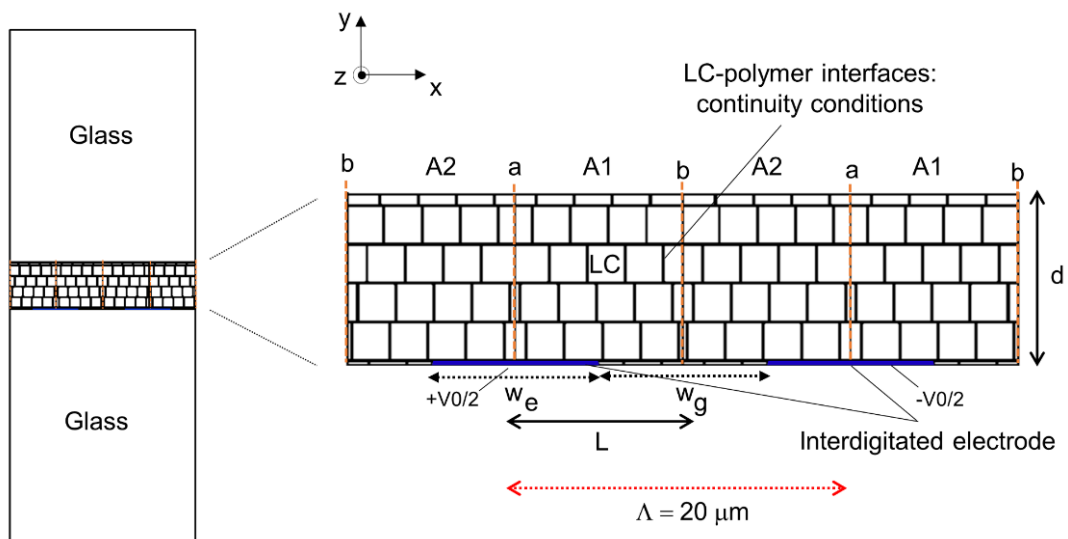


Figure C.2. Geometry of the third supposed polymer structure. The electrode and gap widths i.e., w_e and w_g respectively, both equal to $10 \mu\text{m}$, equal to the cell thickness: $d = 10 \mu\text{m}$.

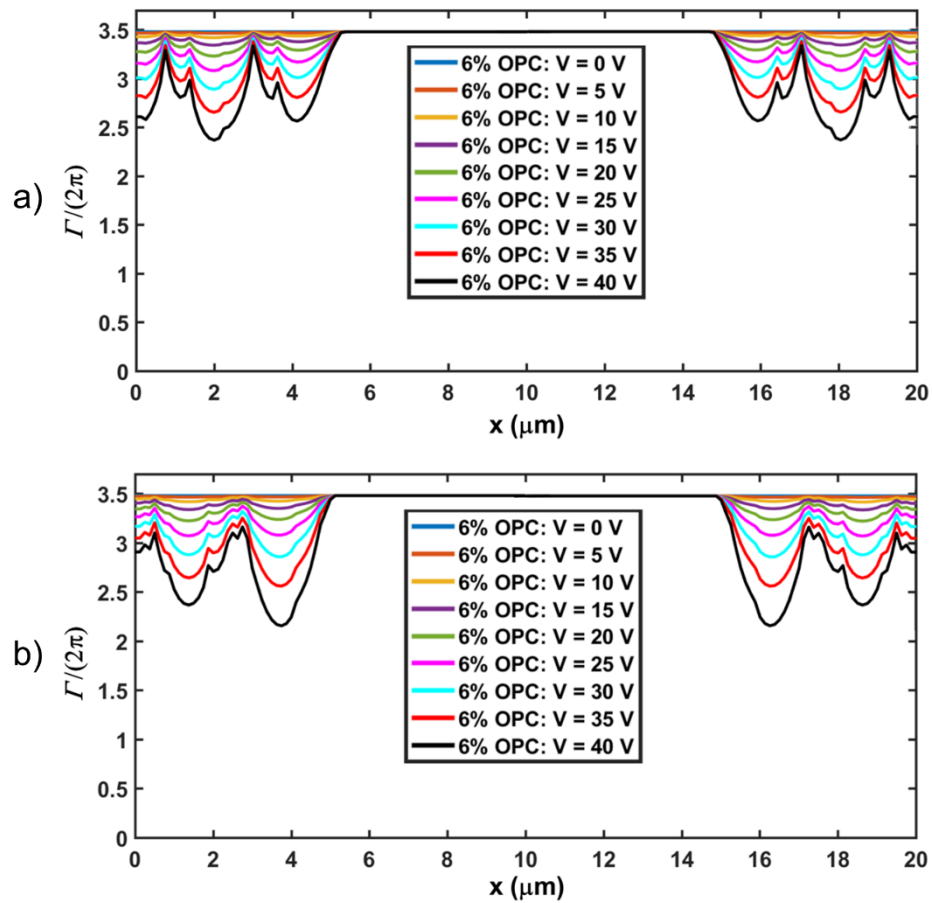


Figure C.3. a), b) Numerically calculated phase change profiles in the IPS test cell filled with polymer cuboids corresponding with the polymer structure shown in the Figures C.1 and C.2, respectively.

References

- ¹ Porch, A., Morgan, D. V., Perks, R. M., Jones, M. O., & Edwards, P. P. (2004). Electromagnetic absorption in transparent conducting films. *Journal of Applied Physics*, 95(9), 4734-4737.
- ² Cai, L. (2019). An On-Glass Optically Transparent Monopole Antenna with Ultrawide Bandwidth for Solar Energy Harvesting. *Electronics*, 8(9), 916.
- ³ Kim, H., Gilmore, A. C., Pique, A., Horwitz, J. S., Mattoussi, H., Murata, H., ... & Chrisey, D. B. (1999). Electrical, optical, and structural properties of indium–tin–oxide thin films for organic light-emitting devices. *Journal of applied physics*, 86(11), 6451-6461.
- ⁴ Colombel, F., Castel, X., Himdi, M., Legeay, G., Vigneron, S., & Cruz, E. M. (2009). Ultrathin metal layer, ITO film and ITO/Cu/ITO multilayer towards transparent antenna. *IET science, measurement & technology*, 3(3), 229-234.
- ⁵ Yasin, T., Baktur, R., & Furse, C. (2011, July). A study on the efficiency of transparent patch antennas designed from conductive oxide films. In *2011 IEEE International Symposium on Antennas and Propagation (APSURSI)* (pp. 3085-3087). IEEE.

Erklärung zur strafrechtlichen Verurteilung

Ich erkläre hiermit, nicht wegen einer Straftat verurteilt worden zu sein, die
Wissenschaftsbezug hat.

(O r t, D a t u m): Magdeburg, den2020

(Unterschrift): Atefeh Habibpournoghadam

Ehrenerklärung

Ich versichere hiermit, dass ich die vorliegende Arbeit ohne unzulässige Hilfe Dritter und ohne Benutzung anderer als der angegebenen Hilfsmittel angefertigt habe; verwendete fremde und eigene Quellen sind als solche kenntlich gemacht.

Ich habe insbesondere nicht wissentlich:

- Ergebnisse erfunden oder widersprüchlich Ergebnisse verschwiegen,
- statistische Verfahren absichtlich missbraucht, um Daten in ungerechtfertigter Weise zu interpretieren,
- fremde Ergebnisse oder Veröffentlichungen plagiiert,
- fremde Forschungsergebnisse verzerrt wiedergegeben.

Mir ist bekannt, dass Verstöße gegen das Urheberrecht Unterlassungs- und Schadensersatzansprüche des Urhebers sowie eine strafrechtliche Ahndung durch die Strafverfolgungsbehörden begründen kann.

Ich erkläre mich damit einverstanden, dass die Arbeit ggf. mit Mitteln der elektronischen Datenverarbeitung auf Plagiate überprüft werden kann.

Die Arbeit wurde bisher weder im Inland noch im Ausland in gleicher oder ähnlicher Form als Dissertation eingereicht und ist als Ganzes auch noch nicht veröffentlicht.

(O r t, D a t u m): Magdeburg, den2020

(Unterschrift): Atefeh Habibpournoghadam

